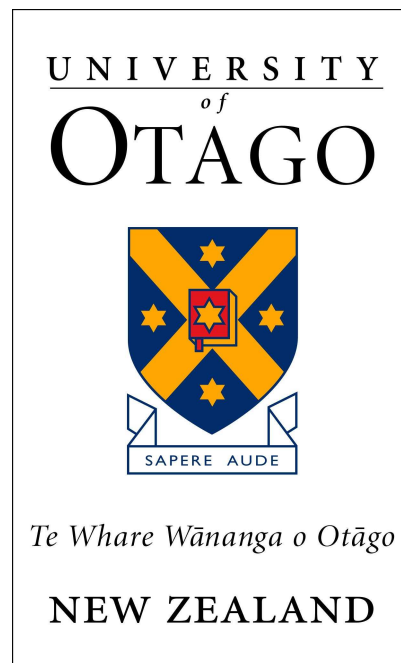


The Power of Many? Linked Wave Energy Point Absorbers

Paul Allen Young

June 30, 2011



Dedication

This thesis is dedicated to my Dad, Christopher Paul Young: one of life's originals.

Abstract

Ocean waves are a largely untapped source of reliable, renewable energy that could help meet the world's demand for electricity while causing very few greenhouse gas emissions. Many distinct wave energy devices are currently under development; a large proportion of these are relatively small devices called *point absorbers* that are likely to need to be installed offshore in reasonably dense arrays. There has been little research published on the design of mooring structures for such arrays and the role that this could play in the performance of the system.

Here we investigate a novel concept of linking point absorber devices together with flexible lines. The concept is explored using an idealised computational model of a chain of surging point absorbers with tension-only linkage forces. Nonlinear drag forces are included and the system is simulated in the time domain to accurately capture hydrodynamic “memory effects”. The system is studied for both monochromatic and polychromatic incident wave fields.

Our results suggest that linking the devices does not offer potential for enhancing the maximum total power capture in a monochromatic wave field, but may yield superior performance in realistic broadband wave spectra. An additional finding is that, for certain parameter choices, individual devices in a chain achieve significantly enhanced power capture in relation to the maximum for a single isolated device. This observation suggests new possibilities for the design of wave energy systems using linked floating bodies to passively transfer power to a main device; an idea that we call “dummy devices”.

Acknowledgements

I think it safe to say that nobody ever undertook a Master's to make friends. I have many people to thank for their support, patience and understanding over the last couple of years.

Firstly, on the academic front I owe a lot to my supervisors Craig Stevens, Patricia Langhorne and Vernon Squire, for doing their best to keep me on the straight and narrow. Special thanks to Craig for being the genesis of the project, and for the intuitive steering throughout – particularly the insistence that it was worth going the extra mile to consider polychromatic wave fields. Pat, thank you for your stellar guidance, your willingness to commit to supervising a topic outside your normal realm, your endless patience, and your tolerance and support of my outside pursuits. Thanks also to Ross Vennel at University of Otago and Murray Smith at NIWA for helpful discussions, and my friends Wynton Moore and Matthew McGovern for reading over the conclusions chapter.

I would like to thank the staff and students of the University of Otago Physics Department, which I have enjoyed being a part of over my undergraduate and postgraduate years. Sandy Wilson deserves special recognition for making life very easy on the administrative side. Inga Smith and Bob Lloyd made days more interesting by always being keen for a conversation about energy issues, as did my office mates Alex, Stefan and Lisa. Outside the department, I also enjoyed the intellectual camaraderie with my compadres in the OPG: Sev Thiebaut, Claire Cohen, Cerys Bailey, Hamish Bowman, and Tim Divett.

Nothing would be possible without the support of my family – Candi, Gemma & Dave, Jess and Julia. Special thanks to my Mum, Candi, for all the love and support over the years. Thank you all for putting up with me through this period of seemingly constant stress and time pressure! Thanks too to the Neilson clan for making me feel like I have a second home.

The same goes for all of my close friends in Dunedin, especially, Scott, Iain, Tosh and Janet. Sometimes when things got AHAF and I just CBF, the only thing that got me through was hanging out with you GCs at our Friday CBIC, or having a hit around on the badminton court. Cheers also to my musical bandmates over this time – life would have been much more

dull without you.

In 2010 I had the great experience of working with a wonderful group of people in the New Zealand Youth Delegation. Thanks to all of you guys for the inspiration and energy, even if it meant I ended up taking a bit longer to finish the old thesis. . .

Finally, thank you to Celia for all the love and support over the last 3 years. Thank you for putting up with the late nights, excessive time spent working and not enough time being spent with you. Yay, it's finally over!

Contents

1	Introduction	1
1.1	The challenge ahead	1
1.2	Why wave energy?	3
1.3	The resource	5
1.4	The technology	9
1.5	The economics	11
1.6	The case for point absorbers	12
1.7	A case for surge?	13
1.8	Linked point absorbers	14
1.9	Research approach and key questions	15
1.10	Thesis overview	16
2	Theoretical background	17
2.1	Linear water wave theory	17
2.1.1	Velocity potential	18
2.1.2	Boundary conditions	19
2.1.3	Linearisation	21
2.1.4	Plane wave solutions	22
2.1.5	Transport of energy	23
2.1.6	Real ocean waves	24
2.2	Wave forces on a floating body	25
2.2.1	Hydrostatics	26
2.2.2	Decomposition of the velocity potential	27
2.3	Radiation force	28
2.3.1	Added mass and radiation resistance	29
2.3.2	Radiated power	30
2.3.3	The Kramers-Kronig relations	31
2.3.4	Formulation in the time domain	31
2.4	Excitation force	32
2.4.1	Diffraction force	32
2.4.2	Small-body approximation	33
2.4.3	Froude-Krylov force	35
2.4.4	Total excitation force	36

2.5	Power capture	36
2.5.1	Mechanical forces	37
2.5.2	1-D linear case	38
2.5.3	Optimisation and resonance	38
2.5.4	Capture width	39
2.6	Nonlinear drag	39
2.6.1	The Morison equation	40
3	Modelling methods and validation	43
3.1	1-D idealisation	43
3.1.1	Incident wave field	45
3.1.2	Hydrodynamic interactions	46
3.2	Master equation	46
3.3	Mooring and linkage forces	46
3.3.1	Two-dimensional effects	47
3.3.2	Mathematical expression	48
3.4	Power take-off	49
3.5	Radiation force	50
3.6	Excitation force	51
3.7	Drag force	52
3.8	Choice of device geometry: semi-submerged sphere	52
3.9	Non-dimensionalised units	53
3.10	Non-dimensionalised master equation	54
3.11	Computational solution method	55
3.11.1	Ramp function	55
3.12	Implementation of memory integral	55
3.12.1	Impulse response function for the semi-submerged sphere	56
3.12.2	Implementation in differential equation solver	60
3.12.3	Computational parameters and performance	61
3.12.4	Discussion	62
3.13	Validation of code under linear conditions	62
3.13.1	Power contributions	64
3.14	Importance of memory integral for lone device	66
3.15	Importance of memory integral for linked chain	68
3.16	Summary of assumptions and conditions	72
4	Lone devices	74
4.1	Linear analysis	75
4.2	Simulation details and parameter space	79
4.3	Resonance	79
4.4	Optimisation of PTO resistance	81
4.5	Other power contributions	84
4.6	Power and capture width matrices	86

5	Linked chains of devices	91
5.0.1	Reference parameter set	91
5.1	Two-device chain	92
5.1.1	Half-wavelength spacing	94
5.1.2	Full-wavelength spacing	96
5.1.3	General spacings	102
5.2	Longer chains	110
5.2.1	Special cases	110
5.2.2	Illustration: three-device chain	113
5.2.3	Secondary interactions	113
5.2.4	Power transfer through linkages and peak power capture for individual devices	122
5.2.5	Novel behavioural regimes	129
5.3	Results for different wave periods	129
5.3.1	Test cases	133
5.3.2	Period-generalised power capture ratio	134
5.3.3	Estimated and actual power capture for particular chains	136
5.4	Results at different wave heights	139
5.5	Results for different PTO resistances	141
5.6	Further explorations	141
5.6.1	Non-uniform spacing and mixed stiffness of mooring and linkage lines	141
5.6.2	Zero resistance on select devices: <i>dummy devices</i>	142
6	Towards a continuous wave spectrum	144
6.1	Methods and technical details	144
6.1.1	Test cases	147
6.2	Comparisons with monochromatic wave fields	147
6.2.1	Lone device	148
6.2.2	Five device chain	151
6.3	Performance of chains compared with lone devices	151
6.3.1	First test case	153
6.3.2	Second test case	153
7	Conclusions	158
	Appendices	161
A	Power transfer by linkage line	162

Chapter 1

Introduction

The world faces difficult challenges to meet its future energy needs and wants without destroying the biosphere's capacity to provide for human sustenance. Improving the prospects of renewable energy technologies is, without a doubt, integral to maintaining humanity's ability to thrive. While it is a fresh actor on the scene, wave energy has a role to play in this new energy future. This thesis looks at a novel extension to current approaches to harnessing wave energy that could potentially increase their viability.

1.1 The challenge ahead

Demand for energy continues to grow globally, and will do for the foreseeable future, assuming no major economic shocks akin to the global financial crisis of 2008. Much of this growth is associated with alleviation of poverty and provision of much-needed energy services in poor regions. Expectations of continued growth in energy consumption are challenged, though, by a number of interacting physical phenomena: most prominent amongst these are the depletion of fossil fuel resources, and human-induced climate change. These are forcing society to rethink how, and why, energy is produced and used.

Today, approximately 69% of global electricity generation and 78% of total final consumption of energy¹ (TFC) is provided from fossil fuels. Nuclear power contributes another 13% of electricity, constituting 3% of TFC, meaning that renewable sources (predominantly biomass and hydro power, and increasingly wind and solar) provide for roughly one fifth of the world's electricity consumption and of its TFC [4, 69].

The need to shift away from dependence on non-renewable resources like fossil fuels and uranium for generating energy is self-evident; it is a matter of when – not if – this must happen. The rate of extraction of any finite resource must begin and end at zero. The extraction rate must therefore, at some point in time, peak at a maximum value and begin an inexorable decline. Predictions can be found dating back many decades (most notably from M. K. Hubbert [42]) that the world would reach “peak oil”

¹TFC excludes the energy lost along the supply chain.

– the maximum production rate of petroleum – sometime near the beginning of the 21st Century. Uncertainties abound as to the precise timing and shape that the peak will have, but detailed analysis of different estimates shows that “there is a significant risk of a peak in conventional oil production² before 2020” [73]. The International Energy Agency’s most recent forecast sees crude oil production climbing slightly to an “undulating plateau” over the next 20 years, but never returning to the high reached in 2006 [5].

What is clear is that from now onwards, fuel prices will stay near current highs or continue trending upwards, and will become more volatile as supply struggles to keep pace with growing demand [5]. Cheap, readily available oil is in decline, and more expensive oil sources (including “unconventional” sources such as tar sands) must be resorted to in order to plug the gap. While relatively little oil is used for electricity generation, there will be flow-on effects of an oil supply crunch to the electricity sector through, for example, increased demand for electric vehicles, as well as other indirect impacts due to the significant role oil plays in the global economy. These market dynamics will in themselves help to stimulate the uptake of renewable energy; indeed they already are, with over half of the total financial investment in new power generation in 2008 and 2009 going towards new renewable capacity³ [69]. Despite these optimistic signs, though, near-term investment in and deployment of renewables must be multiplied many times still in order to avoid potentially catastrophic impacts on society.

One under-appreciated fact is that the building and installation of any new energy infrastructure on a significant scale will itself require the allocation of a significant proportion of the existing energy supply [70] (“energy cannibalism”). In light of this, a smooth “transition” from fossil fuels is made much more difficult and expensive if the world waits until an energy supply crunch is already underway before aggressively ramping up deployment of renewable or alternative energy supply. For this and other reasons, it has been noted by analysts such as Hirsch et al [41] that mitigating disruptive effects of peak oil would require concerted governmental action beginning at least a decade before the peak. Some of these proposed mitigation measures involve substituting coal and natural gas for oil, but these are inherently short-term solutions; while the world’s coal resources are immense, some recent studies suggest that “peak coal” may in fact be reached much sooner than commonly assumed – potentially even within one to two decades [40].

Ultimately, while physical constraints on fossil fuel extraction make a transition to renewable energy inevitable, the profound imperative comes from the need to limit anthropogenic climate change. The release of greenhouse gases (GHGs) from human activities is measurably increasing the heat-trapping properties of Earth’s atmosphere and has been decisively linked to observed warming of the Earth system [61]. This warming includes a rise in the global mean surface temperature of approximately 0.8°C since pre-industrial times, and many associated changes in the biosphere and cryosphere. Carbon dioxide is the most important of the anthropogenic GHGs, estimated to account

²This is defined by the authors of [73] to include crude oil, condensates and natural gas liquids.

³Again, “renewable” here includes hydro and biomass power.

for more than 3/4 of annual emissions when these are weighted in terms of warming potential. Of those CO₂ emissions, roughly 3/4 again comes from the burning of fossil fuels, meaning that energy generation is responsible for more than half of total weighted emissions [61].

Without concerted global action to reduce GHG emissions, the world will almost certainly see continuing warming and harmful impacts that will dwarf those experienced so far. Recognising the immense threats that climate change poses, countries of the world agreed in 1992 through the United Nations Framework Convention on Climate Change to stabilise atmospheric GHG concentrations “at a level that would prevent dangerous anthropogenic interference with the climate system” [1]. In line with ongoing advice from the Intergovernmental Panel on Climate Change, this has now been formally expressed as a goal of limiting global average temperature rise to 2°C above the pre-industrial level, with the prospect of strengthening this to 1.5°C in the future [79]. However, current pledged targets for emissions reductions fall far short of what is required to achieve even the weaker target; according to Climate Action Tracker, the best estimate of the temperature rise by 2100 if all current pledges are met is 3.2°C above the pre-industrial level [2]. There is a high probability that the true temperature rise would be larger, especially when one considers that this estimate does not incorporate the effects of many known warming feedbacks in the climate system. Paleoclimate evidence shows that today’s atmospheric GHG concentrations are associated with far higher temperatures in the past, and may already be sufficiently high to trigger catastrophic effects such as the gradual melting of the Greenland Ice Sheet if they are not brought down rapidly [38].

The rapidly closing window of opportunity, combined with the failure of the world’s governments to deliver meaningful action thus far, has led many scientists to conclude that “there is now little to no chance of maintaining the rise in global mean surface temperature at 2°C” [7]. In crude terms, preserving what chance remains will require that all the low carbon solutions the world can muster be rolled out in as short a time-frame as possible. While the scale of action required is enormous, several studies claim to demonstrate that near-complete “decarbonisation” of global energy systems by 2050 is technically and economically achievable with known technologies [22, 46, 18, 53, 84, 70]. These reports indicate that there is no silver bullet solution for the world’s energy woes; meeting the challenges laid out above will require a wide range of renewable energy and energy efficiency technologies, in conjunction with policy reform to address energy demand. Commercially mature wave energy technology will make the task that little bit easier.

1.2 Why wave energy?

The world’s oceans are an untapped source of power that could add to the renewable energy portfolio, which includes wind, solar, hydro, geothermal and biomass. One of the clear positives in diversifying this portfolio is that it provides more options for meeting energy needs in specific geographical contexts. Another general advantage comes from addressing a core setback of wind and solar power: their intermittency and variability. As

renewables build up to higher penetration of the energy mix, electricity grid operators will face growing difficulties in tailoring the power supply to meet real-time demand. Large-scale energy storage (for example using pumped hydro reserves) and demand-side management will help to address the problem, but both will come at a cost. A diversified supply will have less overall variability than a supply with all its eggs in one basket.

The marine environment offers four distinct renewable energy sources (not including offshore wind): waves, tidal (and other) currents, thermal gradients, and salinity gradients. All four are undergoing research and development, with most attention being devoted to the first two [52]. The categories are sometimes confused and lumped together in public discourse – particularly wave and tidal stream – but each requires unique technology. This thesis focuses exclusively on wave power.

All renewable energy options are subject to specific advantages and disadvantages. Some points worth considering with regards to wave energy are:

- It has a significantly higher energy intensity than solar or wind energy [31], which means it should be possible to attain the same power capacity from a smaller overall structure (assuming similar conversion efficiencies can be achieved). This is advantageous both economically and in terms of energy return on energy investment (EROEI), which will become an increasingly important measure in an energy-constrained world. The energy payback time has been estimated for one example device to be in the vicinity of 1-2 years [13], and the life-cycle GHG emissions per unit of energy are thought to be amongst the lowest of any energy technology [22].
- Because waves are generated by winds and then transmitted over large distances with very little energy loss, conditions can be predicted reasonably well several days in advance by integrating the global wind field [72].
- The wave resource is also more continuous than wind. However, this advantage does not appear to manifest itself in estimates of capacity factor⁴ for wave farms based on current technologies, which are roughly the same as for wind farms: 20–50% dependent on technology and site [13, 21, 23].
- Wave energy will not compete with land use activities such as food production, residential development and aesthetic appreciation. However it will need to contend with other marine activities such as fishing, shipping, aquaculture and recreational use (especially surfing). In some cases it may also be in competition with offshore wind energy developments, although there is potential for synergy [76].
- Considerable uncertainty remains around the environmental impacts of large-scale wave energy installations. The list of potential effects include some positives (for example, structures effectively providing an artificial reef for marine life) along with negatives [17]. There is a common view that the overall environmental impacts will

⁴A device's capacity factor is its annual average power production as a proportion of its rated power capacity.

be comparable with, and possibly smaller than, those for other energy technologies. However, more research is clearly needed in order to be able to fully understand and quantify environmental effects; particularly the indirect impacts due to the removal and dissipation of significant amounts of energy [37]. It is generally thought that devices situated offshore will have greatly reduced impacts compared with those situated nearer to the shoreline [78].

- It is generally thought that there will be less public opposition to wave farms than to onshore wind farms due to the lesser visual impact. However, this may not always prove to be the case, as research shows that there are many other social factors at play in determining the level of public acceptance of wave energy developments [56]. Reducing the unknowns through prior research into the impacts is an important factor in addressing opposition.
- Wave energy devices offer the prospect of direct mechanical desalination of seawater, which could in principle deliver very high overall efficiency due to the removal of lossy energy conversion steps [17].

1.3 The resource

Wave energy is solar in origin; it is generated by winds, which are in turn created by temperature gradients due to absorption of energy from the Sun. Only a very small percentage of the total incident solar energy flux is ultimately transformed to wave energy but, as mentioned in the previous section, this small percentage manifests with very high energy density. The quantity commonly used to express the power available at a site is the *wave energy flux*; this is the power per metre width of wavefront⁵. Original solar power levels on the order of 100 W m^{-2} can give rise to instantaneous wave energy fluxes of over 1,000 kW per metre of wavefront [83].

Figure 1.1 shows a global map of annual mean wave energy flux, \bar{J} , based on modelled data. The world's best wave resources are situated in the 30–60° latitude bands, where the strongest winds blow. The threshold at which offshore sites become economic for wave energy extraction has been estimated at $\bar{J} \approx 20\text{--}30 \text{ kW m}^{-1}$ [3, 72], although this could come down in the future. Many sites have been identified where $\bar{J} > 100 \text{ kW m}^{-1}$ [17]. Moving from the deep sea towards the shoreline, energy flux levels are normally progressively reduced as power is dissipated due to friction with the seabed, although in certain instances the local bathymetry can have a focusing effect.

The total worldwide wave energy resource is not a well constrained quantity. The most commonly cited assessment of the “natural resource” states a range of 9,000–90,000 TWh per year⁶ [17]. The amount that could realistically be extracted will certainly be much smaller. Several estimates exist for this, but comparisons are problematic due to unclear definitions, assumptions and methodologies.

⁵In other words, the power transported through a surface parallel to the wavefront, of unit width and extending from the ocean floor to the surface.

⁶1 TWh (terawatt-hour) = 3.6 GJ.

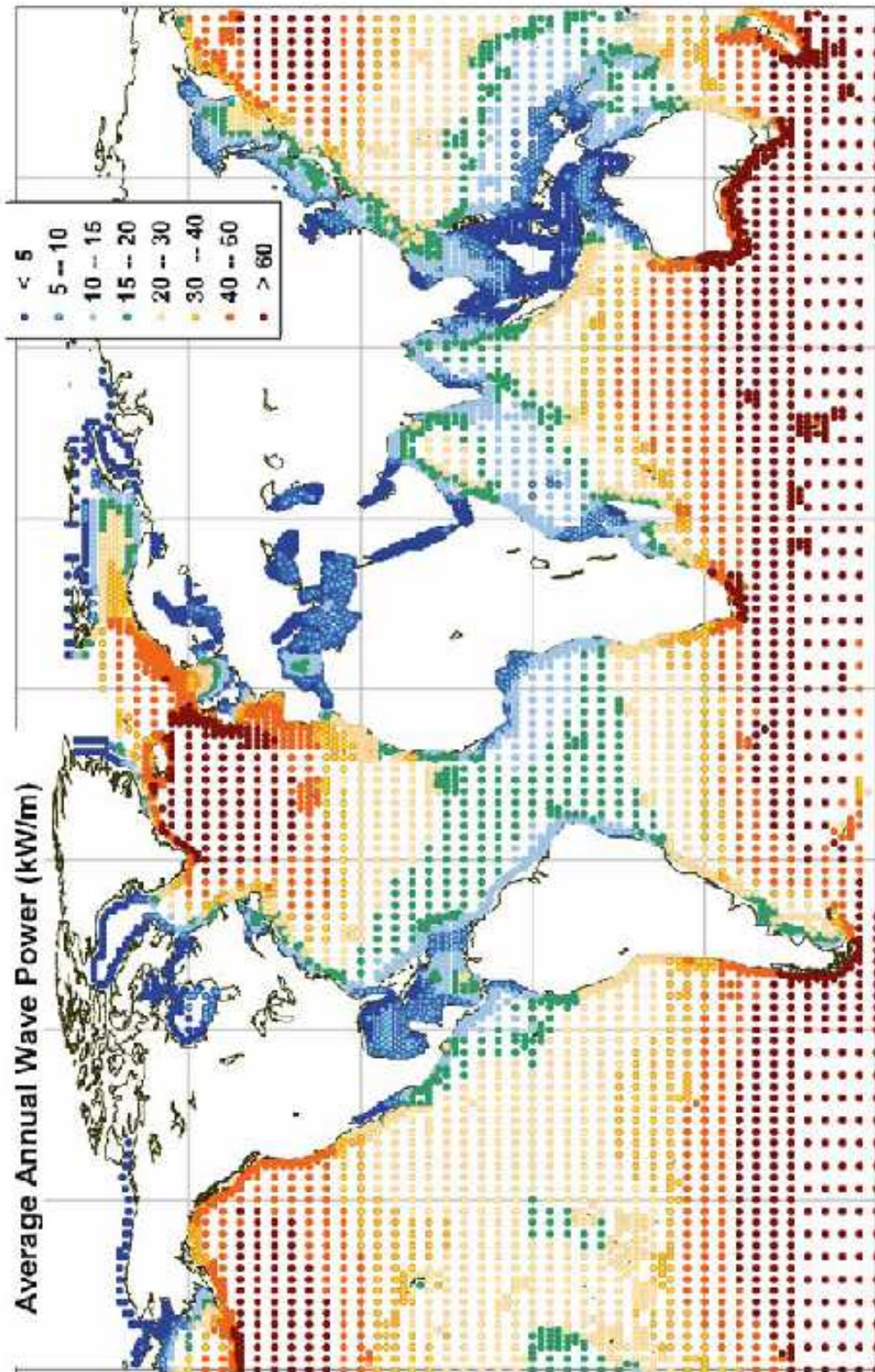


Figure 1.1: Annual mean wave energy flux magnitude in kW m^{-1} , reproduced from Cruz (ed.) [17]. Data from ECMWF WAM model archive; calibrated and corrected by Fugro OCEANOR against a global buoy and Topex satellite altimeter database.

- A report by Thorpe in 1999 claimed that the “economic contribution” of wave energy could be greater than 2,000 TWh yr⁻¹ [78].
- The Wavenet report in 2003 gave a “technical resource” – disregarding economic considerations but taking into account resource accessibility and expected capture and conversion efficiency of devices at the time – of 145–770 TWh yr⁻¹ [3].
- A report by the Carbon Trust in 2006 stated a “practical worldwide wave energy resource” – allowing for “practical and economic factors that combine to make developments commercially attractive” – of 2,000–4,000 TWh yr⁻¹ [13].
- In its Fourth Assessment Report in 2007, the IPCC estimated a technical potential of 4,400 TWh yr⁻¹, using an assumed conversion efficiency of 40%, and stated that the total economic potential will be well below this but did not quantify it [71].

To put these figures in perspective, the IEA reports that worldwide electricity supply in 2008 was 20,181 TWh [4]. The above estimates suggest that at the optimistic end of the scale, it might be possible for wave energy to provide for roughly 10–20% of current world electricity demand. It is important to note that in these assessments, the offshore resource is found to be 1–2 orders of magnitude larger than the shoreline and near-shore resource.

New Zealand has an exceptional wave energy resource by world standards; this can be seen in Figure 1.2. It is slightly unfortunate that the best resource is around the southern coast of the South Island, far from New Zealand’s main population centres. However, economically viable wave energy fluxes are observed over much of the country, including almost the entire West Coast. Smith et al give estimates of New Zealand’s total resource on the order of 1,000 TWh yr⁻¹ [72]. A study by Power Projects Limited claims that up to about 60 TWh yr⁻¹ is practically exploitable, stating that “sites are abundant and geographically dispersed” [52]. This figure exceeds current New Zealand electricity consumption⁷, which was 40.52 TWh in 2008 [4]. Studies done to estimate the wave energy potential for the UK and the US arrived at figures of 13% and 10% of 2008 national electricity consumption, respectively [78, 9, 4].

The mean wave energy flux is only a first indicator of the suitability of a site for power generation. Variability on different time scales is another important consideration. In New Zealand, the available power is demonstrably higher in winter months [72], which is a good match for the country’s electricity demand pattern. The same seasonal variation is true over virtually the entire world, and is even more pronounced in the Northern Hemisphere [17]. Hindcast models by NIWA show that within the annual pattern, sites in New Zealand do experience significant inter-annual variation in their monthly mean wave energy fluxes [72]. In general, relatively rare extreme conditions can make a significant contribution to mean power level at a site, but this contribution will be impossible to harness effectively and, due to the potential for damage, will likely be considered more of a liability than a blessing.

⁷Note that consumption figures do not include transmission losses.

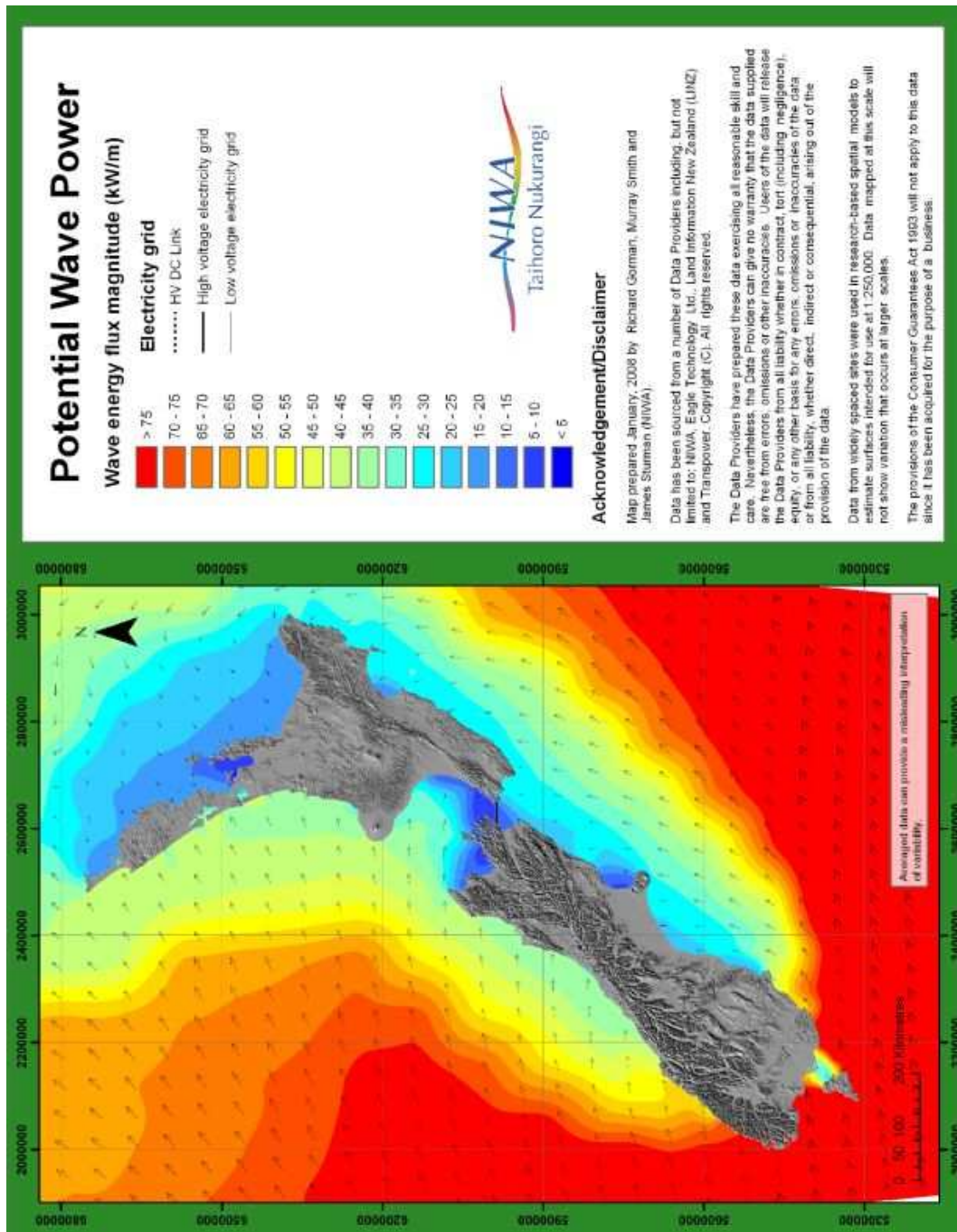


Figure 1.2: Annual mean wave energy flux magnitude in kW m^{-1} around New Zealand, reproduced from Smith et al [72]. Arrows indicate the direction of energy propagation.

1.4 The technology

While the idea of harvesting energy from the oceans can be traced back centuries, serious research into the topic only began in the 1970s in response to the oil price crisis [27]. One of the first device designs to come to prominence and demonstrate that high efficiencies could be achieved – under lab conditions, at least – was the Salter Duck, developed by Professor Stephen Salter and colleagues at the University of Edinburgh [66]. Commercial interest and research funding died away through the 1980s, but picked up again as problems with fossil fuel-based energy production returned to the fore. There is now a large and growing number of companies developing wave energy converters; as at 23 February 2011, the European Marine Energy Centre (EMEC) had 115 independent developers listed on its website [25]. EMEC provides an offshore testing site in Orkney, Scotland; this is one of several such sites to have hosted full-scale devices for testing.

It is a more complex task to extract energy from waves than from the unidirectional flows of the wind and the tides. For this reason, there is much diversity in the design and properties of wave energy devices under development, and the industry is yet to settle on a clear leader. At this point there is even divergence amongst authors on schemes for classifying the devices [27, 20, 39, 17, 72, 52, 25]. Problems arise due to the mixing of classifications for distinct attributes, with the result being that categories are not mutually exclusive. In her PhD thesis, Price gives a detailed analysis of existing classification schemes and proposes a comprehensive new one of her own to address the problems identified [64]. A simple overview is more appropriate here, and we follow the approach of Harris et al in [39].

Most devices can first be described by one of these “operating principles”:

- *Oscillating Water Columns (OWCs)*. These consist of a chamber of air trapped above the water line. Waves incident on the device cause the water level inside the chamber to oscillate, alternately expelling and drawing in air through an attached Wells turbine, which maintains a constant rotation direction through the in- and out-strokes.
- *Overtopping devices*. These are structures consisting of a reservoir above sea level, which is fed by waves running up a focusing ramp. The resulting head is used to drive a turbine as water is expelled through an outlet at the bottom of the reservoir.
- *Oscillating bodies*. In these devices, the wave motion induces translational or rotational motion in one or more component(s). Power take-off mechanisms typically use hydraulic systems or direct drive linear generators.

A second distinguishing feature is the location of the device in terms of the water depth, which is generally classed as either shoreline, near-shore (depths of up to ≈ 25 m) or offshore (depths > 40 m).

The third attribute commonly used for categorising is the orientation or directionality of the device:

Device name	Operating principle	Location	Orientation
Limpet	OWC	Shoreline	Terminator
Wave Dragon	Overtopping	Near-shore/ offshore	Terminator
Pelamis	Oscillating body	Offshore	Attenuator
Archimedes Wave Swing (AWS)			Point absorber (attached)
WET-NZ device			Point absorber (moored)

Table 1.1: Classification of a selected sample of commercial wave energy devices.

- *Terminators.* These are devices that extend parallel to the wavefront and effectively terminate the wave. Overtopping devices and shoreline OWCs are the prime examples.
- *Attenuators.* These are long, compliant or articulated structures that orientate in the direction of the incident waves, with the power typically captured from the relative motion between adjacent segments of the device.
- *Point Absorbers.* These are oscillating bodies that are small in both horizontal directions relative to incident wavelengths. The majority of designs are axisymmetric (i.e. have a vertical axis of symmetry) and operate in *heave* (vertical oscillations), and thus can absorb energy from waves incident from any direction. This is not exclusively the case, however. *Moored* point absorbers are “self-reacting”, with power extracted from the relative motion between two active components, while *attached* point absorbers react against a fixed, floor-mounted structure.

There are several novel designs (Anaconda, for example) that do not fit clearly into any of the categories defined above. Some sources list an additional category of “near-shore surge” devices. A leading example is Oyster: essentially a large flap hinged on the seabed at a depth of ≈ 12 m, which pumps water onshore to drive a hydroelectric turbine. In shallow waters the *surge* motion⁸ of the water particles dominates, and it has been found that surging devices can perform better at shallow depths than offshore, in spite of the reduced overall incident energy flux [34]. Devices such as Oyster could aptly be classified as point absorbers despite differences with the more common offshore, axisymmetric examples.

In Table 1.1, several examples of commercial wave energy devices are classified according to the above scheme. For further information, good reviews of existing design proposals are given by Falcao [27] and Drew et al [20].

Of all the developers surveyed, the only one to have made performance data of their device publicly available is Pelamis Wave Power Ltd. Figure 1.3 shows an “example of a Pelamis power table” (which we refer to herein as a *power capture matrix*) published on

⁸Surge refers to motion in the direction of wave travel.

		Power period (T_{pow} , s)																
		5.0	5.5	6.0	6.5	7.0	7.5	8.0	8.5	9.0	9.5	10.0	10.5	11.0	11.5	12.0	12.5	13.0
Significant wave height (H_{sig} , m)	0.5	idle	idle	idle	idle	idle	idle	idle	idle	idle	idle	idle	idle	idle	idle	idle	idle	idle
	1.0	idle	22	29	34	37	38	38	37	35	32	29	26	23	21	idle	idle	idle
	1.5	32	60	65	76	83	86	86	83	78	72	65	59	53	47	42	37	33
	2.0	57	88	115	136	148	153	152	147	138	127	116	104	93	83	74	66	59
	2.5	89	138	180	212	231	238	238	230	216	199	181	163	146	130	116	103	92
	3.0	129	198	260	305	332	340	332	315	292	266	240	219	210	188	167	149	132
	3.5	-	270	354	415	438	440	424	404	377	362	326	292	260	230	215	202	180
	4.0	-	-	462	502	540	546	530	499	475	429	384	366	339	301	267	237	213
	4.5	-	-	544	635	642	648	628	590	562	528	473	432	382	356	338	300	266
	5.0	-	-	-	739	726	731	707	687	670	607	557	521	472	417	369	348	328
	5.5	-	-	-	750	750	750	750	750	737	667	658	586	530	496	446	395	355
	6.0	-	-	-	-	750	750	750	750	750	750	711	633	619	558	512	470	415
	6.5	-	-	-	-	750	750	750	750	750	750	750	743	658	621	579	512	481
	7.0	-	-	-	-	-	750	750	750	750	750	750	750	750	676	613	584	526
	7.5	-	-	-	-	-	-	750	750	750	750	750	750	750	750	686	622	593
	8.0	-	-	-	-	-	-	-	750	750	750	750	750	750	750	750	690	625

Figure 1.3: Power capture for the Pelamis wave energy converter in kW versus power period in seconds and significant wave height in metres (available from <http://www.pelamiswave.com/>).

the company’s website. Here the mean power captured by the device is plotted against *significant wave height* and *power period*. Notice that the device is idle in conditions of very low wave height, and shuts off in conditions of excessively steep waves in order to avoid damage. The device has a rated capacity of 750 kW and once this is reached, power shedding occurs. It is not stated whether these data are derived from numerical modelling, scale-model testing, or otherwise.

1.5 The economics

The wave energy industry has many technical challenges still to overcome if it is to be able to deliver a meaningful contribution to the world energy supply. In an overview article, Mueller & Wallace summarise the key challenges facing both the wave and tidal energy industries in seven areas, which they label predictability, manufacturability, installability, operability, survivability, reliability and affordability [58]. They identify survivability, reliability and affordability as the most significant objectives. There is an inherent tension here, since designing a device to higher survival specifications necessarily adds to the cost. This, of course, is something that all energy technologies must contend with, but the nature of the ocean environment makes it especially relevant to marine energy.

Ultimately, the cost at which electricity can be reliably delivered to the grid is the

most important metric in assessing the viability of wave energy devices. In basic terms, capital costs and operating and maintenance costs must be weighed up against performance. All three factors are currently subject to uncertainties in how they will scale from single devices up to commercial-scale installations, which makes estimating the electricity costs for any device hard to do with accuracy. Also, as is the case with all renewables, the cost is highly site specific.

The IPCC Special Report on Renewable Energy Sources and Climate Change Mitigation gives a current levelised cost⁹ range for ocean energy (including tidal) of 12–32 UScent₂₀₀₅ kWh⁻¹ – some way above that of non-renewables (3–10 UScent₂₀₀₅ kWh⁻¹ and the more competitive renewables like hydro, wind and geothermal [22]. Of course, the cost is expected to come down significantly as wave energy technology advances along its “learning curve” [13], with some predicting that it could ultimately be one of the cheapest options post-2020, on a par with onshore wind [18]. Meanwhile, the cost of coal-based electricity production will likely rise due to both resource depletion and pricing of CO₂ emissions.

The large uncertainties around price estimates make it difficult to pick a winning device design at this point in time. Proponents of the various designs on offer are all quite adept at talking up the advantages of theirs in particular. It is quite possible that different device types will be better suited to different environments, and a “different horses for different courses” outcome may prevail. Currently, while the Pelamis attenuator has received attention as a frontrunner, it seems that the biggest share of devices under development are point absorbers [25], and there are many good reasons to believe that these will play a prominent role in the future.

1.6 The case for point absorbers

Point absorbers hold promise for delivering a given power output from structures that are “more compact and contain less material” than the alternatives [81]. All other things equal, this lower structural volume means lower capital costs. Of course, the volume is far from the only factor determining the overall cost, but it is a significant one, and moored point absorbers in particular offer prospects for minimising the “dead volume” not involved in power absorption.

One of the reasons that point absorbers ought to perform well for their size is that they are capable of absorbing more power from the wave field than the amount contained in the width of wavefront directly incident upon them: a result proven independently by several authors in the 1970s [27]. The absorption can be understood in terms of destructive interference between an incident plane wave and a ring-shaped wave radiated by the moving body [11]. In more detailed terms, the theoretical maximum *capture width*¹⁰ of an axisymmetric point absorber depends only on the wavelength of the incident waves, and not on the dimensions of the device. A related analogy here is a radio antenna,

⁹This is “the ratio of total lifetime expenses versus total expected outputs, expressed in terms of the present value equivalent” [6].

¹⁰The width of wavefront carrying as much power as the device captures.

for which the absorbed or transmitted power is independent of the wire diameter. An implication of this result is that, as Falnes has put it, “the smaller the structural volume of the converter is, the larger the ratio between the potentially converted power and the mentioned volume” [30].

Arguments like the above can be misleading, however. In practise, for a point absorber to attain a power capture close to its theoretical limit at typical ocean wavelengths would require unrealistically large motion amplitudes [62]. The smaller the device and the longer the wavelength, the larger the motion amplitude needed to realise the optimum power capture. Even if we disregard constraints on the motion¹¹, achieving the optimum power capture would require very low damping, giving an undesirably sharp resonance peak. Indeed, the narrow bandwidth of point absorbers relative to larger devices is a widely acknowledged attribute that was recognised early on as a key issue [27]. Furthermore, heaving bodies cannot attain resonance at typical ocean wavelengths unless they are very large¹².

In spite of the above criticisms, the prospects for point absorbers delivering the cheapest electricity remain good; this is backed up by evidence from independent studies [21, 78]. Researchers have devised various “control strategies” that can partially overcome the above challenges and improve performance at the dominant ocean wavelengths – Falnes gives an overview of these in [30]. Regarding motion constraints, Budal has shown that – for heaving bodies at least – these impose an upper bound on the maximum-power-to-volume ratio, which is approached as the body volume tends to zero [29]. In addition to lower material requirements, smaller-scale devices will likely hold the advantages of easier and cheaper construction, transport and deployment. An aggregate supply from a large number of small devices should have greater reliability than one from fewer large devices. And finally, offshore devices in general are appealing since they will have access not just to higher power levels, but also to a far larger total resource.

The case for point absorbers highlights a point that dampens aspirations of harnessing a large proportion of the available wave energy resource: economic realities make it likely that the most competitive designs will actually leave a significant proportion of the available power in the ocean. Research is vital to attempt to increase the power capture from the most economical designs.

1.7 A case for surge?

In this study we examine a system of point absorbers with the power take-off acting on the surge motion. As mentioned previously, the majority of point absorber designs being investigated consist of axisymmetric, heaving devices. Some of the self-reacting designs – such as P-S Frog [81] and the WET-NZ device [50] – exploit multiple modes including surge and *pitch* (rotation in the plane perpendicular to the wavefront). There are also the devices in the near-shore surge category discussed earlier, which are most

¹¹Constraints could either be physical or due to the range of validity of the theory.

¹²In [27], Falcao shows that the required radius of a heaving hemisphere to give a resonant period of 10 s is 26.2 m.

often actually pitching flaps with a pivot point on the sea bed. While there appears to be relatively limited interest in pursuing surge motion for point absorbers, there are some factors that would seem to make it appealing:

- The theoretical maximum capture width for surge is twice that for heave [17].
- Unlike for heave, small surging devices can be made resonant at the dominant ocean wavelengths assuming an appropriate spring can be provided.
- Constraints on surge motion are less obvious than for heave, where large motion amplitudes could imply the device leaving the water.
- The work of Folley has shown that surging devices will be very well suited for near-shore deployment, and there are indications that this may ultimately be the most economical environment [33, 34].

1.8 Linked point absorbers

Point absorbers will each deliver a small power output and will therefore need to be installed in large arrays containing many units, potentially quite densely packed. This has implications for performance, since the devices will all interact hydrodynamically through the radiated and diffracted waves; again, there is an analogy in this instance with the interactions amongst a network of radio antennae. While the dynamics of arrays have received considerable theoretical attention (see reviews by McIver [54] and Newman [60]), the vast majority of experimental research to date has been focused at the more simple (and cheap) level of studying isolated devices. Advancing understanding of array dynamics is becoming increasingly important as we near the cusp of the first commercial-scale deployments.

While the issue of hydrodynamic interactions is well-represented in the literature, to quote from Vicente et al [80], “little attention seems to have been devoted in the published literature to the mooring design of free-floating point absorbers in dense arrays.” They go on to state that “in such cases, it may be more convenient and economical that only elements in the periphery of the array are directly slack-moored to the sea bottom, while the other elements of the array are prevented from drifting and colliding by connections to adjacent elements.” In other words, the fewer moorings to be installed on the seabed, the better. In their study, the authors examine an array of identical point absorbers located at the grid points of an equilateral triangular grid. The devices considered are spherical buoys with power take-off on the heave motion. Devices on the periphery of the grid are connected to the seabed by a spread set of slack-mooring lines, and a weight is located at the centre of each triangle to pull the three devices towards each other and keep the inter-body mooring lines under tension. While the results of the study are difficult to draw broad conclusions from, they point to the possibility that a mooring system of the kind described could enable the devices to achieve an overall higher power capture than they would if each were moored individually.

In an extensive literature search, the paper by Vicente et al (along with a smaller preceding one by the same authors) was the only serious research found into the idea of linking point absorbers in an array¹³. The only earlier precedent found was a 1983 paper by Carter & Hurdle [14], in which the authors proposed a system of surging bodies located in a square grid, with the power take-off somehow operating on connections between adjacent bodies. However, in the paper itself results were only presented on the properties of a single “lenticular” device. No further work by the authors on the proposed scheme could be found – only a less-than-positive response from Thomas & Evans [77]. Another 2009 paper that has relevance to the linkage concept is one by Engstrom et al [24], in which the authors show that the power capture of a heaving buoy-type device can be enhanced 30–60% by connecting a submerged body of neutral buoyancy in between the buoy at the surface and the power take-off reaction point at the seabed.

While the linkage concept has received little attention – especially for surging devices – the idea appears to have merit and certainly warrants further investigation. In addition to the potential economic advantage of fewer moorings, which are estimated to be a significant component of the capital cost [6], there are broader questions to answer around the possible dynamic effects of various mooring designs. The design of mooring systems for wave energy devices is often discussed in the context of minimising impediment to power capture; the motivation for this research is to see whether in fact a mooring system provides an opportunity to enhance performance.

1.9 Research approach and key questions

An array of point absorbers is a fairly complex system, which will be made more so by the inclusion of material linkages between devices. Given the lack of research into the linkage concept, a sensible starting point is to apply it in an idealised model that is relatively simple and “no-frills”. This way, the effects of the linkages are easily discernible, and a broad investigation of the idea may be carried out to motivate further, more detailed work. That is the approach that we took in this project.

The key questions guiding the work were:

- Is there potential for a system of linked point absorbers to achieve enhanced power output relative to the same number of devices acting in isolation?
- In particular, can performance be enhanced for the longer wavelengths in the ocean’s dominant energy-bearing range, for which small point absorbers perform relatively poorly? Could the multiple size scales of a connected array allow us to tap into “the best of both worlds”?
- Does a linked system offer potential for achieving a broader bandwidth than single devices?

¹³We note that this paper was published in 2009, which was the year following the commencement of this research project.

- Does a linked system exhibit other interesting dynamics?

1.10 Thesis overview

The research that was conducted is presented in this thesis as follows:

- In Chapter 2 we summarise the relevant theoretical background to the study of wave energy devices.
- In Chapter 3 we specify the details of the scheme investigated, describe the computational methods used, and demonstrate the validity of the numerical model.
- In Chapter 4 we present and analyse results on the performance of a single model device forced by a sinusoidal wave.
- In Chapter 5 we present and analyse results on the performance of a linked chain of model devices forced by a sinusoidal wave.
- In Chapter 6 we present and analyse results for both a single device and a linked chain forced by a semi-continuous wave spectrum.
- In Chapter 7 we summarise the conclusions from the research, discuss the limitations, and comment on the broader implications and potential for future work.

Chapter 2

Theoretical background

In this chapter we summarise the established physical theory that underlies the modelling work undertaken in the project. Content here draws largely from the books of Falnes [29], Newman [59], Sarpkaya & Isaacson [68], Landau & Lifshitz [49], and Cruz (ed.) [17]. Other sources are also used where indicated.

A moving fluid can be described mathematically in terms of velocity, pressure and mass density fields. These three quantities are, in general, functions of position and time. A fluid is made up of particles that move around in the global coordinate space; to be clear, the fluid velocity expressed as $\mathbf{u}(\mathbf{x}, t)$ refers to a fixed point in space with coordinates $\mathbf{x} = (x, y, z)$, and not to a fixed fluid particle.

Throughout this thesis we use standard Cartesian coordinates, with the still surface of the water defining the x - y plane (ignoring curvature), and the z -axis vertically upwards. All quantities in this chapter are expressed in S.I. units.

2.1 Linear water wave theory

The presence of a *free surface* allows for the propagation of energy-carrying waves in a fluid. The mathematical description of water waves stems largely from two well-known hydrodynamic equations. The first of these is the continuity equation, expressing conservation of mass. In differential form, this is

$$\frac{\partial \rho}{\partial t} + \nabla \cdot (\rho \mathbf{u}) = 0, \quad (2.1)$$

where ρ is mass density of the fluid and \mathbf{u} is its velocity. Most fluids, including water, are practically incompressible so ρ can be assumed constant in space and time, which reduces the continuity equation to simply

$$\nabla \cdot \mathbf{u} = 0. \quad (2.2)$$

The second important equation is the Navier-Stokes equation, which is derived from Newton's second law of motion and expresses conservation of momentum. For an in-

compressible fluid it is

$$\rho \frac{D\mathbf{u}}{Dt} = -\nabla p + \eta \nabla^2 \mathbf{u} + \mathbf{f}_{\text{ext}}, \quad (2.3)$$

where p is the pressure of the fluid, η is its dynamic viscosity, and \mathbf{f}_{ext} is the external force per unit volume acting on the fluid element in question. Note that the derivative on the left-hand side is the total acceleration¹,

$$\frac{D\mathbf{u}}{Dt} \equiv \frac{\partial \mathbf{u}}{\partial t} + (\mathbf{u} \cdot \nabla) \mathbf{u}. \quad (2.4)$$

The Navier-Stokes equation can be simplified for its application here. Firstly, in waves of a size practical for energy extraction, gravity dominates surface tension as the restoring force [49]. Restricting interest to this regime, we use

$$\mathbf{f}_{\text{ext}} = \rho \mathbf{g} = -\nabla(\rho g z), \quad (2.5)$$

where $g = 9.81 \text{ m s}^{-2}$ is the acceleration due to gravity at Earth's surface. Secondly, we assume water can be treated as an *ideal fluid*; one that is inviscid ($\eta = 0$) as well as incompressible.² Applying this condition and substituting (2.4) and (2.5) into the Navier-Stokes equation (2.3) gives

$$\rho \left(\frac{\partial \mathbf{u}}{\partial t} + (\mathbf{u} \cdot \nabla) \mathbf{u} \right) = -\nabla(p + \rho g z). \quad (2.6)$$

2.1.1 Velocity potential

The assumption that water is an ideal fluid leads to significant mathematical simplification. In particular, it allows us to write the velocity as the gradient of a scalar function called the *velocity potential*,

$$\mathbf{u}(\mathbf{x}, t) = \nabla \phi(\mathbf{x}, t). \quad (2.7)$$

Similarly to the concept of an electric potential in electrostatics, the condition for (2.7) to be valid is that $\nabla \times \mathbf{u}$ (the *vorticity*) be zero, meaning here that the fluid flow is irrotational. Taking the curl of (2.6) and using the two vector identities

$$\mathbf{A} \times (\nabla \times \mathbf{A}) \equiv \frac{1}{2} \nabla A^2 - (\mathbf{A} \cdot \nabla) \mathbf{A}, \quad (2.8)$$

$$\nabla \times \nabla \varphi \equiv 0, \quad (2.9)$$

leads to

$$\frac{\partial}{\partial t} (\nabla \times \mathbf{u}) = \nabla \times [\mathbf{u} \times (\nabla \times \mathbf{u})]. \quad (2.10)$$

¹A fluid particle in a non-uniform velocity field experiences acceleration due to its motion within the field (convective acceleration), as well as from any time variance of the field (local acceleration).

²To illustrate the relative size of the terms in (2.3), the dynamic viscosity of salt water at 15°C is $\eta = 1.22 \times 10^{-3} \text{ N m}^{-2} \text{ s}$ [59].

This equation states that if at any point in time the flow becomes irrotational (for example, if the fluid ever came to rest), it will remain irrotational for all subsequent time. Assuming that the flow has indeed become irrotational, we can write

$$\nabla \times \mathbf{u} \equiv 0. \quad (2.11)$$

which ensures the existence of a velocity potential ϕ satisfying (2.7).³

In spite of the velocity potential being a mathematical abstraction, rather than an observable physical quantity like the velocity, it is convenient to work with because it reduces the vector equation (2.6) into a scalar equation for ϕ . Substituting (2.7) into (2.6) and again using the vector identity (2.8) we obtain

$$\nabla \left(p + \frac{1}{2}\rho u^2 + \rho g z + \rho \frac{\partial \phi}{\partial t} \right) = 0. \quad (2.12)$$

Integration of this gives

$$p + \frac{1}{2}\rho u^2 + \rho g z + \rho \frac{\partial \phi}{\partial t} = C_1 + C_2(t), \quad (2.13)$$

where C_1 and $C_2(t)$ may be arbitrarily chosen without affecting any physical quantities [59]. Choosing $C_2 = 0$ and considering the particular case at the surface of a static fluid ($z = 0$, $p = p_{atm}$ (the ambient atmospheric pressure), $\mathbf{u} = 0$ and $\phi = \text{constant}$) it is clear that we require $C_1 = p_{atm}$. Hence we can rewrite (2.13) as

$$\frac{p_g}{\rho} + \frac{u^2}{2} + g z + \frac{\partial \phi}{\partial t} = 0, \quad (2.14)$$

where $p_g = p - p_{atm}$ is the gauge pressure of the fluid. Note that (2.13) is recognisable as a dynamic version of Bernoulli's equation.

Finally, the continuity equation (2.2) expressed in terms of ϕ (using (2.7)) becomes the familiar Laplace equation,

$$\nabla^2 \phi = 0. \quad (2.15)$$

2.1.2 Boundary conditions

In addition to satisfying equations (2.14) and (2.15) throughout the fluid generally, the velocity potential ϕ must also satisfy boundary conditions describing a particular physical situation. Here we consider a fluid unbounded in the x - y plane, but with boundary conditions to be met on the free surface, on the seabed and on the wetted surface of any floating bodies.

³For a proof of this statement and a detailed discussion of the validity of potential flow theory, see e.g. Landau & Lifshitz [49].

Boundary conditions on a wetted surface

At the boundary between the fluid and a solid surface (assumed rigid), we impose the straight-forward condition that the normal component of the fluid velocity must be equal to that of the velocity of the boundary itself. Physically, this simply asserts that there can be no fluid flow through the boundary. This *kinematic* boundary condition can be expressed mathematically as

$$\left[\frac{\partial \phi}{\partial n} \right]_S = \mathbf{n} \cdot \mathbf{v} \equiv v_n, \quad (2.16)$$

where \mathbf{n} is the unit normal vector to the surface element under consideration, \mathbf{v} is its velocity, and

$$\frac{\partial \phi}{\partial n} \equiv \mathbf{n} \cdot \nabla \phi. \quad (2.17)$$

In the particular case of the seabed, it can obviously be assumed stationary, so $v_n = 0$. If we additionally assume it to be horizontally level and therefore of fixed depth h below the still surface, (2.16) reduces to

$$\left[\frac{\partial \phi}{\partial z} \right]_{z=-h} = 0. \quad (2.18)$$

Boundary conditions on the free surface

Defining the function $\xi(x, y, t)$ such that for any x, y and t , ξ gives the z coordinate of the free surface, we can write a kinematic boundary condition for the free surface as $[u_z]_{z=\xi} = D\xi/Dt$, or

$$0 = \left[\frac{\partial \xi}{\partial t} + (\mathbf{u} \cdot \nabla) \xi - \frac{\partial \phi}{\partial z} \right]_{z=\xi} \quad (2.19)$$

$$= \left[\frac{\partial \xi}{\partial t} + \frac{\partial \phi}{\partial x} \frac{\partial \xi}{\partial x} + \frac{\partial \phi}{\partial y} \frac{\partial \xi}{\partial y} - \frac{\partial \phi}{\partial z} \right]_{z=\xi}. \quad (2.20)$$

This condition states that we expect a fluid particle on the free surface to remain there throughout the wave motion.

Newman [59] shows that the kinematic boundary condition contains sufficient information to uniquely specify the velocity potential. However, this relies on the position and the velocity of the boundary being known *a priori*, which is generally not the case with the free surface. (2.20) can be supplemented by applying (2.14) at the free surface to give the so-called *dynamic* boundary condition. This is useful since a quantity that is generally known on the free surface is the pressure, assumed equal to the ambient air pressure at all times (i.e. $p_g = 0$) since we are neglecting surface tension. Hence,

$$\left[\frac{\partial \phi}{\partial t} + \frac{1}{2} (\nabla \phi \cdot \nabla \phi) \right]_{z=\xi} + g\xi = 0. \quad (2.21)$$

2.1.3 Linearisation

Laplace's equation (2.15) along with the boundary conditions (2.16), (2.20) and (2.21) can be used in general to find the velocity potential for an ideal fluid. Doing so analytically is impossible in virtually all cases, due to the free surface boundary conditions being nonlinear and the fact that $\xi(x, y, t)$ is an initially unknown function. Several wave theories, of varying assumptions and degrees of approximation, have been developed to allow progress – for an overview, see Sarpkaya & Isaacson [68]. Here we opt for the simplest and most amenable to solution; we introduce an additional assumption that the wave height (as well as all dependent dynamic variables) is sufficiently small relative to the wavelength and water depth that terms of second or higher order can be neglected. The resulting theory is variably referred to as linear wave theory, small amplitude wave theory, first-order wave theory or Airy wave theory.

Under this linearisation, the free surface boundary conditions (2.20) and (2.21) become (respectively),

$$\left[\frac{\partial \phi}{\partial z} \right]_{z=0} = \frac{\partial \xi}{\partial t}, \quad (2.22)$$

$$\left[\frac{\partial \phi}{\partial t} \right]_{z=0} = -g\xi. \quad (2.23)$$

All terms that are second order in ϕ , ξ or their derivatives have been neglected, and the boundary conditions are now prescribed at the *time-average* position of the boundary ($z = 0$ in this case). Proof that this latter simplification is consistent with a first-order approximation can be found by considering a Taylor expansion of ϕ about the time-average position.

Taking the partial time derivative of (2.23) and combining with (2.22) eliminates ξ to give the combined surface boundary condition

$$\left[\frac{\partial^2 \phi}{\partial t^2} + g \frac{\partial \phi}{\partial z} \right]_{z=0} = 0. \quad (2.24)$$

Boundary condition (2.16) on the surface of floating bodies is unchanged in the linear approximation except that it too may now be evaluated on the time-average position of the surface, \bar{S} :

$$\left[\frac{\partial \phi}{\partial n} \right]_{\bar{S}} = v_n. \quad (2.25)$$

The seabed boundary condition is unchanged from (2.18), subject to the same assumption of a level seabed.

These linearised boundary conditions in conjunction with Laplace's equation allow ϕ to be found in a wide range of situations. Sarpkaya & Isaacson [68] present a plot by Le Mehauté showing the range of validity of the various wave theories, which says that on deep water⁴, linear theory is applicable for

$$\frac{H}{gT^2} < 0.001, \quad (2.26)$$

⁴ $kh \ll 1$.

where H is wave height and T is wave period. For a 10 second wave, this means an upper limit of about one metre. However, linear wave theory is used extensively throughout the wave energy literature and routinely applied in situations with steeper waves than this. It is generally believed that for the majority of time, wave energy devices will operate under conditions where linear theory provides a sufficient approximation.

2.1.4 Plane wave solutions

We consider a horizontally unbounded fluid in the absence of any submerged bodies, with a seabed of fixed depth h so that its boundary condition is given by (2.18). Suppose that the wave field is unidirectional with no component in the y -direction, viz.

$$\frac{\partial \phi}{\partial y} = 0. \quad (2.27)$$

Let us assume the wave field has sinusoidal time dependence with period T and define the complex amplitude of the velocity potential, $\hat{\phi}$ by

$$\phi(\mathbf{x}, t) \equiv \text{Re} \left(\hat{\phi}(\mathbf{x}) e^{i\omega t} \right), \quad (2.28)$$

where $\omega = 2\pi/T$ is the wave field's angular frequency. The family of solutions for $\hat{\phi}$ satisfying (2.18) and (2.27) as well as the Laplace equation (2.15) can be written

$$\hat{\phi}_n = \epsilon(m_n z) (\alpha_n e^{im_n x} + \beta_n e^{-im_n x}), \quad (2.29)$$

where m_n is an eigenvalue, α_n and β_n are arbitrary constants and

$$\epsilon(m_n z) = \frac{\cosh(m_n(z+h))}{\cosh(m_n h)} = \frac{1 + e^{-2m_n(z+h)}}{1 + e^{-2m_n h}} e^{m_n z}. \quad (2.30)$$

Note that (2.29) is invariant to a sign change in m_n (other than interchanging α_n and β_n), so m_n may be chosen positive.

The free surface boundary condition (2.24) gives the relationship

$$\omega^2 = g m_n \tanh(m_n h). \quad (2.31)$$

For a given ω , this has a unique positive real solution for m_n , plus an infinite series of pure imaginary solutions. The former corresponds to a travelling wave with wavenumber $k \equiv m_0$, while the latter gives a series of evanescent waves, which do not transport energy. Our interest is restricted to the travelling wave. (2.31) gives the *dispersion relationship* relating the wavenumber to the angular frequency, which for the sake of clarity we rewrite

$$\omega^2 = g k \tanh(kh). \quad (2.32)$$

Let us choose a particular case of (2.29),

$$\hat{\phi}(x, z) = -\frac{gH}{2\omega} \epsilon(kz) e^{-ikx}, \quad (2.33)$$

with H a constant, which gives

$$\phi(x, z, t) = -\frac{gH}{2\omega}\epsilon(kz)\cos(kx - \omega t). \quad (2.34)$$

We can now use equations (2.23) and (2.7) to find the corresponding surface elevation and fluid velocity components:

$$\xi(x, t) = \frac{H}{2}\sin(kx - \omega t), \quad (2.35)$$

$$u_x(x, z, t) = \frac{\omega H}{2}\sin(kx - \omega t)\frac{\cosh(kz + kh)}{\sinh(kh)}, \quad (2.36)$$

$$u_z(x, z, t) = -\frac{\omega H}{2}\cos(kx - \omega t)\frac{\sinh(kz + kh)}{\sinh(kh)}, \quad (2.37)$$

where (2.30) and the dispersion relationship (2.32) were also used. The surface elevation (2.35) clearly illustrates that this is a plane wave propagating in the forward x -direction with a peak-to-trough height of H , which we will henceforth refer to simply as the *wave height*. From (2.32), the wave travels with a phase velocity of

$$v_p = \frac{\omega}{k} = \frac{g}{\omega}\tanh(kh), \quad (2.38)$$

The water depth affects the particle velocities and the dispersion relationship. For shallower waters in relation to the wavelength (i.e. when kh is small) the phase velocity is slower and the elliptical trajectories of the water particles are more horizontally elongated. When $kh \gg 1$, simply referred to as *deep water*, the presence of the seabed becomes unimportant and (2.32), (2.36) and (2.37) have the approximate forms

$$\omega^2 \approx gk, \quad (2.39)$$

$$u_x(x, z, t) \approx \frac{\omega H}{2}\sin(kx - \omega t)e^{kz}, \quad (2.40)$$

$$u_z(x, z, t) \approx -\frac{\omega H}{2}\cos(kx - \omega t)e^{kz}. \quad (2.41)$$

Here the fluid particles follow circular trajectories with clockwise polarisation, with speed and trajectory radius diminishing exponentially with distance below the surface ($z < 0$). The approximation is generally considered applicable when the water depth is greater than about half a wavelength; it is straightforward to show that the deep water dispersion relationship (2.39) is accurate to 95% for $h > 0.3\lambda$ and to 99% for $h > 0.42\lambda$.

2.1.5 Transport of energy

It can be shown that the time-average stored energy per unit horizontal area⁵ in a progressive plane wave of the form (2.34) is

$$\overline{E} = \rho g \overline{\xi^2} = \frac{1}{8}\rho g H^2, \quad (2.42)$$

⁵That is, the energy density integrated over the $z \in [-h, 0]$.

with equal potential and kinetic contributions. Wave energy is transported at the group velocity $v_g = d\omega/dk$, which in deep water is

$$v_g = \frac{g}{2\omega} = \frac{1}{2}v_p. \quad (2.43)$$

The *wave energy flux*, J (introduced in Chapter 1), is the time-average power transported per unit width of wave-front. In terms of the preceding two quantities we can write $J = v_g \bar{E}$, hence for deep water

$$J = \frac{\rho g^2 H^2}{16\omega} = \frac{\rho g^2 H^2 T}{32\pi}, \quad (2.44)$$

where $T = 2\pi/\omega$ is the wave period.

2.1.6 Real ocean waves

A monochromatic plane wave described by (2.34)-(2.37) will, of course, never be observed in a real ocean. However, under the assumptions of linear water wave theory, a general sea state may be represented by a linear superposition of plane waves of different frequencies and directions. The 2-D surface elevation can be expressed

$$\xi(x, y, t) = \sum_j \frac{H_j}{2} \sin(k_j(x \cos \theta_j + y \sin \theta_j) + \omega_j t + \phi_j), \quad (2.45)$$

where k_j and ω_j are related by the dispersion relationship (2.32), θ_j is the angle that the j th plane wave makes with the x -axis, and ϕ_j is a phase value.

In the ocean, waves are generated and continually modified through complex interactions between winds and the water surface. The sea states that develop are random in nature, and must be described probabilistically. A sea state is typically expressed in terms of its *energy spectrum* (often just called the *spectrum*). This is conventionally given the symbol S , but here we will use Ψ in order to distinguish it from the spring stiffness, which we introduce later. A full description of the sea state requires Ψ to have a directional dependence, but we will restrict interest⁶ to the direction-integrated energy spectrum (called the *frequency spectrum* by some authors),

$$\Psi(f) = \int_0^{2\pi} \Psi(f, \theta) d\theta, \quad (2.46)$$

where $f = \omega/2\pi$ is frequency. Strictly, $\Psi(f)$ is an energy spectral density; the (time-averaged) ocean energy content per unit horizontal area due to waves in the frequency band $[f_1, f_2]$ is given by

$$\bar{E} = \rho g \int_{f_1}^{f_2} \Psi(f) df. \quad (2.47)$$

⁶We will later assume that the waves are unidirectional: a *long crested* spectrum.

From this equation it can be seen that Ψ has units of $\{\text{length}\}^2 \times \{\text{time}\}$.

The main interest in ocean spectra here is to relate them to a superposition of plane waves for the purposes of modelling. Comparing (2.47) with (2.42), if a single discrete wave component of frequency f_j is present in the frequency band $[f_1, f_2]$, its height H_j is related to Ψ by

$$H_j = \sqrt{8 \int_{f_1}^{f_2} \Psi(f) df}. \quad (2.48)$$

In this manner, a wave field as in (2.45) can be generated according to a given spectrum by choosing a discrete set of frequencies f_j and evaluating the corresponding H_j . Assuming linearity, the plane wave components are non-interacting and the phases ϕ_j may be randomly chosen from a uniform distribution on the interval $[0, 2\pi]$.

Several different spectra have been proposed based on statistical information gathered from measurements of ocean waves, of which a good overview is given in Sarpkaya & Isaacson [68]. One of these, which we choose to use later, is the *Bretschneider spectrum*,

$$\Psi_B(f) = \frac{5H_s^2 f_p^4}{16 f^5} \exp \left[-\frac{5}{4} \left(\frac{f_p}{f} \right)^4 \right], \quad (2.49)$$

where f_p is the frequency at the peak of the spectrum, and H_s is the *significant wave height*: this is defined as the average wave height of the highest one-third of waves, and is found to be close to the wave height that would be reported by a trained observer.

2.2 Wave forces on a floating body

We now consider a body submerged in the fluid. The body will experience time-varying forces due to the influence of waves. In turn, the presence and motion of the body exerts forces on the fluid and causes the generation of additional waves.

The motion of a floating body can be fully described by six components corresponding to three translational and three rotational modes, which are given the names surge, sway, heave, roll, pitch and yaw. The diagram in Figure 2.2 illustrates these modes for a ship-like body with an elongated axis. For an axisymmetric body with a unidirectional incident wave field, the convention is to define the x -axis (and the surge mode) in the direction of the wave. For the sake of simplicity, we will restrict analysis here to the translational modes of motion. The force on the body and the body's velocity are written as three-component vectors with the components corresponding to surge, sway and heave in that order.

The total force acting on an arbitrary submerged body can be calculated from

$$\mathbf{F} = - \iint_S p \mathbf{n} dS, \quad (2.50)$$

where p is the fluid pressure, S is the *submerged* surface of the body and \mathbf{n} is the unit

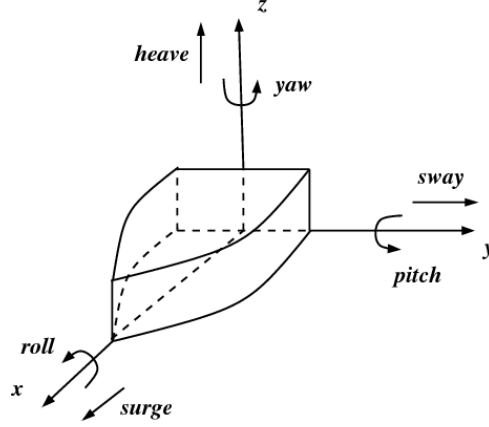


Figure 2.1: Translational and rotational modes of motion for a ship-like body. Source: <http://bit.ly/kI0n5Z>.

vector normal to the area element dS . From (2.14) we can write

$$\mathbf{F} = \iint_S \left[-p_{atm} + \rho \left(\frac{u^2}{2} + gz + \frac{\partial \phi}{\partial t} \right) \right] \mathbf{n} dS \quad (2.51)$$

$$\approx \iint_{\bar{S}} (-p_{atm} + \rho gz) \mathbf{n} dS + \rho \iint_{\bar{S}} \frac{\partial \phi}{\partial t} \mathbf{n} dS, \quad (2.52)$$

to first order accuracy. The first integral in (2.52) is the hydrostatic force on the body, which we call \mathbf{F}_{hs} . The second integral is the hydrodynamic force, which we will further decompose in subsection 2.2.2.

2.2.1 Hydrostatics

The j th component of the hydrostatic force may be written

$$F_{hs,j} = \oiint_{\bar{S} + \bar{S}_w} (\rho gz - p_{atm}) \mathbf{e}_j \cdot \mathbf{n} dS - \iint_{\bar{S}_w} (\rho gz - p_{atm}) \mathbf{e}_j \cdot \mathbf{n} dS, \quad (2.53)$$

where \mathbf{e}_j is the unit vector in the j th dimension ($j = 1, 2, 3$), and S_w is the cross-sectional surface of the body in the water surface plane. The divergence theorem can be applied to the closed surface integral as follows

$$\oiint_{\bar{S} + \bar{S}_w} (\rho gz - p_{atm}) \mathbf{e}_j \cdot \mathbf{n} dS = \iiint_{\bar{V}_s} \nabla \cdot \{ (\rho gz - p_{atm}) \mathbf{e}_j \} dV \quad (2.54)$$

$$= \iiint_{\bar{V}_s} \rho g \delta_{j3} dV \quad (2.55)$$

$$= \rho g \bar{V}_s \delta_{j3}, \quad (2.56)$$

where V_s is the submerged volume of the body and δ is the Kronecker delta. (2.56) is clearly recognisable as the static buoyancy force.

As one might predict, the second integral in (2.53) gives the force exerted by the atmosphere on the exposed part of a surface-piercing body. Under linear water wave theory, where S_w may be taken as the cross-sectional surface of the body in the $z = 0$ plane, we have

$$\iint_{\bar{S}_w} (\rho g z - p_{atm}) \mathbf{e}_j \cdot \mathbf{e}_3 dS = p_{atm} \bar{A}_w \delta_{j3}, \quad (2.57)$$

where A_w is the area of S_w . The total hydrostatic force is therefore

$$\mathbf{F}_{hs} = (\rho g \bar{V}_s - p_{atm} \bar{A}_w) \mathbf{e}_3. \quad (2.58)$$

2.2.2 Decomposition of the velocity potential

Recall that the total hydrodynamic force is given by the second integral on the right-hand side of (2.52). Under the assumption of linearity, the velocity potential may be decomposed into three components as follows:

$$\phi = \phi_i + \phi_d + \phi_r. \quad (2.59)$$

The incident potential ϕ_i represents the undisturbed incident wave field, the diffraction potential ϕ_d represents the disturbance to this incident wave field due to diffraction (or scattering) by the body, and the radiation potential ϕ_r represents the wave field generated by the motion of the body in the fluid.

The total velocity potential ϕ must satisfy the kinematic boundary condition (2.25) on the wetted surface of the body, S . First, considering a stationary body so that $v_n = \phi_r = 0$, we see that the diffraction potential must satisfy

$$\left[\frac{\partial \phi_d}{\partial n} \right]_{\bar{S}} = - \left[\frac{\partial \phi_i}{\partial n} \right]_{\bar{S}} \quad (2.60)$$

for a given incident wave field. Now considering a body undergoing forced motion in the absence of any incident wave field, the radiation potential simply satisfies the same condition as ϕ , viz.

$$\left[\frac{\partial \phi_r}{\partial n} \right]_{\bar{S}} = v_n. \quad (2.61)$$

Under the assumption of linearity, the diffraction potential is independent of the body motion and (2.60) and (2.61) apply in the general case. Additionally, all three components of the total velocity potential must independently satisfy the Laplace equation (2.15) throughout the fluid, and boundary conditions for the free surface (2.24) and the seabed (2.18).

For a sinusoidal incident wave field with angular frequency ω , linearity also implies that all dynamic variables share this same harmonic time dependence. Let us define

complex amplitudes for the all of the potentials as in (2.28), and for the body velocity so that

$$\mathbf{v} = \text{Re} (\hat{\mathbf{v}}e^{i\omega t}) = \frac{1}{2} (\hat{\mathbf{v}}e^{i\omega t} + \hat{\mathbf{v}}^*e^{-i\omega t}), \quad (2.62)$$

where * denotes the complex conjugate. The free surface boundary condition (2.24) may then be rewritten for the diffraction and radiation potentials in terms of their complex amplitudes,

$$\left[-\omega^2 \hat{\phi}_{(d,r)} + g \frac{\partial \hat{\phi}_{(d,r)}}{\partial z} \right]_{z=0} = 0, \quad (2.63)$$

while all other boundary conditions are unchanged in form for $\hat{\phi}_{(d,r)}$.

Finding solutions for $\hat{\phi}_{(d,r)}$ is known as the *diffraction problem* and the *radiation problem*, respectively. In fact, the problems as specified above are not yet complete as they do not possess unique solutions. Particularly, if ϕ_1 is a solution, then so is $\phi'_1 = \phi_1 + C\psi$, where ψ satisfies (2.15), (2.63), (2.18) and

$$\left[\frac{\partial \psi}{\partial n} \right]_{\bar{S}} = 0. \quad (2.64)$$

It is therefore necessary to impose a *radiation condition*, which asserts that any surface waves other than the incident field must radiate away from the body. Consideration of conservation of energy gives, in cylindrical polar coordinates (r, θ, z) ,

$$\hat{\phi}_{(d,r)} \propto A(\theta, z)r^{-1/2}. \quad (2.65)$$

Solving the diffraction or radiation problems is a difficult computational challenge, achievable analytically only for a small class of very simple geometries.

2.3 Radiation force

The waves generated due to a body's motion in a fluid exert a reaction force back on the body which we call the *radiation force*,

$$\mathbf{F}_R = \rho \iint_{\bar{S}} \frac{\partial \phi_r}{\partial t} \mathbf{n} dS. \quad (2.66)$$

Following the decomposition of the velocity potential in 2.2.2, calculating the radiation force only requires information about the body motion, and not the incident field.

To begin, we assume a sinusoidal body motion of frequency ω , with velocity amplitude $\hat{\mathbf{v}}$. Under the linearity assumption, we may decompose the radiation potential as follows:

$$\hat{\phi}_r = \sum_k \varphi_k \hat{v}_k, \quad (2.67)$$

where $\varphi_j(x, y, z)$ is the amplitude of the velocity potential that is generated by the body oscillating in the j th mode with unit velocity amplitude. Like ϕ_r , the φ_j must

satisfy the Laplace equation and the boundary conditions for the free surface (2.63) and seabed (2.18). The only distinction comes in the wetted surface boundary condition (2.61); taking $\partial/\partial n$ of (2.67) and comparing gives

$$\left[\frac{\partial \varphi_j}{\partial n} \right]_{\bar{S}} = n_j, \quad (2.68)$$

recalling that \mathbf{n} is the unit normal vector to the surface element in question.

Writing (2.66) in terms of these φ_j and the complex amplitude $\hat{\mathbf{F}}_{\mathbf{R}}$, we have for the j th component

$$\hat{F}_{R,j} = i\omega\rho \iint_{\bar{S}} \sum_k \varphi_k \hat{v}_k n_j dS \quad (2.69)$$

$$= \sum_k \left\{ i\omega\rho \iint_{\bar{S}} \varphi_k n_j dS \right\} \hat{v}_k \quad (2.70)$$

$$\equiv \sum_k -Z_{jk}(\omega) \hat{v}_k, \quad (2.71)$$

where we have defined the *radiation impedance* matrix, \mathbf{Z} . This can now more conveniently be expressed in vector form as

$$\hat{\mathbf{F}}_{\mathbf{R}} \equiv -\mathbf{Z}(\omega) \hat{\mathbf{v}}. \quad (2.72)$$

Using (2.68), an alternative expression for the radiation impedance matrix is

$$Z_{jk}(\omega) = -i\omega\rho \iint_{\bar{S}} \varphi_k \frac{\partial \varphi_j}{\partial n} dS. \quad (2.73)$$

From (2.71), $-Z_{jk}$ is the k th component of the radiation force amplitude caused by oscillation with unit velocity amplitude in the j th mode.

$$Z_{jk} = Z_{kj}. \quad (2.74)$$

2.3.1 Added mass and radiation resistance

In general, the radiation impedance is complex and the radiation force is not in phase with the velocity. \mathbf{Z} may be decomposed into real and imaginary parts as follows:

$$\mathbf{Z}(\omega) \equiv \mathbf{R}_r(\omega) + i\omega \mathbf{M}_a(\omega), \quad (2.75)$$

where matrices \mathbf{R}_r and \mathbf{M}_a are both real (as is ω). Defining the complex amplitude $\hat{\mathbf{a}} = i\omega \hat{\mathbf{v}}$ for the acceleration of the body, (2.72) can be written

$$\hat{\mathbf{F}}_{\mathbf{R}} = -(\mathbf{R}_r(\omega) \hat{\mathbf{v}} + \mathbf{M}_a(\omega) \hat{\mathbf{a}}). \quad (2.76)$$

\mathbf{R}_r corresponds to the part of the radiation force in phase with the velocity, and so is referred to as either the *radiation resistance* or *added damping* matrix – we opt for the former name. \mathbf{M}_a corresponds to the part in phase with the acceleration, and is called the *added mass* matrix, since its dynamic effect is to increase the body’s inertia as if its mass were greater than its true value.⁷ Added mass is a well-known phenomenon that also arises in the study of bodies submerged in a fluid with no free surface, and can be understood in terms of the additional fluid mass accelerated with the body. It should be emphasised that the value of the added mass here (which depends on the frequency of the body’s oscillatory motion) is not the same as in the case where there is no free surface (where it is a constant).

2.3.2 Radiated power

The generation of outgoing waves by the motion of the body means that power is radiated away. In general when a force \mathbf{F} acts on a body moving with velocity \mathbf{v} , the rate of work done on the body (i.e. the power transfer to the body) is $\mathbf{F} \cdot \mathbf{v}$. Applying this to the radiation force and using (2.62), the instantaneous rate of work done on the body due to wave radiation is

$$P_R(t) = \frac{1}{4} \left(\hat{\mathbf{F}}_{\mathbf{R}} \cdot \hat{\mathbf{v}} e^{2i\omega t} + \hat{\mathbf{F}}_{\mathbf{R}} \cdot \hat{\mathbf{v}}^* + \hat{\mathbf{F}}_{\mathbf{R}}^* \cdot \hat{\mathbf{v}} + \hat{\mathbf{F}}_{\mathbf{R}}^* \cdot \hat{\mathbf{v}}^* e^{-2i\omega t} \right). \quad (2.77)$$

We are generally only interested in the time-average of the above quantity, which we will simply label P_R . The first and last terms in the bracket together represent a harmonic oscillation of frequency 2ω and hence make zero contribution to the time-average. Noting that $\mathbf{A} + \mathbf{A}^* = 2 \operatorname{Re}(\mathbf{A})$, and using (2.74)–(2.75), we get

$$P_R \equiv \overline{P_R(t)} = \frac{1}{2} \operatorname{Re} \left(\hat{\mathbf{F}}_{\mathbf{R}} \cdot \hat{\mathbf{v}}^* \right) \quad (2.78)$$

$$= -\frac{1}{2} \operatorname{Re} \left(\hat{\mathbf{v}}^T Z^T \hat{\mathbf{v}}^* \right) \quad (2.79)$$

$$= -\frac{1}{2} \hat{\mathbf{v}}^T \mathbf{R}_r^T \hat{\mathbf{v}}^*, \quad (2.80)$$

where the superscript T denotes the matrix transpose. In the simplest case of motion in a single mode j only,

$$P_R = -\frac{R_r}{2} |\hat{v}|^2, \quad (2.81)$$

where $R_r = (\mathbf{R}_r)_{jj}$. Note that $P_R \leq 0$ under our definition.

The preceding analysis shows that the radiation resistance directly relates to the *active power* radiated by an oscillating submerged body, and hence to the amplitude of the radiated waves. The added mass contributes only to the *reactive power*, and is related to the evanescent waves generated in the near-field, which do not transport power in time-average.

⁷In fact, it is possible under some circumstances for a body to have negative added mass when it is near the free surface [55].

2.3.3 The Kramers-Kronig relations

It turns out that the added mass and radiation resistance of a body are not independent, but are in fact related to one another through the *Kramers-Kronig relations*. These relations are a general feature of linear systems, occurring in any instance where the system exhibits a causal response to the input. In hydrodynamics, one way of expressing the Kramers-Konig relations is

$$M_a(\omega) - M_a(\infty) = \frac{2}{\pi} \int_0^\infty \frac{-R_r(y)}{\omega^2 - y^2} dy, \quad (2.82)$$

$$R_r(\omega) = \frac{2\omega^2}{\pi} \int_0^\infty \frac{M_a(y) - M_a(\infty)}{\omega^2 - y^2} dy, \quad (2.83)$$

where $M_a(\infty)$ denotes the high-frequency limit of the added mass. The integrands clearly exhibit a singularity at $y = \omega$, and these integrals are to be interpreted as *principle value integrals*. For a function $f(x)$ that is singular at $x = a$, the principle value integral is

$$\lim_{\epsilon \rightarrow 0^+} \left[\int_0^{a-\epsilon} f(x) dx + \int_{a+\epsilon}^\infty f(x) dx \right]. \quad (2.84)$$

2.3.4 Formulation in the time domain

The analysis thus far has been for a body undergoing a steady sinusoidal oscillation, leading to the expression (2.72) for the radiation force amplitude. More generally, this allows us to write the *frequency domain* expression for the radiation force,

$$\mathbf{F}_R(\omega) = -Z(\omega)\mathbf{v}(\omega). \quad (2.85)$$

If the motion contains more than one frequency component – which will occur when the body is either (i) in a transient state, (ii) exhibiting a nonlinear response to a sinusoidal forcing, or (iii) forced by a multi-frequency spectrum – it is strictly necessary to study the system in the time domain. While (2.85) is simple in form, transforming it to the time domain is non-trivial because of the frequency dependence of the radiation impedance; taking the inverse Fourier transform results in a *convolution integral*. The Kramers-Kronig relations allow the time domain radiation force to be written in many forms, one of which is

$$\mathbf{F}_R(t) = -M_a(\omega)\ddot{\mathbf{x}} - \int_0^t K(\tau)\dot{\mathbf{x}}(t - \tau) d\tau, \quad (2.86)$$

where the dots over the top of \mathbf{x} denote derivatives with respect to time. K is called the *impulse response function*, and is given by

$$K(\tau) = \frac{2}{\pi} \int_0^\infty R_r(\omega) \cos(\omega\tau) d\omega. \quad (2.87)$$

As the name suggests, K gives the radiation force that would result if the body were to undergo a unit velocity impulse. Experience affirms that the waves generated by this

motion will cause forces to act back on the body for some time, though the magnitude will decay relatively rapidly. The physical implication is that, for any motion, the radiation force exhibits *memory effects*: it depends on the body's motion over some window of past time, not just the instantaneous velocity and acceleration. In line with this, we refer to the integral in (2.86) from now on as the *memory integral*. An example of an impulse response function is given in Figure 3.3 (note that this is plotted in scaled units introduced in Section 3.9). The function shows an oscillatory force with amplitude decay, which one might expect based on either experience or logical reasoning.

2.4 Excitation force

The *excitation force* is the name given to the force on the body resulting from the incident and diffraction potentials together:

$$\mathbf{F}_E = \rho \iint_{\bar{S}} \frac{\partial}{\partial t} (\phi_i + \phi_d) \mathbf{n} dS. \quad (2.88)$$

Following from the discussion of the decomposition of the velocity potential in 2.2.2, the excitation force in the linear regime is independent of the motion of the body, and is equal to the total hydrodynamic force that would act on the body if it were held fixed.⁸ To calculate it, information is only required about the incident wave field and the body geometry.

The excitation force may be further split into two components corresponding to the incident and diffraction potentials alone, called the *Froude-Krylov force* and *diffraction force* respectively.

2.4.1 Diffraction force

The diffraction force is given by

$$\mathbf{F}_{\text{dif}} = \rho \iint_{\bar{S}} \frac{\partial \phi_d}{\partial t} \mathbf{n} dS. \quad (2.89)$$

Recall from the discussion of boundary conditions in 2.2.2 that the diffraction potential ϕ_d and the radiation potential ϕ_r share the same boundary conditions except for on the wetted surface of the submerged body, where their boundary conditions are (2.60) and (2.61) respectively. Following Newman [59], we may write these in an alternative way as

$$\left[\frac{\partial \phi_d}{\partial n} \right]_{\bar{S}} = -\mathbf{n} \cdot \mathbf{u}_i, \quad (2.90)$$

$$\left[\frac{\partial \phi_r}{\partial n} \right]_{\bar{S}} = \mathbf{n} \cdot \mathbf{v}, \quad (2.91)$$

⁸The distinction between the stationary body and moving body cases is a second-order effect.

where $\mathbf{u}_i \equiv \nabla\phi_i$ is the undisturbed fluid velocity due to the incident wave field. Expressing the equations in this manner makes it evident that, in the linear regime, the diffraction potential is equal to the radiation potential that would be induced if the body were forced to move with a velocity equal and opposite that of the incident wave field on the wetted surface. Applying this observation to (2.67), we can therefore express the complex amplitude of the diffraction potential as

$$\hat{\phi}_d = - \sum_k \varphi_k \hat{u}_{i,k}, \quad (2.92)$$

and the j th component of the complex amplitude of the diffraction force as

$$\hat{F}_{dif,j} = -i\omega\rho \iint_{\bar{S}} \sum_k \varphi_k \hat{u}_{i,k} n_j dS \quad (2.93)$$

$$= - \sum_k i\omega\rho \iint_{\bar{S}} \varphi_k \frac{\partial\varphi_j}{\partial n} \hat{u}_{i,k} dS. \quad (2.94)$$

Notice that we now have an expression for the diffraction force purely in terms of the radiation potential amplitudes φ_j and the incident wave field. This is one statement of the *Haskind relations*. It means that the total hydrodynamic force on the body can be found by solving only the radiation problem, and not the diffraction problem – a vast simplification.

2.4.2 Small-body approximation

On superficial comparison of (2.73) with (2.94) it may seem that the diffraction force can be expressed in terms of the radiation impedance \mathbf{Z} . However, this is not the case in general since, unlike $\hat{\mathbf{v}}$, $\hat{\mathbf{u}}_i$ is a function of the coordinates and cannot be taken outside the surface integral. On the condition that the extent of the body is a small fraction of the incident wavelength, though, the undisturbed fluid velocity is approximately constant over its volume so, for a body centred at \mathbf{x}_0 ,

$$\hat{F}_{dif,j} \approx \sum_k \left\{ -i\omega\rho \iint_{\bar{S}} \varphi_k \frac{\partial\varphi_j}{\partial n} dS \right\} \hat{u}_{i,k}|_{\mathbf{x}=\mathbf{x}_0} \quad (2.95)$$

$$= \sum_k Z_{jk}(\omega) \hat{u}_{i,k}|_{\mathbf{x}=\mathbf{x}_0}. \quad (2.96)$$

This is known as the *small-body approximation* and is commonly invoked in the study of wave energy point absorbers, which are small in relation to the wavelength by definition. In physical terms, the approximation is equivalent to neglecting all scattered waves [48]. Mathematically, it may be expressed

$$ka \ll 1, \quad (2.97)$$

where a is the characteristic length-scale of the body and k is the wavenumber. (2.95) corresponds to taking the first term in a Taylor expansion of $\hat{u}_{i,k}$ about $\mathbf{x} = \mathbf{x}_0$, thus the approximation is zeroth-order in ka .

Using (2.75), the diffraction force amplitude (2.96) can be expressed in terms of the added mass and damping as

$$\hat{\mathbf{F}}_{\text{dif}} = \mathbf{R}_r(\omega) \hat{\mathbf{u}}_{\mathbf{i}}|_{\mathbf{x}=\mathbf{x}_0} + \mathbf{M}_a(\omega) \hat{\mathbf{a}}_{\mathbf{i}}|_{\mathbf{x}=\mathbf{x}_0}. \quad (2.98)$$

It can be shown [29] that for a small body on deep water, the radiation impedance is dominated by the added mass and it is consistent with a zeroth-order approximation to take

$$\hat{\mathbf{F}}_{\text{dif}} \approx \mathbf{M}_a(\omega) \hat{\mathbf{a}}_{\mathbf{i}}|_{\mathbf{x}=\mathbf{x}_0}. \quad (2.99)$$

Clearly though, for a body undergoing oscillatory motion, the validity of using a position independent excitation force must depend not only on the size of the body, but the amplitude of its oscillations. Let us define the displacement of the device from its time-averaged position,

$$\mathbf{s}(t) \equiv \mathbf{x}(t) - \bar{\mathbf{x}}. \quad (2.100)$$

Iversen states in [45] that for a floating body moving in surge, nonlinear effects will be of little importance on the condition that

$$ks_x|_{\text{max}} \ll 1. \quad (2.101)$$

Here we verify this for a single device in 2-D by considering a Taylor series expansion. In deep water ($kh \gg 1$), the x -component of the local fluid acceleration⁹ for an incident velocity potential given by (2.34) is

$$a_{i,x}(x, z, t) = \frac{\partial u_x}{\partial t} \quad (2.102)$$

$$= -\frac{\omega^2 H}{2} \cos(kx - \omega t) \frac{\cosh(kz + kh)}{\sinh(kh)} \quad (2.103)$$

$$\approx -\frac{gkH}{2} \cos(kx - \omega t) e^{kz}, \quad (2.104)$$

where we have used the deep-water dispersion relation (2.39) in the final line. The Taylor series expansion about $\mathbf{x}_0 = (x_0, z_0)$ is

$$\begin{aligned} a_{i,x}(x, z, t) &= a_{i,x}(x_0, z_0, t) + (x - x_0) \left. \frac{\partial a_{i,x}}{\partial x} \right|_{(x_0, z_0, t)} + (z - z_0) \left. \frac{\partial a_{i,x}}{\partial z} \right|_{(x_0, z_0, t)} + \dots \\ &\approx -\frac{gkH}{2} e^{kz} [\cos(kx_0 - \omega t) - ks_x \sin(kx_0 - \omega t) + ks_z \cos(kx_0 - \omega t) + \dots]. \end{aligned} \quad (2.105)$$

Assuming a position independent excitation force is thus a zeroth-order approximation in ks as well as ka .

⁹This neglects advective acceleration of the fluid particles - see discussion on p18.

2.4.3 Froude-Krylov force

The Froude-Krylov force is given generally by

$$\mathbf{F}_{\mathbf{FK}} = \rho \iint_{\bar{S}} \frac{\partial \phi_i}{\partial t} \mathbf{n} dS \quad (2.106)$$

where, as has been discussed, in linear wave theory the surface integral can be evaluated on \bar{S} . This is equal to the force that would act on the volume of water filling the place of the submerged section of the body if the body were not there, purely due to a pressure gradient induced by the incident wave field. For this reason it is often referred to as a “virtual buoyancy” force [19, 74]. In some instances, particularly for narrow bodies where diffraction effects are very small, this may give a reasonable approximation to the total excitation force.

The surface integral (2.106) can be simplified with the same method used in Section 2.2.1 for the hydrostatic force, by including the water-plane surface of the body S_w to form a closed surface integral, and applying the divergence theorem.

$$F_{FK,j} = \rho \iint_{\bar{S} + \bar{S}_w} \frac{\partial \phi_i}{\partial t} \mathbf{e}_j \cdot \mathbf{n} dS - \rho \iint_{\bar{S}_w} \frac{\partial \phi_i}{\partial t} \mathbf{e}_j \cdot \mathbf{e}_3 dS \quad (2.107)$$

$$= \rho \iiint_{\bar{V}_s} \nabla \cdot \left(\frac{\partial \phi_i}{\partial t} \mathbf{e}_j \right) dV - \delta_{j3} \rho \iint_{\bar{S}_w} \frac{\partial \phi_i}{\partial t} dS. \quad (2.108)$$

The integrand of the volume integral is just

$$\frac{\partial}{\partial x_j} \left(\frac{\partial \phi_i}{\partial t} \right) = \frac{\partial}{\partial t} \left(\frac{\partial \phi_i}{\partial x_j} \right) = \frac{\partial}{\partial t} u_{i,j} = a_{i,j}, \quad (2.109)$$

and also using (2.23) in the integral over \bar{S}_w we have

$$F_{FK,j} = \rho \iiint_{\bar{V}_s} a_{i,j} dV + \delta_{j3} \rho g \iint_{\bar{S}_w} \xi dS, \quad (2.110)$$

recalling that ξ is the surface elevation.

Under the small body approximation $ka \ll 1$ as outlined in section 2.4.2, the integrands in (2.110) may both be evaluated at the body centre and taken outside the integral to give, in vector form,

$$\mathbf{F}_{\mathbf{FK}} = \rho \bar{V}_s \mathbf{a}_i + \rho g \bar{A}_w \xi \mathbf{e}_3. \quad (2.111)$$

The first term is the “virtual buoyancy” force while the second, contributing in the heave mode only, is a first-order¹⁰ correction to the hydrostatic buoyancy force (2.58).

¹⁰i.e. First-order in the surface elevation ξ – the expression is still zeroth-order in ka .

2.4.4 Total excitation force

The total excitation force is simply the sum of the diffraction and Froude-Krylov forces. (2.111) is a general expression for the Froude-Krylov force, but (2.99) only gives the complex amplitude of the diffraction force for a sinusoidal incident wave. We can therefore write the excitation force in the frequency domain,

$$\mathbf{F}_{\mathbf{E}}(\omega) = [\rho\bar{V}_s + M_a(\omega)] \mathbf{a}_i(\omega) + [\rho g \bar{A}_w \xi(\omega)] \mathbf{e}_3, \quad (2.112)$$

where in accordance with the linear approximation, the fluid acceleration and surface elevation are to be evaluated at $\mathbf{x} = \mathbf{x}_0$. It appears from the form that this will give rise to a convolution integral in the time domain, in a similar fashion to the radiation force. However, unlike the device velocity, the fluid motion will be a known input for our purposes. If the wave field consists of a discrete sum of plane waves of different frequencies ω_j and heights H_j , each described by (2.34)–(2.37), and the body is located on deep water with a mean position of $x = z = 0$, the frequency domain inputs are

$$\xi(\omega) = \frac{i}{2} \sum H_j \delta(\omega - \omega_j), \quad (2.113)$$

$$\mathbf{a}_i(\omega) = -\frac{1}{2} \sum_j \omega_j^2 H_j \delta(\omega - \omega_j) \begin{bmatrix} 1 \\ 0 \\ i \end{bmatrix}, \quad (2.114)$$

where δ is the Dirac delta function. In the time domain, the surge component of the excitation force is simply

$$F_{E,x}(t) = -\frac{1}{2} \sum_j [\rho\bar{V}_s + M_a(\omega_j)] \omega_j^2 H_j \cos(\omega_j t). \quad (2.115)$$

We emphasise that this form for the excitation force applies only to cases in which the small-body approximation is valid.

2.5 Power capture

When an immersed body can move in response to waves incident upon it, the body absorbs power from the wave field. Conversely, as described in Section 2.3.2, a moving body also radiates power in the form of generated waves. If we consider the simple case of an unconstrained floating body with no resistive or dissipative forces acting, it is clear that, in the long-term time average, no energy will be removed from the wave field. The explanation for this is that all energy absorbed by the body is radiated away again. In order for a floating body to be removing net energy from the ocean, there must therefore be external forces acting to resist its motion – this is what the power take-off (PTO) system of any wave energy device will do. These resistive and/or dissipative forces will cause the body to oscillate with a phase such that its radiated wave causes destructive

interference with the incident wave, and the energy content of the ocean is reduced by the same amount as the energy removed due to the external forces.

It is important to distinguish between the amount of “useful” power captured by the PTO system, and the total amount absorbed by the moving body (henceforth called “the device”), some of which will be lost due to radiation and other parasitic forces. We adopt the unambiguous terms *power capture* and *excitation power* to refer to the two aforementioned quantities. Just as for the radiated power in Section 2.3.2, we will use these terms to refer to the time-average values rather than the instantaneous values. We define the quantities P_E and P_C consistent with P_R , as the rate of work done *on* the device by the incident waves and the PTO system respectively;

$$P_E = \overline{\mathbf{F}_E \cdot \mathbf{v}}, \quad (2.116)$$

$$P_C = \overline{\mathbf{F}_{PTO} \cdot \mathbf{v}}, \quad (2.117)$$

where \mathbf{F}_{PTO} is the force exerted by the PTO system on the device. Again similarly to the radiated power, $P_C \leq 0$. We will use the terms “power capture” and “radiated power” to refer to the magnitudes of P_C and P_R , with the tacit understanding that these represent power transferred from the device to the PTO system and fluid, respectively.

2.5.1 Mechanical forces

As explained above, any PTO mechanism must resist the motion of the body. This is generally parameterised as a “dashpot” force, negatively proportional to the body’s velocity:

$$\mathbf{F}_{PTO} = -R\mathbf{v}, \quad (2.118)$$

where R is a positive constant that we will call the *PTO resistance* (a matrix in the general case). Note that an expression like (2.118) assumes that the body is reacting against a structure that is fixed relative to the seabed; this is the case for some “attached” point absorber designs (see Section 1.4), but for moored point absorbers the reaction must be either against a second submerged body or against some sort of internal mass. This issue is revisited in Section 3.4.

In practise, a PTO system may exert additional force components. One such possibility is a restoring “spring” force, of opposite sense to the displacement of the body. Such a force may also be provided independently from the PTO system, intentionally or not. For a partially submerged body, a restoring heave force is provided naturally due to buoyancy. Most relevantly, a restoring force can be provided by a mooring structure designed to keep the body in position. These restoring forces may be nonlinear, but we restrict interest to those that may be approximated as a linear spring, viz.

$$\mathbf{F}_S = -S\mathbf{x}, \quad (2.119)$$

where S is the *spring constant* or *stiffness* (again, always positive and a matrix in general).

2.5.2 1-D linear case

We consider now a generic device confined to one degree of freedom, with PTO and spring forces as parameterised above, and forced by a single sinusoidal wave of frequency ω . Writing the radiation force in terms of the added mass and radiation resistance as in (2.76), an equation of motion for the device is

$$(M + M_a)\hat{a} + (R + R_r)\hat{v} + S\hat{x} = \hat{F}_E. \quad (2.120)$$

This has the appearance of a classic second order differential equation: the damped, driven harmonic oscillator. While the situation is similar, we emphasise that (2.120) is a frequency domain equation in which the coefficients M_a and R_r – as well as the excitation force – depend on ω . Relating the device's displacement and acceleration amplitudes to its velocity amplitude, with the time dependence as defined in (2.28), (2.120) can be solved for \hat{v} to give

$$\hat{v} = \frac{\hat{F}_E}{R + R_r + i[(M + M_a)\omega - S/\omega]}. \quad (2.121)$$

Combining this with (2.117) and (2.118) gives

$$P_C = -\frac{R}{2}|\hat{v}|^2 = \frac{-(R/2)|\hat{F}_E|^2}{(R + R_r)^2 + ((M + M_a)\omega - S/\omega)^2}. \quad (2.122)$$

2.5.3 Optimisation and resonance

It is easily seen from (2.121) and (2.122) that, regardless of the value of R , the power capture is highest when S is chosen so that the body is resonant – that is, its velocity is in phase with excitation force. This occurs for

$$S = (M + M_a)\omega^2 \equiv S_{res}(\omega). \quad (2.123)$$

It is also straightforward to show from (2.122) that, for a given spring stiffness, the value of R delivering the highest power capture is

$$R = \sqrt{R_r^2 + ((M + M_a)\omega - S/\omega)^2} \equiv R_{opt}(\omega, S). \quad (2.124)$$

The maximum power capture is therefore achieved when $S = S_{res}(\omega)$ and

$$R = R_{opt}(\omega, S_{res}(\omega)) = R_r(\omega), \quad (2.125)$$

and is simply

$$|P_C|_{max} = \frac{|\hat{F}_E|^2}{8R_r}. \quad (2.126)$$

The corresponding body velocity amplitude is

$$\hat{v} = \frac{\hat{F}_E}{2R_r} \equiv \hat{v}_{opt}. \quad (2.127)$$

Practically, there are various reasons why it will be impossible to reach, or even come close to reaching, optimal performance; we examine this issue further in Chapter 4.

2.5.4 Capture width

It was mentioned in Section 1.6 that point absorbers are theoretically capable of absorbing more power from the wave field than the amount directly incident upon their physical width. For a terminator type system, or a point absorber operating in a narrow channel (e.g. in a wave tank test), a standard measure of efficiency may be used, but for a point absorber operating in open ocean, the *capture width* is a more appropriate performance metric. The capture width, d , is the power capture divided by the incident wave energy flux (power per metre of wavefront),

$$d \equiv \frac{|P_C|}{J}. \quad (2.128)$$

It therefore gives the width of wavefront transmitting equal power to that captured by the device. Independent derivations by several authors¹¹ showed that the theoretical maximum power capture for a device operating in one of the translational modes is

$$d_{max} = \frac{n\lambda}{2\pi}, \quad (2.129)$$

where $n = 1$ for heave and 2 for surge or sway. This perhaps surprising result can be explained in terms of the 3-D interference effects between the incident plane wave and the ring-shaped wave radiated by the moving body. The same comments made at the end of the previous section about practical limitations to achieving the theoretical maxima apply here.

2.6 Nonlinear drag

In the preceding sections, we have considered the hydrodynamics of a body in the context of an ideal fluid – one that is incompressible, irrotational, and has zero viscosity – so that potential flow theory applies. We then assumed that the surface waves are sufficiently small that the system can be linearised. A large proportion of the theoretical wave energy literature operates under these assumptions. Indeed, the foundational book *Ocean Waves and Oscillating Systems* by Falnes [29] deals entirely in the ideal, linear regime.

It is well-known, however, that the assumption of zero viscosity leads to the conclusion of zero hydrodynamic force on a body moving with constant velocity in an unbounded fluid. This is at odds with common experience of the dissipative drag force that acts in such a situation, so the assumption clearly fails to capture some important effects on submerged bodies. This problem, known as d’Alembert’s Paradox, was resolved by Prandtl with his *boundary layer* theory. This states that even in fluids with very low viscosity there is a small region of fluid surrounding any boundary in which viscous effects are important and potential flow theory is inapplicable.

¹¹For one derivation see Falnes [29], and see Cruz [17] for references to others.

The existence of boundary layers explains how a drag force arises when a submerged body undergoes motion in a low-viscosity fluid. In addition to a *skin friction* component due to friction between the wetted surface and the fluid, there is a *form drag* component due to the phenomenon of flow separation. A separation of the boundary layer from the body can occur, resulting in the presence of a wake and generation of eddies and vortices, which creates a drag force on the body due to the pressure difference between the wake and the upstream. The form drag is the dominant contribution for a fluid of low viscosity¹², and has an increasing effect on the dynamics for decreasing body size.

Newman [59] shows by dimensional analysis that for a body moving relative to a fluid with fixed speed v_r , the drag force must be of the well-known quadratic form

$$F_D = \frac{1}{2}\rho C_D A v_r^2, \quad (2.130)$$

where A is the cross-sectional area of the body “seen” by the fluid and C_D is the *drag coefficient*. C_D is a dimensionless quantity that depends on the surface properties (e.g. roughness) of the body and another dimensionless quantity called the *Reynold’s number*,

$$Re = \frac{\rho v_r D}{\eta}, \quad (2.131)$$

where D is the characteristic linear dimension of the body and η is the kinematic viscosity of the fluid.

2.6.1 The Morison equation

A drag force of the form (2.130) was first tested for application to oscillatory wave flows by Morison et al in 1950, for the case of cylindrical piles [57]. The hydrodynamic force equation used by the authors, which has since become known as the Morison equation, has been widely adapted and used in ocean engineering. In its original form, it gave the total inline (surge) force on a small stationary body due to an oscillatory flow $u(t)$,

$$F(t) = \rho V_s C_M \dot{u}(t) + \frac{1}{2}\rho C_D A u(t) |u(t)|, \quad (2.132)$$

where C_M is called the inertia coefficient (dimensionless). The first term on the right-hand side, often called the inertial force, is identified as the small body excitation force from potential flow theory (2.112) if

$$C_M = 1 + M_a/\rho V_s \equiv 1 + C_A. \quad (2.133)$$

For oscillatory flows, the drag coefficient is found to also depend on the Keulegan-Carpenter (KC) number,

$$KC = \frac{u_{max} T}{D}, \quad (2.134)$$

¹²More accurately, for a flow with high Reynold’s number (see following paragraph).

where u_{max} is the maximum flow speed in a cycle, T is the cyclic period and D is again the characteristic linear dimension of the body.

In the case that the body can move in response to the forcing, the Morison equation can be generalised to

$$F(t) = \rho V_s \dot{u}(x, t) + \rho V_s C_A [\dot{u}(x, t) - \ddot{x}(t)] + \frac{1}{2} \rho C_D A [u(x, t) - \dot{x}(t)] |u(x, t) - \dot{x}(t)|. \quad (2.135)$$

Here, the inertial force has been split up. The first term is the Froude-Krylov force (2.111). The second term represents the small-body diffraction force (2.99) combined with a small-body approximation to the radiation force (2.76). The drag force (the third term) is now cast in terms of the relative velocity between the fluid and the body.

The Morison equation can be seen as an heuristic approach of adding the hydrodynamic force from two limits: low KC number (the inertial force), and high KC number (the drag force). It is thus a semi-empirical equation in which the coefficients are to be determined experimentally, offering a purely pragmatic solution to a difficult problem. It has been criticised for failing to give an accurate parameterisation in certain regimes or situations (see Sarpkaya & Isaacson [68] for discussion on this). In addition, there are practical difficulties surrounding the application of the equation, particularly in time-dependent flows. The drag coefficient depends on the relative velocity and will vary over a cycle, but for practical reasons a cycle-averaged constant value is virtually always used. Determining the coefficient values is difficult to do with accuracy (see Wolfram & Naghipour [82] for an overview of different techniques used). These two problems are amplified when assessing the forces in a realistic ocean spectrum rather than a sinusoidal wave field. There is also debate on issues such as whether the ideal value of inertia coefficient from potential flow theory may be used or both coefficients must be found experimentally [51, 67], and whether the total fluid acceleration Du/Dt ought to be used rather than the local acceleration $\partial u/\partial t$ [44].

Nevertheless, in spite of its flaws and limitations the Morison equation has been extensively applied in the field of ocean engineering. Its success lies in it being a simple model that gives reasonable prediction of the forces experienced by “small” offshore structures, especially in a probabilistic (rather than deterministic) sense [12]. Despite attempts, no major improvements or alternatives have emerged to challenge the Morison equation’s general practical usefulness. However, from work presented earlier this chapter it is apparent that the modified equation (2.135) will have inadequacies in dealing with cases where the body motion is of large amplitude and/or contains a broad range of frequency components: cases that are of interest to the present study. This is because the equation does not include any radiation resistance term and does not employ the correct time-domain formulation of the radiation force. The more accurate memory integral expression in (2.86) can be incorporated into (2.135) to address this shortcoming. Chitrapu & Ertekin [16] did just this in one study, comparing simulated results using this and the standard Morison formulation for floating platforms undergoing large amplitude response¹³. While there is broad agreement, the two result sets exhibit quite significant

¹³The modified force equation in the study also included effects of wave diffraction/scattering, rather

departures.

Formulations similar to that used by Chitrapu & Ertekin are rare in the wave-energy literature. The Morison-type quadratic drag force is most often neglected so that the system remains linear and can be studied in the frequency domain. There are questions surrounding how large an effect the nonlinear drag will have on the dynamics in different contexts that have not been satisfactorily resolved. In one paper by Caska & Finnigan [15], in which nonlinear drag was included in the study of a cylindrical bottom-pivoted (i.e. pitching) wave energy absorber, the authors state: “It was found that the nonlinear drag term, which is often neglected in studies on wave energy conversion, has a large effect on performance.” Clearly the legitimacy of neglecting nonlinear drag will depend largely on flow parameters such as the KC number. Iversen in [45] proposed a criterion that the eddy shedding process for a point absorber is negligible if the displacement amplitude of the body satisfies

$$|s_{max}| \lesssim \frac{D}{\pi}. \quad (2.136)$$

This is derived from (2.134) and based on a study of oscillating flow past a cylinder in which eddy shedding was found to be of little importance when $KC \lesssim 2$, “whereas for $KC \gtrsim 5$ there exists a distinct turbulent wake oscillating back and forth.” The effects will obviously vary for different body geometries and surface roughness, though, and generalisation of Iversen’s result is problematic.

We conclude by summarising that the issue of the importance of nonlinear drag forces on the performance of wave energy devices is quite poorly understood and often avoided entirely. The characterisation of such forces in theoretical studies is difficult, and the Morison equation is still widely considered to be the best tool for this job. There is evidence to suggest that drag forces could have significant effects on wave energy systems, particularly for small devices.

than neglecting them as in the small-body approximation and the Morison equation.

Chapter 3

Modelling methods and validation

In this chapter, we present the details of the idealised computational model developed for the purpose of studying linked wave energy point absorbers. This model was developed and coded by the author using MATLAB. We also describe herein the simplifications and assumptions (further to those introduced in Chapter 2) that were made in order to keep the project reasonable in scope and to focus efforts on the key research questions laid out in Section 1.9. Finally, we verify the performance of the computational code and test the importance of using the correct time-domain formulation of the radiation force, which includes memory effects. For ease of reference, we present in Table 3.1 a list of definitions of symbols used in this chapter and those to follow.

3.1 1-D idealisation

In general, a floating body is free to move in six modes of motion, as described in Section 2.2 and illustrated in Figure 2.2. These modes are generally not independent; there is potentially strong coupling between them, dependent on the geometry of body and the local environment.

We start by assuming that incident waves are *unidirectional*, and define the x -axis to have the same direction and sense as the incident wave. If, in addition, the devices are symmetric about the x -axis, then there is no variation in the y -direction and the system is fully represented in two dimensions with motion in surge, heave and pitch only.

This study is a first foray into the idea of linked point absorbers, and so the intention is to keep the mathematical and computational complexity to a minimum and undertake a preliminary investigation of the concept to inform more detailed work in the future. To this end, we simplify the system even further to a representation in one spatial dimension, with motion in *surge only*. In doing so, we implicitly neglect coupling between surge and other modes of motion. Specifically, we consider surface piercing devices with their centres at $z = 0$, and neglect changes in their submerged volume.

A schematic diagram of the surge-only model of a linked chain, for the example of three devices, is given in Figure 3.1, with the devices represented as circles. Explanations of the mooring and linkage forces and the power take-off forces are given in Sections 3.3

Symbol	Definition	Symbol	Definition
a	Device radius	P_D	Power dissipated by drag
A	Cross-sectional area of device	P_E	Excitation power
B	“Added damping” parameter used by Hulme [43]	P_{ML}	Power transferred by mooring and linkage lines
C_D	Drag coefficient	P_R	Radiated power
d	Capture width	$r(t)$	Ramp function
f	Frequency	R	Power take-off resistance
F_D	Drag force	R_r	Radiation resistance
F_E	Excitation force	S	Stiffness of mooring and linkage lines (when the same)
F_{ML}	Force from mooring and linkage lines	S_L	Stiffness of linkage lines
F_{PTO}	Power take-off force	S_M	Stiffness of mooring lines
F_R	Radiation force	t	Time
g	Acceleration due to gravity (9.81 m s^{-2})	t_r	Ramp-time
H	Wave height (trough to peak)	T	Wave period
k	Wavenumber	u	Fluid velocity
$K(t)$	Impulse response function	x	Displacement of device
L	Inter-device spacing	v	Velocity of device
M	Physical mass of device	λ	Wavelength
M_a	Added mass of device	ρ	Density of seawater ($1,025 \text{ kg m}^{-3}$)
n	Number of devices in chain	ϕ	Phase
P_C	Power capture	ω	Angular frequency

Table 3.1: Definitions of symbols used in Chapters 3–6.

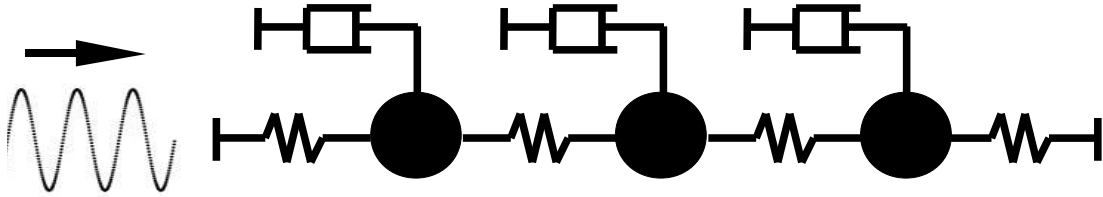


Figure 3.1: Schematic of the 1-D surge-only model of a linked chain of three devices.

and 3.4 respectively. While the system appears very simple, the nonlinear effects of the inter-device linkages make it dynamically rich. This model serves as a useful tool for studying the effects of the linkages without the added complexity of multi-dimensionality.

From this point on, unless explicitly stated otherwise, all equations and analyses refer to the 1-D surge-only model. Dynamic quantities are expressed in a vector of length n , where n is the number of devices in the particular simulation to which the quantity refers. The j th component corresponding to the j th device in the chain, counted in the direction of the incident wave. Device properties such as added mass and radiation resistance are assumed to be the same for all devices, and the corresponding variables are therefore reduced from matrices to scalars.

3.1.1 Incident wave field

The unidirectional wave field is made up of sinusoidal components, as defined by the velocity potential in (2.34). For reasons described below in Section 3.8, we assume deep water in all cases ($kh \gg 1$, where k is wavenumber), removing the water depth h as a parameter. From (2.40), the fluid velocity and (local) acceleration fields are given by

$$u(x, t) = \sum_j u_j(x, t) = \frac{1}{2} \sum_j \omega_j H_j \sin(k_j x - \omega_j t + \phi_j), \quad (3.1)$$

$$\dot{u}(x, t) = \sum_j \dot{u}_j(x, t) = -\frac{1}{2} \sum_j \omega_j^2 H_j \cos(k_j x - \omega_j t + \phi_j), \quad (3.2)$$

where H_j , ω_j , k_j and ϕ_j are the height, angular frequency, wavenumber and phase of the j th sinusoidal component of the wave field, respectively. As discussed in Section 2.1.6, the phases are randomly chosen from a uniform distribution on the interval $[0, 2\pi]$. Throughout Chapters 4 and 5 the wave field consists of a single frequency sinusoid, so the summations and indices can be dropped from (3.1)–(3.2) and we choose the phase $\phi = 0$.

In our surge-only model, the results for deep water can in fact be re-interpreted for the finite depth case. By comparison of (2.36) and (2.40), the case with wave height H on deep water has the same surface fluid velocity amplitude as the case with water depth h' and wave height $H' = H \tanh(k'h')$. The dispersion relationship is also modified so that, for a fixed wave period value, $k' = k / \tanh(k'h')$. As will be shown by later results, the dynamics would be unaffected by the change in wavelength if the device spacing were adjusted by the same factor to preserve the ratio of spacing to wavelength. Thus, following the above reasoning, one would expect the power capture results for the case with infinite water depth, wave height H , wavenumber k and device spacing L to be the same as for the family of cases with water depth h' , and $(H', k', L', T') = (H \tanh(k'h'), k / \tanh(k'h'), L \tanh(k'h'), T)$. We note, however, that the hydrodynamic parameters of the device do depend on water depth in a difficult-to-determine manner, so this equivalence between results for different water depths is not complete. Probably more significant still is that this 1-D discussion neglects the scaling of the heave motions with water depth, which will have a bearing on real-world dynamics and results.

3.1.2 Hydrodynamic interactions

In our model, we expressly neglect the hydrodynamic interactions between devices. In reality, the radiated and diffracted waves due to one body will have an effect on all others. As discussed in review articles by McIver [54] and Newman [60], these interactions are generally sensitive to the geometry of the array due to interference effects. However, for the conditions that we are investigating – devices that are very small in relation to the incident wavelength, and oscillating with relatively small amplitudes so that the radiated energy is small – the hydrodynamic interactions between devices are likely to have relatively small effect and it is justifiable to neglect them for this preliminary study. One consequence of doing so is that the wave is not diminished in height as it travels along the chain, as one might expect it to be. However, this depends on how the wave “rebuilds” in the device’s wake. Parameterising such effects would be difficult without fully including hydrodynamic interactions. Without access to data or appropriate software for doing so (see Section 3.8), we are left with little choice but to neglect them.

3.2 Master equation

The full set of forces that we consider to act on the devices in the x -direction is: the hydrodynamic excitation, radiation and drag forces; and the mechanical forces from the mooring and linkage lines and the power take-off system. Using Newton’s Second Law, the force equation is

$$M\ddot{\mathbf{x}} = \mathbf{F}_E + \mathbf{F}_R + \mathbf{F}_D + \mathbf{F}_{ML} + \mathbf{F}_{PTO}, \quad (3.3)$$

where M is the device mass (assumed the same for all devices). We now detail the implementation of each force term, beginning with the mechanical forces.

3.3 Mooring and linkage forces

The mooring and linkage lines are idealised here as massless, tension-only springs. Catenary, drag and inertia effects on the lines are all neglected. This means that a line only exerts a force on a device when the line is extended beyond its natural length, and when this happens the force is linearly proportional to the extension length. This tension-only parameterisation has been employed in other wave energy studies [50] and also in studies of long-line mussel farms [65]. In both cited examples, the mooring forces also include a dashpot response to account for line damping – for simplicity, we opt to neglect such a term, noting that the damping effect could be bundled in with the other linear resistance or quadratic drag terms.

The linear force parameterisation is obviously very simplistic and there are questions about how well it will represent real situations. However, in a paper on the influence of moorings on wave energy devices, Fitzgerald & Bergdahl conclude [32]:

“Evidence from literature study suggests that the use of an equivalent linear impedance for moorings is valid for the consideration of their influence on the power production of wave energy converters, provided it is understood that:

1. The mooring linearisation will only be valid at a certain reference static configuration of the device and mooring system.
2. Performance motion amplitudes referred to mooring attachment points are small relative to the water depth and induce mooring tensions that are small relative to the equilibrium pretension.
3. The resulting linear impedance is most valid for amplitudes close to the amplitude at which the linearisation calculation was carried out.”

For a detailed discussion on the drag effects of different types of mooring lines, see [10].

3.3.1 Two-dimensional effects

Perhaps the most obvious criticism that could be levelled against the surge-only model is associated with the action of the mooring lines. Clearly, regardless of the geometry of the device, the mooring lines will introduce significant coupling between the surge, heave and pitch modes. The strength of this coupling will depend on the the water depth and the horizontal distance between the device and the mooring point. It should be obvious that the 1-D representation will be more accurate for cases in which the mooring line is at a shallower angle to the seabed.

A further point to consider is that – even if the lines do exhibit a linear response to extension – the variation of the restoring force for horizontal displacements will only be approximately harmonic for small amplitude oscillations. We demonstrate this here with some original analysis.

Consider a single device on the surface of water of depth h with one mooring line pulled “just taut” to its natural length L , forming an angle θ to the horizontal seabed. If the device undergoes a small horizontal displacement δ that stretches the line (with no motion in the y -direction), it is straight-forward to show that to first order in δ , the line’s new length is

$$L' \approx L + \delta \cos \theta \quad (3.4)$$

and the new angle to the seabed, θ' , satisfies

$$\cos \theta' \approx \cos \theta + \frac{\delta}{L} (1 - \cos^2 \theta). \quad (3.5)$$

These expressions can then be used to find the x -component of the restoring force F_{ML} :

$$(F_{ML})_1 = -S (L' - L) \cos \theta' \quad (3.6)$$

$$\approx -S\delta \cos^2 \theta, \quad (3.7)$$

for spring stiffness S . Thus the restoring force is harmonic to first-order, with an effective spring stiffness of $S \cos^2 \theta$ for strictly horizontal motion. This first-order approximation is valid for

$$\delta \ll \frac{L}{2 \cos \theta}. \quad (3.8)$$

For example, a mooring angle of 30° and water depth $h = 50$ m means an extension of 3 m gives $\delta / (L/2 \cos \theta) \approx 5\%$. This is on the order of the maximum extension observed under the standard conditions we apply later, so the use of a harmonic restoring force seems acceptable. However, for the cases we examine with higher wave heights and shorter wave periods, the motion of the devices extends into the regime where the mooring forces could become substantially nonlinear.

Accurate representation of the linkage lines in 1-D is less of a concern, since under all but extreme conditions the lines would remain reasonably close to horizontal. With this point in mind, one can actually envisage ways in which the physical system might be engineered to match the 1-D model more closely, if this were desired. For example, extra submerged body with large inertia might be connected between the outermost devices and their mooring points, such that the line connected to these devices lie much closer to horizontal. This would have similar effects to reducing the water depth (but obviously without any change to wave parameters). This type of scheme is in fact not too different to the common set-up of a long-line mussel farm [65, 75].

3.3.2 Mathematical expression

We proceed with parameterisation of the mooring and linkage forces as harmonic forces, operating in tension only. The Heaviside step function,

$$\mathcal{H}(x) = \begin{cases} 0, & x < 0 \\ 1, & x \geq 0 \end{cases}, \quad (3.9)$$

is useful in expressing the latter attribute. The displacement of Device j from its starting position is defined as follows,

$$x'_j(t) \equiv x_j(t) - x_j|_{t=0}. \quad (3.10)$$

In all simulations, mooring and linkage lines are set as “just taut” when the devices are in their starting positions; that is, the devices’ starting positions define the natural lengths of the lines. The total force from the mooring and/or linkage lines acting on

Device j may thus be expressed

$$F_{ML,j}(\mathbf{x}) = \begin{cases} -S_M x'_j \mathcal{H}(x'_j) + S_L [x'_{(j+1)} - x'_j] \mathcal{H}(x'_j - x'_{(j+1)}), & j = 1, \\ -S_L [x'_j - x'_{(j-1)}] \mathcal{H}(x'_j - x'_{(j-1)}) + \\ S_L [x'_{(j+1)} - x'_j] \mathcal{H}(x'_{(j+1)} - x'_j), & 2 \leq j \leq n-1, \\ -S_L [x'_j - x'_{(j-1)}] \mathcal{H}(x'_j - x'_{(j-1)}) + S_M x'_j \mathcal{H}(-x'_j), & j = n, \end{cases} \quad (3.11)$$

where S_M and S_L denote the stiffness of the mooring and linkage lines respectively¹. In virtually all cases that we examine, we set $S_M = S_L \equiv S$, and the devices have a regular spacing that we label L . In the special case of $n = 1$ (i.e. a lone device), (3.11) reduces to a simple symmetrical, linear spring force about the device's starting position.

Note that in a real mooring line, the stiffness is given by $S = AY/L$, where Y is the Young's modulus of the material, and A and L are the natural cross-sectional area and length of the line respectively. For convenience, we opt to treat S as an independent parameter, and simply note that in practise this would require the cross-sectional area to be adjusted accordingly with L .

3.4 Power take-off

The power take-off is parameterised in the model by the standard dashpot force given in (2.118), which we rewrite here for convenience

$$\mathbf{F}_{\text{PTO}}(\dot{\mathbf{x}}) = -R\dot{\mathbf{x}}, \quad (3.12)$$

where R is the PTO resistance. As mentioned in Section 2.5.1, this implies the main body of the device is reacting against a point that is fixed relative to the seabed, which would seem to require some sort of built structure. While perhaps feasible, it is rather difficult to envisage a practical scheme of this nature for an array of surging point absorbers. It seems that to be practical, a surging point absorber would need to be self-reacting. Two devices that offer insight here are the WET-NZ device [50] and the P-S Frog [81], both previously mentioned in Section 1.4. Both devices offer power take-off for some combination of surge, heave and pitching motion, the former using the motion of a small buoyant float relative to a large vertical spar buoy, and the latter using an internal sliding mass cased inside the body.

Early in this project there were intentions to experiment with a more realistic PTO model, but unfortunately time constraints did not allow this to happen. We consider this a secondary concern since the focus for this research is on the effects of the inter-device linkages. Furthermore, the PTO model employed ought not to differ dramatically from cases where the main body is reacting against supplementary bodies of large inertia.

¹In principle, each line could have a different stiffness, but we preclude that possibility here.

3.5 Radiation force

The correct formulation of the radiation force in the time domain was presented in Section 2.3.4, culminating in the expression (2.86). This contains a memory integral of the impulse response function multiplied by the velocity history, making (3.3) a second-order integro-differential equation. Strictly, this formulation should be used in any instance where the device is not in steady-state sinusoidal motion of a single frequency. In practise, if the motion is non-sinusoidal but is dominated by a single frequency, then one would expect that assuming constant values for the added mass and radiation resistance should deliver a reasonably accurate radiation force, especially if the variation in the hydrodynamic parameters over the range of frequencies present in the motion is small. The widespread use of the Morison equation lends weight to this view (see discussion in Section 2.6.1).

For incident wave fields with multiple frequency components, it is clearly essential to use the correct memory integral form. The majority of investigation in this project was for monochromatic sinusoidal wave fields, though (Chapter 6 is the exception); it is tempting to simply assume that the device responses in these conditions will be predominantly single frequency. There are two sources of nonlinearity in the model used here: the quadratic drag, and the tension-only device linkages. The former alone is not expected to cause a dramatic departure from the linear case. However, it is difficult to predict *a priori* how large the nonlinear effects of the device linkages will be. Perhaps the best indication is given by a study by Greenhow and White [36] where the performance of point absorbers with a “latching” control mechanism² was studied using the correct time domain radiation force as well as a version with constant hydrodynamic parameters. The authors concluded that, “[...] the full memory model is essential for studying either transient motion or motion with nonlinear constraints.”

One thing that is reasonably certain prior to examination is that the nonlinear effects here will be sensitive to the spacing of the devices and the stiffness of the linkages. This makes it important to capture the nonlinearities accurately, since the effects of linking the devices in a chain are at the heart of the motivation for this research. Results presented later in this chapter (Section 3.14) show that for a single frequency forcing the device linkages do indeed give rise to significant high frequency motion components.

The code was applied using two different versions of the radiation force: the correct time domain formulation, which we call the “memory integral” version, and the approximation using constant values for added mass and radiation damping corresponding to the incident wave frequency, which we call the “constant coefficients” version. To be clear, these are

$$\mathbf{F}_{\mathbf{R},\text{MEM}}(\dot{\mathbf{x}}, \ddot{\mathbf{x}}) = -M_a(\infty)\ddot{\mathbf{x}}(t) - \int_0^t K(\tau)\dot{\mathbf{x}}(t-\tau) d\tau, \quad (3.13)$$

$$\mathbf{F}_{\mathbf{R},\text{CC}}(\dot{\mathbf{x}}, \ddot{\mathbf{x}}) = -M_a(\omega_i)\ddot{\mathbf{x}}(t) - R_r(\omega_i)\dot{\mathbf{x}}(t), \quad (3.14)$$

² “[...] whereby the device is deliberately held fixed for parts of the oscillation to allow the body velocity and wave force to be in phase during the motion part of the cycle.” [36]

where ω_i denotes the angular frequency of the monochromatic incident wave, M_a is the added mass, R_r is the radiation resistance, and $K(\tau)$ is the impulse response function (calculated from (2.87)). As discussed in Section 2.4.2, it is consistent with the zeroth-order small-body approximation to drop the term proportional to velocity from (3.14), but we maintain it here in order to be able to make consistent comparisons between these two parameterisations of radiation force.

3.6 Excitation force

In Section 2.4.4, we discussed the time domain formulation of the excitation force for a wave field made up of distinct sinusoidal components, arriving at (2.115). This expression relies on the assumption that the body size and the motion amplitude are both small in relation to the wavelength. In Section 2.4.2 we showed that it is acceptable to evaluate the fluid acceleration at a body's time-averaged centre if the maximum displacement from its time-average position, s_{max} , satisfies $ks_{max} \ll 1$. The lower limit of the relevant wavelength range is ≈ 100 m, for which 10% of k^{-1} is ≈ 1.6 m. Simulation results presented later will show that this threshold is exceeded slightly in standard scenarios, and considerably under more extreme scenarios tested.

Furthermore, the nonlinearities introduced by the drag and especially the device linkages mean that the use of time-averaged positions is less simple than it might sound. Whereas in a fully linear case the devices' time-averaged positions under steady-state motion will be the same as their static equilibrium positions, here the time-averaged positions cannot be easily predicted prior to running the simulation. In fact, they are often found to differ quite markedly from the static equilibrium positions (the default starting positions in the simulations). Thus, to evaluate the quantities at the true time-averaged device positions means considerable practical disadvantage³, while opting to use the static equilibrium positions regardless causes an error that is additive to that described in the previous paragraph. Instead, we opt to simply evaluate the fluid acceleration at the devices' real-time positions, viz.

$$\mathbf{F}_{\mathbf{E}}(\mathbf{x}, t) = - \sum_j [\rho \bar{V}_s + M_a(\omega_j)] \dot{\mathbf{u}}_{\mathbf{j}}(\mathbf{x}, t), \quad (3.15)$$

where the components of local fluid acceleration $\dot{\mathbf{u}}_{\mathbf{j}}$ are evaluated from (3.2), ρ is the fluid density and \bar{V}_s is the time-averaged submerged volume of the device.

The force (3.15) is straight-forward to implement in the time domain, and the real-time device positions are already used in evaluating the instantaneous drag force. However, it does mean being inconsistent in order of approximation. For example, it raises the question of whether the total fluid acceleration Du/Dt , which includes higher order convective acceleration terms, should be used rather than just the local fluid acceleration

³One might conceive of an iterative procedure whereby the devices' time-average positions are evaluated from the results of a simulation, it is then rerun using these values to calculate $\mathbf{F}_{\mathbf{E}}$, and so forth until the results converge to an acceptable accuracy. Such a process would be both cumbersome and computationally expensive.

$\partial u/\partial t$. Additionally, the excitation force will no longer be strictly sinusoidal, calling into question the veracity of the time domain formulation in Section 2.4.4⁴. From a practical standpoint though, we consider that these concerns are insignificant when assessed against the other assumptions and simplifications inherent in the model. Furthermore, the inclusion of the nonlinear drag term described in the following section already means that the model equation is heuristic in nature, rather than a consistent theoretical approximation.

3.7 Drag force

To account for energy losses due to eddy-shedding and viscous drag we include a hydrodynamic drag force, parameterised as in the Morison equation for relative motion, (2.135):

$$\mathbf{F}_D(\mathbf{x}, \dot{\mathbf{x}}, t) = \frac{1}{2}\rho C_D A [\mathbf{u}(\mathbf{x}, t) - \dot{\mathbf{x}}] |\mathbf{u}(\mathbf{x}, t) - \dot{\mathbf{x}}|, \quad (3.16)$$

where C_D is the drag coefficient and A is the cross-sectional area of the device “seen” by the fluid flow. As discussed in Section 2.6, the drag coefficient for oscillatory motion is a function of flow parameters including the Keulegan-Carpenter and Reynold’s numbers, which depend on the body’s velocity as well as the wave period. However, taking account of these dependencies is very difficult and impractical, and we opt for the common approach of simply assuming a fixed value for C_D (see [15], for example). Determining a precise value is not possible given the number of dependencies, but typical values are of order unity. In virtually all cases we use the value $C_D = 0.5$.

3.8 Choice of device geometry: semi-submerged sphere

The original intention for this study was to leave the device design as generic as possible. If we were to assume a fixed value for added mass, as in the Morison equation, the only geometrical quantities needing to be specified would be the submerged volume and cross-sectional area of the device (both assumed fixed in the surge only model). However, the decision to implement the more accurate time domain formulation of the radiation force makes it necessary to specify further properties. Specifically, (3.13) shows that information is required about the device’s hydrodynamic parameters – the added mass and radiation resistance – over the entire frequency spectrum⁵ These parameters depend on the geometry of the device and also the local environment in which it is situated. As discussed in Section 2.3, finding the added mass and radiation resistance parameters through (2.73) requires solving a boundary value problem that can only be done with computational methods for most body geometries. There are commercially available

⁴Unlike for the radiation force, though, we can be confident that this forcing will be dominated by the incident frequencies.

⁵Due to the Kramers-Konig relations (2.82)–(2.83), it is in fact sufficient to know just the radiation resistance over the frequency spectrum, plus the value of added mass in the infinite frequency limit.

Quantity:	Dimensional relation:	Example conversion factors:	
		$a = 2 \text{ m}$:	$a = 3\text{m}$:
Position	$x = a x'$	2 m	3 m
Time	$t = \sqrt{a/g} t'$	0.45 s	0.55 s
Velocity	$\dot{x} = \sqrt{ag} \dot{x}'$	4.4 ms^{-1}	5.4 ms^{-1}
Acceleration	$\ddot{x} = g \ddot{x}'$	9.8 ms^{-2}	9.8 ms^{-2}
Mass	$m = \frac{2}{3}\pi\rho a^3 m'$	$1.7 \times 10^4 \text{ kg}$	$5.8 \times 10^4 \text{ kg}$
Force	$F = \frac{2}{3}\pi\rho a^3 g F'$	$1.7 \times 10^5 \text{ N}$	$5.7 \times 10^5 \text{ N}$
Spring stiffness	$S = \frac{2}{3}\pi\rho a^2 g S'$	$8.4 \times 10^4 \text{ Nm}^{-1}$	$1.9 \times 10^5 \text{ Nm}^{-1}$
PTO resistance	$R = \frac{2}{3}\pi\rho a^{5/2} g^{1/2} R'$	$3.8 \times 10^4 \text{ Nsm}^{-1}$	$1.0 \times 10^5 \text{ Nsm}^{-1}$
Power	$P = \frac{2}{3}\pi\rho a^{7/2} g^{3/2} P'$	$7.5 \times 10^5 \text{ W}$	$3.1 \times 10^6 \text{ W}$

Table 3.2: Relations between non-dimensionalised units (dashed) and the corresponding S.I. units of important quantities. The example conversion factors (multiply to convert non-dimensionalised to S.I units) are evaluated to two significant figures, using a seawater density of $\rho = 1,025 \text{ kg m}^{-3}$ and gravitational acceleration of $g = 9.81 \text{ m s}^{-2}$.

software programmes for this purpose, such as WAMIT⁶, but we did not have access to any such package for this project.

Thankfully, we were able to find one source in the literature giving comprehensive data on the hydrodynamic parameters for a particular geometry. In [43], Hulme presents in tabulated form the added mass and damping parameters for the surge and heave modes of a floating hemisphere on deep water ($kh \gg 1$), calculated exactly using a series expansion of the velocity potential in terms of spherical harmonics. Although it is not made clear in the paper itself, other authors have interpreted the hemisphere case as identical to a complete, half-immersed sphere [26, 28]. To make use of these data, we thus opt for our model device to be a solid sphere that is neutrally buoyant when half-submerged in stationary waters; we refer to this design henceforth as the “semi-submerged sphere”, following Falnes [28]. For consistency with Hulme’s data we also assume deep water, and from this point on all work is done under the approximation $kh \gg 1$ (with the possible reinterpretation for other depths as discussed in Section 3.1.1). We are also still operating in the small-body approximation $ka \ll 1$, where a now has the specific interpretation of the device radius.

3.9 Non-dimensionalised units

The specification of a length-scale for the device introduces the possibility of nondimensionalisation. While this can make interpretation of the results more obtuse, it delivers the major benefit of removing the device radius as a variable, so that each simulation now represents an infinite group of situations corresponding to different values of a .

⁶<http://www.wamit.com/>

Units of length, time and mass are scaled by a , $\sqrt{g/a}$ and $\rho\bar{V}_s$ respectively. Note that we can now write $\bar{V}_s = \frac{2}{3}\pi a^3$, and that the condition that the device is neutrally buoyant when semi-submerged means that in fact $\rho\bar{V}_s = M$, the (true) mass of the device⁷. The resulting non-dimensionalised units are presented in Table 3.2 with their relationship to the corresponding S.I. units, and example conversion factors for the cases $a = 2$ m and 3 m.

Note that, for example, all quantities of length, such as wave height, are scaled in the same way as position. The impulse response function has the same units as spring stiffness (N m^{-1}) and thus is subject to the same scaling, given in Table 3.2. The expression given for $K(\tau)$ in (2.87) is unchanged when expressed in nondimensional form. This is true of all relations from Chapter 2 that do not contain a , g or ρ . Here we list some of the important relations that do undergo changes: the small-body approximation (2.97) becomes simply $k' \ll 1$; the dispersion relationship on deep water (2.39) becomes

$$(\omega')^2 = k'; \quad (3.17)$$

and finally, the scaled incident wave-energy flux of a plane wave (2.44) is

$$J' = \frac{3}{64\pi^2}(H')^2 T'. \quad (3.18)$$

For the remainder of this thesis, all quantities will be expressed in the non-dimensionalised units, unless it is explicitly stated otherwise. For ease of notation, though, we subsequently drop the dashes that distinguish the scaled quantities from their S.I. counterparts.

3.10 Non-dimensionalised master equation

Dividing the master equation (3.3) by $\rho\bar{V}_s g$ and expressing it in terms of the non-dimensionalised quantities in Table 3.2 heralds only one change: the cancellation of the mass term on the left-hand side, leaving simply $\ddot{\mathbf{x}}(t)$. The expressions for the mooring, power take-off and radiation forces are unchanged in form, while those for the excitation and drag force terms undergo minor changes when expressed in the scaled units:

$$\mathbf{F}_E(\mathbf{x}, t) = -\frac{1}{2} \sum_j [1 + M_a(\omega_j)] \dot{\mathbf{u}}_j(\mathbf{x}, t), \quad (3.19)$$

$$\mathbf{F}_D(\mathbf{x}, \dot{\mathbf{x}}, t) = \frac{3}{8} C_D [\mathbf{u}(\mathbf{x}, t) - \dot{\mathbf{x}}] |\mathbf{u}(\mathbf{x}, t) - \dot{\mathbf{x}}|. \quad (3.20)$$

Combining the force expressions presented in the preceding sections into the master equation yields a system of n coupled, second-order scalar differential equations. This can be recast as a system of $2n$ coupled first-order differential equations by introducing the redundant variable \mathbf{v} , as follows

$$\dot{\mathbf{x}} = \mathbf{v}, \quad (3.21)$$

$$\dot{\mathbf{v}} = \mathbf{F}_E(\mathbf{x}, t) + \mathbf{F}_R(\mathbf{v}, \dot{\mathbf{v}}) + \mathbf{F}_D(\mathbf{x}, \mathbf{v}, t) + \mathbf{F}_{ML}(\mathbf{x}) + \mathbf{F}_{PTO}(\mathbf{v}). \quad (3.22)$$

⁷This also means that the average density of the device must be half that of seawater.

Either version of the radiation force (3.13)–(3.14) contains a term proportional to the device acceleration $\dot{\mathbf{v}}$, which can simply be subtracted from both sides of (3.22). The system can thus be re-expressed as one vector equation

$$\frac{d}{dt} \begin{bmatrix} \mathbf{x} \\ \mathbf{v} \end{bmatrix} = \begin{bmatrix} 0 & 1 \\ 0 & 0 \end{bmatrix} \begin{bmatrix} \mathbf{x} \\ \mathbf{v} \end{bmatrix} + \begin{bmatrix} 0 \\ (1 + M_a)^{-1} \sum \mathbf{F}(\mathbf{x}, \mathbf{v}, t) \end{bmatrix}, \quad (3.23)$$

where $\sum \mathbf{F}$ denotes the sum of all force contributions in (3.22) with the exclusion of the aforementioned term. The added mass M_a in (3.23) is evaluated at $\omega \rightarrow \infty$ for the memory integral version of the radiation force, and at $\omega = \omega_i$ for the constant coefficients version.

3.11 Computational solution method

With the system expressed as a first-order differential equation as in (3.23), it can be numerically solved in MATLAB using the built-in function `ode45`. This solver uses a fourth-order Runge-Kutta method to propagate the solution forward in time from specified initial conditions. The detailed workings of this solver are available in the MATLAB help file and elsewhere (e.g. [63]).

3.11.1 Ramp function

In order for the simulations to be well-behaved and converge smoothly to the steady-state solution, it is necessary to gradually ramp up the wave forcing on the device over time. We define the *ramp-time* t_r as the time when the full forcing amplitude is reached. A number of different ramp shapes were experimented with, beginning with a linear ramp, but this was found to often cause instability due to its sharp edges. The ramp function ultimately chosen was

$$r(t) = \begin{cases} \frac{1}{2} [1 - \cos(\pi t/t_r)], & t < t_r \\ 1, & t \geq t_r \end{cases} \quad (3.24)$$

which we call the *cosine ramp*. Note that this ramp is applied to the fluid velocity by multiplication, so the fluid acceleration for $t < t_r$ is found using the differentiation chain rule as follows:

$$\frac{d(ru)}{dt} = r\dot{u} + \frac{dr}{dt}u = r\dot{u} + \frac{\pi}{2t_r} \sin\left(\pi \frac{t}{t_r}\right) u. \quad (3.25)$$

3.12 Implementation of memory integral

The most difficult aspect in the development of the simulation code was the computational implementation of the memory integral in the radiation force. In this section we detail how the impulse response function was obtained from the data given by Hulme [43], and how the memory integral was implemented in the solver.

3.12.1 Impulse response function for the semi-submerged sphere

In [43], Hulme provides tabulated data for the added mass and radiation resistance⁸ of a semi-submerged sphere, exact to four decimal places. As stated earlier, the nondimensional form of the impulse response function is unchanged from (2.87). Using the dispersion relation $k = \omega^2$, $K(\tau)$ can be alternatively expressed in terms of the wavenumber, rather than the wave frequency:

$$K(\tau) = \frac{1}{\pi} \int_0^\infty \frac{R_r(k)}{\sqrt{k}} \cos(\sqrt{k} \tau) dk. \quad (3.26)$$

Hulme provides his results in a nondimensional form but uses the alternative time scaling of ω , rather than $\sqrt{a/g}$, so that the scale factor for the radiation resistance is $\rho \bar{V}_s \omega$. The result of this is that the values given by Hulme for radiation resistance, which he labels B , are related to the scaled radiation resistance used here by

$$B = \frac{R_r}{\sqrt{k}}. \quad (3.27)$$

We emphasise that k in this expression is the non-dimensionalised wavenumber. The different time scaling used by Hulme has no effect on the scaling of the added mass, obviously.

Hulme gives the added mass and radiation resistance for select values of k in the (scaled) range 0-10, as well as the short- and long-wavelength limits. We fitted a polynomial to these data. The function chosen, designed to automatically satisfy the asymptotic values, was

$$B_{fitted}(k) = \frac{3k^3}{k^5 + c_4 k^4 + c_3 k^3 + c_2 k^2 + c_1 k + 8/3\pi}. \quad (3.28)$$

Using a standard least-squares fitting function, with equal weighting on all data points, the following values were obtained for the c_j (to three decimal places):

$$(c_1, c_2, c_3, c_4) = (9.635, -12.884, 11.035, -1.164) \quad (3.29)$$

The top plot in Figure 3.2 shows how the fitted function compares to the values from Hulme. The normalised sum of the squares of the residuals is 1.29×10^{-6} .

The Kramers-Konig relation (2.82) can be applied using the fitted radiation resistance function to evaluate added mass at any wavenumber. Recasting the equation in terms of k rather than ω gives

$$M_a(k) - M_a(\infty) = \frac{1}{\pi} \int_0^\infty \frac{B(y)}{y - k} dy. \quad (3.30)$$

Inputting B_{fitted} from (3.28) and defining $g(y)$ as the denominator of the integrand, *Mathematica* gives the following expression for the integral:

$$\int_{y_1}^{y_2} \frac{B(y)}{y - k} dy = \text{RootSum} \left(g(z), \frac{3z^3 \log(y - z)}{g'(z)} \right) \Bigg|_{y=y_1}^{y=y_2}, \quad (3.31)$$

⁸Hulme refers to this as added damping.

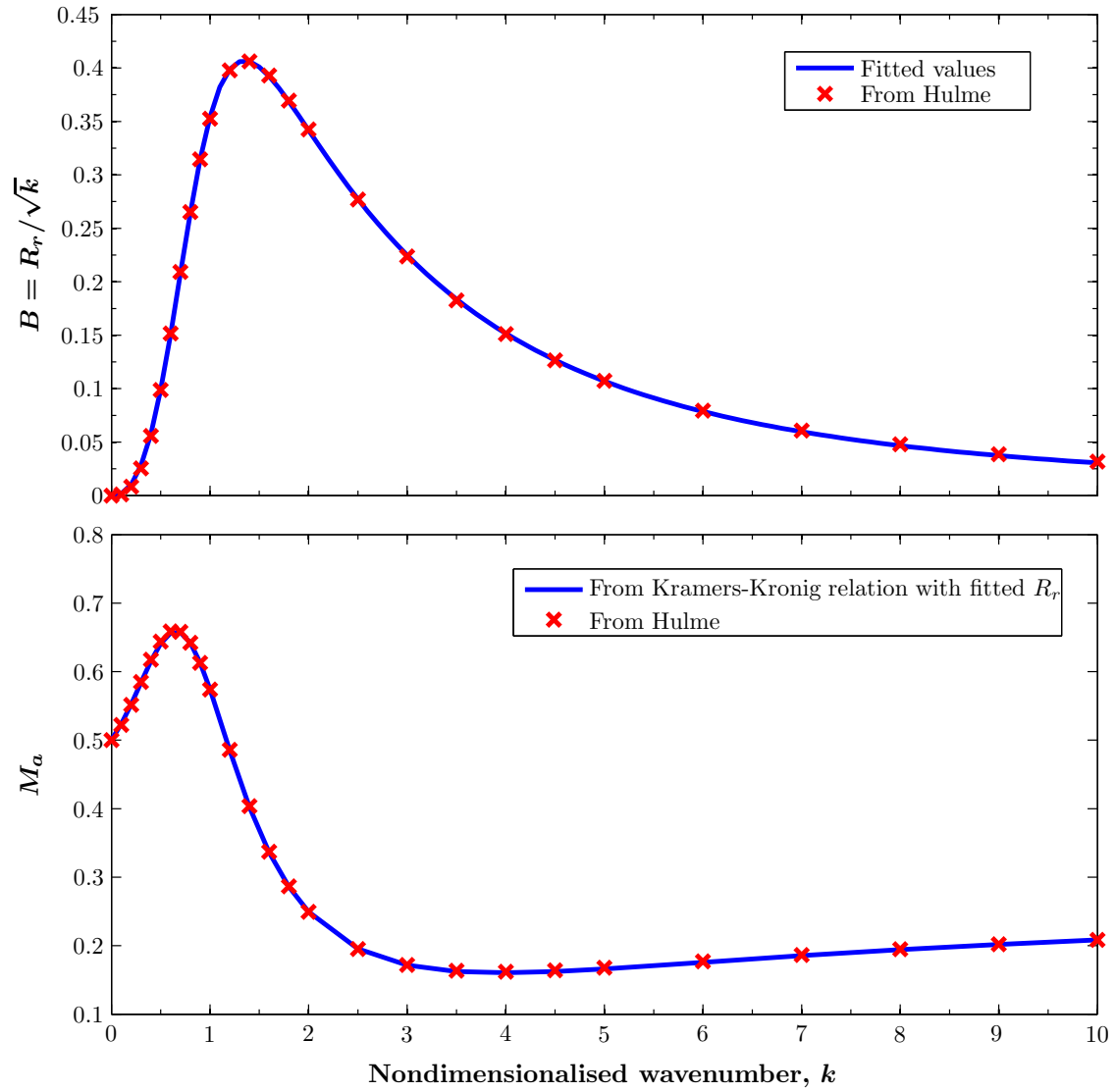


Figure 3.2: Non-dimensionalised radiation resistance (top) and added mass (bottom) for the semi-submerged sphere moving in surge. Values of $B = R_r / \sqrt{k}$ were taken from Hulme [43] and a polynomial of the form (3.28) was fitted to these. The fitted polynomial is input into the Kramers-Konig relation (2.82) to find added mass for any wavenumber k .

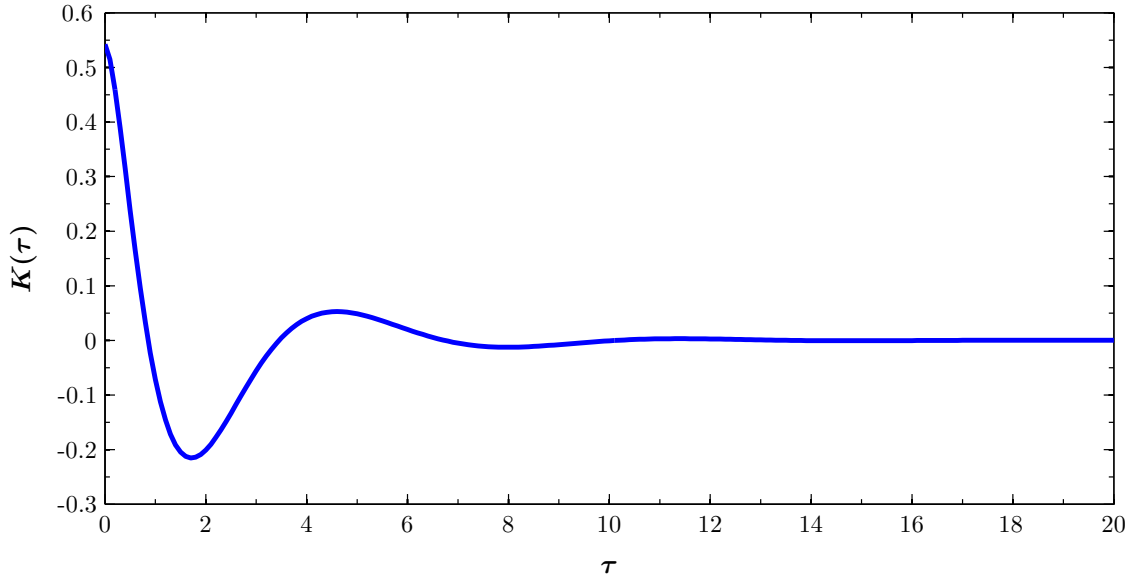


Figure 3.3: Non-dimensionalised impulse response function for the semi-submerged sphere moving in surge, evaluated using the fitted radiation resistance function (3.28) shown in Figure 3.2.

where $\text{RootSum}(g(z), form)$ represents the sum of $form(z)$ for all z that satisfy the polynomial equation $g(z) = 0$. We evaluate the integral in (3.30) in MATLAB as follows: (1) the roots function is used to find the solutions to $g(z) = 0$; (2) the integral is treated as a principal value integral as in (2.84) by splitting it into two with integration limits $[0, k - \epsilon]$ and $[k + \epsilon, y_{max}]$; (3) the two integrals are evaluated using (3.31). We used the values $\epsilon = 10^{-10}$, $y_{max} = 1000$, which were tested to ensure sufficient convergence. The lower plot in Figure 3.2 shows added mass values obtained from the method described, compared with the values given by Hulme. The normalised sum of the squares of the residuals here is 1.45×10^{-6} , virtually the same as for the B values.

With the fitted B function, the impulse response function can be evaluated from (3.26). The integration method is similar to that described above for finding the added mass values. The result is presented in Figure 3.3. This is in qualitative agreement with the impulse response functions of many other bodies (e.g. [36]) and also for the heave mode of the semi-submerged sphere shown in [29].

As a check that the impulse response function is accurate and that the memory integral code is working as expected, the code was applied to evaluate the radiation force associated with sinusoidal motion of unit amplitude, across the frequency spectrum. The amplitudes and phases of the results are plotted in Figure 3.4, and compared with those for the analytical results from the frequency domain expression $\hat{\mathbf{F}}_{\mathbf{R}} = -Z(\omega)\hat{\mathbf{v}}$. The agreement is excellent, giving confidence in the performance of the memory integral code.

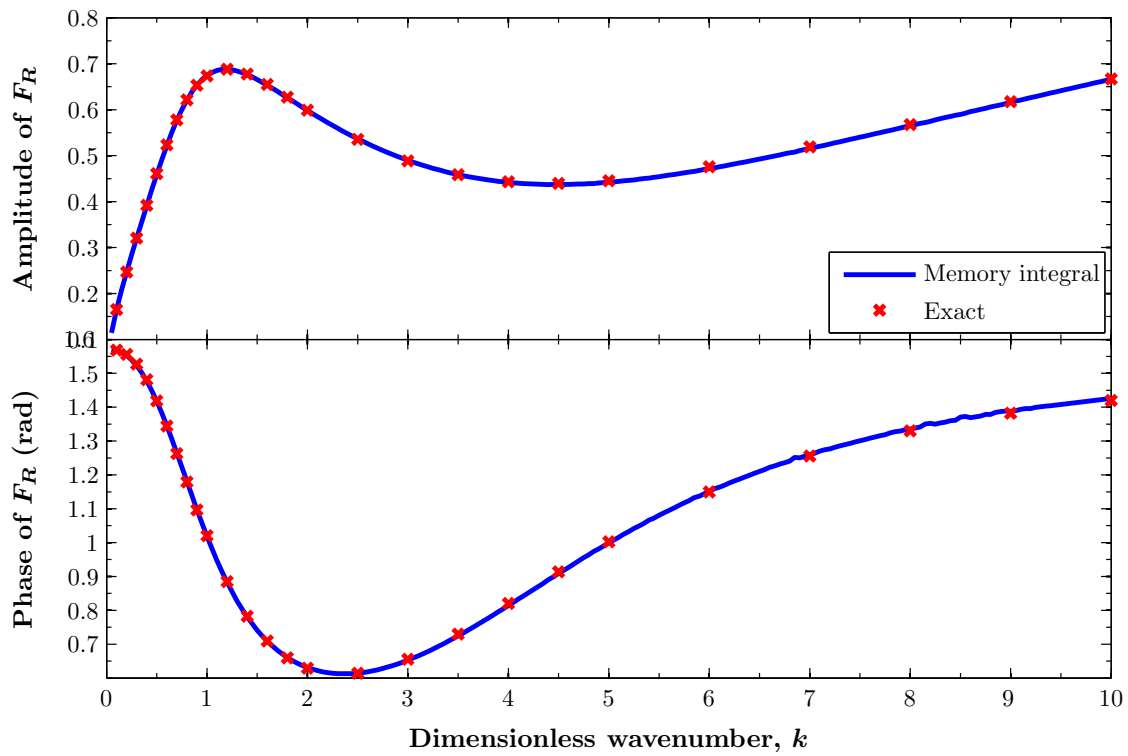


Figure 3.4: Amplitude and phase of the radiation force evaluated using the memory integral with the impulse response function shown in Figure 3.3, for a forced sinusoidal velocity of unit amplitude. These are shown to be in good agreement with analytical results evaluated using the added mass and radiation resistance values from Hulme [43].

3.12.2 Implementation in differential equation solver

As a simulation progresses, past velocity values must be stored over a time window τ_f that is sufficiently long that the impulse response function at $\tau = \tau_f$ has decayed to an acceptably low magnitude. Calculating the radiation force then requires the numerical integration of the product of this velocity history with the impulse response function. Clearly, carrying this out every time the force functions are called imposes a significant computational cost. Furthermore, the impulse response function is not an analytically known function; it requires one evaluation of (3.26) for each distinct value of τ . As the `ode45` solver uses an adaptive step size (with the derivatives evaluated at four intermediate values per time step), the precise values of τ required would in general be different at each step, requiring an untold number of evaluations of (3.26) over the course of a simulation run⁹.

To avoid excessive computation times, an approximating procedure was employed: the memory integral was only evaluated at intervals of Δt_s , and assumed constant in between. Values of $K(\tau)$ at discrete times $\tau = 0, \Delta t_s, 2\Delta t_s, \dots, \tau_f$ were evaluated and stored in a numerical array we call \mathbf{K} , as follows:

$$\mathbf{K} = \begin{bmatrix} K(0) & 0 & \cdots & 0 \\ 0 & K(\Delta t_s) & \ddots & \vdots \\ \vdots & \ddots & \ddots & 0 \\ 0 & \cdots & 0 & K(\tau_f) \end{bmatrix}. \quad (3.32)$$

A maximum step size of Δt_s was enforced in the `ode45` solver, and the velocity history was updated with a new value when the simulation time first reached or passed the next integer multiple of Δt_s .

In early attempts, the values of \mathbf{v} at the *start* of each interval were recorded and used in the integration, but it was discovered that this introduced a lag of $\Delta t_s/2$ in the radiation force, which carried through into the resultant device velocity. While this lag was very small and difficult to detect by the eye, amounting to $\approx 0.13\%$ of a period for the trial values used, it was found have an appreciable impact of $\approx 5\%$ on the excitation power¹⁰, due to this quantity being highly sensitive to the phase between \mathbf{v} and \mathbf{F}_E .

Clearly, when a quantity is being assumed fixed over a time interval, using the value at the *middle* of the interval will deliver the most accurate results. The following procedure was ultimately settled upon to correct the anomalous time lag:

1. When the simulation time first reaches or passes $t = m\Delta t_s$ (where m is an integer), an approximate velocity vector at $t = (m + 1/2)\Delta t_s$ is calculated using the first order projection $\Delta \mathbf{v} = \dot{\mathbf{v}} \Delta t_s/2$. This is appended to the front of the velocity history and the memory integral is evaluated using trapezoidal numerical integration.
2. The value of the memory integral calculated in step 1 is used until the simulation time first reaches or passes $t = (m + 1/2)\Delta t_s$, at which point the approximate

⁹We discuss alternative ways around this problem in Section `sec:memintdiscussion`.

¹⁰This was defined in Section 2.5.

velocity calculated in the previous step is replaced by the current value and the memory integral is corrected.¹¹

3. The value calculated in step 2 is used for the remainder of the time interval, and the procedure is then repeated for $m = m + 1$, and so forth until the end.

Under this revised procedure, the maximum time step was set to $\Delta t_s/2$, which unfortunately doubles the number of iterations required. The procedure can be expressed mathematically by defining a time-dependent velocity history matrix $V_H(t)$ as follows:

$$V_H(t) = [\mathbf{v}(\bar{t}), \mathbf{v}(\bar{t} - \Delta\tau), \dots, \mathbf{v}(\bar{t} - \tau_f)], \quad (3.33)$$

where

$$\bar{t} = \left(\left\lfloor \frac{t}{\Delta\tau} \right\rfloor + \frac{1}{2} \right) \Delta\tau, \quad (3.34)$$

and $\lfloor x \rfloor$ denotes the largest integer not greater than x (using the floor function). The memory integral is obtained by numerically integrating with respect to time along the rows of the matrix product $V_H \times \mathbf{K}$.

For the purposes of evaluating the (time-averaged) radiated power, the radiation force over the simulation should either be evaluated anew from the velocity values returned at the end of the simulation, or the stored values interpolated to the actual time grid $t = 0, \Delta t_s, 2\Delta t_s, \dots, t_f$ from the midpoints. If this is not done, the time lag of $\Delta t_s/2$ manifests itself between \mathbf{F}_R and \mathbf{v} , causing a significant error in the radiated power.

We note that an approach very close to that described here was employed by Jefferys in [47] and Greenhow & White in [36], although in neither paper is there mention of evaluating the memory integral at the midpoints of the time intervals for which it is assumed constant.

3.12.3 Computational parameters and performance

For all simulations, we used a time resolution for the radiation force of $\Delta t_s = 0.05$, and the impulse response function was truncated at $\tau_f = 40$. Under these conditions, running the simulation with the memory integral takes $\sim 50\%$ longer than with the constant coefficients version of the radiation force if the same maximum time step is enforced – this difference can be attributed to the numerical integrations. If a fully adaptive step size is allowed when using the constant coefficients version, though, the running time is roughly 1% of that for the memory integral version. Employing the memory integral clearly comes at considerable computational cost. However, the running times are still very manageable; a simulation of a chain of five devices run to $t_f = 1200$ takes ≈ 200 s on the Apple Power Mac G4 computer used for this project.

The choice of parameters (given above) was very conservative to ensure accurate performance of the memory integral code; it is probable that they could be slackened

¹¹It is not necessary to re-evaluate the entire integral here; we simply correct for the change by integrating over the first time step.

somewhat without major impact on the accuracy. By comparison, in their similar integration schemes Jefferys [47] and Greenhow & White [36] both use time steps of 0.1 s, with the impulse response function truncated at 6 s and 10 s respectively. For a device with a 2 m radius, these correspond to $\Delta t_s \approx 0.2$ and $\tau_f = 12$ and 20 in the scaled units. However, these papers date from 1984 and 1997 respectively; computational power is much less of a limiting factor in the current work, and we have adopted more stringent practices.

3.12.4 Discussion

There are several possible alternative methods for implementing the memory integral to the one we have used. One approach would be to fit an equation to the impulse response vector and, every time the radiation force function is called, evaluate $K(\tau)$ on the exact time grid on which the velocity history is known. It is likely that this would end up being faster over the entire simulation, since it would not be necessary to enforce a maximum time step size in the solver. However, it is possible that this scheme would result in more integrations, so it is difficult to say with certainty that the simulation running time would be reduced. On another note, the integrations may lose accuracy if the adaptive time steps grow too large, and it is hard to know how well the solver would handle this.

Another variation would be to still use a stored numerical vector for the impulse response function, but have it interpolated for the exact velocity history time grid each time it is called. This method raises similar issues to previous one and it is uncertain how its efficiency and performance would stack up relative to the method we used.

A distinct alternative that has been used by several authors [85, 47, 15] replaces the memory integral with an approximation known as a “state-space model”. The equation of motion is then an ordinary differential equation and computation is many times more efficient. However, after investigation it appears that this method is not applicable to the present study because of the nonlinear inter-device coupling through the linkage lines.

To conclude, in hindsight it is quite likely that a more computationally efficient memory integral algorithm could be developed, and savings in simulation time could almost certainly have been made by increasing Δt_s and reducing τ_f somewhat, with little impact on the accuracy of the results.

3.13 Validation of code under linear conditions

It has already been shown in Figure 3.4 that for a generated sinusoidal velocity, the memory integral code returns the correct radiation force to a good degree of accuracy. Here we present evidence to assure that the code is also behaving as it should in the context of the `ode45` solver.

A single symmetrically-moored device in the absence of nonlinear drag (i.e. $C_D = 0$) and with the excitation force evaluated at the device’s mean position rather than its instantaneous position (i.e using (2.115) rather than (3.15)) is an entirely linear system

for which solutions can be evaluated analytically (see Section 2.5). Simulations were run to test agreement with the analytical solutions under these conditions. The code was tested using both the memory integral and constant coefficients versions of the radiation force, (3.13)–(3.14). The steady-state motions returned by both versions are found to agree closely with the analytical solutions.

In Figure 3.5 we compare the position versus time results for a particular choice of parameters. Overall, the agreement is very good and the three curves are essentially indistinguishable to the eye. The differences of the returned displacement values from the analytical solution, which we call $x_{an}(t)$, for the two result sets are superimposed in green. Measured as the normalised sum of the squares of the residuals, the memory integral version performs better than the constant coefficients version: 3.8×10^{-9} compared to 1.5×10^{-8} . A fairer comparison, though, is made by running the constant coefficients version with an imposed maximum time step equal to that used in the memory integral: this gives 2.5×10^{-20} for the aforementioned metric. The plots of the differences from the analytical solution show that the constant coefficients version is giving the correct phase but an amplitude that is slightly too small. For the memory integral version the amplitude agrees more closely and the error is predominantly in the phase. A straightforward calculation based on the observed phase and amplitude of $(x_{an} - x)$ can be done to show that this phase error is very small – on the order of 10^{-5} radians¹². This is well beyond the level of accuracy we require.

	Analytical		Simulated	
	Frequency domain	Numerically integrated (c.c.)	Memory integral	Constant coefficients
$P_E(\times 10^{-3})$	8.82	8.82	8.82	8.82
$P_C(\times 10^{-3})$	-8.81	-8.81	-8.81	-8.81
$P_R(\times 10^{-6})$	-9.48	-9.51	-7.38	-9.51
P_{ML}	0	1.44×10^{-19}	8.12×10^{-11}	-1.13×10^{-6}
P_{net}	0	-3.03×10^{-8}	1.00×10^{-6}	9.72×10^{-7}

Table 3.3: Power contributions for the example presented above in Figure 3.5, evaluated by four different methods: (i) exact analytical solution from the complex amplitudes; (ii) numerical integration of the analytical solution in the time domain; (iii) numerical integration of the solution from a simulation using the memory integral radiation force; (iv) numerical integration of the solution from a simulation using the constant coefficients radiation force. Note that all units are non-dimensionalised.

¹²This is an order of magnitude smaller than the error caused by evaluating the radiation force at the start, rather than the middle, of each time interval for which it was assumed constant, as discussed in Section 3.12.2.

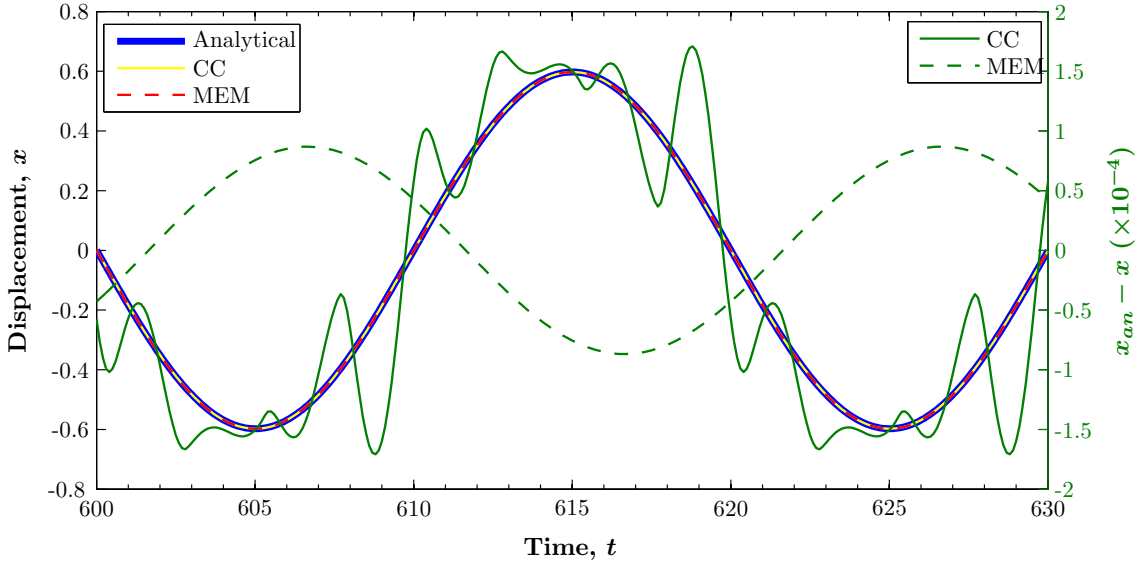


Figure 3.5: Steady-state motion of a single device under linear conditions ($C_D = 0$ and position-independent excitation force) for non-dimensionalised parameters $(H, R, S, T) = (1.25, 0.5, 0.15, 20)$. The analytical solution and two different numerical solutions, using the memory integral (MEM) and constant coefficients (CC) versions of the radiation force (3.13)–(3.14), are plotted (left axis). The differences of each of the numerical solutions from the analytical solution are also plotted in green (right axis, note the scale factor).

3.13.1 Power contributions

We coin the term *power contributions* to describe the time-averaged power transfer associated with each of the forces acting on the devices, when they are in steady-state motion. We introduced the radiated power in Section 2.3.2, followed by the excitation power and power capture in Section 2.5. The two power contributions remaining are the power dissipated by drag and the power transferred through the mooring and linkage lines. We define the five associated symbols P_R, P_E, P_C, P_D and P_{ML} consistently as the time-average rate of work done *on* a device by the corresponding forces. For simplicity, we leave these as scalar quantities that will always be used in reference to a particular device. As discussed in Section 2.5, P_R and P_C are always negative (or zero), but we use the terms “radiated power” and “power capture” to refer to their respective magnitudes. For P_E and P_D it is slightly subtle; these are normally positive and negative respectively, but later on we will see instances where this is not the case. However, we will generally use the terms “excitation power” and “power dissipated by drag” to refer to the magnitude with the sign implicitly understood. As shown by later results, the power transfer through the mooring and linkage lines can be positive or negative so it is vital to mention the sign. Positive P_{ML} means that the device in question is *receiving*

time-average power via the lines, and negative P_{ML} means it is losing power.

Finally, we define a further term P_{net} as the sum of the power contributions. Theoretically, P_{net} will be exactly zero if the device in question is in steady-state motion. In practise, we observe small non-zero values that provide information about the accuracy of the power contribution terms, and the simulations more generally.

Table 3.3 gives the power contributions for the same example discussed earlier and presented in Figure 3.5. The level of agreement with the analytical results here is the truly important performance metric for our purposes. In the table, we present two different analytical comparisons: in the first column, we give the exact result evaluated from the complex amplitudes using $P = \frac{1}{2}\text{Re}(\hat{F} \cdot \hat{v}^*)$; in the second column, the result is obtained by numerically evaluating the integral

$$P = \frac{1}{mT} \int_{t_0}^{t_0+mT} F(t)v(t) dt, \quad (3.35)$$

where m is a whole number¹³. The third and fourth columns show the power terms obtained by applying (3.35) with the velocities and forces returned from simulations using the the memory integral and constant coefficients versions of the radiation force respectively. Note that we omit the power dissipated by drag here, since it is identically zero in all cases.

The salient point to note is that the excitation power and power capture are in perfect agreement to three significant figures across all assessments. The exact power capture values returned by the memory integral and constant coefficients cases only differ from the analytical result by +0.02% and -0.05% respectively.

Comparing the first two columns of the table, there is a numerical error on the order of 10^{-8} introduced in the radiated power, which carries through to give a non-zero net power. This error must result from the numerical differentiation of the velocity to give the acceleration $\dot{v}(t)$, which is used in evaluating F_R retrospectively. Note that this differentiation is not necessary *during* the simulation.

The constant coefficients simulation has a larger error $\sim 10^{-6}$ in the mooring power; this is simply attributable to the solving algorithm, and could be reduced if desired by imposing a maximum step size. Because the memory integral simulation does limit the step size, it returns a more accurate mooring power. However, it exhibits an error in the radiated power, which is wrong by $\sim 20\%$. If the radiated power is evaluated using the velocity returned from the memory integral simulation, but with F_R calculated retrospectively using the *constant coefficients* radiation force, the result is -9.51×10^{-6} , in line with the other methods. This discrepancy must therefore be attributed to the interpolation procedure described in Section 3.12.2.

The level of agreement with analytical results detailed in this section is deemed to be entirely acceptable. The power capture, which is the quantity of the most importance, has been shown to agree to well within one tenth of a percent in the example given. Quantitative effects on the results due to the assumptions and simplifications made

¹³Note that the constant coefficients version of the radiation force is used in this calculation.

would certainly overwhelm this tiny numerical error. Smaller quantities such as the radiated power are of secondary importance; the larger errors shown in P_R for the memory integral code are tolerable, and we do not bother investigating any further how this might be reduced.

3.14 Importance of memory integral for lone device

In this and the following section, we examine the discrepancy between results obtained using the memory integral and constant coefficients versions of the radiation force in the presence of the nonlinearities. This is done under the assumption that the memory integral version is the more accurate of the two, since it properly accounts for the frequency dependence of the hydrodynamic parameters, and its performance has been thoroughly verified in the linear regime. The key question to be addressed is whether the constant coefficients version, which is much more desirable from a computational perspective, gives sufficiently accurate results for the purposes of the study.

First, the level of agreement between results for the two versions of radiation force was tested for a single device with a non-zero drag coefficient and with the fluid acceleration being evaluated at the device's instantaneous position in the excitation force (3.15). Figure 3.6 shows results from a series of simulations where drag coefficient C_D and spring stiffness S were varied with the other parameters held fixed. Values of drag coefficient up to $C_D = 2$ were explored, while S was varied from 0.05 to 0.3, passing through the resonance value of $S \approx 0.15$ for this wave period ($T = 20$). The plots in the left column show the power contributions obtained from the two simulation sets, and the difference between the two values at each point is plotted in the right column. P_{ML} is not shown, since it is essentially zero in all cases.

The first point to note, which is not demonstrated in the figure, is that on its own the position dependence of the excitation force has negligible effect on the power contributions; the results for $C_D = 0$ are virtually identical when the simulation is run using the position-independent excitation force (2.115). We note that the maximum excursion is less than $0.1k^{-1}$ at all data points except $C_D = 0, S = 0.15$ (see discussion in Section 2.4.2). The discrepancy between the two simulation sets for $C_D = 0$ (blue lines) is therefore numerical in nature.

Examination of the figure shows that the nonlinear drag causes an increasing discrepancy between the two simulation sets as the drag coefficient is increased. For the three larger power contributions (P_E , P_C and P_D), the discrepancy does not exceed 0.5% – certainly a negligible error for our purposes. As one might expect since it is the radiation force that is calculated differently between the two simulation sets, the largest differences are observed in P_R . We showed in Table 3.3 that in the fully linear case there was a $\approx 20\%$ error in the P_R value when evaluated retrospectively by the memory integral code, which we attributed to the process of interpolating the stored values of radiation force to the true time grid. In the absence of nonlinear drag (the blue line), the discrepancy between the P_R values does not deviate much from this as S is varied. However, when C_D is non-zero the discrepancy shows major variations, with the

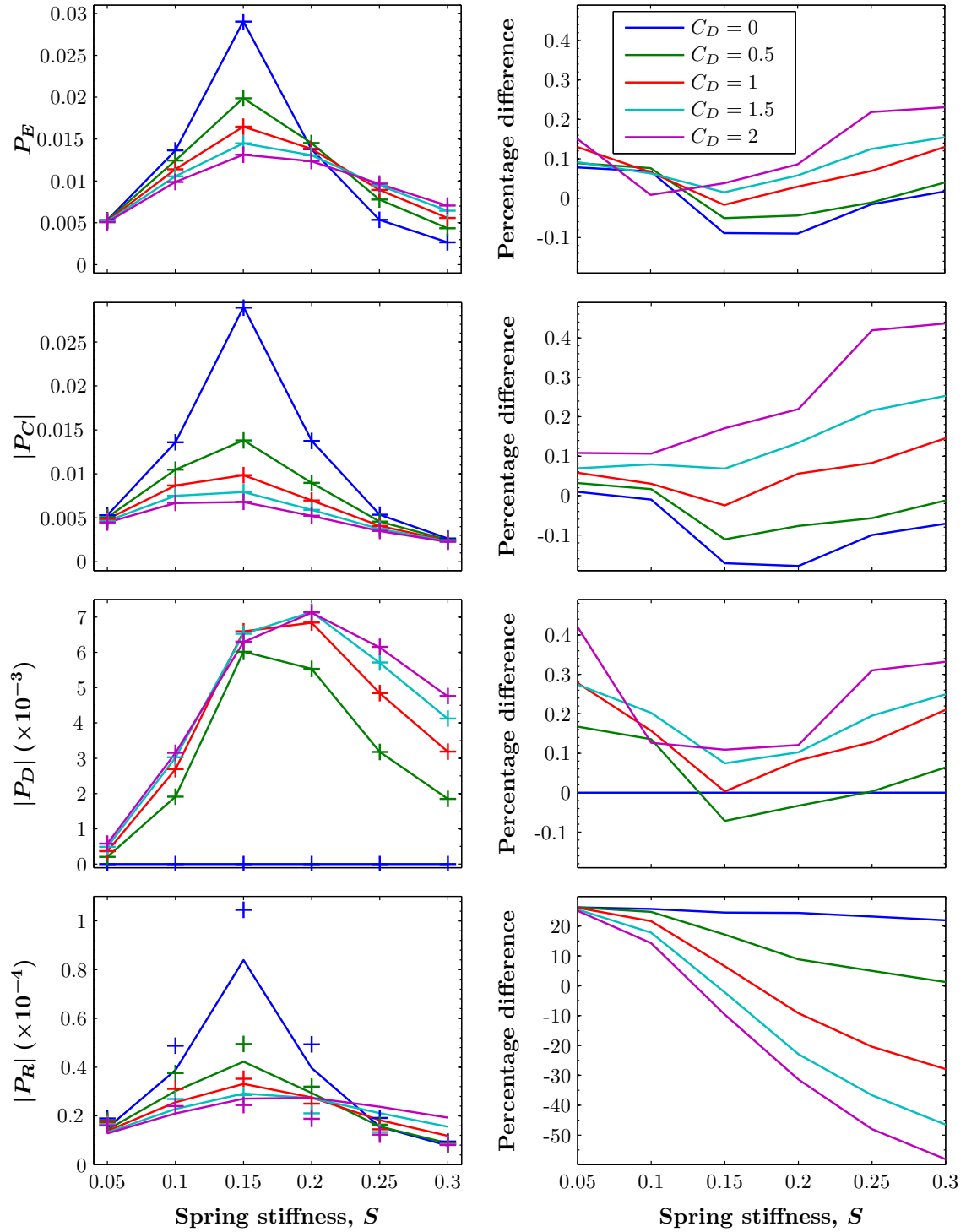


Figure 3.6: Power contributions versus spring stiffness, for a lone device with $(H, R, T) = (1.25, 0.15, 20)$, and the five values of C_D shown in the legend. The left-hand plots show the power contributions from simulations using the memory integral (solid line) and constant coefficients versions of the radiation force (plusses), and the right-hand plots show the percentage difference of the latter from the former.

constant coefficients causing an underestimation of P_R by progressively larger margins as either C_D or S is increased over the ranges examined. This is precisely what we would expect, since the radiation resistance increases steeply with the motion frequency (see Figure 3.2), and the motion should exhibit increased high frequency components for higher C_D .

While there is significant effect on the radiated power due to assuming constant values for radiation resistance and added mass, there is overall a very small effect on the dynamics, evidenced by the close agreement between the two simulation sets for all the other power terms. Radiated power is $< 0.5\%$ of the excitation power, and it is a term of relatively little interest in this study.

We conclude that the constant coefficients version of the radiation force is perfectly adequate to use in simulations of the single device. Results presented in this section suggest that it is unlikely to introduce an error $> 1\%$ in any of the important power terms, for parameters reasonably close to those used here. We have not ruled out significantly larger errors in cases of very large wave heights and/or very low power take-off resistances, but we deem these to be of less practical interest.

3.15 Importance of memory integral for linked chain

Here we examine the effects of the choice of radiation force function when simulating connected chains of devices. We present and analyse just one example series: a five-device chain with the (initial) spacing between the devices being one wavelength, i.e. $L = T^2/2\pi = \lambda$. The other parameters are chosen as $(C_D, H, R, T) = (0.5, 1.25, 0.15, 20)$, and S is varied from 0.05 to 0.8.

There is a large amount of data associated with the simulation series. We start by comparing the most important performance metric: power capture. This is plotted against S for all five devices in the top pane of Figure 3.7. There is a single data set for the memory integral version, plotted in solid lines, but three separate data sets for the constant coefficients version, plotted with three different markers; this is to test the robustness of the results. The first data set, plotted with plusses, used a simulation ramp-time (defined in Section 3.11.1) of $t_r = 1000$, while the second, plotted with crosses, used a much longer ramp-time of 3000. The third set, plotted with circles, also had $t_r = 1000$, but a maximum time-step of 0.05 was imposed in the solver. For this section, we will refer to these simulation sets as CC1, CC2 and CC3 respectively. The set of simulations using the memory integral, which we refer to here as MEM, were also carried out with a ramp-time of 1000.

The first point to note is that all sets are in good agreement up to $S \approx 0.2$. Above this, the MEM and CC results part company, exhibiting large discrepancies of up to $\sim 50\%$ in some instances. The discrepancy is not smoothly varying; in other words, the results from the two versions of the code are qualitatively different.

The results from the different CC sets line up very closely, with the exception of a few data points. Specifically, major differences are evident at $S = 0.3$ and, to a lesser extent, at $S = 0.45$. For the former, the CC1 and CC3 results agree closely, but the

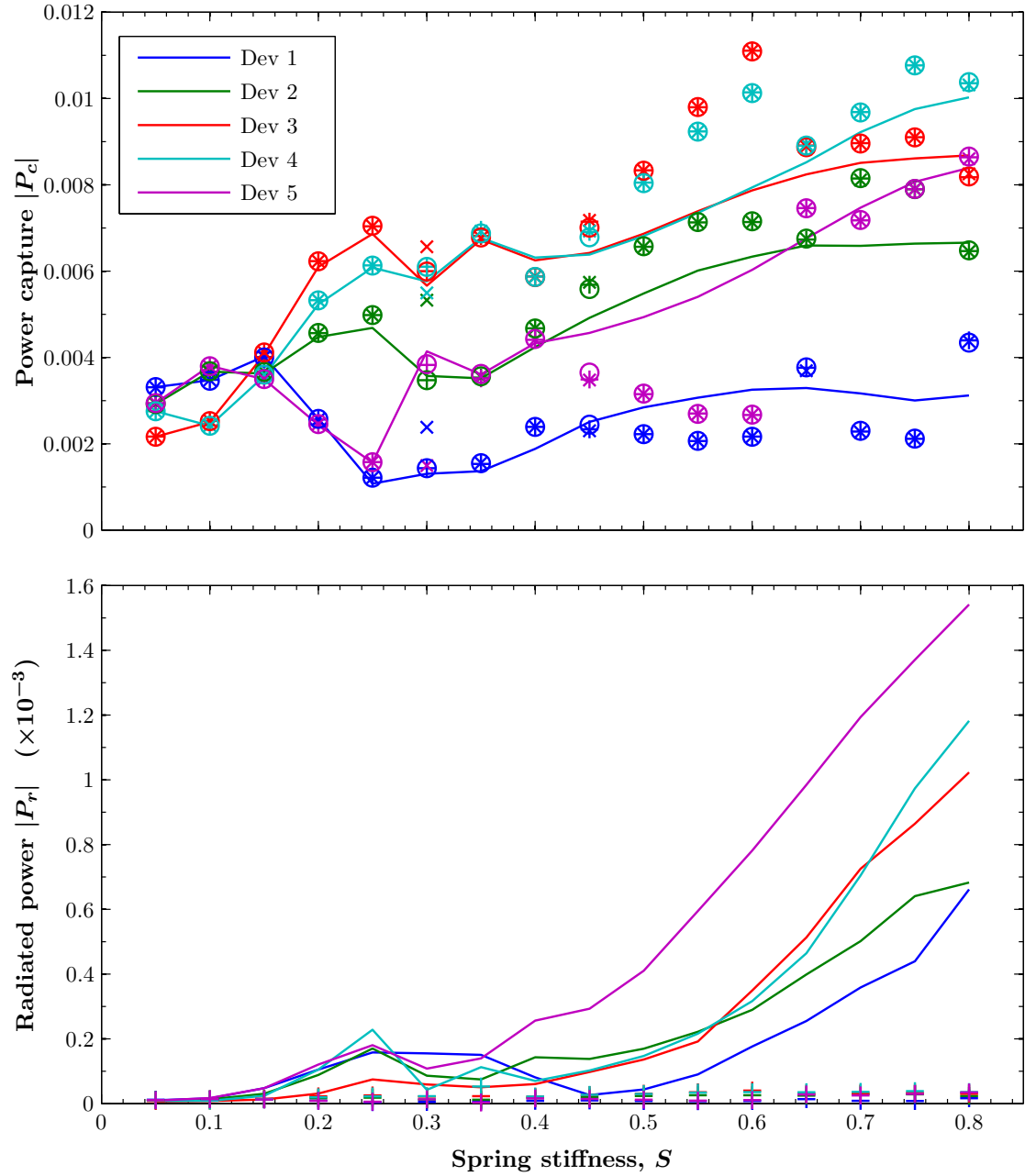


Figure 3.7: Power capture (top) and radiated power (bottom) versus spring stiffness for each device in the five-device chain with $(C_D, H, L, R, T) = (0.5, 1.25, \lambda, 0.15, 20)$. The solid lines are from the simulation set using the memory integral (MEM). The markers are results from three separate sets of simulations using the constant coefficients version of the radiation force: pluses, ramp-time $t_r = 1000$ (CC1); crosses, $t_r = 3000$ (CC2); circles, $t_r = 1000$ and maximum step size of $\Delta t = 0.05$ enforced (CC3). Note that CC2 and CC3 are not plotted in the bottom pane, as they cluster closely with CC1.

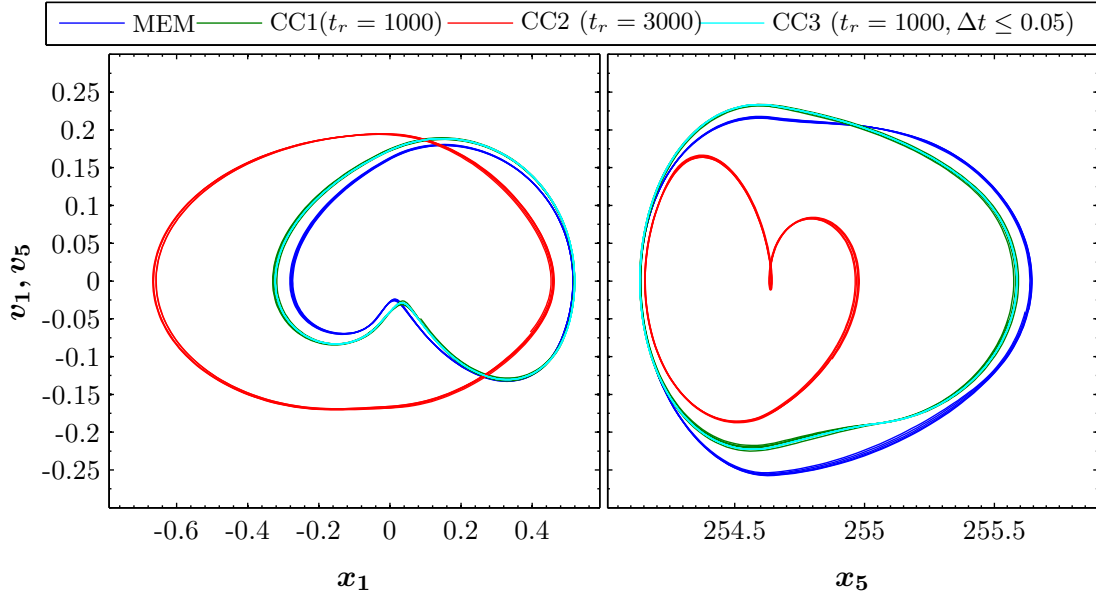


Figure 3.8: Phase plots of the motions of Devices 1 and 5 of the five-device chain, for $(C_D, H, L, R, S, T) = (0.5, 1.25, \lambda, 0.15, 0.3, 20)$. The curves are drawn over a time interval of $100 = 5T$. The different colours show results from the four separate simulation sets described in the main text and in the caption of Figure 3.7.

CC2 simulation gives a markedly different result. To shed light on the nature of this discrepancy, phase plots of the motion for $S = 0.3$ are presented in Figure 3.8. The curves are plotted over a time window of 100, giving five “loops” in phase-space. The reasonably narrow apparent width of the curves shows that all the simulations here do reach a steady state that is close to periodic. The anomalous CC2 values here do not result from any numerical issues; they reflect that the system is genuinely in a different steady state from the other simulations. Note that the common steady state in the CC1 and CC3 simulations much more closely resembles that of the MEM simulation.

This instance of bistability is the only one found in the current simulation series. At the other S values for which there is a visible discrepancy between the CC results, most notably $S = 0.45$, this is found to result instead from the motion being aperiodic; that is, steady-state motion has not been reached. The difference between the power capture values from the different CC series in these instances is of similar size to the difference *within* the individual simulations if the integration limits are varied (as much as $\sim 10^{-4}$, but normally much smaller). An illustrative example is given in Figure 3.9, for $S = 0.8$. The MEM simulation returns a solution with near-precise periodic repetition, but all of the CC simulations exhibit aperiodic phase-space trajectories. The lower plot in the figure shows the power capture associated with the different frequency components of the motion of Device 1, obtained by taking the discrete Fourier transform of the velocities. It appears here that the system, as defined in the CC simulations, may have crossed a threshold into chaotic behaviour. If this is the case, one likely reason that this does not

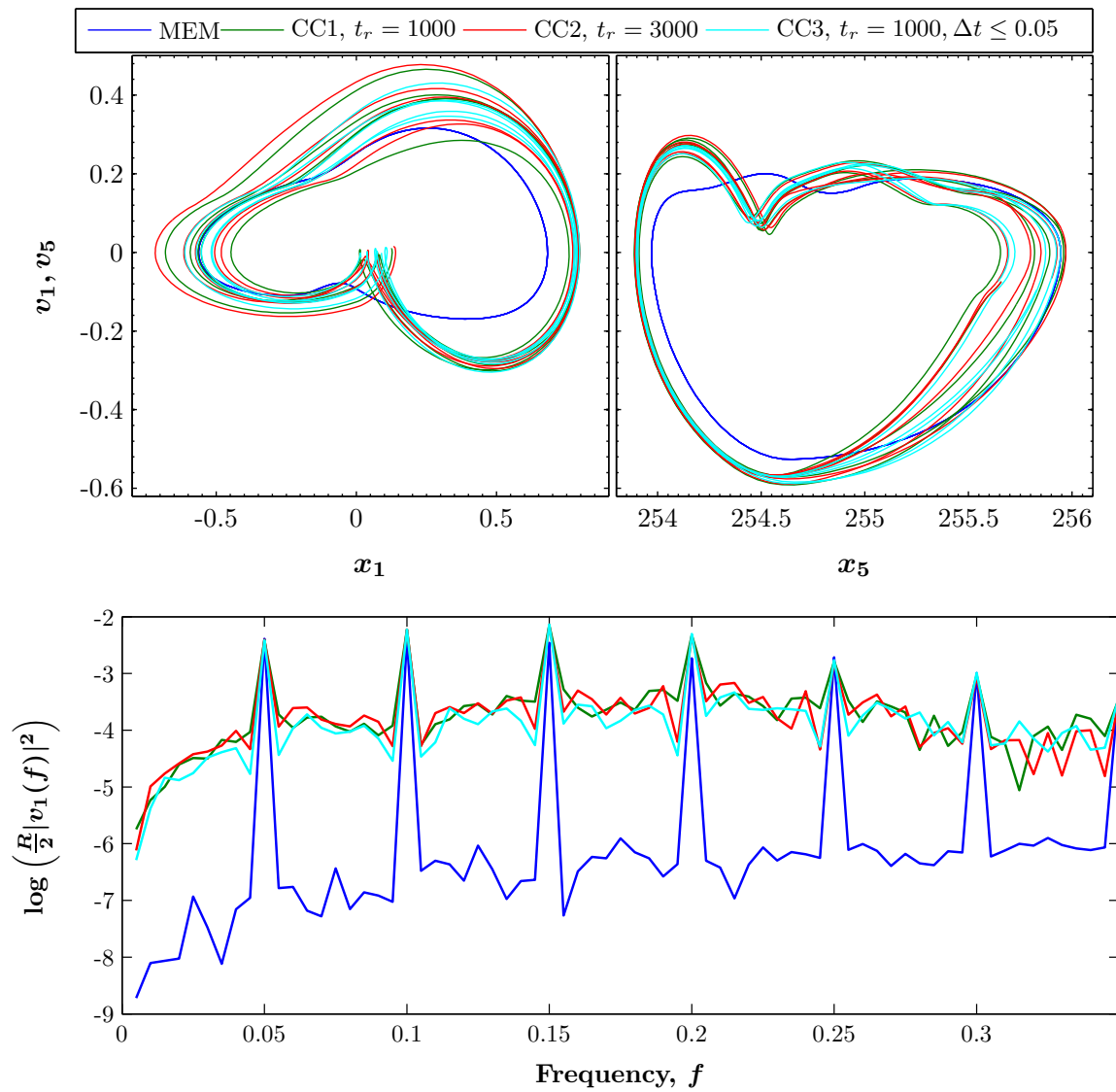


Figure 3.9: Top: Phase plots of the motions of Devices 1 and 5 of the five-device chain, for the same parameter set in Figure 3.8 except for $S = 0.8$. Bottom: Frequency analysis of power capture of Device 1. The different colours show results from the four separate simulation sets described in the main text and in the caption of Figure 3.7.

occur in any of the MEM simulations is the hugely increased damping due to radiation, as shown in the bottom pane of Figure 3.7 (although we note that the radiation damping reaches at most $\sim 10\%$ of the damping due to the power take-off here).

Related to this observation of apparently chaotic motion, an example is presented in Figure 3.10 where the MEM simulation exhibits *subharmonic oscillations* – in this case, oscillations at a frequency half of that of the incident wave. The phenomenon of *period doubling* is known as a potential route to chaos. The MEM system here, however, does not exhibit chaotic motion and has stable subharmonic oscillations for $S = 0.6, 0.65, 0.7$. Extra MEM simulations were run at these values using a ramp-time of 1500 to check if the subharmonic oscillations remained present, and they did; they appear to be a robust feature of the system. It seems likely that period doubling is the mechanism by which the chaotic behaviour is brought about in the CC simulations.

In summary, the results presented here illustrate by example that for connected chains of devices, simulations using the constant coefficients version of the radiation force can return substantially different results to those using the memory integral. The qualitative effect on the results is quite dramatic in the example shown here. The results using the memory integral are more trustworthy since this is the correct time domain formulation, and we would expect this to give a more accurate representation of the real world. Furthermore, regardless of the validity of either method, the memory integral is generally more robust and stable, even compared with the constant coefficients version run with a similar maximum time step enforced. This is likely due to two factors: greater damping due to the correct radiation resistance associated with high frequency motion; and reduced sensitivity to small numerical perturbations due to these being “averaged out” in the memory integral. On consideration of all of these factors, we opt to use the memory integral for all simulations with more than one device, in spite of the extra computational cost that this brings.

3.16 Summary of assumptions and conditions

- Linear wave theory.
- Body size and oscillation amplitude small in relation to incident wavelengths.
- Unidirectional waves.
- No coupling between modes of motion.
- No hydrodynamic interactions between devices.
- Massless mooring and linkage lines with tension-only spring forces.
- Constant drag coefficient C_D .
- For simulations of lone devices, constant added mass and radiation resistance.

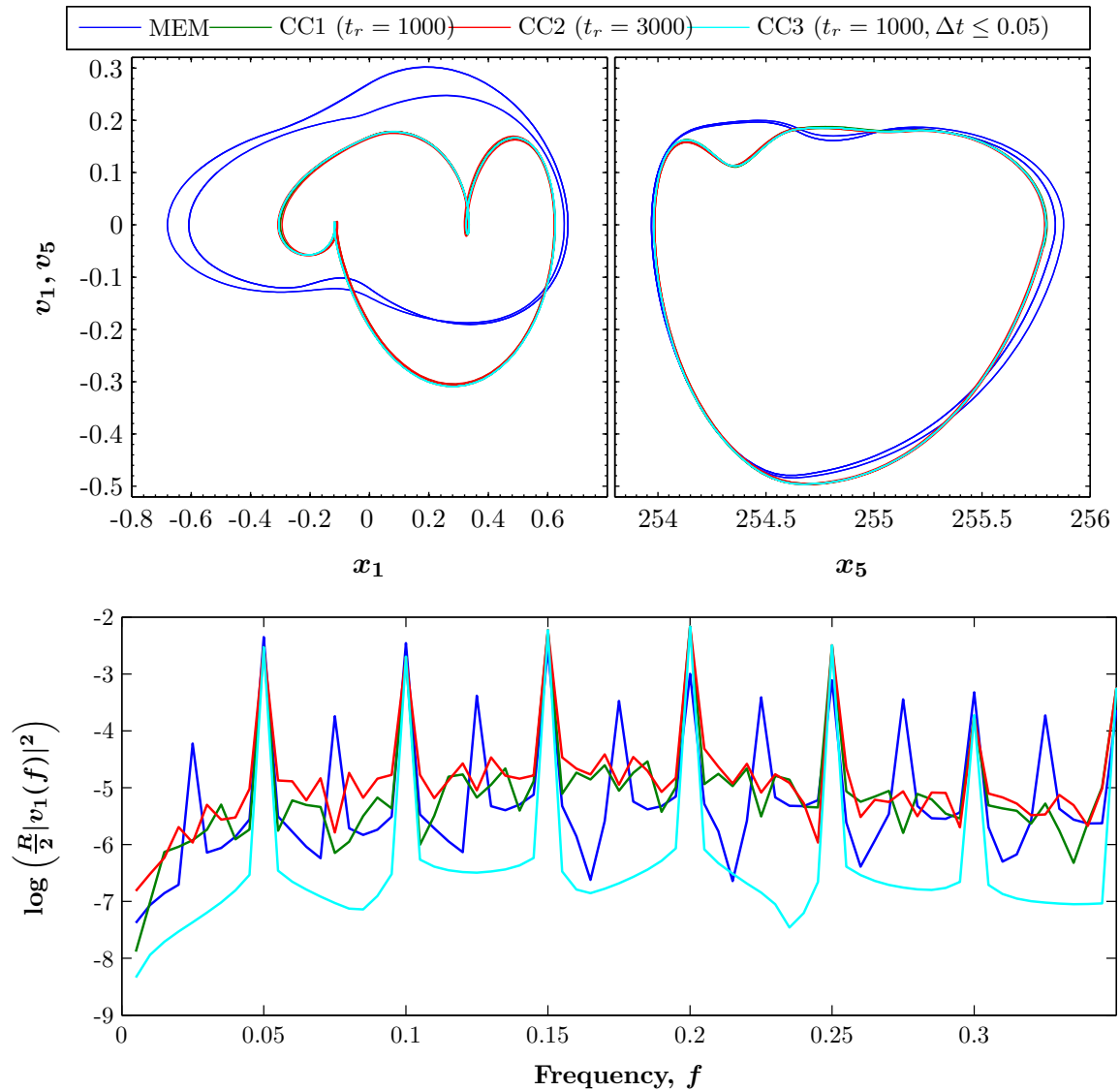


Figure 3.10: Top: Phase plots of the motions of Devices 1 and 5 of the five-device chain, for the same parameter set in Figure 3.8 except for $S = 0.7$. Bottom: Frequency analysis of the power capture of Device 1. The different colours show results from the four separate simulation sets described in the main text and in the caption of Figure 3.7.

Chapter 4

Lone devices

In this chapter, we examine the performance of a single model device in isolation (henceforth referred to as a lone device) forced by a monochromatic incident wave field. We begin with some analytical results for the linear system in the absence of the quadratic drag force. The remainder of the results in the chapter are from simulations, and include the influence of drag. These lone device simulations used the “constant coefficients” version of the radiation force, (3.14), for reasons discussed in Section 3.14.

Note that in this chapter all quantities are in nondimensional form, as defined in Section 3.9, except where explicitly stated otherwise. All symbols are as defined in Table 3.1. Figure 4.1 shows a scale for converting the nondimensionalised wave period axis to read period in seconds, for device radii of $a = 2$ m and 4 m. The red bars highlight the dominant energy-bearing period range for typical deep water sites ≈ 8 –12 s. The nondimensionalised period can alternatively be interpreted to read the device radius for a fixed value of period in seconds; the top scale demonstrates this conversion for a period of 9 s. Care is required in comparing results for different device radii since this requires several unit conversions – a point raised again later. Other useful unit conversions were given in Table 3.2.

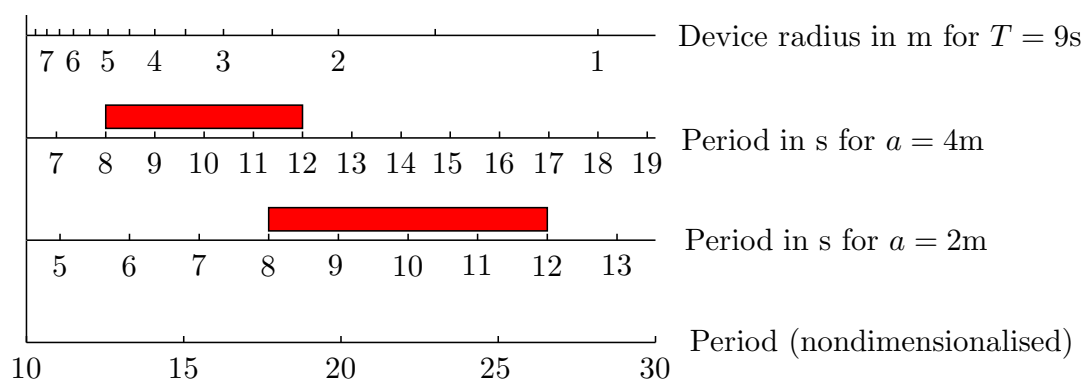


Figure 4.1: Three conversion scales for the nondimensionalised period axis.

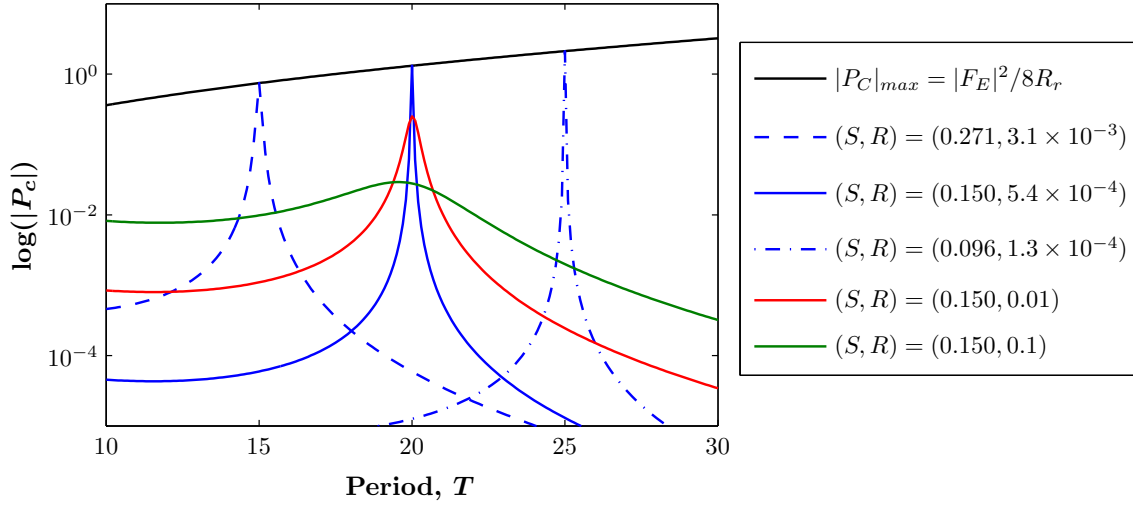


Figure 4.2: Log of the power capture versus wave period, for the linear device with spring stiffness S and PTO resistance R as specified in the legend, and an incident wave height of $H = 1$. The black curve shows the theoretical upper bound. Note that this and all other figures in this chapter, with the exception of Figure 4.4, are in nondimensionalised units. Figure 4.1 allows conversion to period in seconds.

4.1 Linear analysis

This section draws upon the background presented in Section 2.5 to examine the performance of a lone device in the absence of drag, i.e. for drag coefficient $C_D = 0$. Under the nondimensionalisation, all equations in Section 2.5 are unaltered in form, except that the device mass M is simply replaced by 1. For the sake of clarity, equation (2.123) for the resonance condition becomes, in terms of the period,

$$S = (1 + M_a) \left(\frac{2\pi}{T} \right)^2 \equiv S_{res}(T), \quad (4.1)$$

where M_a is the added mass, which also depends on T .

Figure 4.2 demonstrates one of the general problems with point absorbers, first touched upon in Chapter 1. The black curve shows the upper bound of power capture per unit wave height versus period, evaluated from (2.126). The blue curves show the performance for three example cases in which the spring stiffness and PTO resistance are optimised for the particular period values of 15, 20 and 25; that is, $S = S_{res}(T)$ and $R = R_r(T)$ (the radiation resistance; see (2.125)). These curves reveal that achieving the maximum power capture for any particular wave period comes with the trade-off of very narrow bandwidth. At higher T , the potential power capture is higher but the trade-off is amplified. The red and green curves give the power capture when the spring stiffness is selected for resonance at $T = 20$, but with PTO resistances of 0.01 and 0.1 respectively – far above the optimal R value. In the latter case, the peak power cap-

ture is roughly 50 times lower than in the optimal case, but the device has a far broader bandwidth and so would be likely to perform better in a realistic sea state where a broad band of wavelengths is present.

What is not shown in Figure 4.2 is the amplitude of motion of the device in these scenarios. The displacement amplitudes at the peak power capture for the five cases as listed top to bottom in the legend are, to the nearest whole length unit (i.e. device radius): 52, 222, 705, 23, and 2. All but the last of these are certainly physically unrealistic – the larger values, wildly so. Furthermore, amplitudes this large violate the assumptions of linear wave theory and the small-body approximation from which the governing equations are derived. In short, the detail in Figure 4.2 and the previous paragraph is largely irrelevant in practical terms. Rather than considering theoretical maximum results, it is necessary to consider how performance can be optimised under a set of realistic constraints.

Suppose that there is a constraint on the excursion of the device as a proportion of its radius, which we can denote (in the nondimensional units) with the fixed upper limit x_{lim} . From (2.121) and (2.123), the displacement amplitude at resonance but for general R has magnitude

$$|\hat{x}| = \frac{|\hat{F}_E|}{\omega(R + R_r)}, \quad (4.2)$$

where \hat{F}_E is the excitation force amplitude. Rearranging this and setting $|\hat{x}| \leq x_{lim}$ gives a lower limit on the PTO resistance at resonance,

$$R \geq \frac{|\hat{F}_E|}{\omega x_{lim}} - R_r \equiv R_{lim}. \quad (4.3)$$

By plugging this back into (2.122), we find that the power capture must obey the inequality

$$|P_C| \leq \frac{1}{2} \left(|\hat{F}_E| \omega x_{lim} - R_r \omega^2 x_{lim}^2 \right) \equiv |P_C|_{lim}. \quad (4.4)$$

It is easy to show that this is identical to a result derived by Evans and reported by Folley [34], expressed in terms of the ratio of constrained to unconstrained amplitude. Folley demonstrates that when the motion is highly constrained, the first term dominates and the power capture is proportional to the excitation force. This is not surprising because (4.4) is of the form $|P_C| = P_E + P_R$ (an alternative starting point for the derivation), so the observation is simply that the radiated power is small.

In Figure 4.3, we present results for four different levels of constraint: $x_{lim} = 1, 2, 4$ and 6. The bounds on PTO resistance and power capture are evaluated from (4.3) and (4.4) as a function of T . The plots of $|P_C|_{lim}$ in subfigure (b) show that, whereas in the unconstrained case the upper bound for the power capture increases monotonically with wave period (see Figure 4.2), in the constrained case the upper bound declines rapidly with period in spite of the higher incident power. This is disappointing for the prospects of designing a small point absorber that can effectively harness energy in the dominant period range of the ocean.

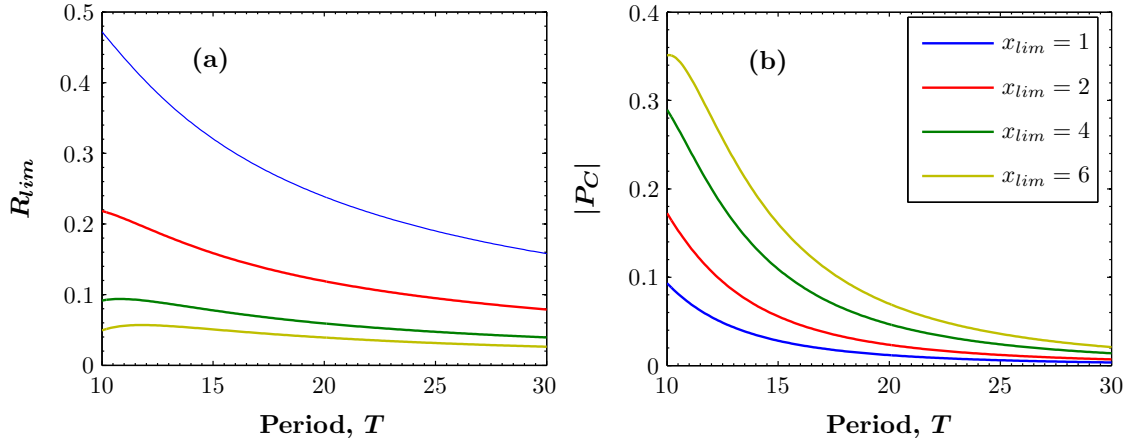


Figure 4.3: (a) Lower bound of PTO resistance in order to obey the constraints shown in the legend, for a linear device at resonance. (b) Corresponding upper bound of power capture within the constraints, for unit wave height (nondimensionalised). Figure 4.1 allows conversion to period in seconds.

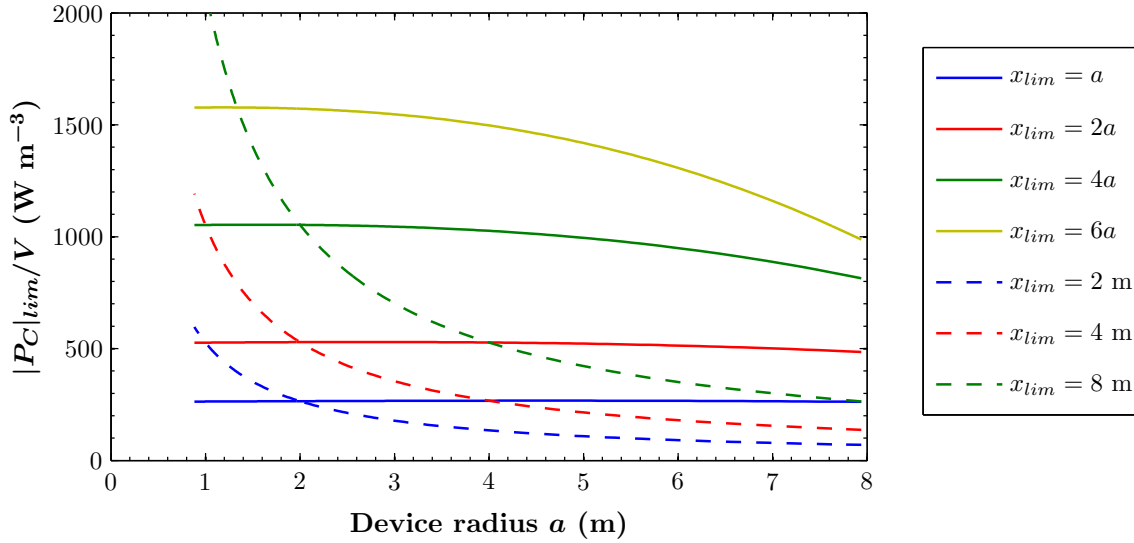


Figure 4.4: Upper bound of power-to-volume ratio for a wave of period 9 s and height 2 m, plotted against device radius. The solid lines are for constraints of a maximum excursion proportional to device radius, while the dotted lines are for constraints of a fixed maximum excursion in metres. Note that this is in S.I. units while Figure 4.3 is in nondimensionalised units.

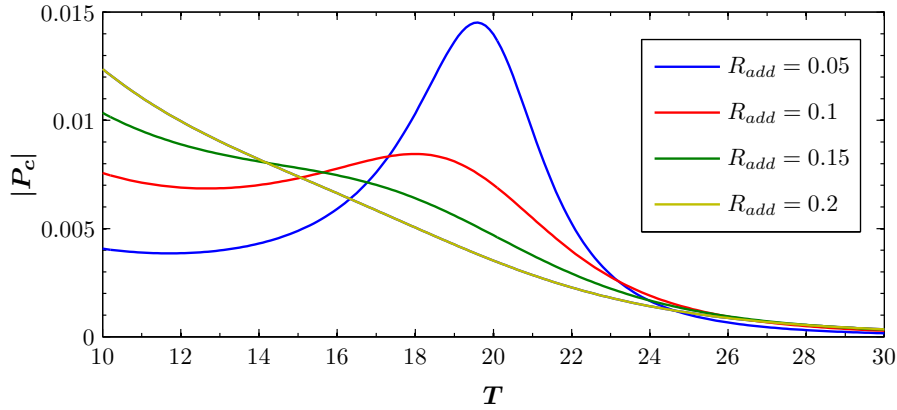


Figure 4.5: Power capture versus wave period for a linear device resonant and optimised at $T = 20$, when there is an additional dashpot force with resistance R_{add} acting. Note that the PTO resistance in each case is $R = R_{add} + R_r(T = 20) \approx R_{add}$. Figure 4.1 allows conversion to period in seconds.

Considering a fixed value of wave period in seconds so that the T -axis represents device radius, as in the scale in Figure 4.1, it may appear at first from Figure 4.3(b) that the performance is superior for larger devices. However, several conversions are necessary in order to draw a correct comparison; particularly subtle is that the data are for a constant *nondimensionalised* wave height (which depends on a), but we must compare results for the same wave height in metres¹. In Figure 4.4, the solid curves show the results from Figure 4.3(b) converted into power-to-volume ratios in W m^{-3} and plotted against device radius, for an incident wave with a period of 9 s and height of 2 m. We observe that in the highly constrained scenarios, the upper bound of the power-to-volume ratio is virtually independent of a , but as the constraint is loosened, smaller devices perform more and more favourably. The explanation is that while the maximum *excitation* power per unit volume grows linearly with device radius for these constraint conditions², large devices radiate away a greater proportion of this power and less is captured by the PTO system.

In practise, the constraint on a surging device will likely differ from the form presented above, where the maximum excursion is some multiple of the device radius. For the kind of linked system we will later examine, a more apt constraint may be a fixed maximum excursion, independent of a . The dashed curves in Figure 4.4 show how the optimum performance of the device is affected by a constraint of this form. The three example cases are chosen to match with the former constraint condition for $a = 2$. The results show that with a fixed maximum excursion, the maximum power-to-volume ratio declines rapidly with increasing device radius.

¹Because the system is linear here, this is accounted for by scaling the power capture proportional to the incident wave energy flux (preserving the capture width).

² $P_E \leq |\hat{F}_E||\hat{v}|$, excitation force is proportional to submerged volume and the maximum allowed velocity amplitude is proportional to a .

In addition to motion constraints, another limiting factor on the power capture in the real world is the presence of other dissipative forces. Even if the enormous motion amplitudes shown earlier did not pose mechanical or theoretical problems, there are friction and drag forces not accounted for that will act to limit the motion. Nonlinear drag is considered in the following sections, but here let us assume the forces can be parameterised as an additional linear dashpot with resistance R_{add} ; the effect on all equations in Section 2.5 is simply to replace R_r with $R_{add} + R_r$. The curves in Figure 4.5 show power capture of a device resonant and optimised at $T = 20$ for different values of R_{add} . As the additional resistance on the device is increased, the sharp resonance peak is damped until it disappears completely. The peak also shifts left to occur at a wave period below the resonant value. Note that the same behaviour is evident in Figure 4.2 when the PTO resistance is set well above the optimum value.

To summarise this section, physical constraints mean that small point absorbers cannot come close to achieving the upper bound of power capture predicted by linear theory. However, the analysis presented here strongly backs up the claim that small point absorbers still offer the best performance in relation to their size. We now turn to the results from modelling of the device when the nonlinear drag term is included.

4.2 Simulation details and parameter space

The full parameter space for the lone device consists of PTO resistance R , spring stiffness S , and drag coefficient C_D , with incident wave parameters height H and period T . Here we first present results from a large series of simulations with fixed “reference values” of wave height $H = 1.25$ and drag coefficient $C_D = 0.5$. The series covers every combination of the following values for R , S and T :

$$\begin{aligned} R &\in [0, 0.025, 0.050, \dots, 0.7]; \\ S &\in [0.01, 0.03, 0.05, \dots, 0.51]; \\ T &\in [10, 11, 12, \dots, 30]. \end{aligned} \tag{4.5}$$

All simulations were run to a time of $t_f = 1200$, with a ramp-time of $t_r = 1000$. Power contributions were calculated by time averaging the product of force and velocity, as in (3.35), over the largest possible whole number of cycles contained in the time window $[1050, 1200]$.

4.3 Resonance

As shown in Section 2.5.3, in the linear case the power capture is maximised if and only if the device’s velocity is in phase with the excitation force, both occurring when the resonance condition (4.1) is met. In nonlinear systems (in this case, for $C_D \neq 0$), resonance is not a well-defined state. For our purposes, we will define resonance as the state in which power capture is maximised as a function of the spring stiffness. We refer to the associated S value as the resonant spring stiffness, S_{res} . The exact

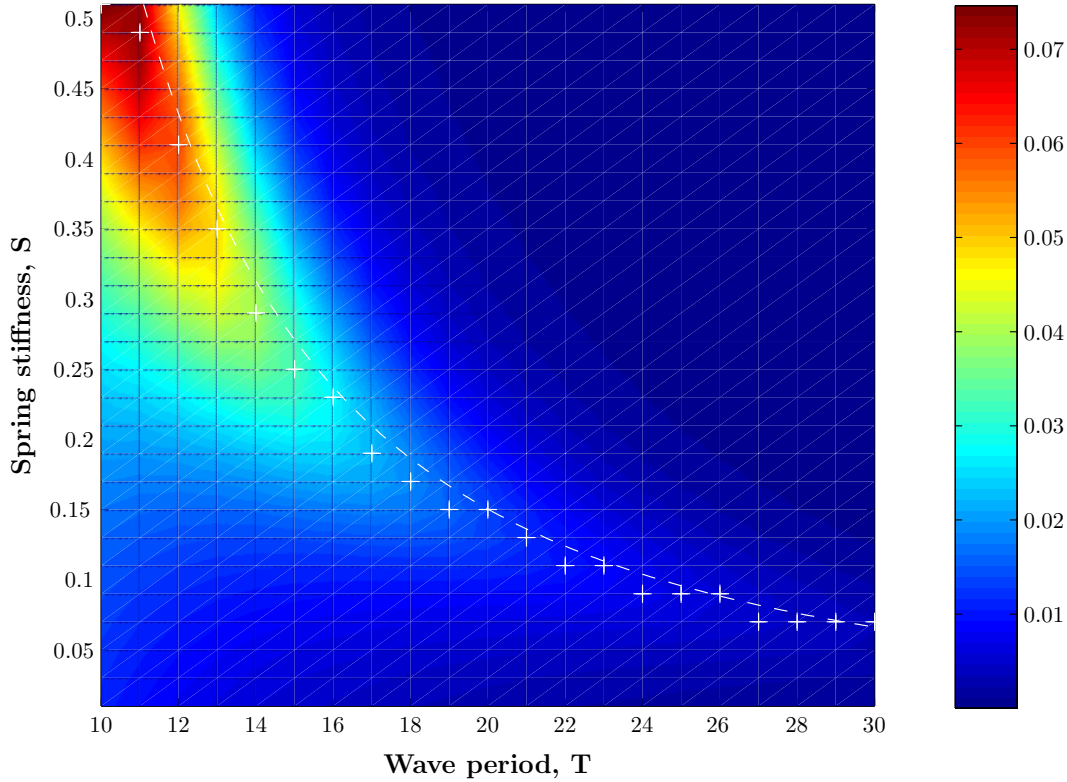


Figure 4.6: Power capture plotted against wave period and spring stiffness for the lone device with $R = 0.15$, $H = 1.25$ and $C_D = 0.5$. The white crosses show the values of S_{res} evaluated from these results, and the white dashed line is the linear resonance condition (4.1). Figure 4.1 allows conversion to period in seconds.

resonance condition is non-trivial here and S_{res} may also depend on any or all of the other parameters, viz. R , H and C_D .

Figure 4.6 shows simulated results of power capture versus T and S for fixed PTO resistance $R = 0.15$. The white crosses show the S values giving the highest power capture for each value of wave period – that is, they give $S_{res}(T)|_{R=0.15}$. The white dashed line is the linear resonance condition (4.1). The two curves are a close match, showing that, in this parameter range, divergence from the linear resonance condition is slight. The limited resolution of the grid of simulation results ($\Delta S = 0.02$) underplays how close the fit truly is – this is particularly obvious when examining the curves closely for $T \gtrsim 20$. Nevertheless, the nonlinear drag has a genuine effect causing S_{res} to be slightly smaller than in the linear case, particularly at lower values of wave period, where the motion amplitude is higher.

As Figure 4.6 only shows results for one value of R , it does not illustrate any effect the PTO resistance may have on the resonance of the device. Figure 4.7 shows the resonant spring stiffness, evaluated from simulations, against wave period for several

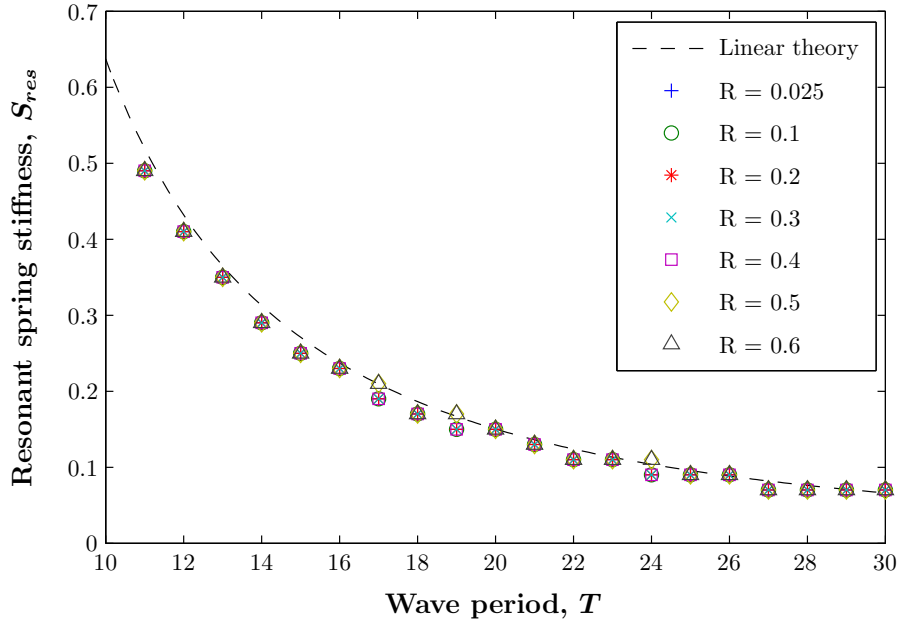


Figure 4.7: Resonant spring stiffness $S_{res}(T)|_R$ evaluated from simulations for the set of R values shown in the legend, with $H = 1.25, C_D = 0.5$. The dashed line shows the linear resonance condition (4.1). Figure 4.1 allows conversion to period in seconds.

different values of R . All data sets up to $R = 0.4$ coincide entirely, while the two sets for higher R differ at just three of the T values. Again, this apparently sudden divergence is an artefact of the coarse resolution. Examination over the entire range of R values stated in (4.5) shows that the selection presented in Figure 4.7 is representative of a very slight increasing trend in S_{res} as R is increased – this is in line with the expectation that the device will conform more and more to the linear case as the linear resistance term further dominates the quadratic drag.

It is likely that for very low values of $R < 0.025$ (or alternatively, for much higher C_D or H) the nonlinearity gives a more pronounced effect on the resonance of the device, however this is of less practical interest and we do not explore any further. Figure 4.7 shows that within the range defined in (4.5), S_{res} can essentially be thought of as independent of R , which simplifies exploration of the parameter space considerably. Later it will be shown that this result extends to multiple connected devices.

4.4 Optimisation of PTO resistance

The value of PTO resistance giving maximum power capture for a given spring stiffness is, in the linear case, given by (2.124). Again, under nondimensionalisation the only change is to replace M by 1, giving

$$R_{opt}(S, T) = \sqrt{R_r^2 + ((1 + M_a)\omega - S/\omega)^2}. \quad (4.6)$$

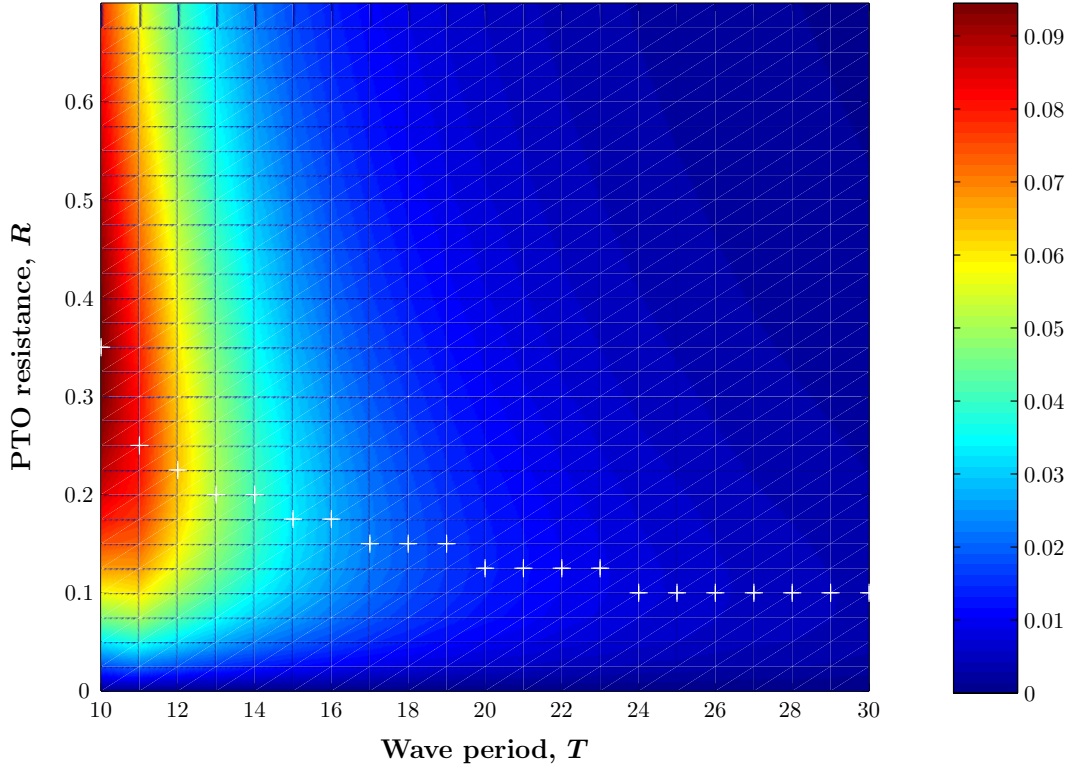


Figure 4.8: Power capture for the resonant lone device (i.e. when $S = S_{res}(T)$), versus wave period and PTO resistance. The white crosses show the optimum R values $R_{opt}(S = S_{res}(T), T)$. Figure 4.1 allows conversion to period in seconds.

One would expect this relationship to be modified when $C_D \neq 0$ since the nonlinear drag acts as a competing resistance element. In this case, R_{opt} may also depend on H and C_D . For the present analysis these are still held fixed while the dependence of R_{opt} on S is examined, and we will simply write $R_{opt}(S, T)$ for conciseness.

R_{opt} is determined numerically simply by finding the R value giving the peak power capture for each combination of S and T . To illustrate this, Figure 4.8 shows the power capture as a function of T and R when the spring stiffness is chosen as $S = S_{res}(T)$. The white crosses are situated at the peak power capture for each frequency – that is, they give $R_{opt}(S = S_{res}(T), T)$.

The upper plot in Figure 4.9 shows the R_{opt} values determined from simulations for all combinations of S and T . Note that, consistent with (4.6), for a given frequency, R_{opt} has its smallest value when $S = S_{res}$. The bottom plot in this figure shows the corresponding power capture when $R = R_{opt}$. Comparison of this with Figure 4.6 shows how power capture is enhanced when the PTO resistance is tuned to its optimal value for the parameters, rather than having the fixed value $R = 0.15$. Note that the two plots are on different colour scales.

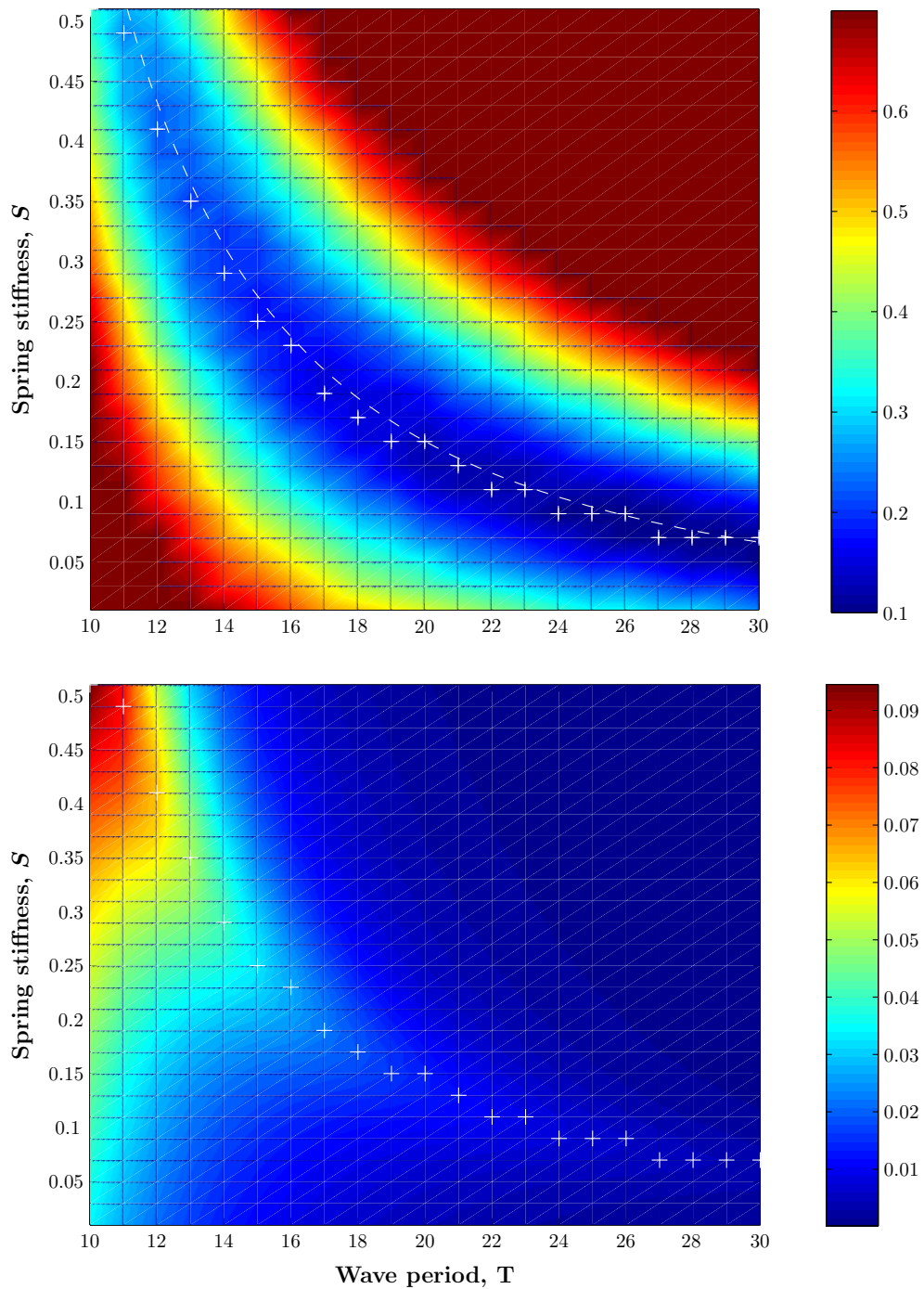


Figure 4.9: Top: Optimised PTO resistance R_{opt} as a function of wave period and spring stiffness. Bottom: Power capture for the lone device with $R = R_{opt}(T, S)$. The white crosses show $S_{res}(T)$ (c.f. Figure 4.7). Note that the range of R_{opt} is clipped since we do not have data for $R > 0.7$. Figure 4.1 allows conversion to period in seconds.

In Figure 4.10(a), power capture versus wave period is shown for four different scenarios: the black dashed line shows the result when PTO resistance and spring stiffness are always tuned to R_{opt} and S_{res} respectively – this gives the maximum power capture that the device can obtain at the different wave periods; the blue line shows the result when only the PTO resistance is tuned, and the spring stiffness has the fixed value $S = 0.15$; the green line shows the result when only spring stiffness is tuned and the PTO resistance is fixed at $R = 0.15$; the red line shows the result when both R and S are fixed at the values previously mentioned, which are chosen so that the device is approximately resonant and optimised³ at $T = 20$. Figure 4.10(b) shows the parameter values used in plotting the power capture curves above: $S_{res}(t)$, as seen before in previous figures such as Figure 4.7; and $R_{opt}(S_{res}(T), T)$, as shown in Figure 4.8.

Figure 4.10(a) makes it clear that tuning the spring stiffness for resonance makes a far bigger improvement to the device’s performance over the wave period range than tuning the PTO resistance. This is indicative of the smaller range of variation of R_{opt} compared with S_{res} , shown in subfigure (b). Unfortunately, spring stiffness would be the more difficult parameter to tune in practice, although the ability to do so over a reasonable time scale is conceivable, for example with a mechanism to wind the moorings tighter. Alternatively, resonance tuning could instead be achieved by varying mass (e.g. by exchanging water with the surrounding ocean) or added mass (e.g. by geometric deformation). Any of these proposals would surely create new difficulties and complexity, though.

Examining both plots in Figure 4.10 also sheds some interesting light on the effects of the nonlinear drag term. The black dashed curve in subfigure (a) showing the maximum power capture that the device can achieve here resembles the blue curve in Figure 4.3(b), which shows the upper bound of power capture for a linear device ($C_D = 0$) under the motion amplitude constraint $|\hat{x}|_{max} \leq 1$. The red power capture curve in subfigure (a), for $R = S = 0.15$, resembles the red curve in Figure 4.5, which is the maximum power capture for a linear device with an additional linear resistance of $R_{add} = 0.1$ acting (although the former curve is smaller in magnitude). Noting that when such an additional resistance is acting on the linear device the optimum PTO resistance is given by $R_r + R_{add}$, the plot of R_{opt} in subfigure (b) here could allow an “effective linear resistance” to be deduced. While the radiation resistance grows rapidly with decreasing T , (from $\approx 10^{-4}$ at $T = 30$ to ≈ 0.05 at $T = 10$), the R_{opt} data shown still imply a significant growth in this effective linear resistance as T is decreased. This is not surprising as the amplitudes of the fluid velocity and the device velocity are both higher for smaller T (at fixed H), so one would expect drag to have a proportionally larger effect.

4.5 Other power contributions

A brief look at the power contributions other than power capture is warranted. Figure 4.11 shows all five power contributions (as defined in Section 3.13.1) as S is varied for

³It can be seen in Figure 4.10(b) that the optimal PTO resistance is actually closer to 0.125, but using $R = 0.15$ gives the same power capture to four decimal places: $|P_C| = 0.0138$.

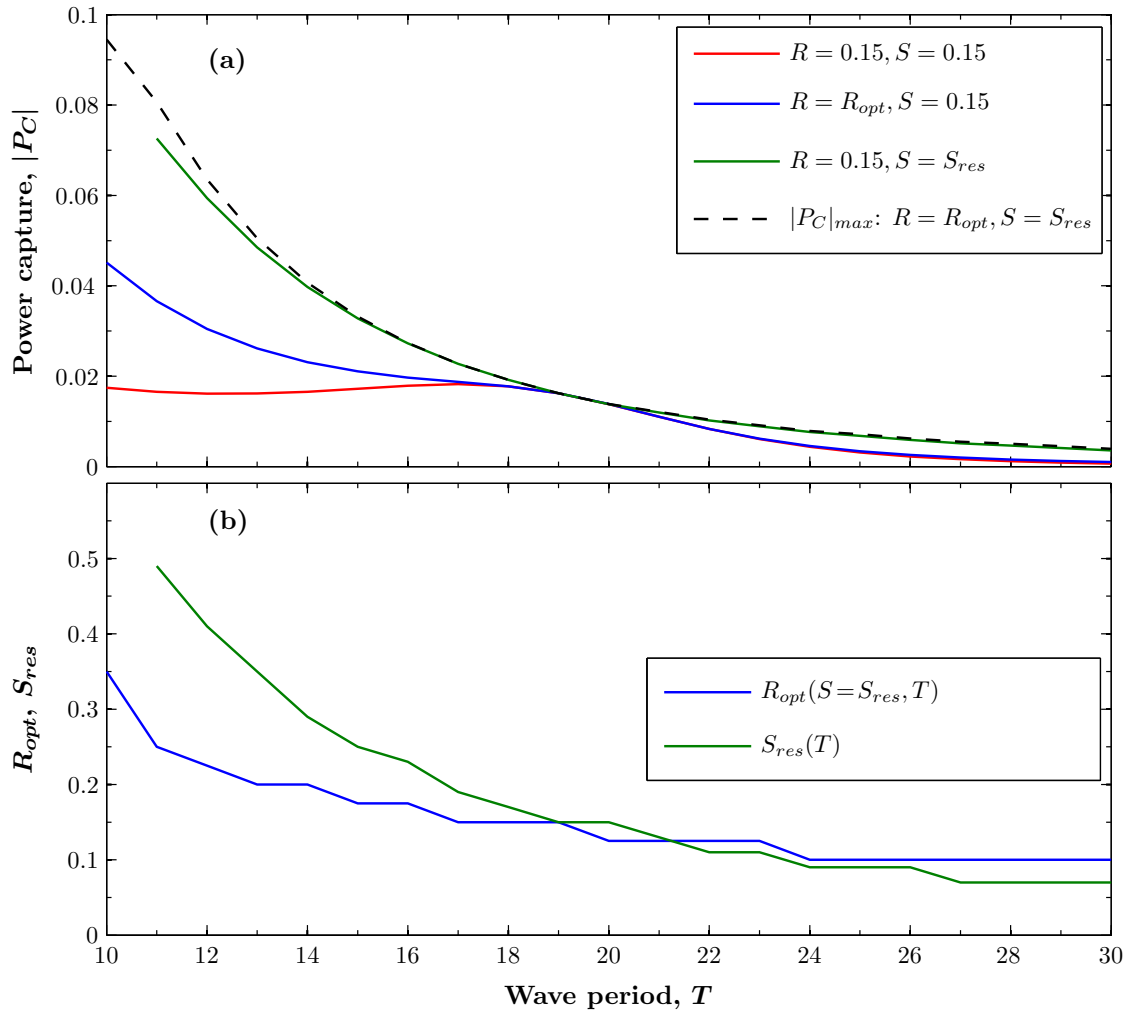


Figure 4.10: (a) Power capture curves for the lone device with $H = 1.25, C_D = 0.5$, and R and S as described in the legend. (b) Optimal PTO resistance and resonant spring stiffness, as used in (a). Figure 4.1 allows conversion to period in seconds.

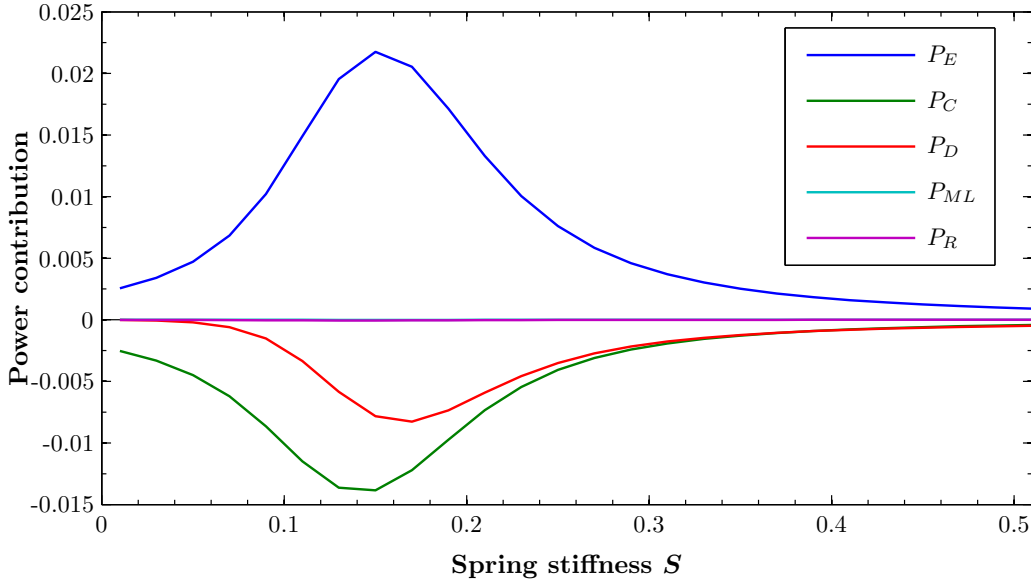


Figure 4.11: Power contributions for the lone device with $R = 0.15$ at wave period $T = 20$.

$R = 0.15$. As expected, the moorings contribute zero power in time average, and the radiated power is also negligible⁴. It is interesting to observe that the power dissipated by drag peaks at a higher S value than the excitation power, and is approximately equal to the power capture for $S \gtrsim 0.4$. This behaviour is related to the phase between the device velocity and the local fluid velocity.

4.6 Power and capture width matrices

In this section the effects of the incident wave height H on power performance are examined. Recall that the incident wave energy flux J for a monochromatic plane wave is given in nondimensional form by (3.18) and the capture width is given by $d = |P_C|/J$. In the linear case, the capture width is independent of H since the device's motion amplitude is proportional to H , and thus the power capture is, like J , proportional to H^2 . In the presence of nonlinear drag, this proportionality no longer holds and we observe that the capture width curves differ for different values of wave height. This makes the capture width a less useful measure since it depends on properties of the wave field, rather than solely on properties of the device. This also poses difficulties for predicting the power capture of the device in a continuous spectrum from the monochromatic results, which is discussed in Chapter 6.

In this section, and particularly in the following chapter, we choose a reference set for the PTO resistance and spring stiffness parameters: $R = S = 0.15$. As shown in the

⁴It is slightly larger when the memory integral is used, but still negligible in relation to the larger forces.

previous section, these are close to the optimal values for the lone device when $T = 20$ and $H = 1.25$, corresponding to 9.0 s and 2.5 m for a device with radius $a = 2$ m. Figure 4.12(a) and (b) show power capture and capture width respectively plotted against T and H for the aforementioned R and S values. Such plots will be referred to as the *power capture* and *capture width matrices*. The power capture matrix in (a) can be compared with that of the Pelamis WEC in Figure 1.3 and is clearly qualitatively similar, but shows a weaker performance at the longer wave periods. Note that for $a = 2$ m, the H values in Figure 4.12(a) line up exactly with those in the Pelamis power matrix, and the T values align very closely, ranging from 4.5 s to 13.6 s. The peak power of approximately 0.12 would in this case translate to 90 kW.

The capture width matrix in Figure 4.12(b) shows three main features. Firstly, the capture width tapers off for longer wave periods, which has been discussed earlier as a well-known property of point absorbers. Secondly, at every wave period, the capture width declines with increasing wave height. This is unsurprising as the nonlinear drag plays a proportionally larger role as the amplitudes of the fluid and device velocity increase. Thirdly, for very low wave heights there is a noticeable local maximum at $T \approx 18$, but it is reduced to a plateau by $H \approx 0.75$ and gradually becomes difficult to detect for higher wave heights. This strongly suggests a link to the behaviour shown in Figure 4.5 for a linear device as the additional resistance is increased. It appears that the effective resistance due to the nonlinear drag grows rapidly at small wave heights, but the growth tapers off.

Figure 4.13(a) shows the capture width matrix for the same set up as in the previous figure, except that the PTO resistance has the optimal value for each combination of T and H . These optimal values R_{opt} are illustrated in Figure 4.13(b)⁵. The contrast in capture width between shorter and longer wave periods is more pronounced in this figure than in Figure 4.12(b), which should be expected since the value $R = 0.15$ used in the earlier figure was chosen to be optimal for $T = 20$. The decline in capture width with increasing wave height is still present here but is mitigated somewhat by R_{opt} increasing with wave height, to counteract the increasing effective resistance due to drag.

Figure 4.14 shows how drag has an increasing effect on the dynamics of the device as wave height is increased; specifically, on the presence of higher-order frequency modes in the motion. The plot shows the percentage of the power capture associated with motion at the first three multiples of the incident wave frequency. The mode with double the incident frequency shows especially rapid growth and is approximately a quadratic function of wave height. Overall, the total from the higher-order modes does not exceed 0.5% in the parameter range shown.

⁵Note that the columns for $T = 10, 11$ would in fact have values of R_{opt} outside the range explored, which stops at $R = 0.7$.

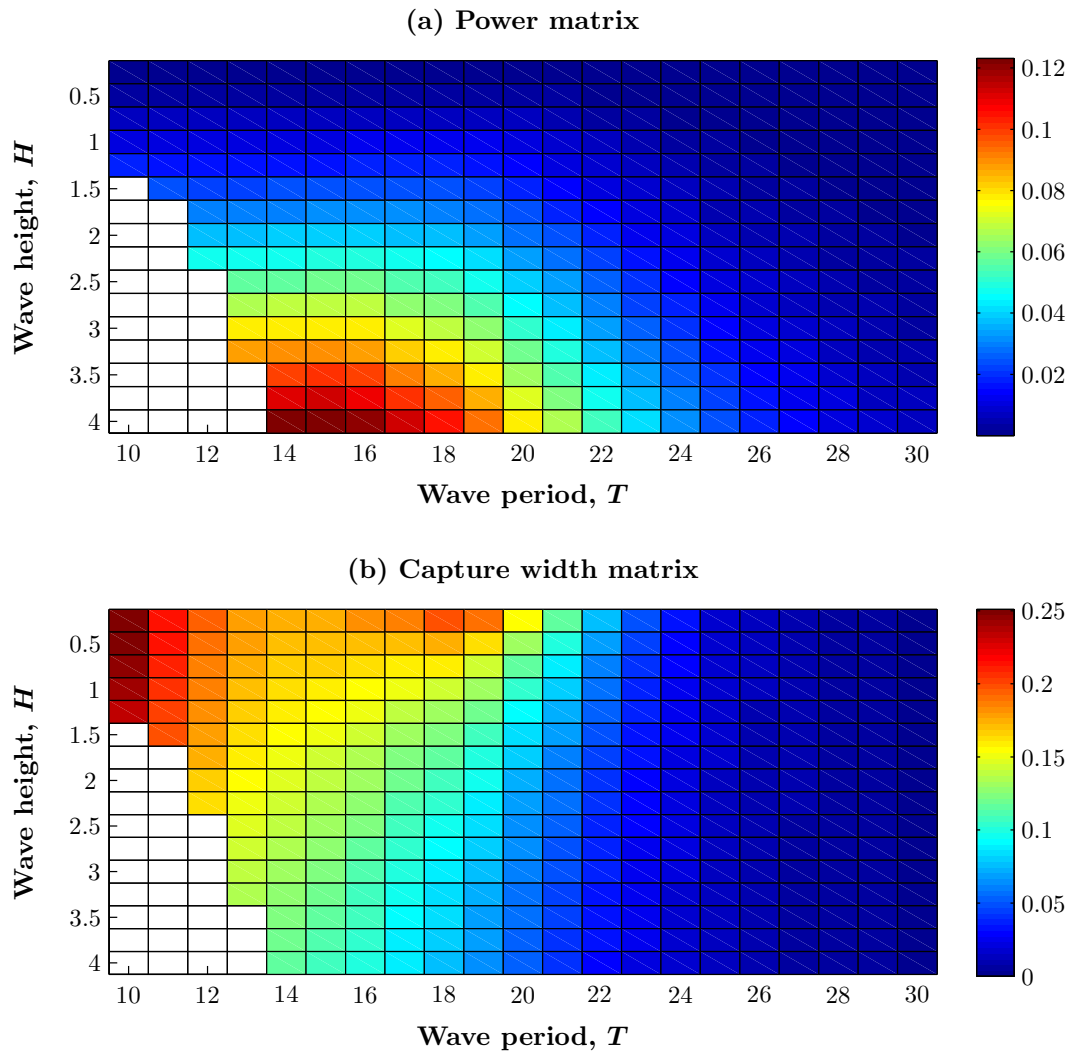


Figure 4.12: (a) Power capture and (b) capture width matrices for the lone device with $S = 0.15$, $R = 0.15$ and $C_D = 0.5$. Note that the blank cells correspond to simulations where the wave steepness was too high for the device to come to a steady oscillation after a ramp time of $t_r = 1000$. Figure 4.1 allows conversion to period in seconds.

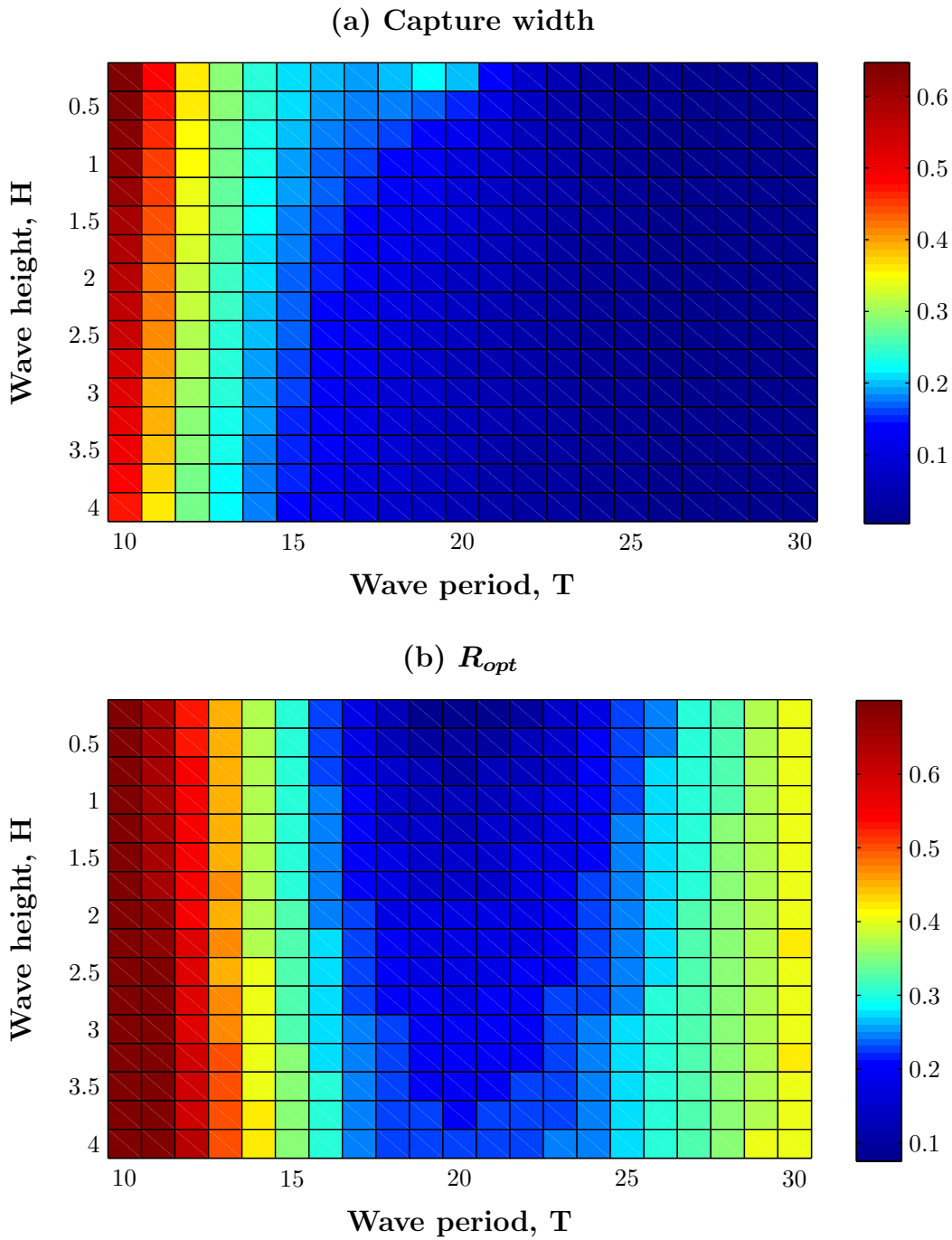


Figure 4.13: (a) Capture width matrix for the lone device with $S = 0.15$, $R = R_{opt}$ and $C_D = 0.5$. (b) Optimal PTO resistance, as used in the corresponding cells in (a). Figure 4.1 allows conversion to period in seconds.

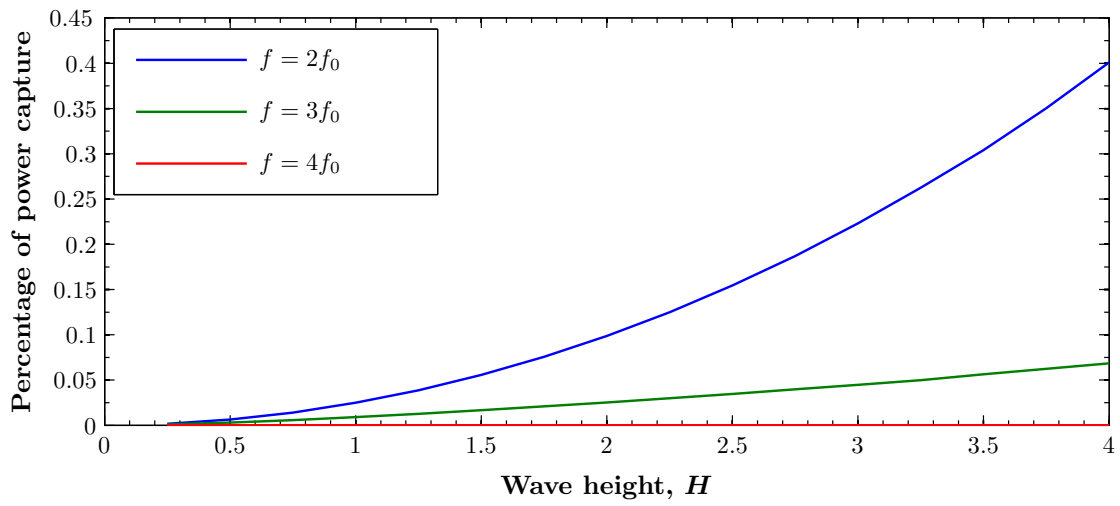


Figure 4.14: Percentage of the total power capture associated with motion at the first three multiples of the incident wave frequency, $f_0 = 1/T$, for $T = 20$, $R = S = 0.15$ and $C_D = 0.5$.

Chapter 5

Linked chains of devices

In this chapter results are presented from simulations of chains of devices, linked together with lines that act as tension-only springs, as described in Section 3.3.2. These simulations all used the “memory integral” version of the radiation force, (3.13). Once again, all quantities are expressed in nondimensional form as defined in Section 3.9, unless explicitly stated otherwise.

As compared with a lone device, exploration of linked chains introduces two new parameters: number of devices, n , and device spacing, L . This is in addition to the device PTO resistance R and drag coefficient C_D , stiffness of the mooring and linkage lines¹, S , and incident wave period T and height H . In principle, L , S , R and even C_D could be given independent values for each component of the chain. The potential parameter space is thus immense, and exploration of it is necessarily limited in scope. Attention is predominantly restricted here to cases where all components share the same parameter values, with a small number of exploratory forays made into the wider parameter regime to examine further possibilities.

5.0.1 Reference parameter set

As was done for the lone device, we selected the following fixed “reference” values for a subset of the available parameters:

$$(C_D, H, R, T)_{ref} = (0.5, 1.25, 0.15, 20). \quad (5.1)$$

The effects of varying L and S were then explored for different numbers of devices n , the results of which follow. Later, results will be presented examining the sensitivity of the results to variance of the four parameters in (5.1). In any figures in this chapter where values of variables are not specified, the reference values have been used.

¹In select instances these are given separate values S_M and S_L .

5.1 Two-device chain

To begin, we present and analyse results from the simplest case: two linked devices. Developing an understanding of the interactions here makes it easier to understand the more complex dynamics of longer chains.

A large series of simulations was carried out using the reference parameter set (5.1) with S and L being varied. From the results, power contributions were calculated as described in Section 3.13.1. Figure 5.1 shows contour plots of the power contributions for both devices individually and the per-device mean, over the domain

$$\begin{aligned} L/\lambda &\in [1/16, 1/8, 3/16, \dots, 5/4], \\ S &\in [0.05, 0.07, 0.09, \dots, 0.69], \end{aligned} \quad (5.2)$$

expressing the device spacing relative to the incident wavelength, λ . Note that the different power contributions are each plotted on a different colour scale, with the magnitude decreasing down the rows (i.e. from P_E to P_R). Simulation runs were carried out for $0.69 < S < 0.99$ but are excluded from the plots here in order to focus attention on the important region of the domain.

In Figure 5.1, there are no data for ($S > 0.35, L < \lambda/2$). The justification for excluding this part of the domain from simulations is that we observe an approximate symmetry in the response of the chain about $L = \lambda/2$, and thus much computational time can be saved for little detriment by exploring only half of the domain. The symmetry is clearly evident for $S < 0.35$, where the plots for Device 2 (second column) closely resemble a mirror image of the plots for Device 1 (first column)². The resultant per-device mean plots (third column) are approximately symmetric about $L = \lambda/2$. This symmetry in response is to be expected since, for example, when $L = \lambda/4$ the phase of the incident wave at device one's position leads that at device two's position by $\pi/2$, while when $L = 3\lambda/4$ the phase lead is $3\pi/2$, equivalent to a *lag* of $\pi/2$.

We emphasise that the symmetry discussed in the previous paragraph is not exact, however. This is because the fluid velocity and the excitation force are evaluated at the devices' instantaneous positions (not their time-average positions), and thus the symmetry of the situation is broken due to Doppler shifting; a device sees a shorter effective wavelength during the part of its motion when it is moving in the opposite direction to the incident wave and *vice versa*. Asymmetric effects become more noticeable in longer chains, as evidenced in later sections.

Periodicity of results in relation to device spacing

One might predict that there would be no difference in behaviour between the cases $L = L_0$ and $L = L_0 + \lambda$. This prediction is indeed borne out. A set of simulations was carried out for $S \in [0.05, 0.07, \dots, 0.35], L/\lambda \in [17/16, 9/8, \dots, 2]$ and compared with the results over the same S values and $L/\lambda \in [1/16, 1/8, \dots, 1]$. Power capture values were

²Recall that the devices are numbered in order in the direction of wave travel.

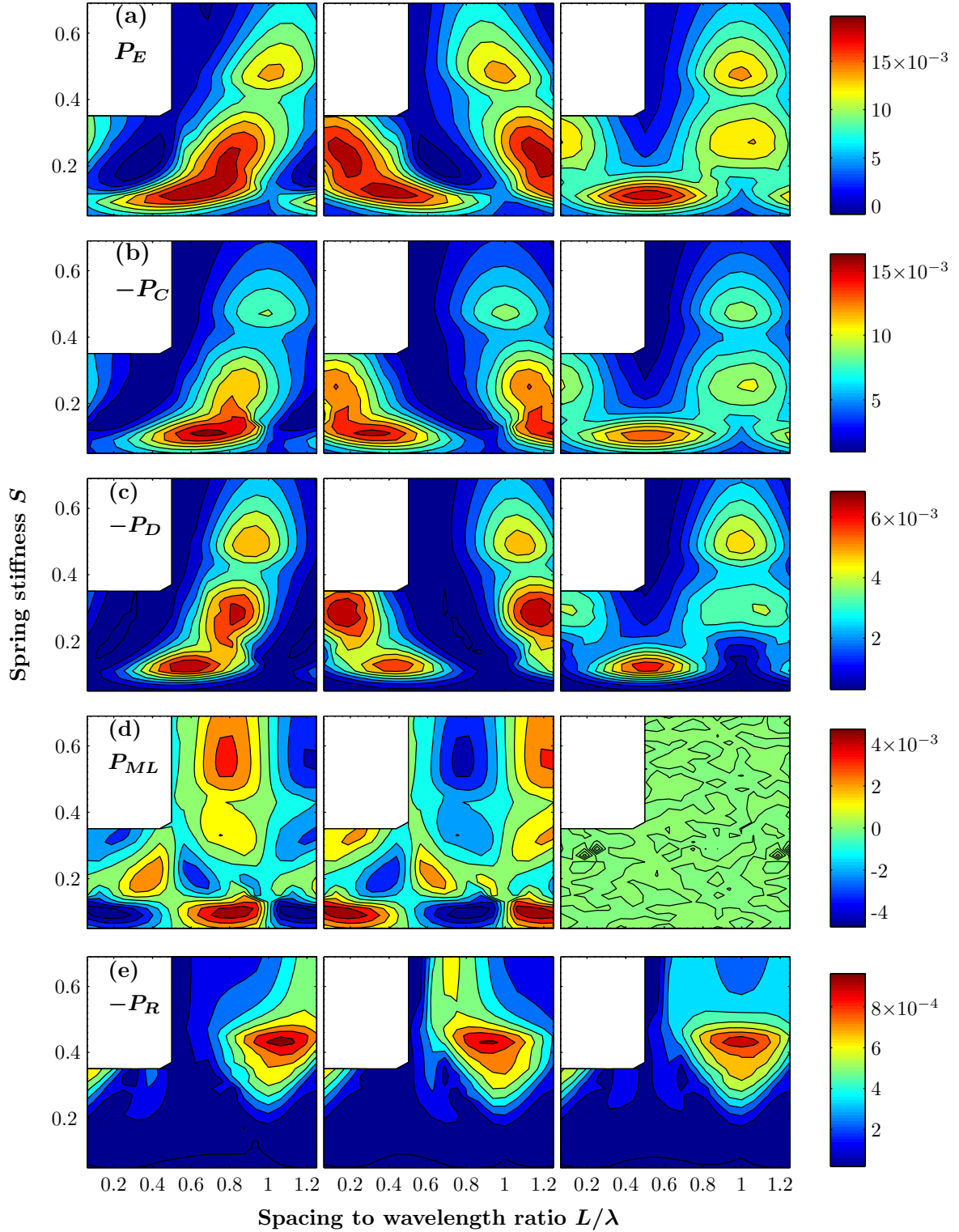


Figure 5.1: Power contributions for Device 1 (left column) and Device 2 (middle column), and the per-device mean (third column) of a two-device chain with reference parameters (5.1). (a) Excitation power, (b) power capture, (c) power dissipated by drag, (d) power transfer through mooring and linkage lines, and (e) radiated power. Note that the rows are on different colour scales, and that no data exist for $S > 0.35, L < \lambda/2$. These plots, and all others in this chapter, are in the nondimensionalised units.

calculated and it was found that

$$|P_C(L_0) - P_C(L_0 + \lambda)| < 3 \times 10^{-14} \quad (5.3)$$

for both devices and all S values. This confirms that exploration can be limited to a domain with L spanning one wavelength. Note though that care must be taken in selecting the L values since as the device spacing is reduced to zero, a threshold might be reached whereby adjacent devices cross one another in the simulation, representing a collision in the real world. This does not occur for the smallest device spacing in the present set of simulations, $L = \lambda/16$. Note that in Figure 5.1, results have been plotted out to $L/\lambda = 5/4$ to aid visualisation, particularly around $L = \lambda$.

Special cases

It is clear from Figure 5.1 that the dynamics of the two-device chain are very rich and provide much material for discussion. To begin with, neglecting the internal dynamics and focusing on the performance of the system as a whole, the plots in the third column show peaks in total power absorption and capture centred on $L/\lambda = 1/2$ and 1. In fact, much of the behaviour over the full domain can be broadly understood in terms of these two special cases: half-wavelength and full-wavelength spacing. We will now examine these in more detail.

5.1.1 Half-wavelength spacing

When the devices are separated by half a wavelength, the local water velocities at their respective positions have a phase difference of π , and so one might expect that the motions of the devices will be in anti-phase. This is indeed what is broadly observed, although discussion of phase becomes problematic when the motion of the devices becomes visibly non-sinusoidal.

Figure 5.2 shows two examples of the steady-state motion of the devices at half-wavelength spacing. Parts of the cycle in which the mooring and linkage lines are in tension are shown in the figure by the different coloured line segments, as described in the caption. The case with $S = 0.11$, shown in subfigure (a), achieves the highest mean power capture (and also mean excitation power) per device: 0.0136. This is very close to the maximum observed power capture of the lone device for these same wave parameters: 0.0138, achieved with $S = 0.15 \approx S_{res}(T = 20)$. Table 5.1 shows how the other power contributions compare to the aforementioned case for the lone device; the excitation power and power dissipated by drag are both lower in magnitude by about 0.002.

The similarities discussed above are not a coincidence. The actions of the mooring and linkage lines in Figure 5.2(a) closely resemble what we see for a lone device taut-moored from both sides: a continuous restoring force with only one of the lines in tension at any point in time. The reason that the maximum in power capture occurs at a lower value of S here than for the lone device can be understood as follows: whenever the linkage line is in tension, it is being simultaneously stretched by roughly equal amounts

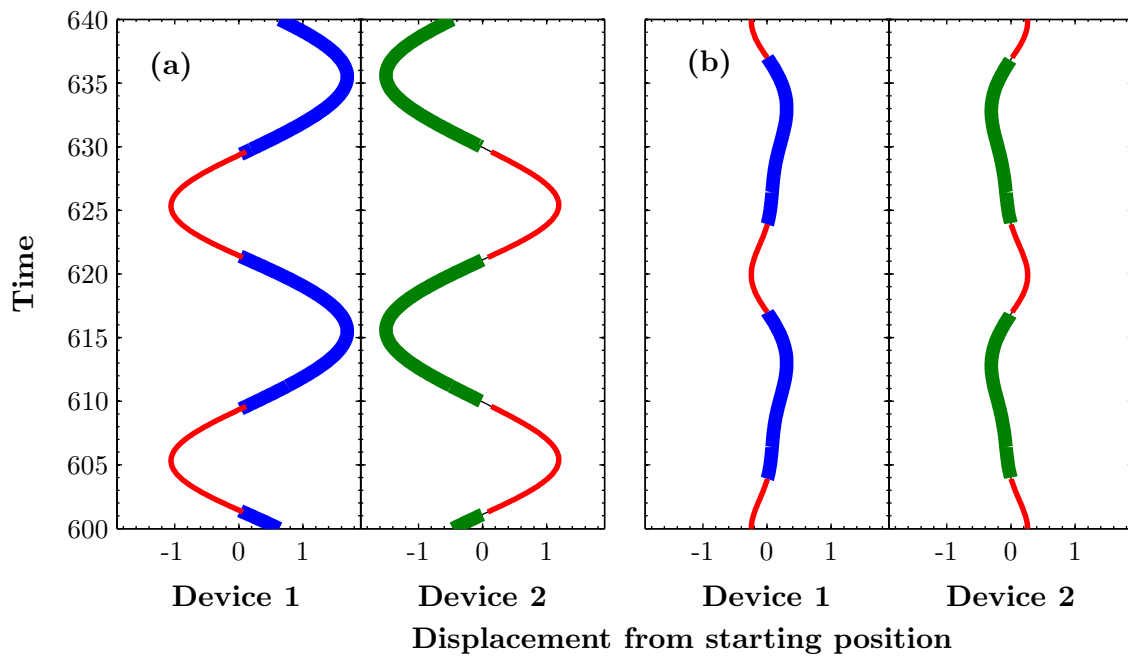


Figure 5.2: Simulation results for two linked devices spaced half a wavelength apart for $T = 20$ and (a) $S = 0.11$, (b) $S = 0.39$. The blue and green segments of the motion indicate when the mooring line is in tension on Devices 1 and 2 respectively. The red segments indicate when the linkage line is in tension. Where the thin black line is visible, none of the lines are in tension.

	$n = 1$	Per-device mean for $n = 2$
P_E	0.0218	0.0197
P_C	-0.0138	-0.0136
P_D	-0.0078	-0.0060
P_{ML}	-7×10^{-6}	-6×10^{-8}
P_R	-6×10^{-5}	-2×10^{-5}

Table 5.1: Comparison of power contributions for the single device with $S = 0.15$, and the means for two linked devices with $S = 0.11, L = \lambda/2$, and other parameters given by the reference set (5.1).

at either end. Thus, from either device’s perspective, the line has an “effective” stiffness of $\sim 2S$ when $L = \lambda/2$. We emphasise that this applies only to the linkage line and not to the mooring lines, so the situation is asymmetric³.

At higher values of S , both devices’ oscillation amplitudes diminish, and high frequency motion components become visible. Figure 5.2(b) shows one illustrative example, with $S = 0.39$. In Figure 5.3, the power contributions for the two devices are plotted against S for half-wavelength spacing⁴. Comparison of this with Figure 4.11 for the lone device with $S = 0.15$ shows a high degree of similarity, once the modification to S described above is taken into account. There are regions where there is substantial difference in response of the two devices, caused by the Doppler shift asymmetry, and evidenced by power being transferred through the connections (i.e. non-zero P_{ML}).

To summarise: putting aside the small intricacies noted here, the response of two linked devices at half-wavelength spacing can be thought of as broadly similar to the lone device, with a modified dependence on S .

5.1.2 Full-wavelength spacing

When the devices are separated by precisely one wavelength, the phase of the incident wave at their positions is the same, and one might initially expect the devices to exhibit identical motion. However, since the devices are moored from opposite sides and interacting through the (non-rigid) linkage line, this is generally not the case.

Figure 5.4 shows four examples of the steady-state motion of the devices at full-wavelength spacing and different S values. In (a), for $S = 0.13$, the linkage line is in tension at all times and the motion appears close to sinusoidal with the two devices in phase. When examined closely though, the turning points in the motion of whichever device is being acted on by its mooring line precede the turning points in the other device by approximately 0.3 time units, or 1.5% of a period.

When S is increased above 0.13, the linkage line no longer remains in tension for the entire period. Figure 5.4(b) shows one example, where $S = 0.27$. Here the motion

³This could be compensated for by choosing distinct S values for the different lines.

⁴Note that these correspond to slices at $L/\lambda = 1/2$ of the contour plots in Figure 5.1.

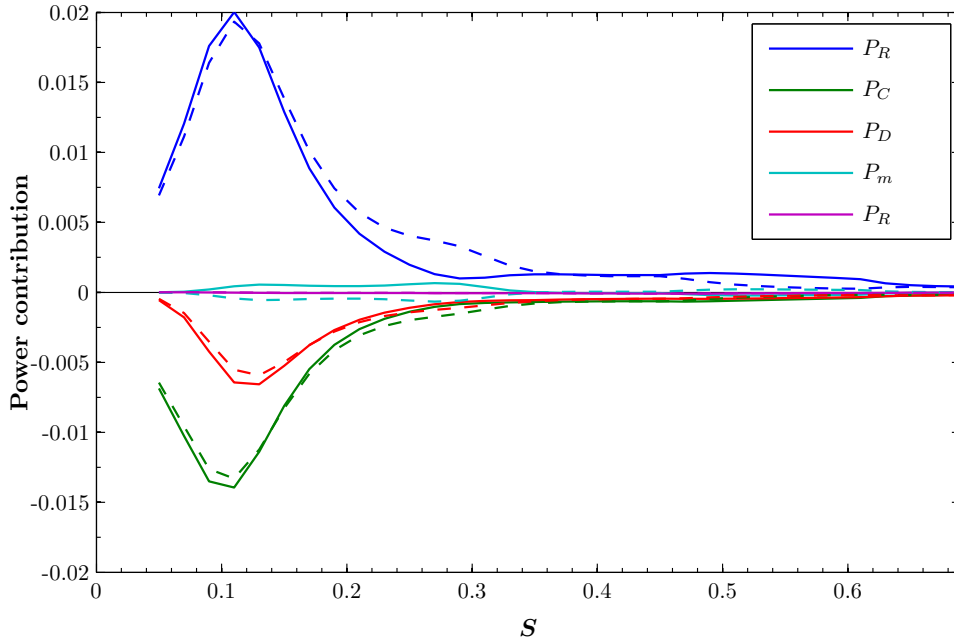


Figure 5.3: Power contributions for Device 1 (solid lines) and Device 2 (dashed lines) versus line stiffness S , for the two-device chain with half-wavelength spacing at wave period $T = 20$ (as in Figure 5.2).

is visibly non-sinusoidal and both devices experience segments of their cycles where both attached lines are slack. In particular, the linkage line is slack while either device undergoes its turning point due to being acted on by its mooring line, and there is a delay of approximately 2.4 time units, or 12% of a period, before the other device reverses direction. In subfigure (c), where $S = 0.39$, high frequency motion components are even more visible, and the delay between turning points is approximately 3.2, or 16% of a period.

When S is increased further, as in subfigure (d) with $S = 0.77$, high-frequency components are dampened and the motions more closely resemble two in-phase sinusoids. The example shows visibly flattened peaks; here at the same time the devices experience a restoring force from their mooring lines, they feel a force in the opposite direction from the active linkage line. The other device, whose mooring line is slack, is actually the first to reverse direction.

Acknowledging the complexities described above, the behaviour of the two linked devices at full-wavelength spacing over the full range of S values can be loosely classified into qualitative regimes: at low ($S \lesssim 0.2$) and high ($S \gtrsim 0.5$) values of spring stiffness, the motions of the two devices are similar, close to sinusoidal and roughly synchronised with one another; in the S range between, the motions of both devices are strongly affected by the presence of high frequency components, and are more visibly distinct from one another.

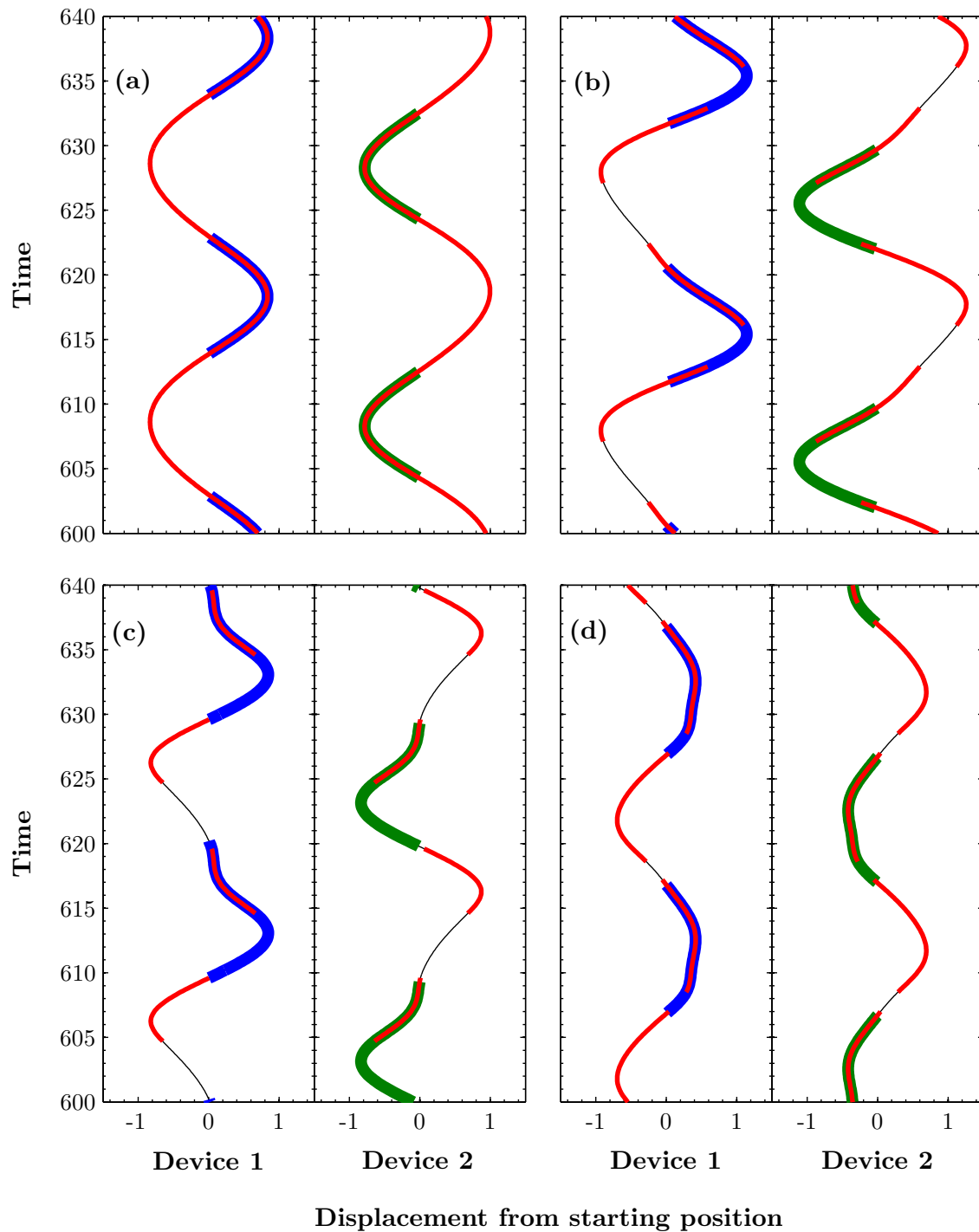


Figure 5.4: Simulation results for two linked devices with full-wavelength spacing at $T = 20$ and (a) $S = 0.13$, (b) $S = 0.27$, (c) $S = 0.39$, and (d) $S = 0.77$. The coloured line segments show when the mooring and linkage lines are in tension, as described in Figure 5.2.

A hypothesis was developed that, in the former regime detailed above (i.e. at low and high S), the behaviour of the linked devices can be explained in relation to a single device with double the mass (including added mass), volume and PTO resistance. To test this⁵, a series of runs was undertaken with $L = \lambda$ where the linkage line, rather than having the same stiffness as the mooring lines, had a fixed value of $S_L = 1000$. Note that the linkage was still tension-only and so the combined structure was not entirely rigid. However, in all cases the linkage line was found to be taut at all times during the steady-state motion. Figure 5.5(a) has the resulting power capture for this test series plotted in black. Comparison with Figure 4.11 for the lone device shows that the test series has a virtually identical peak power capture per device ($|P_C|_{max} \approx 0.014$) occurring at an S value approximately twice as high ($S \approx 0.3$, c.f. 0.15). It is straightforward to show that this agrees with linear theory results (2.123) and (2.126) for a doubling of the device's mass and volume⁶.

Plotted along with the power capture results for the test series in Figure 5.5(a) are those from the main series⁷ with the default setup where the mooring and linkage lines always have the same stiffness ($S_L = S_M = S$). There is some difference between the power capture curves for the two devices, although they practically overlap for $S > 0.4$. Outside of the region $0.2 \lesssim S \lesssim 0.5$, the mean power capture curve resembles that of the test series, but with a peak shifted to a higher S value. In the low- and high- S limits, the two curves look to converge.

Further analysis of the main series is given in Figure 5.5(b). Plotted here are the percentages of time for which the different lines are active over a complete cycle (refer back to the examples in Figure 5.4 for graphical illustration). Of particular interest is the curve for the linkage line (red), declining from 100% for $S < 0.15$ to a minimum of 50% at $S = 0.39$, and then rising again to flatten off at approximately 85% as S is increased. Note that this minimum coincides with the local minimum in the power capture curves in (a).

Fourier analysis offers further enlightenment on the dynamics. The Fourier series coefficients,

$$c_{p,q} = \frac{1}{\tau} \int_0^\tau x_p(t) e^{i2\pi f_q t} dt, \quad (5.4)$$

were evaluated for $\tau = mT$, where m is a whole number, using the FFT function in MATLAB. As expected, non-negligible coefficient amplitudes are found only for integral multiples of the incident wave frequency, i.e. for $f_q = qf = q/T$, with q an integer. With these coefficients evaluated, the contributions of the different *frequency modes* to the total power capture are easily calculated⁸.

⁵An alternative approach would be to use a single device with doubled volume. However, changing a means that multiple unit conversions are necessary in order to compare results, so the described approach was chosen for simplicity.

⁶ $\hat{F}_E \rightarrow 2\hat{F}_E$ and $R_r \rightarrow 2R_r$, so $|P_C|_{max} \rightarrow 2|P_C|_{max}$. This total power capture is shared equally between the the two devices in the test series.

⁷These plots correspond to slices at $L = \lambda$ of the contour plots in Figure 5.1(b).

⁸A discrepancy of up to 0.5% is observed between the actual power capture and that calculated by summing up the contributions from all frequency modes. This error can be attributed to the FFT

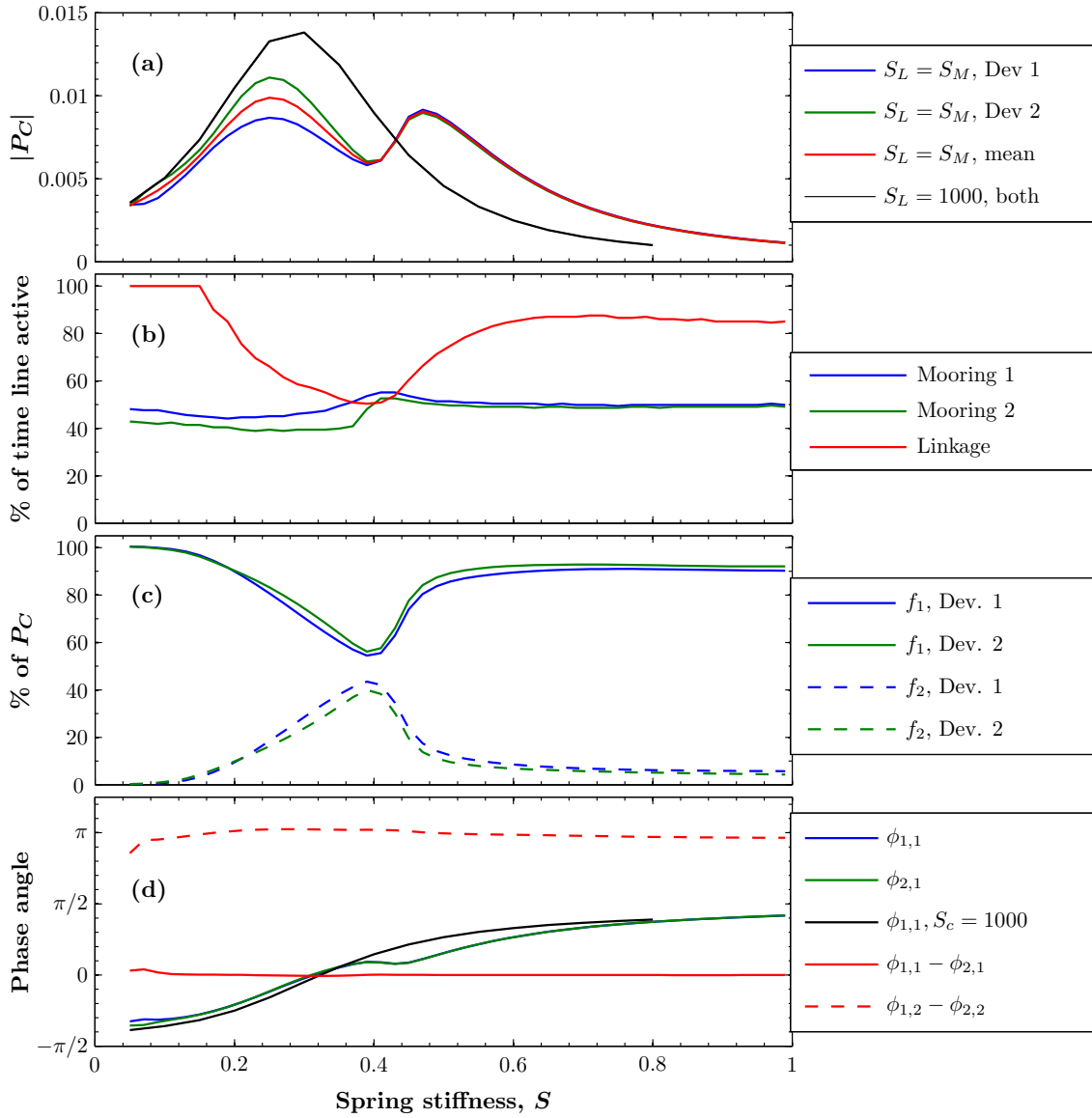


Figure 5.5: Analysis of two linked devices at full-wavelength spacing for $T = 20$. (a) Power capture. The blue, green and dashed red lines show results for Device 1, Device 2 and their mean respectively, for the default setup where the mooring and linkage lines have the same stiffness (viz. $S_L = S_M \equiv S$). The black line shows the result for Device 1 or 2 (no discernible difference) when the linkage line has a fixed stiffness of $S_L = 1000$. (b) Percentage of one complete cycle for which the mooring and linkage lines are in tension (default setup). (c) Contributions of the first two frequency modes to the total power capture (default setup). (d) Phases of the frequency modes, as defined in (5.5).

Plotted in Figure 5.5(c) are the power capture contributions from the first two frequency modes as a percentage of the total, for both devices. The combined contribution from all modes of higher order ($q \geq 3$) over this parameter range never rises above 4%. This plot clearly demonstrates the significant role that the mode with twice the wave frequency, f_2 , plays in the dynamics for $0.2 \lesssim S \lesssim 0.5$. The f_2 power capture contribution is more than 10% of the total throughout this region, peaking at about 40% (for both devices) when $S = 0.39$. This feature again coincides with the local minimum in the total power capture curves in subfigure (a).

The phases of the Fourier coefficients contain useful information. We express the phases here as

$$\phi_{p,q} = \arg(c_{p,q}) - \pi/2 \quad (5.5)$$

so that they are zero when a device's displacement is in phase with the local water velocity, meaning that its velocity is in phase with the excitation force⁹. Phases of the f_1 mode are plotted in Figure 5.5(d) (blue and green), along with that for the test series with $S_L = 1000$ (black) for comparison. The shape of the latter is that of the classic harmonic oscillator. The blue and green curves do not depart dramatically from this, but do exhibit a kink centred around $S \approx 0.4$. Most interestingly, for all S , the phase difference between the f_1 modes of the two devices is virtually zero (solid red line), while for the f_2 modes it is always close to π (dashed red line).

The preceding observations together paint a reasonably clear and consistent picture of the dynamics of the two linked devices at full-wavelength spacing. The motions are well-represented as a superposition of in-phase motion at the incident wave frequency ($f_1 = 1/T$) and anti-phase motion at twice this frequency ($f_2 = 2f_1$). The linkage line is the key driver of the f_2 motion, as evidenced by the correlation between the percentage of the cycle for which the line is slack and the percentage that the f_2 motion contributes to the total power capture (Figure 5.5(b) and (c), respectively). In particular, the peak f_2 power capture contribution occurs at $S \approx 0.39$ when the linkage line is undergoing alternating active and slack periods each lasting 5 time units ($= T/4$) – see Figure 5.4(c). That the peak occurs at this S value is consistent with the peak power capture for *half*-wavelength spacing occurring at $S \approx 0.1$ (see Figure 5.3), since the motion frequency here is doubled and from the linear resonance condition (4.1) we expect $S_{res} \propto f^2$ (neglecting the frequency dependence of the added mass).

The results here suggest, disappointingly, that it is not possible to achieve “the best of both worlds” and simultaneously have near-optimal response at the incident wave frequency while also tapping into power at higher frequencies. Rather, strong oscillations at higher frequencies appear to come at the expense of good performance at f_1 , and do not compensate the total power sufficiently. This makes sense in light of the explanation above, since high frequency response is stimulated by periods of slackness in the linkage line, while response at f_1 is maximised when the devices move together as one.

process.

⁹This applies only for $L = \lambda$; a more general expression is given later. Also, the statement is only approximately true since it does not take account of the true position of the device; the phase of the water velocity is simply evaluated at the device's starting position.

One final summary point is that it has been shown here that, unsurprisingly, the performance of the linked devices converges to that of a lone device as the stiffness of the linkage line is increased. Note though that we would only expect this to be the case for full-wavelength spacing.

5.1.3 General spacings

The power contributions corresponding to the five distinct forces have already been plotted for the entire two-device simulation series in Figure 5.1. Having examined the two special cases in the preceding sections, we now examine the rest of the parameter space with reference to these.

To begin, examples of the steady-state motions for one particular spacing value, $L/\lambda = 13/16 = 0.8125$, are plotted in Figure 5.6. In subfigure (a), where $S = 0.09$, the motions are close to sinusoidal with a phase difference of approximately $\pi/2$, and Device 1 has a slightly larger amplitude than Device 2. In subfigure (b), where $S = 0.15$, Device 2 is pulled far to the left so that its mooring line is permanently in tension, and its motion is highly suppressed while Device 1 oscillates near-sinusoidally with a large amplitude. It appears that the motion of Device 2 has a dominant frequency twice that of the incident wave, and it can be thought of as alternating between “in phase” and “out of phase” with the extrema of Device 1. In subfigure (c), where $S = 0.23$, both devices are moving approximately sinusoidally at the incident wave frequency and are in phase. This resembles what was seen for $L = \lambda$ at low spring stiffness values $S \lesssim 0.15$, as in Figure 5.4(a), except here Device 1 has a significantly larger amplitude than Device 2. Comparing subfigures (c)-(f) with Figure 5.4(a)-(d) shows that as S is increased from here, the behaviour is qualitatively similar to the full-wavelength spacing case. Consistent with this, the amplitudes of the two devices look to converge at high S values.

As mentioned earlier, the per-device mean power plots show prominent features centred on $L = \lambda/2$ and λ – specifically, the per-device mean power capture in Figure 5.1(b) has three approximately symmetric peaks: one centred on $L = \lambda/2$, and two on $L = \lambda$. We have seen that the former is associated with resonant anti-phase motion between the two devices, and the latter two are both associated with synchronised motion, with the “disturbance” in between associated with resonant oscillation at $f_2 = 2/T$. By inspection, these peaks in the mean power capture are formed by three mirror-image pairs of peaks in the individual device power captures. For example, the central peak in the mean is the resultant from peaks centred at $(L/\lambda, S) \approx (0.7, 0.1)$ for Device 1 and $(0.3, 0.1)$ for Device 2.

Peak power capture

The first and most important observation from Figure 5.1(b) is that the peaks for the individual devices are obviously higher than for the per-device mean. That is, while it appears to be impossible for the chain as a whole to better the maximum power capture of two separate lone devices for this wave period, the devices can individually reach

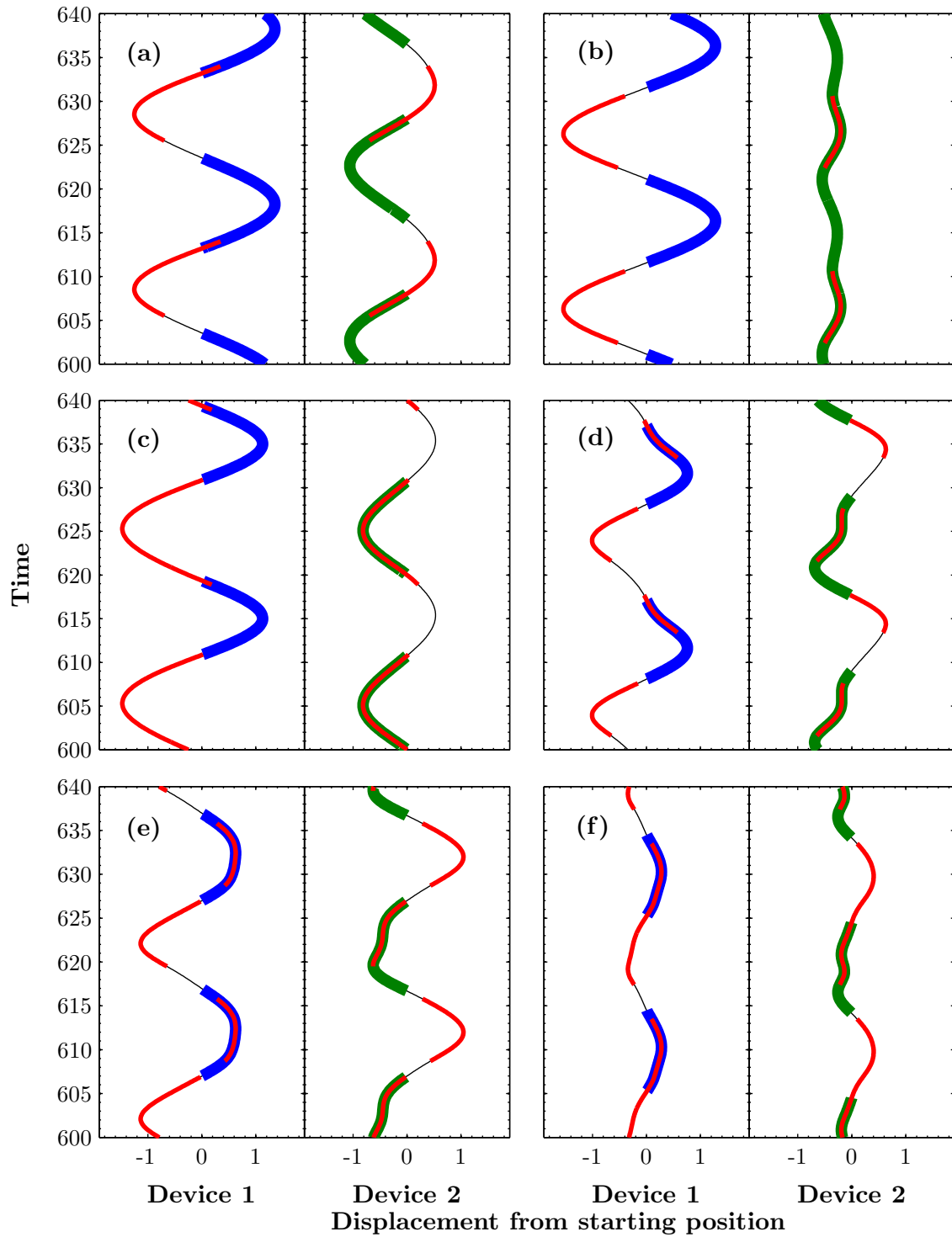


Figure 5.6: Simulation results for two linked devices spaced at $L/\lambda = 13/16$ for $T = 20$ and (a) $S = 0.09$, (b) $S = 0.15$, (c) $S = 0.23$, (d) $S = 0.39$, (e) $S = 0.51$ and (f) $S = 0.99$. The line segments are coloured as described in Figure 5.2.

	$n = 1$	$n = 2$, Dev. 1, $S = 0.11$	
	$S = 0.15$	$L/\lambda = 9/16$	$L/\lambda = 11/16$
P_E	0.0218	0.0207	0.0194
P_C	-0.0139	-0.0157	-0.0171
P_D	-0.0078	-0.0067	-0.0060
P_{ML}	-7×10^{-6}	0.0017	0.0038
P_R	-6×10^{-5}	-2×10^{-5}	-1×10^{-5}

Table 5.2: Power contributions for Device 1 in the two-device chain, for two parameter choices, compared to the case of maximum power capture for a lone device. For Device 1 of the chain, $(S, L/\lambda) = (0.11, 9/16)$ is the data point with the highest excitation power, and $(0.11, 11/16)$ gives the highest power capture. Note that all other parameters here are fixed at the reference values (5.1).

power captures in excess of the lone device maximum. Interestingly, this is in spite of neither device achieving as high an *excitation* power as the lone device does at its peak power capture. This is possible because the linkage line is capable of transferring significant amounts of mechanical power (in time-average) from one device to the other.

The preceding point is illustrated in Table 5.2. The data point with the maximum excitation power for Device 1 is $(L/\lambda, S) = (9/16, 0.11)$. The power capture here is higher than the lone device maximum, due in part to the lower excitation power being compensated by reduced dissipation due to drag, but more importantly by a time-average power transfer of 0.0017 from Device 2 via the linkage line. A higher power capture still is reached at the data point $(11/16, 0.11)$. The excitation power here is lower than the previous example by 0.0013, but this is more than compensated for by an increase of 0.0021 in the power transfer from Device 2, and also a reduction of 0.0007 in the drag dissipation.

Clearly, the maximum power capture achieved by the individual devices involves a compromise between absorbing more excitation power and receiving more power via the linkage line, with drag dissipation also playing a part in tipping the balance towards one or the other. Relating this to the plots in Figure 5.1 for Device 1, both P_E and P_D peak at roughly $(0.6, 0.12)$, while P_{ML} peaks at around $(0.8, 0.1)$. The peak power capture falls approximately halfway in between these at $(0.17, 0.11)$.

Fourier components

Fourier analysis is again useful to shed some light on the results. The amplitudes of the first two Fourier coefficients $c_{p,1}$ and $c_{p,2}$, calculated as in (5.4), are presented in Figure 5.7(a)–(b). Subfigure (c) shows the contributions of these first two frequency modes to the total power capture, for Device 2 only.

The strong resemblance between Figures 5.7(a) and 5.1(b) suggests that wherever the power capture has significant magnitude, it is predominantly associated with the

f_1 mode¹⁰. Meanwhile the f_2 plots in Figure 5.7(b) closely resemble the plots of P_R in Figure 5.1(e), which shows two things: first, that the radiated power is a good proxy for detecting the presence of high-frequency motion components¹¹; second, that the f_2 components are by far the most significant of the higher frequency components over this domain, as was observed for $L = \lambda$ in Figure 5.5. These points are reinforced by Figure 5.7(c); note that the total power capture contribution from frequency modes f_3 and higher reaches as much as 27% near the top of the S range, but the overall power capture is low in this region.

Since we are now dealing with spacings other than one wavelength, it is necessary to generalise (5.5) and define a new quantity measuring the phase of the devices' displacements relative to the *local* phase of the water velocity (i.e. taken at the devices' specific starting positions):

$$\phi_{p,q}^L = \arg(c_{p,q}) - \pi/2 + kx_p|_{t=0}, \quad (5.6)$$

where k is wavenumber. We will call this the *local phase*. Note that it reduces to (5.5) for $x_p|_{t=0} = 0, \lambda, \dots$. Phase *differences* between devices are still measured using the *absolute* phase, not (5.6).

In Figure 5.8 we present local phases and phase differences for the first two frequency modes. Comparing the local phases of the f_1 coefficients with their amplitudes in Figure 5.7(a) shows reasonable correlation between large motion amplitudes and local phases close to zero, and between small motion amplitudes and local phases close to $\pm\pi$ (as for a standard linear oscillator¹²), but other factors are also clearly at play. One such factor is power transfer between the devices via the linkage line, which we examine further below. First, we attempt here to divide the domain into approximate regions of similar qualitative behaviour, presented in Figure 5.9.

Region classification

The regions in Figure 5.9 have been selected manually, by inspection; we emphasise that they should only be taken as indicative. To explain these, in addition to examining the Fourier analysis in Figures 5.7–5.8 it is helpful to refer back to Figure 5.6, which gave examples of the motion for several S values when $L/\lambda = 13/16$.

When S is small, high-frequency motion components are negligible and the spacing length has little effect on the local phase of the oscillation – that is, the phases of both devices are predominantly determined by the local wave forcing. This applies for a region extending up to $S \approx 0.11$, labelled ‘A’ in the figure.

Recall that for $L = \lambda/2$, resonance occurs at $S \approx 0.11$ (see Figure 5.3). We observe that for spacings $\lambda/4 \lesssim L \lesssim 3\lambda/4$ there is a small range of S values centred on about 0.13 in which the devices “lock in” to this resonance and oscillate in anti-phase, similar to the

¹⁰Note that P_C is proportional to the square of the motion amplitude and so features are comparatively broader in the present plots.

¹¹In the nondimensional units the radiation resistance $R_r \propto \omega^7$ at small ω (derived from (3.28)), hence radiated power is heavily weighted towards higher frequency oscillations.

¹²Recall that local phase of zero implies the velocity is in phase with the excitation force.

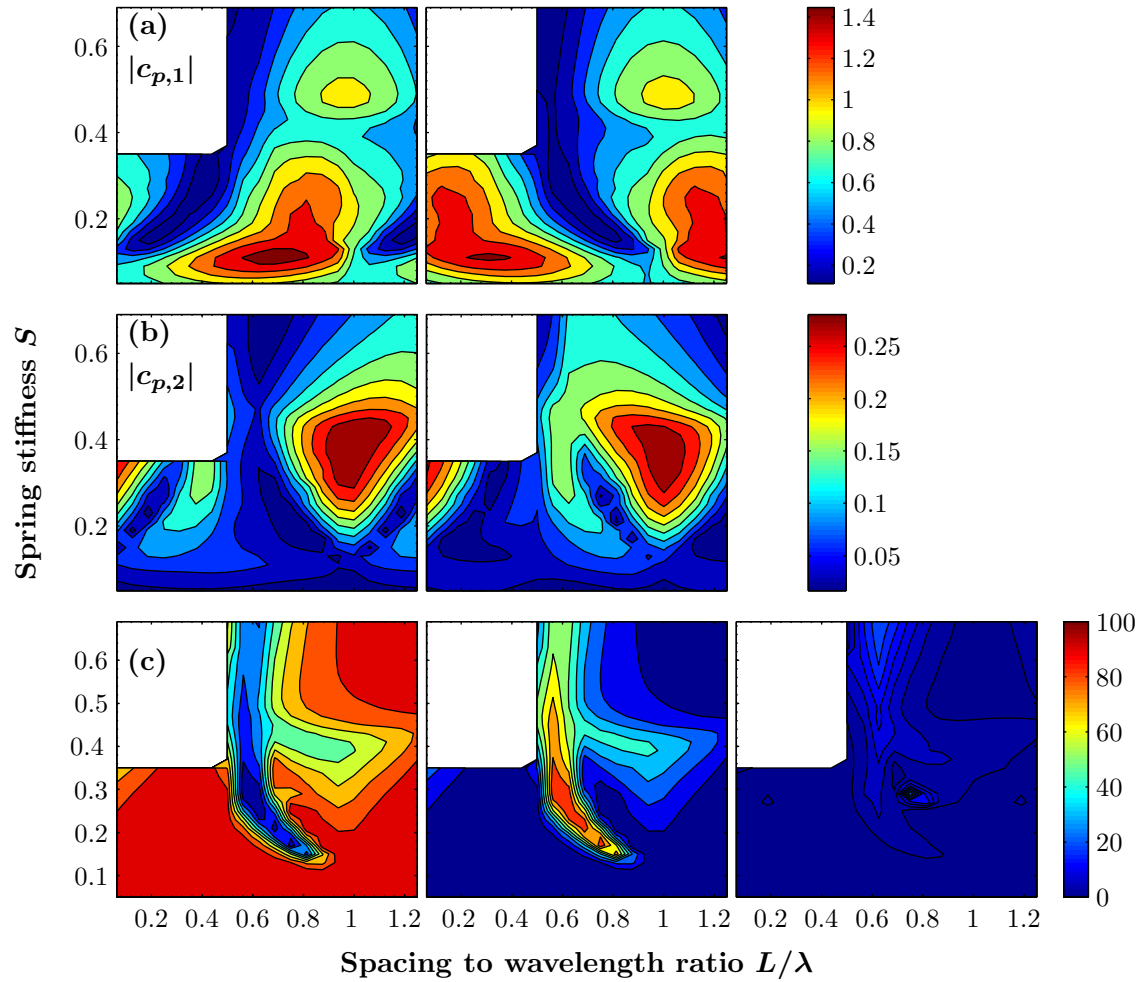


Figure 5.7: Fourier coefficients and frequency mode contributions to total power capture for the two-device chain. (a) Magnitude of the first Fourier coefficient for Device 1 (left) and Device 2 (right). (b) Magnitude of the second Fourier coefficient for Devices 1 (left) and 2 (right). (c) Percentage contribution to total power capture by frequency modes, for Device 2 only: f_1 (left), f_2 (middle) and the remainder (right).

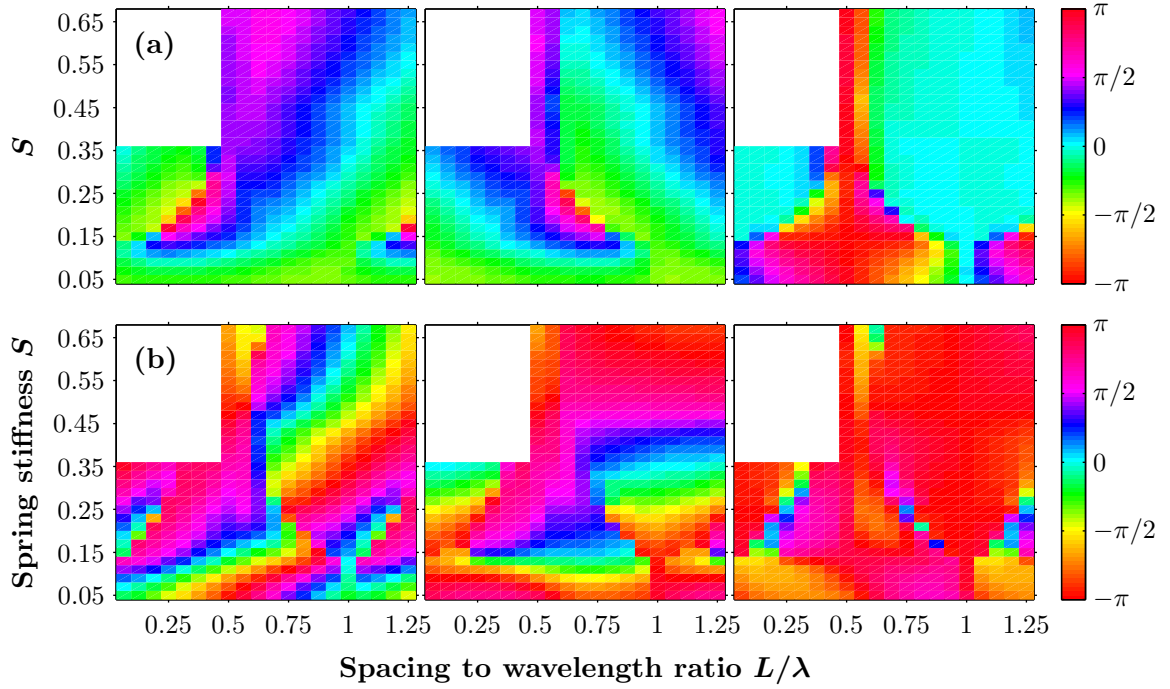


Figure 5.8: Phases of the Fourier coefficients. Individual phases are measured relative to the local water velocity as in (5.6), while differences use the a fixed reference point. (a) Local phases of the first Fourier coefficients for Device 1 ($\phi_{1,1}^L$, left) and Device 2 ($\phi_{2,1}^L$, middle) and phase difference ($\phi_{1,1} - \phi_{2,1}$, right). (b) Same description as (a) except for the second Fourier coefficients.

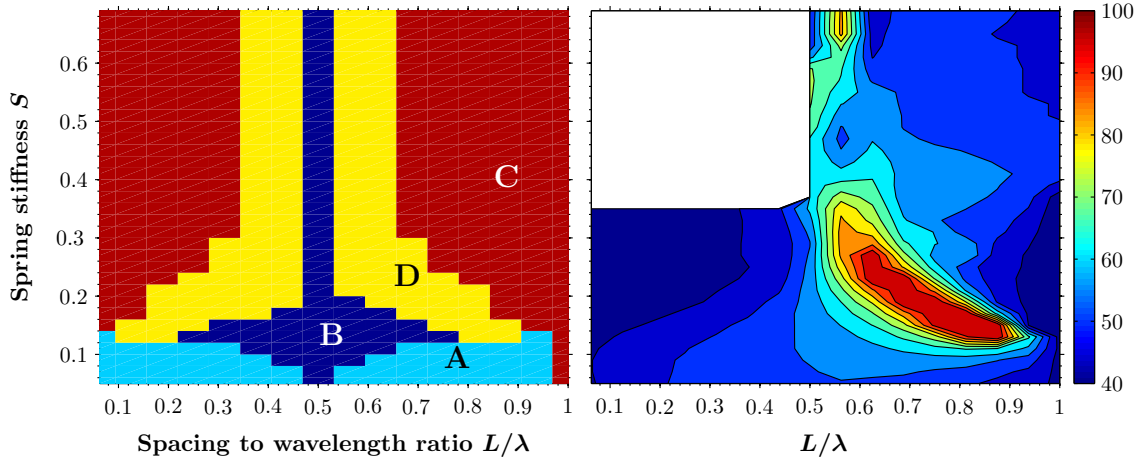


Figure 5.9: Left: Division of the domain into approximate behavioural regimes, as described in the main text. Right: Percentage of cycle for which the mooring line on Device 2 is in tension.

$L = \lambda/2$ case. This can be seen in the phase difference plot on the right of Figure 5.8(a), occurring in the roughly diamond-shaped region, labelled ‘B’ in Figure 5.9. The motion here resembles Figure 5.2(a) but with generally different oscillation amplitudes for the two devices.

Similarly, for spacings within about 30% of a whole number of wavelengths, the devices “lock in” to in-phase motion at a certain S value. This is indicated by the lower boundary of the region labelled ‘C’ in Figure 5.9. High frequency motion components are virtually absent here: see the example of Figure 5.6(c). This is shown up in Figure 5.7(b) by the ‘v’ shapes in which the amplitudes of the f_2 mode are small for both devices. As S is increased from here, oscillation in the f_2 mode becomes significant. Importantly, we now see from Figure 5.8 that the f_1 and f_2 modes remain close to in-phase and anti-phase respectively over the whole of region C. This adds weight to the earlier observation of the qualitative similarities between Figures 5.6(c)-(f) and 5.4(a)-(d), and we may state that behaviour in region C broadly resembles the $L = \lambda$ case.

The final region, labelled ‘D’, can be thought of as transitional between the regions B and C described above. Figure 5.6(b) gives a perfect example where the behaviour could be described as “halfway between” in-phase and anti-phase. The lower part of this region ($S \lesssim 0.35$) is characterised by the motion of one of the devices being highly suppressed and predominantly in the f_2 mode, while the other device oscillates strongly in the f_1 mode. This shows up very clearly in the plots of the Fourier component amplitudes in Figure 5.7. Looking at the phase of the f_1 components in Figure 5.8(a), we see that the small motion amplitude is because the device is being forced to move in opposition to the excitation force. The excitation power in this region for the suppressed device is in fact *negative* at some data points; the device is being driven by the linkage line (refer to Figures 5.1(a) and (d)). The right-hand plot in Figure 5.9 shows another characteristic of the behaviour in region D: the suppressed device is pulled closer to the other device so that its mooring line is in tension for a large proportion of each cycle, reaching 100% in many instances, such as in Figure 5.6(b). This behavioural regime gives important results in longer chains, which will be discussed in later sections.

Behaviour towards the upper S limit of the domain shown here, and beyond, has further complexities that we do not attempt to analyse.

Power transfer through the linkage line

We seek here to improve understanding of the influence of the inter-device linkages, especially their role in transferring power. Similarities between the plots of P_{ML} in Figure 5.1(d) and the phase differences of the f_1 mode in Figure 5.8(a) suggest that the phase difference is an important determinant of this power transfer. In particular, the plots hint at a relationship whereby the power transfer from Device 1 to Device 2 is maximised when Device 1 leads Device 2 by $\pi/2$, and *vice versa* for a lag of $\pi/2$.

It can indeed be shown¹³ that if the motions of the two devices are sinusoidal about their starting positions with common frequency ω , amplitudes A_1 and A_2 respectively,

¹³See Appendix A.

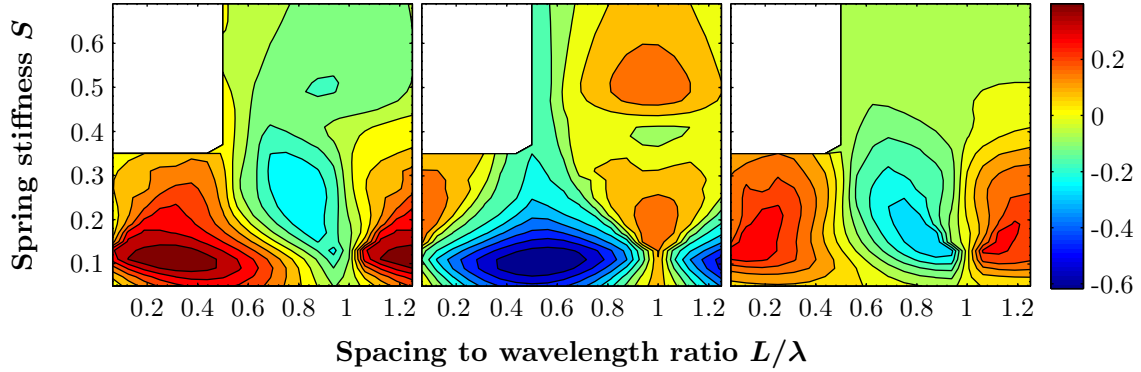


Figure 5.10: Left: Time-average displacement of Device 1 from its initial starting position. Middle: Time-average separation between the two devices minus initial spacing length L . Right: Mean time-average displacement of the two devices - i.e. the time-average displacement of the the centre of mass.

and Device 1 leading Device 2 with a phase difference of ϕ , the (time-averaged) power transfer between Devices 1 and 2 via the linkage line of stiffness S is

$$(P_{ML})_{1,2} = \mp \frac{A_1 A_2 S \omega}{4} \sin \phi. \quad (5.7)$$

This relationship is modified if the devices have a mean separation different to the initial spacing (and natural length of the linkage line), L ; it is straight forward to test this numerically. If the mean separation is greater than L , so that the line is in tension for a greater proportion of time, the peak power transfer is increased and occurs at a smaller phase difference compared with (5.7). The opposite is true if the mean separation is less than L . The middle plot in Figure 5.10 shows the time-average separation of the devices for the simulation series, and we see zones in which the chain is shortened (centred on $L = \lambda/2$) and extended (centred on $L = \lambda$) relative to the rest length, with a reasonably sharp transition in between. Note the correspondence between this plot and the behavioural regions presented in Figure 5.9.

We have so far referred to “power transfer via the linkage line” without giving consideration to the role of the mooring lines. This is valid if the device motions are sinusoidal, since the mooring lines do not contribute power in time-average even when there is a non-zero mean displacement from the starting positions. A simple explanation of why this is true is that, regardless of any offset in the motion centre, the force is symmetric about the turning point while the velocity is antisymmetric. Therefore, whenever the motion is predominantly of a single frequency (see Figure 5.7), it is legitimate to refer to P_{ML} as power transferred through the linkage line.

The preceding analysis gives some level of understanding of what affects P_{ML} when the motion is near-sinusoidal: power transfer is proportional to the oscillation amplitudes, frequency and spring stiffness, is zero for in-phase or anti-phase motions, and is maximised at phase differences $\approx \mp\pi/2$, moderated by how much the chain is shortened

or extended relative to the rest length. This, with reference to Figures 5.7(a), 5.8(a) and 5.10, gives a good qualitative explanation for the shape of the P_{ML} graph, Figure 5.1(d), apart from the diamond-shaped region centred on $L = \lambda$ in which the f_1 and f_2 frequency modes are of comparable importance. In this region, analysis of P_{ML} is much more complex. First, the work done by the mooring lines on the devices may be non-zero. Second, power may be transferred not only between the devices but also between different frequency modes of either device (indeed, this is what gives rise to the high-frequency motion in the first place). We do not attempt a detailed analysis of the power transfer in this multi-frequency regime.

5.2 Longer chains

Having developed some understanding of the interactions between two linked devices, we examine the dynamics of linked chains with more than two devices. These are far more complex and it is not possible to continue with the same rigour or breadth with which we have treated the two-device results. It is necessary to be selective and focus attention on results relevant to maximising power capture.

5.2.1 Special cases

The analysis of the two special cases for two linked devices, presented in Sections 5.1.1 and 5.1.2, is found to extend reasonably well to longer chains.

Half-wavelength spacing

Recall that when the two devices were separated by half of a wavelength, the behaviour resembled that of the single, symmetrically-moored device, but with a modified dependence on S due to the fact that the linkage line is simultaneously stretched from both sides when the devices are moving in anti-phase (refer to Figure 5.3). Figure 5.11 shows the power capture versus spring stiffness for chains of three, four, five and ten devices. The per-device mean power capture curves show only minor variation across the four cases; as the number of devices is increased, the height of the peak diminishes slightly and its position shifts to a lower S value. The latter observation makes sense since all additional devices added to the interior of the chain will be subject to the “effective” spring stiffness $2S$ from either side, whereas the devices at the ends of the chain are reacting against a fixed mooring on one side. Thus as n is increased we would expect the position of the peak to converge to half of the value that gives resonance for the lone device – that is, $\approx 0.15/2 = 0.075$. Meanwhile, the diminished height of the peak is associated with a growing spread in the power capture curves of the individual devices.

While the mean power capture curves do not exhibit much change as the number of devices is increased, there are dramatic changes in how this power capture is distributed amongst the devices. The plots show that up to an S value slightly above where the peak in the mean occurs, the response is reasonably equal along the chain, and inspection of the simulation results shows that the motions are near-sinusoidal with adjacent devices

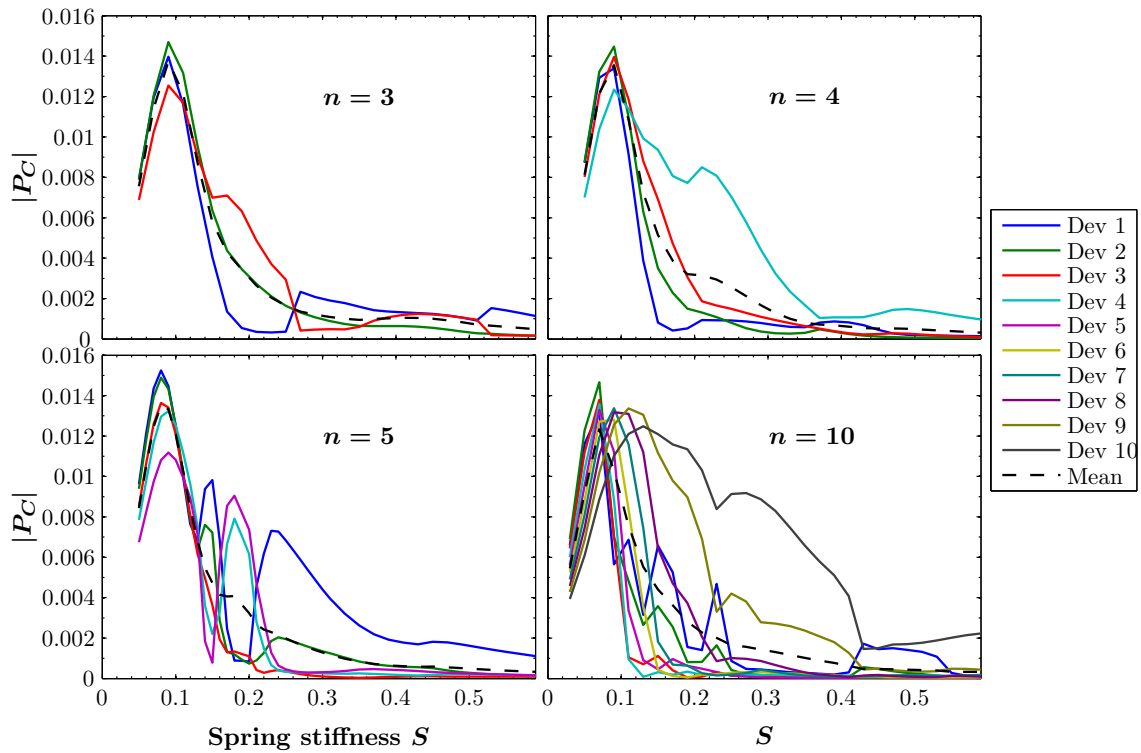


Figure 5.11: Power capture per device versus spring stiffness for chains of three, four, five and ten devices, with half-wavelength spacing and all other parameters given by the reference set (5.1). Note that the $n = 5$ plot has a resolution of 0.01 in S , while for all the other plots the resolution is 0.02.

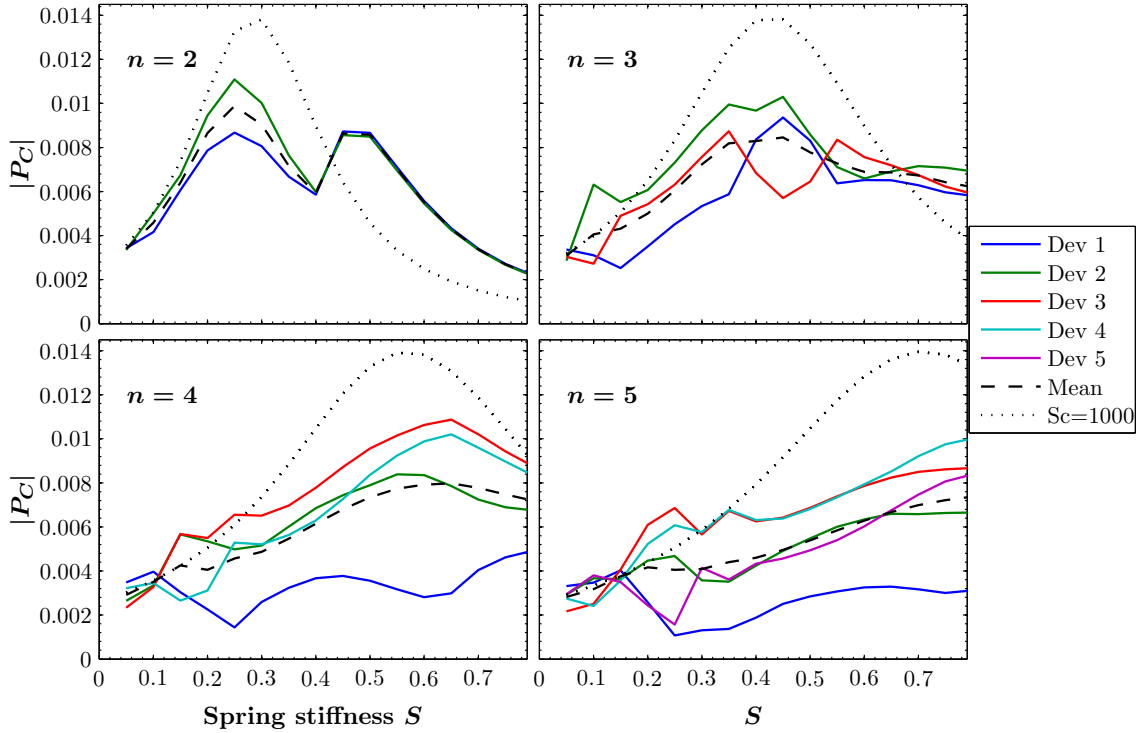


Figure 5.12: Power capture versus spring stiffness for chains of two, three, four and five devices, with full-wavelength spacing and all other parameters given by the reference set (5.1). The black dotted lines show the power capture for any one of the devices when the chain is linked with very rigid springs ($S_L = 1000$) so that it essentially behaves as one body with the combined mass. Note that the $n = 2$ plot is reproduced from Figure 5.5(a).

moving in anti-phase. When the spring stiffness is above a certain threshold, though, the behaviour of the chain is strongly heterogeneous, often with one or two devices capturing much more power than the rest of the chain combined. It is quite interesting that, in spite of this, the overall mean power capture is fairly consistent.

Full-wavelength spacing

In Section 5.1.2 we discussed the results for two linked devices separated by one wavelength in relation to those for a single body with twice the mass, which we modelled by two devices with a very rigid linkage line ($S_L = 1000$). In Figure 5.12, similar results are presented for chains of three, four and five devices, along with the repeated two-device results for comparison.

First, note that the results for the rigidly-linked chains show no change in the maximum power capture per device, with the peak occurring at an S value linearly proportional to the number of devices (and hence the total mass). The results from the

standard series with $S_L = S_M$ show similar qualitative development. The maximum value of per-device mean power capture is always much less than that of the lone device, and this looks as if it may show a decreasing trend with increasing n , although it is difficult to say with any certainty based on this limited data set. The per-device means (black dashed lines) agree very closely with the lone device up to a certain S value where they suddenly diverge; interestingly, the S value at which this occurs appears to increase with increasing n . Finally, there looks to be a general trend to increased spread in the response of the individual devices as the number in the chain is increased.

5.2.2 Illustration: three-device chain

In this section we explore the dynamics of a three-device chain as an example. We begin by looking at the power contributions over the L and S domain, presented in Figure 5.13. This can be compared with the two-device results in Figure 5.1 (but note that L range here only extends to $17\lambda/16$, compared to $5\lambda/4$ in the two-device plots).

The obvious difference to the two-device chain is that with an odd number of devices, there is one in the centre. The approximate symmetry of the chain response about $L = \lambda/2$ persists, with the pattern for the central device (Device 2) roughly symmetric and those for the outside devices (Devices 1 and 3) mirroring one another. Superficially, results for the outside devices are not too far from what was observed for the two-device chain, although there are important departures.

Figure 5.14 shows the per-device mean excitation power, power capture and power dissipated by drag. Like for the two-device chain, these three power terms show strong qualitative similarities. All have their maximum values at the primary peak centred on $L = \lambda/2$, associated with sinusoidal oscillations with adjacent devices in anti-phase. Centred on $L = \lambda$ is the feature associated with the chain oscillating roughly akin to one combined body. Note that this is shifted to a higher S value compared with the two-device chain, as explained in the previous section.

5.2.3 Secondary interactions

In addition to the features in Figure 5.14 described in the previous paragraph, which can be related to those seen for the two-device chain, there is something new: two smaller peaks centred on $(L/\lambda, S) \approx (0.25, 0.17)$ and $(0.75, 0.17)$. At these spacings, the two outer devices are separated by $\lambda/2$ or $3\lambda/2$; this suggests a hypothesis that these “secondary peaks” are associated with anti-phase motion between Devices 1 and 3. The plots of per-device excitation power in Figure 5.13(a) provide further evidence to this claim – observe that for Device 1, the dominant, diagonal feature in the range $\lambda/2 < L < \lambda$ is “shadowed” by one of a similar shape but much smaller magnitude in the range $0 < L < \lambda/2$. Note that this feature does not manifest in the power capture plot, because it happens to coincide very closely with a region of negative P_{ML} ; the extra power absorbed by Device 1 is largely transferred down the chain, providing a visible boost to the power capture of Device 3.

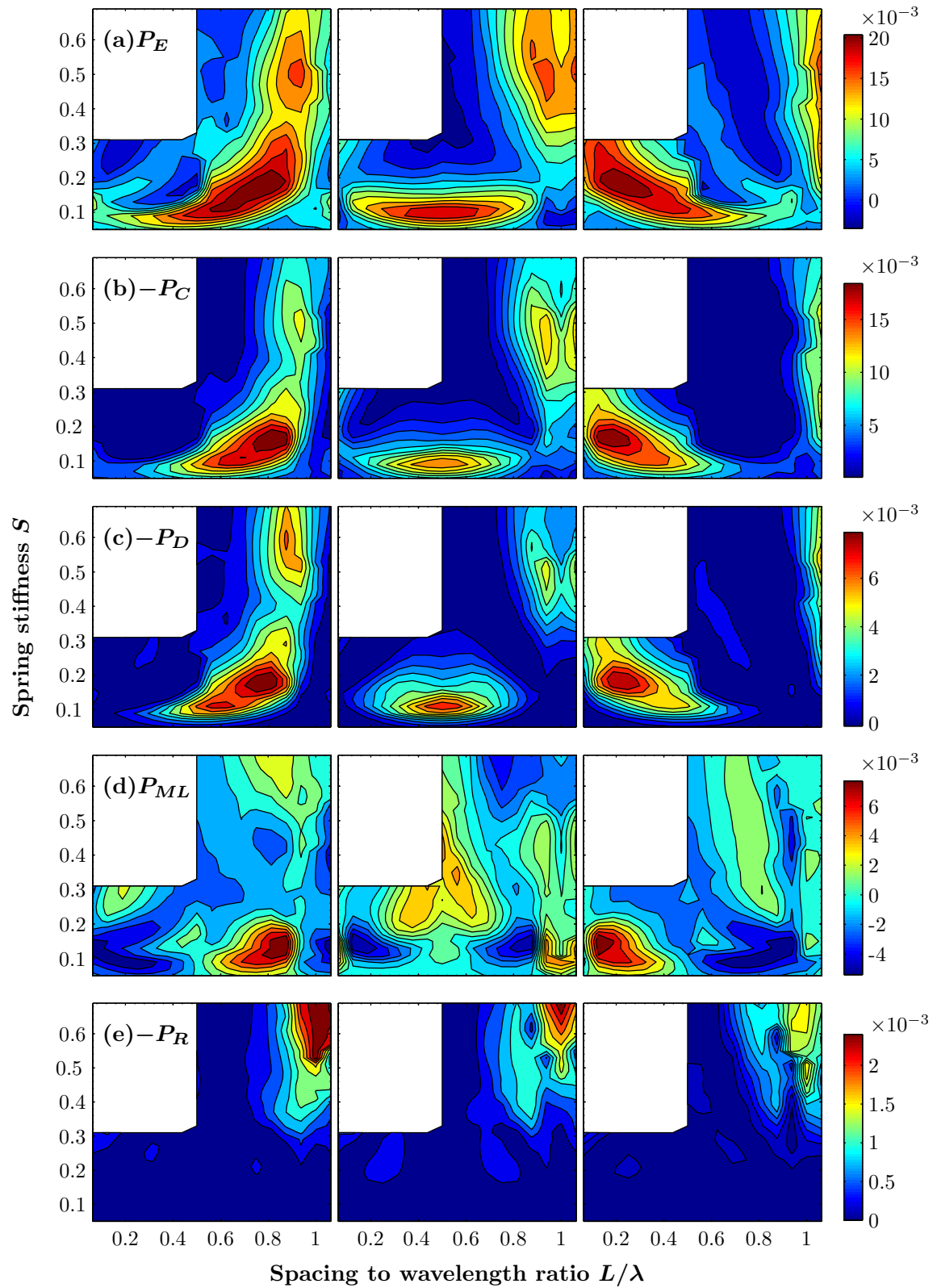


Figure 5.13: Power contributions for Devices 1-3 (left-right) for the three-device chain with the reference parameter set. Note that the different power contributions are on different colour scales, and that no data exist for $S > 0.31, L < \lambda/2$.

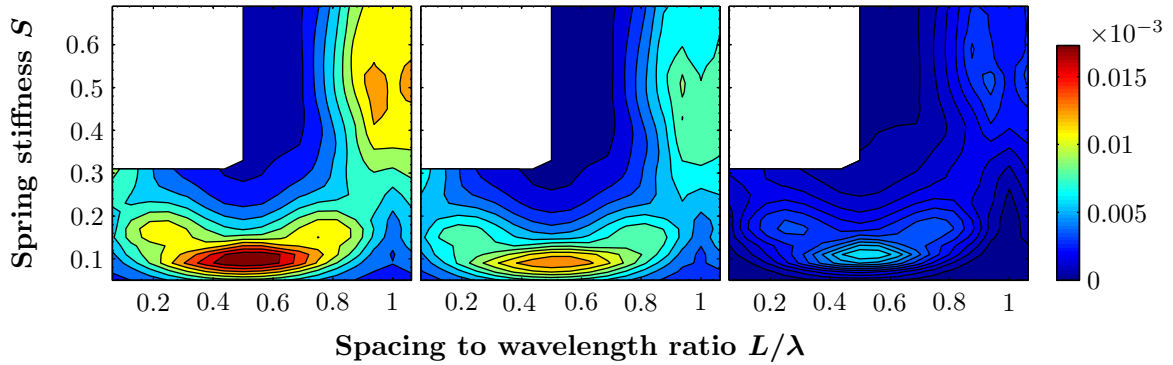


Figure 5.14: Per-device mean power contributions for the three-device chain with the reference parameter set. Left: excitation power; middle: power capture, right: power dissipated through drag.

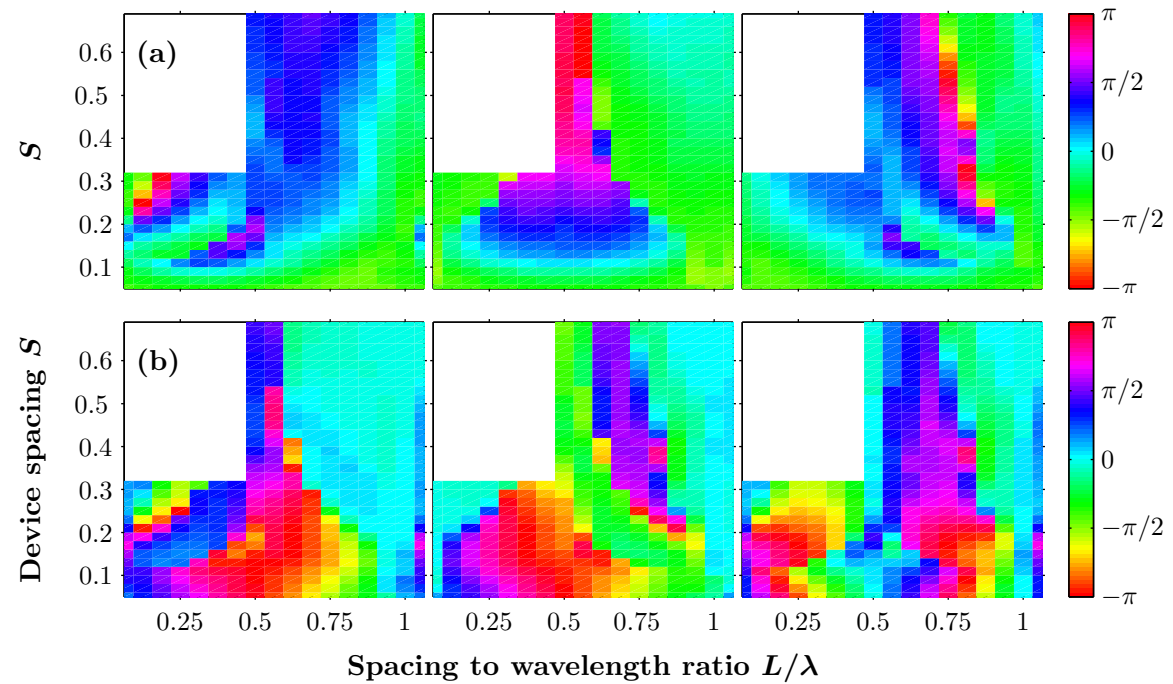


Figure 5.15: (a) Local phases (relative to local fluid velocity) of the f_1 Fourier components for Devices 1-3 (left-right). (b) Phase differences of the f_1 components – left: $\phi_{1,1} - \phi_{2,1}$, middle: $\phi_{2,1} - \phi_{3,1}$, right: $\phi_{1,1} - \phi_{3,1}$.

Figure 5.15 shows local phases and phase differences of the f_1 frequency modes for the three devices. As we may have guessed, the “shadow” feature around $\approx (0.25, 0.17)$ in P_E for Device 1 coincides with a region in which the device’s displacement is approximately in phase with the local water velocity. Importantly, comparing to Figure 5.8, this occurs where in the two-device chain, Device 1 would be close to $\pi/2$ out of phase with the local water velocity and absorbing very little power. Looking at the phase difference plots, the secondary peaks in the mean power capture do coincide exactly with a phase difference of π between the f_1 components of Devices 1 and 3 (see the red regions in far right plot), further supporting the hypothesis described above.

The current analysis is simplistic, however, since the situation is complicated by the presence of the middle device, and we have not yet examined the importance of higher frequency motion components. Figure 5.16 shows the steady-state motion and power contributions for $(L/\lambda, S) \approx (0.25, 0.17)$, corresponding to one of the secondary power capture peaks. There are several noteworthy features. Firstly, the motion of Device 3 is close to sinusoidal, while the presence of high-frequency components is visible in the motions of Device 1 and, especially, Device 2. Secondly, the maxima in the Device 3 displacement line up very closely with the displacement minima in both Devices 1 and 2. Thirdly, Device 1 is pulled to the right so that its mooring is permanently in tension, and Device 2 is also pulled to the right with the Device 1-2 linkage in tension at all times except for an instant when Device 2 reaches its left-most position. These observations bear resemblance to the behaviour of the two-device chain in the region of the domain we labelled ‘D’, which was discussed earlier in relation to Figure 5.9.

The percentages of the cycle for which the Device 1 mooring and the Device 1-2 linkage are in tension are presented in Figure 5.17. The Device 1 mooring is permanently in tension over nearly all of $(0 < L < \lambda/2, 0.1 < S < 0.3)$, coincident with the region of low power capture by Device 1. The Device 1-2 linkage remaining in tension for nearly the entire cycle is a rarer case. The example presented in Figure 5.16 sits at the centre of a feature at $(0.25, 0.17)$ in the right-hand plot of Figure 5.17, which coincides with – and appears to be related to – the “shadow” feature in the excitation power of Device 1 and the secondary peak in the mean power capture. This seems consistent with the earlier hypothesis: when the Device 1-2 linkage is (near-) permanently in tension, Device 2 can act most effectively as a conduit for interactions between Devices 1 and 3. A variation on this idea is that Devices 1 and 2 could be seen as behaving somewhat similarly to one combined body, moving counter to Device 3. This interpretation seems appropriate at least for the important part of the cycle in which the Device 2-3 linkage is active.

As the number of devices is increased, the dynamics grow in complexity and there is further evidence of interactions between non-adjacent devices. Initially, for each additional device, a new secondary peak is observed in the plot of mean excitation power per device. This is shown for the four- and five-device chains in Figure 5.18 (left column)¹⁴; for four devices there appear to be peaks centred on $\approx (0.25, 0.13)$ and $(0.16, 0.23)$, and for five devices, $\approx (0.25, 0.13)$, $(0.19, 0.18)$ and $(0.13, 0.30)$. The peaks occur at spacing

¹⁴Note that the five-device series was carried out with twice the resolution in L and S of the other series.

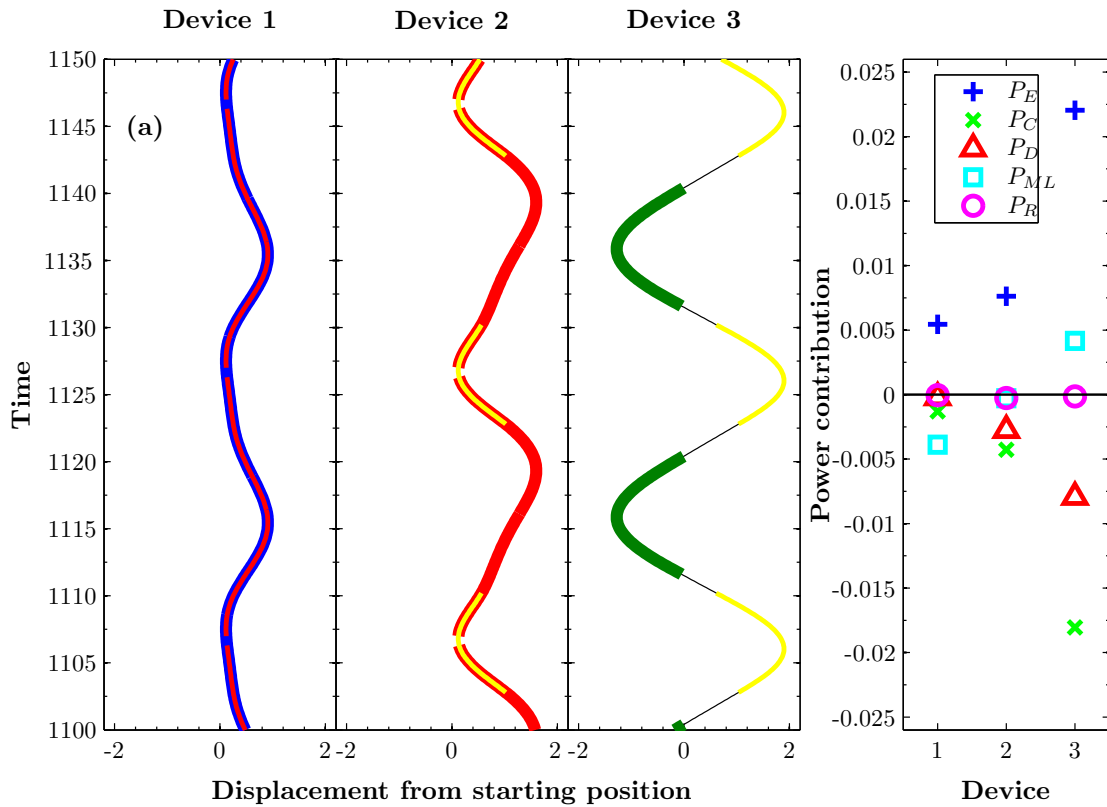


Figure 5.16: Steady-state motion and power contributions for the three-device chain with $L = \lambda/4$, $S = 0.17$, and all other parameters as in the reference set. The coloured line segments show when the mooring and linkage lines are in tension, similarly to the earlier figures for two devices. The blue and green segments represent the mooring lines on Devices 1 and 3 respectively. The red and yellow segments represent the Device 1-2 and 2-3 linkage lines respectively. When the black line is visible, none of the lines on the device are in tension.

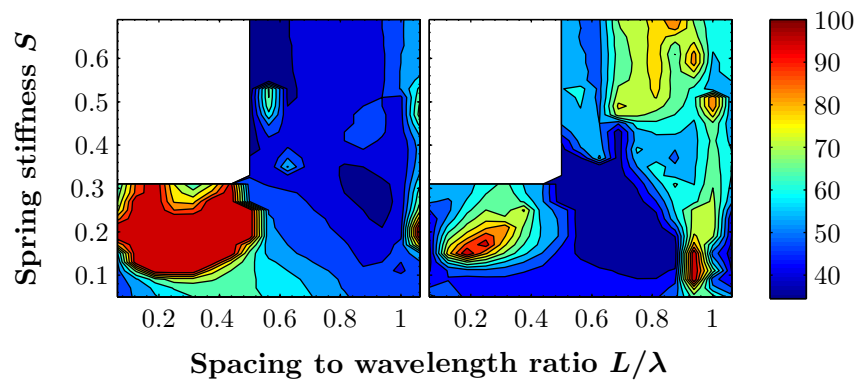


Figure 5.17: Percentage of the cycle in tension for Device 1 mooring (left) and Device 1-2 linkage (right) for the three-device chain with the reference parameter set.

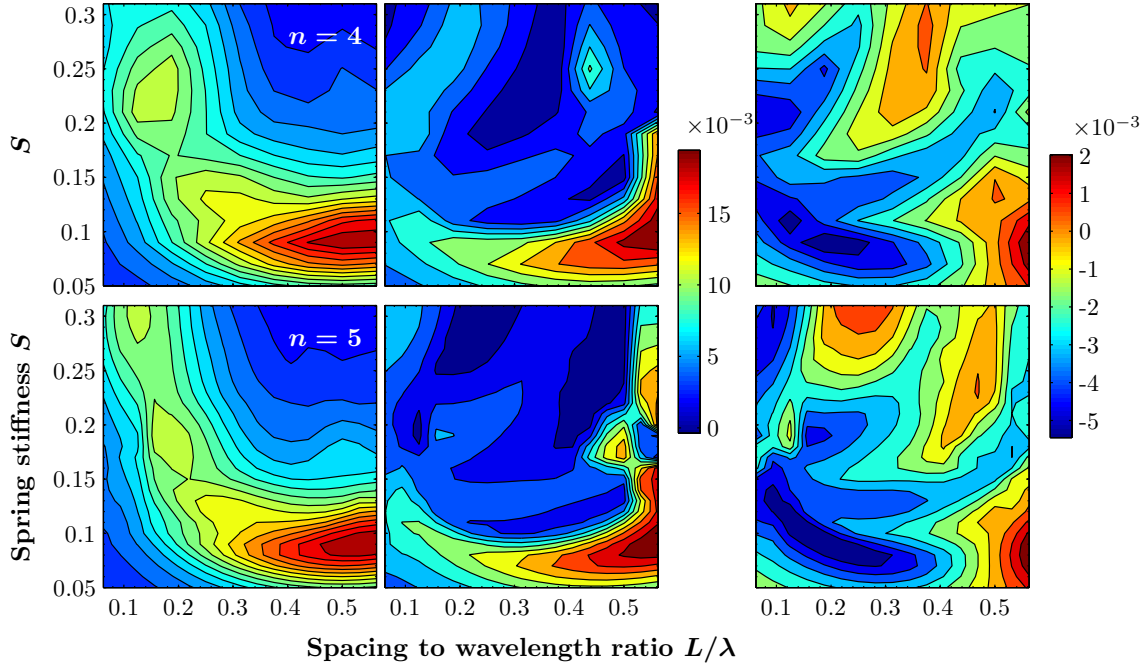


Figure 5.18: Results for four-device and five-device chains with the reference parameter set. Left column: mean excitation power per device; middle column: Device 1 excitation power; right column: Device 1 power transfer from moorings and linkages. Note that the right column is on a different colour scale to the other columns, as shown.

values roughly corresponding to when different pairs of devices in the chain are separated by half of a wavelength, in accordance with the hypothesis presented above. This explains the appearance of successive peaks as additional devices are added to the chain.

Figure 5.19 shows the steady-state motion for the four-device chain at the data points closest to the two secondary peaks specified in the previous paragraph. At the first one where $L = \lambda/4$, we see that the Device 1 mooring and Device 1-2 linkage are permanently in tension, and Devices 1 and 3 are moving in anti-phase. Note how this relates to the three-device chain shown in Figure 5.16. Near the second peak, where $L = 3\lambda/16$, the motions are more non-sinusoidal but we can say that Devices 1 and 4 are moving roughly opposite to one another, particularly at the outer extrema of their motions. Here there are moments when the mooring and linkage lines on Devices 1 and 2 fall slack but, importantly, for almost all of the time interval in which Device 4 is being acted on by its linkage line, all the other linkage lines are also in tension. Figure 5.20 shows very similar dynamics to this in the five-device chain, corresponding to the peak at $(0.19, 0.18)$. Observe that the relationship this bears to the four-device chain in Figure 5.19(b) is very similar to the relationship between the four-device chain in Figures 5.19(a) and the three-device chain in 5.16, indicative of a pattern.

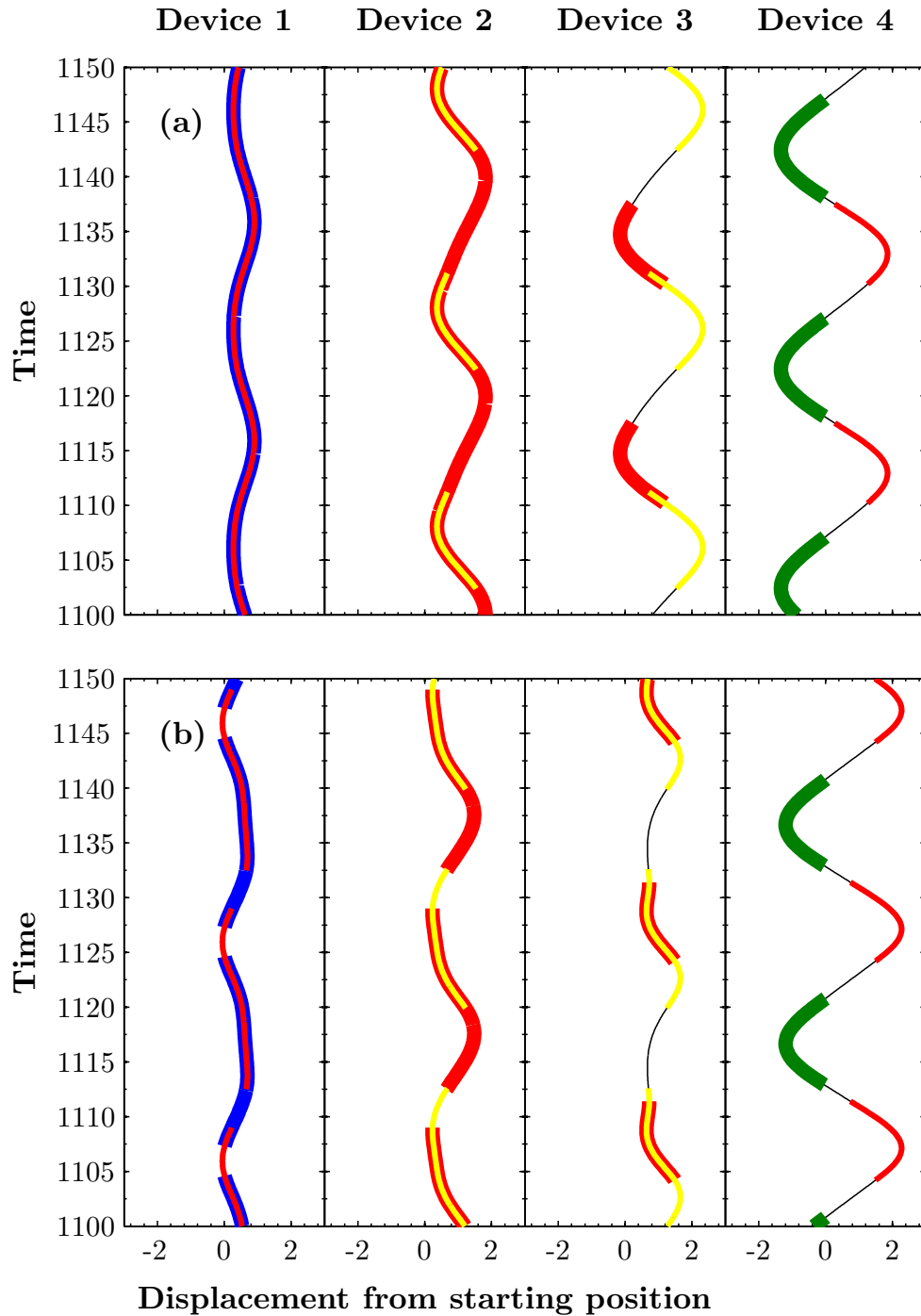


Figure 5.19: Steady-state motion for the four-device chain with (a) $L = \lambda/4, S = 0.13$, (b) $L = 3\lambda/16, S = 0.23$. All other parameters as in the reference set. The coloured segments show when the mooring and linkage lines are in tension, similarly to previous figures: the blue and green segments represent the mooring lines; and the red and yellow segments represent alternate linkage lines, i.e. linkage 1-2: red; linkage 2-3: yellow; linkage 3-4: red.

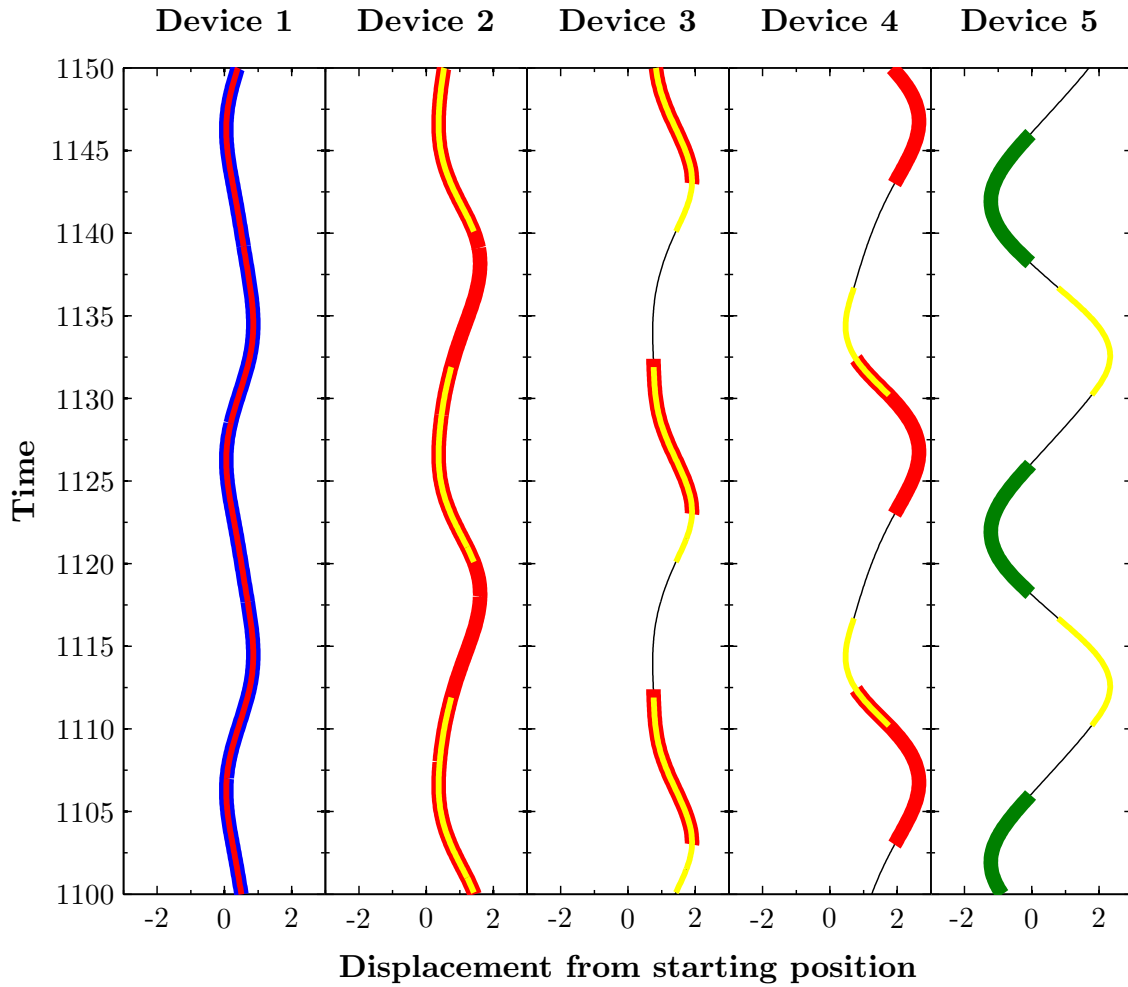


Figure 5.20: Steady-state motion for the five-device chain with $L = 3\lambda/16$, $S = 0.19$, and all other parameters as in the reference set. The coloured segments show when the mooring and linkage lines are in tension, as explained in the caption of Figure 5.19.

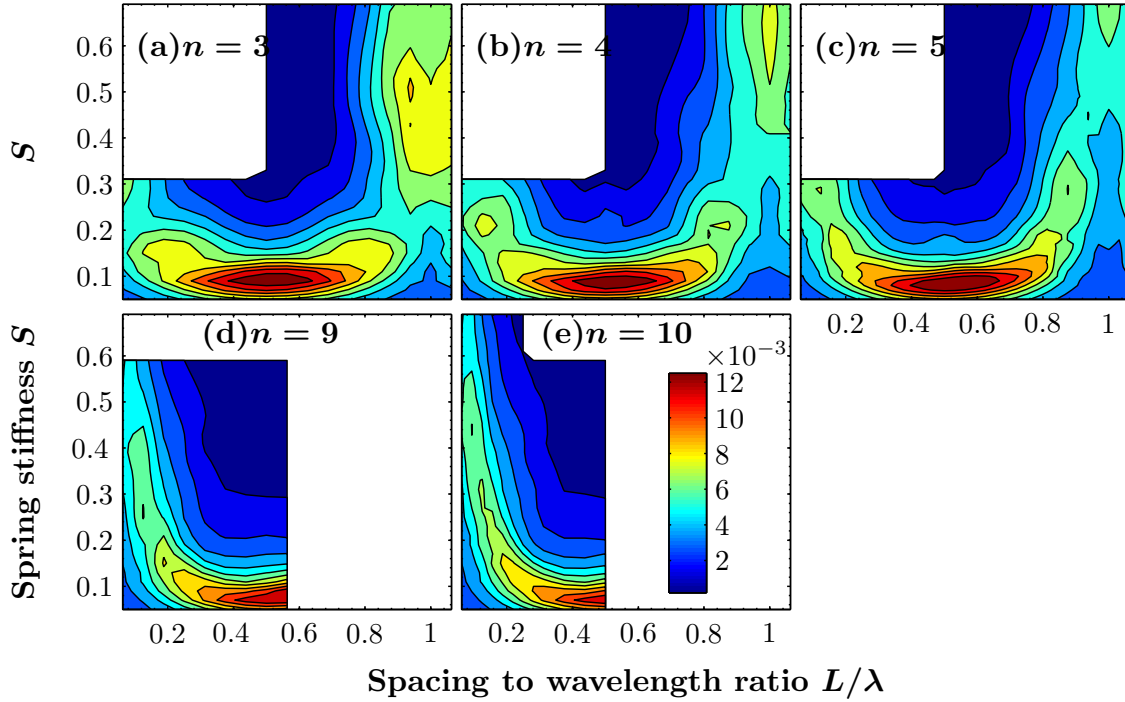


Figure 5.21: Mean power capture per device for chains of (a) three, (b) four, (c) five, (d) nine and (e) ten devices. All plots are on the colour scale shown.

Summary

The preceding examples have illustrated a pattern that explains the development of the per-device mean excitation power, and hence the mean power capture, as functions of the variables L and S . We have provided evidence to show that the peaks seen in the mean power plots are associated with anti-phase interactions between pairs of devices in the chain. Interactions between non-adjacent devices are enabled when all of the linkage lines in between them are in tension throughout the important time interval when the devices undergo their outer extrema.

Mean power capture plots for chains of three, four, five, nine and ten devices are presented in Figure 5.21. Two key points are evident: firstly, the higher order peaks¹⁵ are of diminishing height with the increasing number of devices in between; secondly, the peaks flatten out as the number of devices is increased, with the plot tending towards a smooth horseshoe-like shape. This has relevance for selecting chain parameters to optimise performance in a continuous wave spectrum.

¹⁵That is, those corresponding to a greater number of devices between the two undergoing the anti-phase interaction.

5.2.4 Power transfer through linkages and peak power capture for individual devices

Like we concluded for the two-device chain in Section 5.1, it appears impossible for the per-device mean power capture to exceed the maximum value achieved by the lone device at this same wave period, for a chain of any number of devices. In fact, in the results shown in Figure 5.21, the peak power capture diminishes for larger n – although we caution that this could be due to limited resolution in the L - S domain, as the centre peak gradually shifts upwards from $L = \lambda/2$ with increasing asymmetry as n is increased. Regardless, there are certainly no signs of improvement in longer chains. The question of whether a linked chain can outperform the lone device across a spectrum of wave periods has not yet been addressed, however – this is tackled later.

It *is* possible, however, for particular devices in the chain to achieve much enhanced power capture (compared with the lone device) at the expense of the others. We saw in Section 5.1 that for the two-device chain, the highest power capture was reached by Device 1: 0.0171 compared with 0.0139 for the lone device, or a 23% enhancement. Further improvements are found to be possible in longer chains, with the best performances recorded by the devices at the ends of the chain. For the remainder of this section, we will focus on the power performance of the device at the down-wave end of the chain (e.g. Device 5 for the five-device chain), which we will refer to as the “end device”. It may seem strange to focus on one device’s performance at the expense of the others in the chain; we will discuss the potential importance and application of this idea (introducing a concept we call “dummy devices”) further in Section 5.6.2 and in Chapter 7. While results suggest that the first device might generally achieve a slightly higher maximum power capture than the end device¹⁶, this occurs at a much higher spacing value for the former than for the latter (see for example Figure 5.13(b)), and chains with smaller spacings would almost certainly be more practical. We will also describe in Section 5.3 another reason why the end device is the most favourable.

As was discussed in Section 5.1, the peak power capture that a device attains, and the parameter values at which this occurs, depend predominantly on a compromise between the device absorbing more excitation power itself and receiving more power from the other devices via the linkage lines¹⁷. This statement is perhaps misleadingly simple though, since these two power contributions are not independent of one another; both have two-way cause-and-effect relationships with the steady-state motion of the device. For a *fixed* velocity amplitude, P_E depends on the phase between the device velocity and the local fluid acceleration, while P_{ML} depends on the relative motion of the adjacent linked device(s). However, these power terms are also a feedback into the amplitude and phase of the device velocity; thus, there is interplay between P_E and P_{ML} . Of course, similar relationships apply for P_D , the power dissipated by drag.

In spite of the complexities, the salient point is that the power absorbed directly from the wave field and the power received via the linkages will in general be maximised

¹⁶This may also be due to limited resolution in the parameter domain.

¹⁷Drag losses also play a part. Radiated power is always found to be negligible whenever power capture is high.

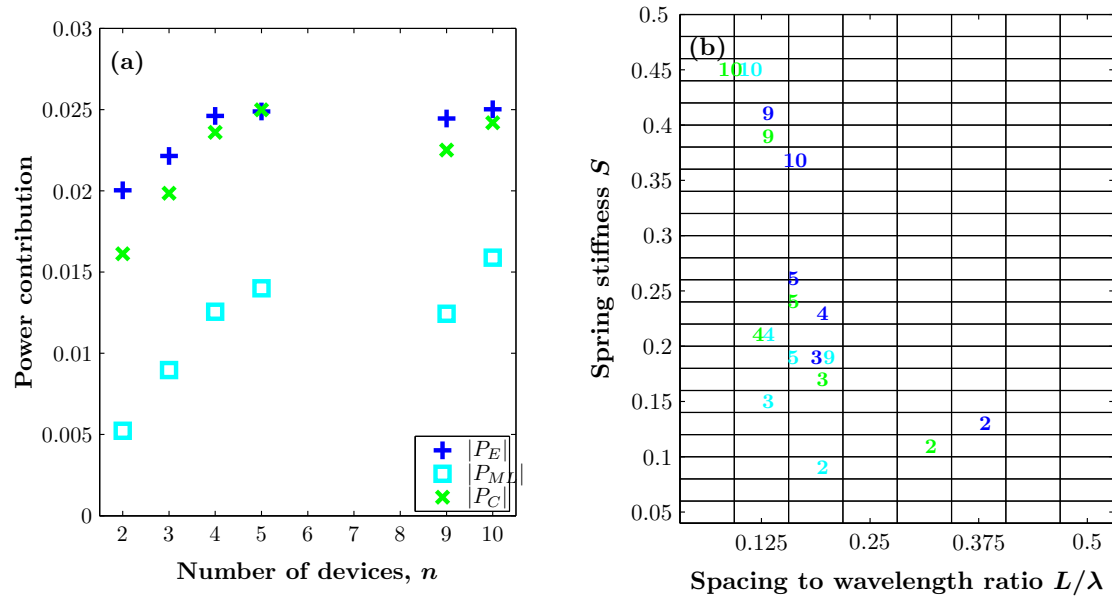


Figure 5.22: (a) The maximum excitation power, power transfer through linkages and moorings, and power capture attained by the end device, versus the number of devices in the chain. To be clear, the maxima in the different power contributions do not in general occur at the same parameter values. (b) The S and L values corresponding to the maxima plotted in (a). For example, the green ‘3’ has grid coordinates corresponding to the maximum power capture for the three-device chain. The grid shown applies for the $n = 3, 4, 5$ and 9 simulation series, while the $n = 5$ and 10 series were carried out with twice the resolution, hence why several of the data points for these n values lie on the grid lines.

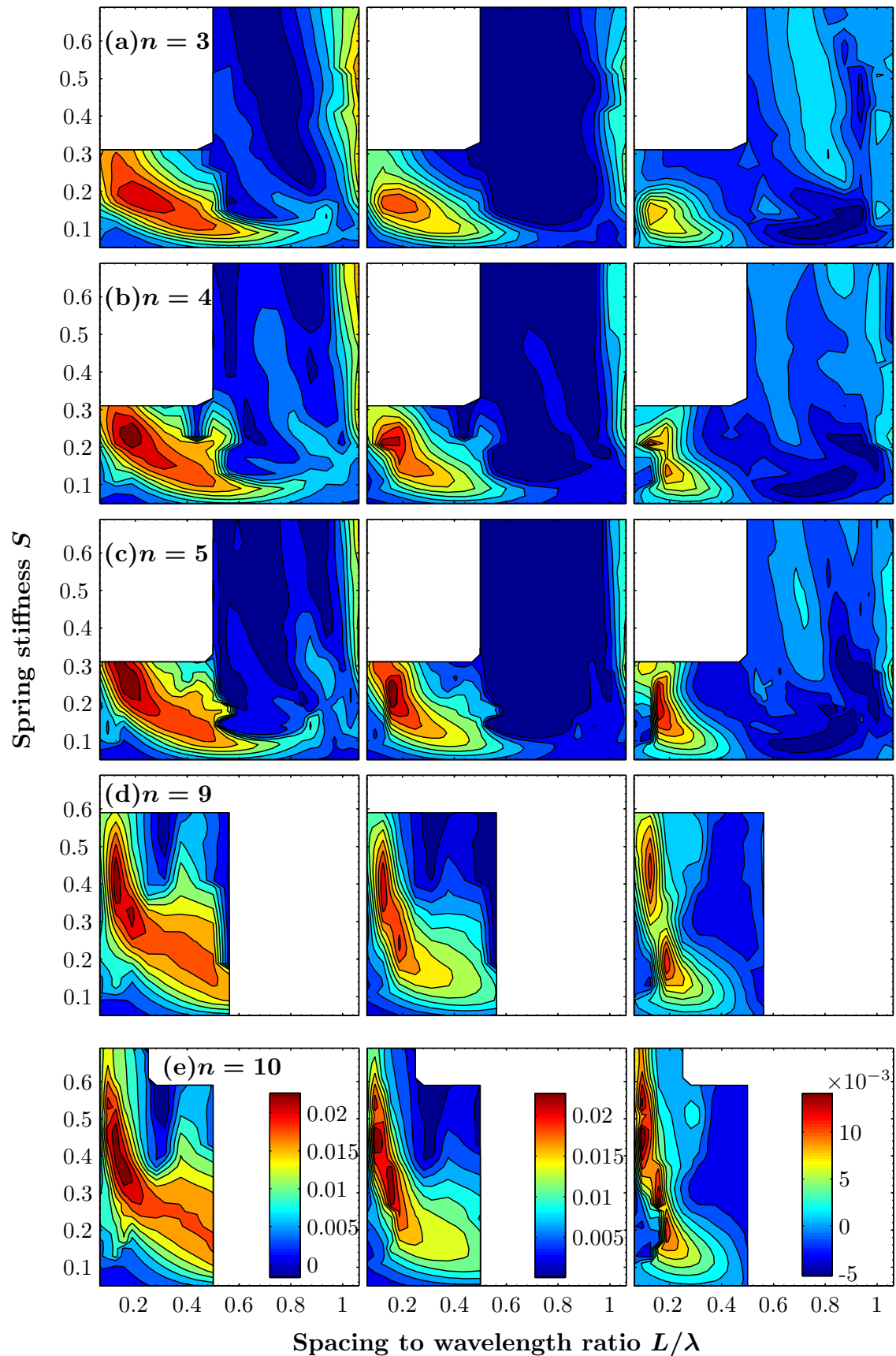


Figure 5.23: Power contributions for the end device of chains of (a) three, (b) four, (c) five, (d) nine and (e) ten devices. Left column: excitation power, P_E . Middle column: power capture, P_C . Right column: power transfer from linkage and mooring lines, P_{ML} . The columns are each on separate colour scales, given in the bottom row.

at different parameter values, and the maximum power capture (which depends only on velocity amplitude) is determined by these complementary factors. In Figure 5.22(a), we present the maximum values found for excitation power, power transfer through linkages, and power capture, for the end device in chains with different n . The values of L and S at which these maximum values occur are shown in subfigure (b). It may be possible for the chain geometry to be set up such that P_E and P_{ML} are simultaneously maximised but, as these plots demonstrate, we do not witness any examples of this in our investigations. Figures 5.24 and 5.25 show the power contributions for *all* devices in the chain at those (L, S) combinations giving the best power capture in the end device.

We emphasise that the maximum values obtained for the power contributions depend to an extent on the parameter grid used, especially in the presence of features that are narrow with respect to the grid resolution. Full contour plots of P_E , P_C and P_{ML} versus L and S for all the n values studied except $n = 2$ are given in Figure 5.23. Note that, as stated in the caption of Figure 5.22, the five- and ten-device series were carried out with twice the resolution of the others – that is $\Delta L = \lambda/32$ and $\Delta S = 0.01$. The plots show that there certainly are narrow features present, even in relation to this higher resolution, and particularly for P_{ML} . As an indication, when the $n = 5$ case is assessed on the more sparse grid, the highest values of P_{ML} and P_C drop to 0.012 at $(3\lambda/16, 0.17)$ and 0.022 at $(3\lambda/16, 0.19)$ respectively, while the maximum value noted for P_E is unaffected to two decimal places. The values plotted in Figure 5.22 should thus be considered as having error bars on the order of ± 0.002 , at least. The narrowness of the features looks to intensify for higher n ; when P_{ML} is plotted for the $n = 10$ case with the same resolution as for $n = 9$, the pronounced differences between the two plots disappear and they are hard to distinguish. This heightened sensitivity to the spacing and spring stiffness is not a beneficial trait from a practical view-point.

The coarse resolution and reasonably limited data set make it hard to draw definitive or precise conclusions in relation to Figure 5.22. However, we can be quite confident that the initial increasing trend in all of the power contributions is robust. For a start, we obtain a very similar result if we assess the highest values observed for Device 1 of the chains, despite the growing asymmetry in the chain dynamics about $L = \lambda/2$. Furthermore, the result makes good sense, as follows. Across all cases examined, there is little variation in the minimum P_{ML} value recorded for each device: all fall in the range -0.055 to -0.045 . Because the power contribution from the linkages must sum to give a net value of zero for the chain, the maximum possible P_{ML} for any one device is thus $\approx 0.05 \times n$, which would be attained if all other devices were to have their minimum values at the same (L, S) combination. This is indeed close to what we observe for the initial trend for the end device in Figure 5.22. An illustration of what is happening can be seen in Figure 5.24 (although these show the power contributions when $|P_C|$ is maximised, rather than P_{ML}) – power is transferred down the chain to the end device, with each subsequent linkage line transferring more than the previous. For example, for the four-device chain shown in subfigure (c), the first linkage line is transferring ≈ 0.005 from Device 1 to Device 2. The total P_{ML} for Device 2 is also ≈ -0.005 , so the second linkage line must be transferring ≈ 0.01 from Device 2 to Device 3.

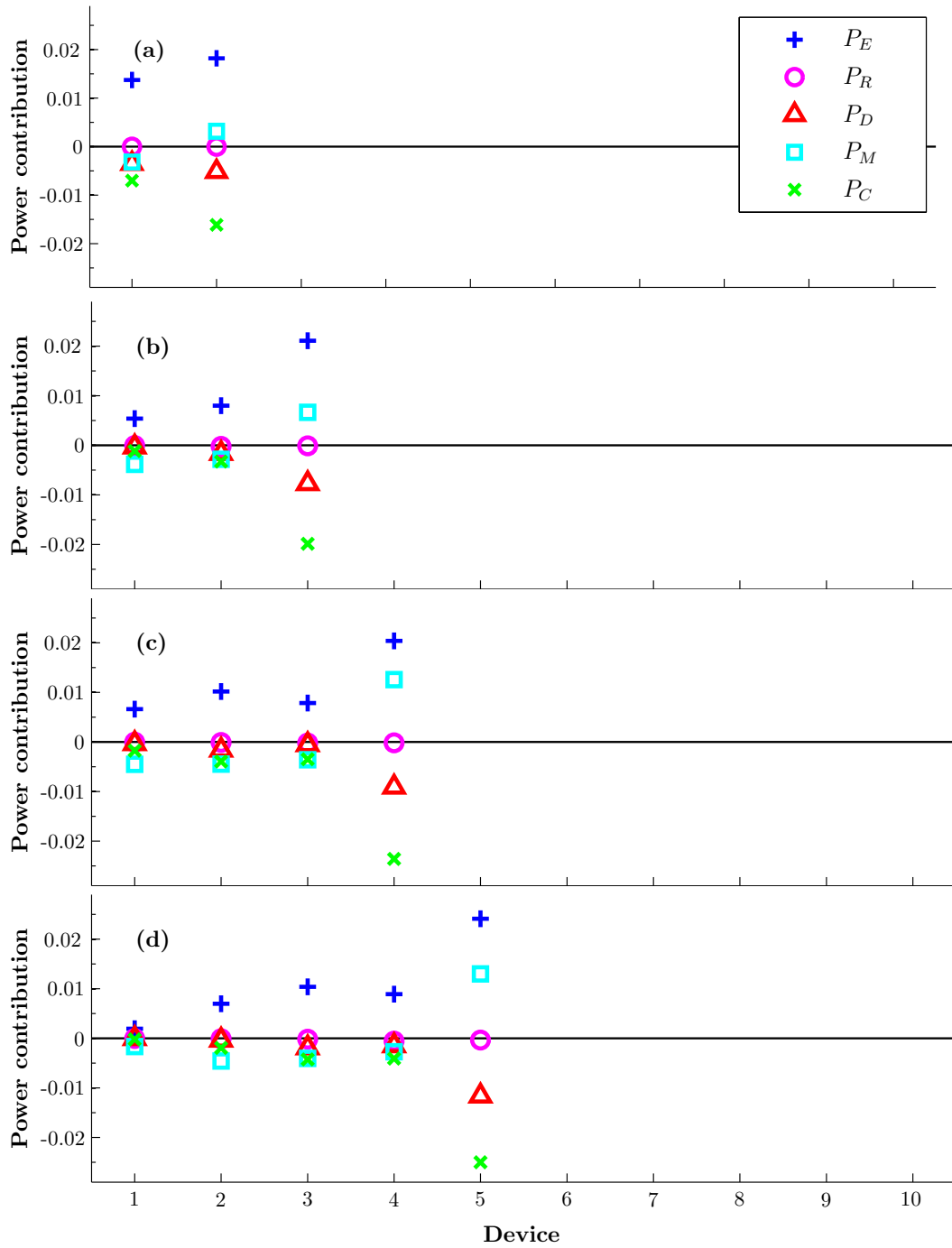


Figure 5.24: Power contributions for the whole chain at the L and S combination with the highest power capture attained by the end device, for $n = 2$ to 5. The values of $(L/\lambda, S)$ are: $(5/16, 0.11)$ for $n = 2$; $(3/16, 0.17)$ for $n = 3$; $(1/8, 0.21)$ for $n = 4$; and $(5/32, 0.24)$ for $n = 5$.

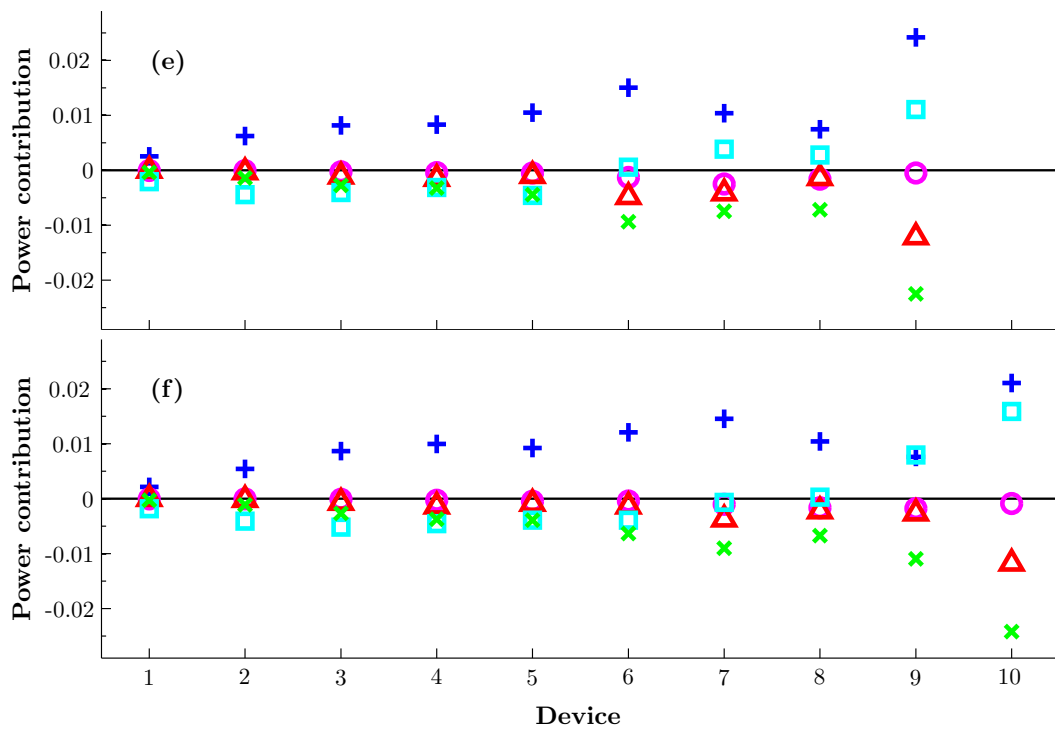


Figure 5.25: Power contributions for the whole chain at the L and S combination with the highest power capture attained by the end device, for $n = 9$ and 10 . The legend is the same as for Figure 5.24. The values of $(L/\lambda, S)$ are: $(1/8, 0.39)$ for $n = 9$; $(3/32, 0.45)$ for $n = 10$.

The data suggest that this trend does not continue, however, and that there is little gain to be had in extending the number of devices beyond $n \approx 5$. In the example in Figure 5.25(f), which has the highest observed values of P_{ML} and P_C for the end device when $n = 10$, a significant share of the power transferred down the chain ends up boosting the second-to-last device (Device 9). Furthermore, while the end device does still attain a slightly higher P_{ML} here than the maximum for $n = 5$, this does not translate to a higher power capture due to worse alignment with the maximum excitation power. It is possible, in light of the narrow features shown up in Figure 5.23, that a significantly better performance could be found with a higher resolution sweep of the parameter space, and even that the increasing trend seen for small n might continue. Even if this were the case though, the sensitivity to perturbation might make it difficult to realise practically and, as will become clear in the following section, the width of the features is potentially of more importance than their height when considering device performance across a range of wave periods.

Overall, we do not arrive at an entirely satisfactory explanation for the shape of the end device P_{ML} plots in Figure 5.23. However, we suspect that secondary interactions are one important determinant. It was shown earlier that, for $L < \lambda/2$, these are associated with the early devices in the chain experiencing enhanced power absorption but negative P_{ML} , meaning the extra power absorbed is largely transferred down the chain (see particularly Figure 5.18). We also note visible correlation between secondary peaks in the per-device mean power capture (Figure 5.21) and features in the end device P_{ML} plots.

Summary

The end device in a linked chain can achieve significant gains in power capture relative to a lone device for the same incident wave field. Results presented in this section suggest that the possible improvement grows as the number of devices is increased from two to about five, but further gains are likely to be small beyond this point. Due to the small body of data available, though, we do cannot rule out the possibility of significantly higher power capture in longer chains, especially at large S and small L where the behaviour becomes increasingly nonlinear. However, if further gains are possible, they would require very accurate tuning of S and L to the incident wavelength, meaning the system would be sensitive to perturbations and the gains may not be practically achievable. From an applied viewpoint, considering additional costs associated with longer chains, the optimum chain length would almost certainly be reached below $n = 10$.

One other comment to make is that the investigation here used a fixed value of PTO resistance $R = 0.15$ for all devices in the chain. While this is the optimum value for a lone device for this wave period, the higher motion amplitudes achieved by the end device mean that the R value to optimise *its* power capture is almost certainly higher. Thus, the power capture gains presented here could surely be improved upon, but the extent is unknown.

5.2.5 Novel behavioural regimes

As a final comment on the dynamics of the chain at the reference wave period $T = 20$, we report briefly on some observations of the system locking into novel behavioural regimes, which lead to sharp features in the power contribution plots. An example for the ten-device chain is shown in Figure 5.26. Here adjacent devices look to “pair up”¹⁸ so that the chain essentially behaves as if it were made up of five devices of twice the mass. The power contributions show the even-numbered devices absorbing the majority of the power while the odd-numbered devices are largely being driven by the linkage lines. If the power contributions are averaged for each “pair”, Figure 5.27 shows that they compare very closely with the power contributions for the five-device chain with almost the same spacing and half the spring stiffness. The type of collective behaviour on display here is what gives rise to the sharp “gaps” observed around $S \approx 0.15$, $L \lesssim \lambda/8$ in the P_{ML} plots for the end device of chains of $n \geq 4$ (see Figure 5.23). In this region, the second-to-last device is the one receiving the largest power transfer via the linkages. As S is increased, a “role swap” between the paired devices takes place quite suddenly.

5.3 Results for different wave periods

We conducted an investigation to test how results for other values of wave period compare with the $T = 20$ case. Here we present results from simulations of a three-device chain for wave periods $T = 15, 20, 25$ and 30 . Other simulations run with four- and five-device chains give results consistent with those presented here. The PTO resistance, wave height and drag coefficient remain fixed at the reference values listed in (5.1).

Based on logical reasoning, one might expect equivalence between results for different wave periods where the ratio of device spacing to wavelength is the same. Similarly, but perhaps less obviously, it is reasonable to expect some degree of equivalence between scenarios with the same ratio of spring stiffness to S_{res} , the resonant spring stiffness for the lone device at the same wave period. For convenience here we define the *spacing ratio*, l , and *spring stiffness ratio*, s , as follows:

$$l(T) = L/\lambda(T) = 2\pi LT^{-2}, \quad (5.8)$$

$$s(T) = S/S_{res}(T) = \frac{S}{(2\pi)^2(1 + M_a(T))}T^2. \quad (5.9)$$

Figure 5.28 shows the power capture of Device 3, expressed as a percentage of the maximum value for the data set, versus l and s for the four trial wave period values. A high degree of similarity is indeed evident. The maximum values, indicated by white plusses on the figure, are found at $(l, s) = (3/16, 1.152)$ in all cases¹⁹. The variation evident between the plots can be summarised qualitatively as a broadening of features in the s dimension (becoming less “peaked”) as T is increased.

¹⁸I.e. Device 1 & Device 2, Device 3 & Device 4, etc.

¹⁹Note that the $T = 25$ and 30 data have been interpolated onto the same grid as the $T = 20$ data, for which the resolution is $1/16$ in l and 0.136 in s .

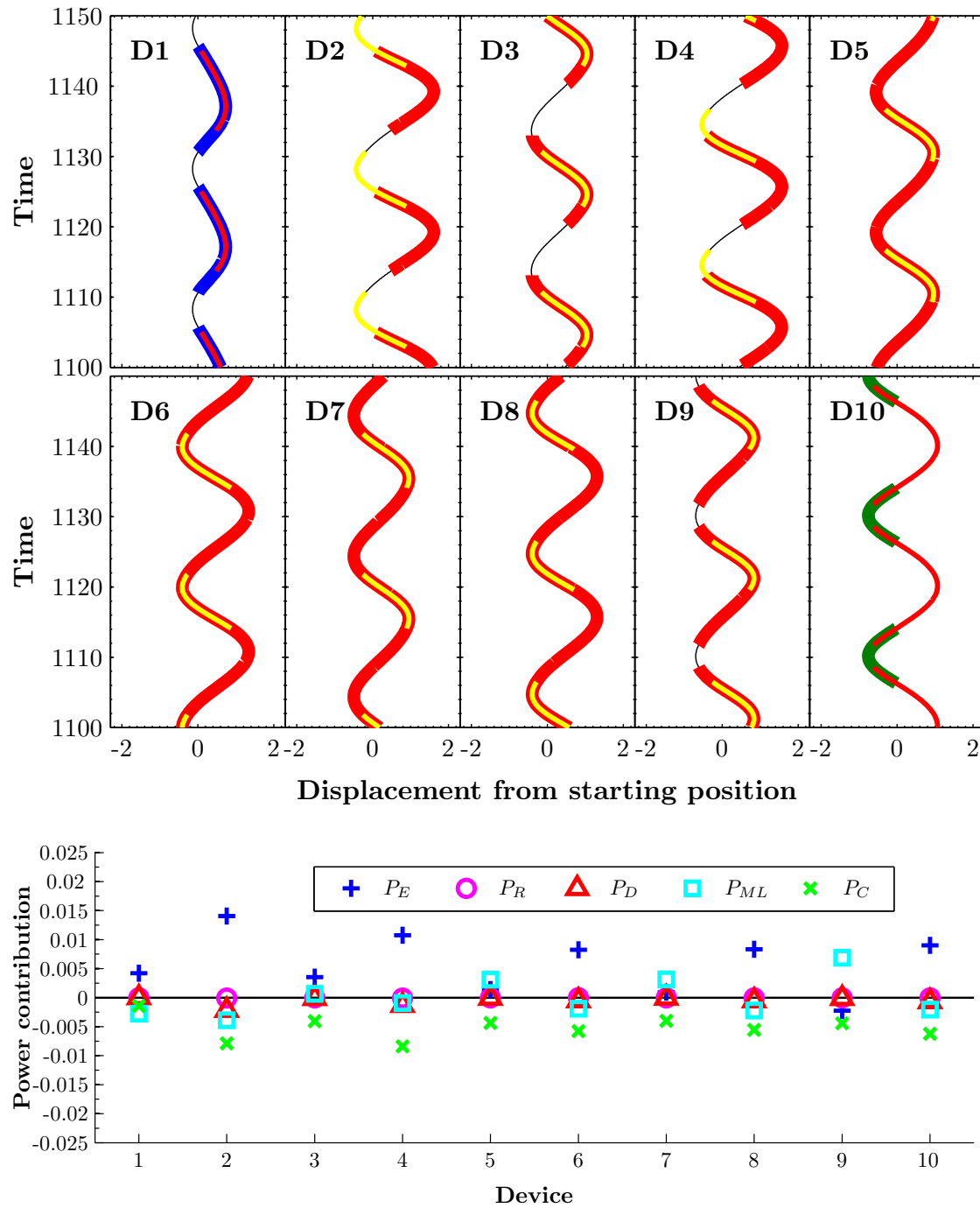


Figure 5.26: Top: Steady-state motion and power contributions for the ten-device chain with $L = \lambda/8$, $S = 0.15$, and all other parameters as in the reference set. The coloured line segments show when the mooring and linkage lines are in tension, as described in the caption of Figure 5.19. Bottom: power contributions for the same example.

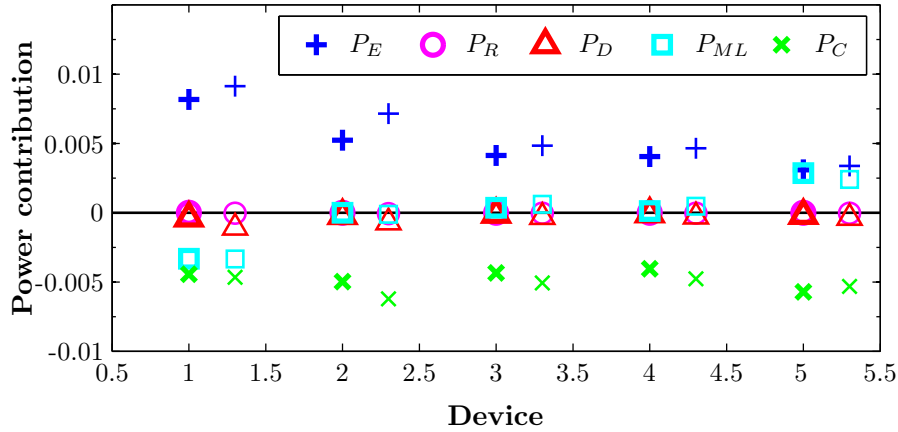


Figure 5.27: Power contributions for the five-device chain with $L = 5\lambda/32$, $S = 0.07$ (bold symbols), compared with the mean power contributions for adjacent pairs (i.e. Device 1 & Device 2, Device 3 & Device 4, etc.) in the ten-device chain shown in Figure 5.26, with $L = \lambda/8$, $S = 0.15$ (regular symbols, plotted to the right of the $n = 5$ series). All other parameters as in the reference set.

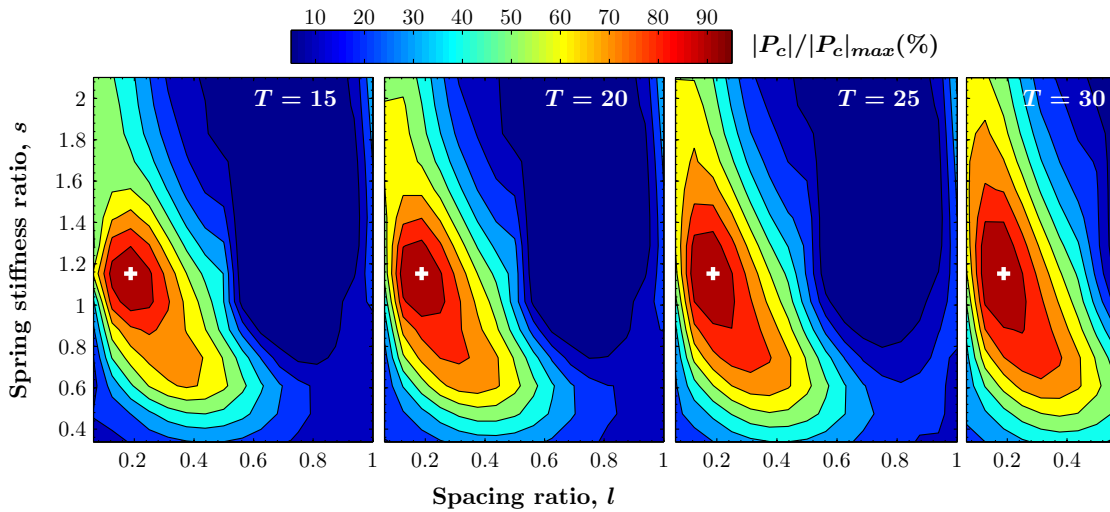


Figure 5.28: Power capture for the end device of the three-device chain (i.e. Device 3), expressed as a percentage of the maximum value for each data set. Simulations were run with different combinations of device spacing and spring stiffness for the three wave period values shown, with all other parameters as given in (5.1). On the axes are device spacing and spring stiffness, expressed as ratios to the wavelength and resonant spring stiffness respectively, as defined in (5.8)-(5.9). Contours are drawn at levels of 10%, 20%, ... 90%. The white pluses show the maximum power capture for each data set. Note that the other three data sets have been interpolated onto the same grid as the $T = 20$ data using cubic spline interpolation.

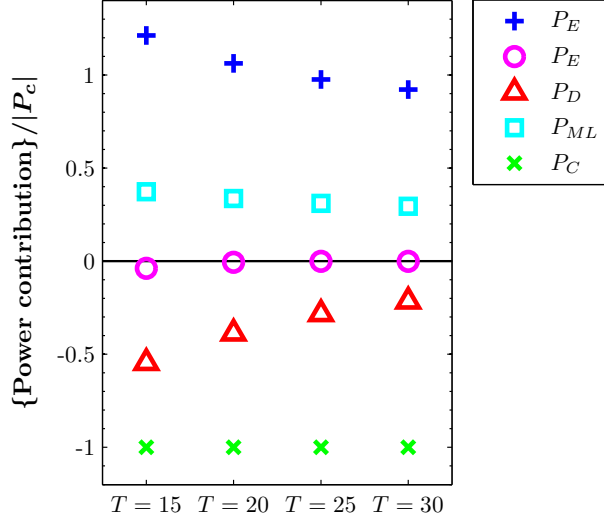


Figure 5.29: Power contributions as a proportion of the power capture, for the cases of maximum power capture in the end device of the three-device chain at the four period values shown. These cases correspond to the white plusses shown on Figure 5.28, and all have parameters $(l, s) = (3/16, 1.152)$ relative to their respective T values.

As a brief aside, we attempt an explanation of this last observation by analogy with a lone, fully linear device (i.e. a damped harmonic oscillator). The power capture in this case is given by (2.122). Defining R_T as the total resistance from all sources, (2.122) may be rewritten as

$$P_C = -\frac{R|\hat{F}_E|^2}{2R_T^2} \times \left[1 + \left(\frac{S_{res}/\omega}{R_T} \right)^2 \left(1 - \frac{S}{S_{res}} \right)^2 \right]^{-1}. \quad (5.10)$$

This form makes it clear that P_C is maximised when $S = S_{res}$, and we can also see that it will be 50% of the maximum when

$$S = S_{\pm} \equiv S_{res} \left(1 \pm \frac{R_T}{S_{res}/\omega} \right). \quad (5.11)$$

The “width” of the power capture curve (versus S) can then be characterised by $\Delta S \equiv S_+ - S_-$. Expressing this as a proportion of S_{res} , we have

$$\Delta s \equiv \frac{\Delta S}{S_{res}} = 2 \frac{R_T}{S_{res}/\omega}. \quad (5.12)$$

Note that this is very similar to the expression we would derived for the device’s bandwidth (in terms of $\Delta\omega$).

This linear result is strictly not valid for our purposes, due (predominantly) to the presence of nonlinear drag. However, we may attempt to apply it if we can derive an

estimate of the *effective* linear resistance due to the nonlinear drag. To do so, we use the data plotted in Figure 5.29: the power contributions, as a proportion of the power capture, for the cases giving peak power capture in Device 3 (shown by the white plusses in Figure 5.28). The magnitudes of all other power contributions decline relative to the power capture with increasing T ; in particular, the dissipation due to drag declines from 55% to 39% to 28% to 22% over the four T values shown. We use these proportions to infer an effective resistance due to nonlinear drag R_{eff} as follows:

$$R_{eff} = \frac{P_D}{P_C} R \quad (5.13)$$

Combining R_{eff} with the PTO and radiation resistances and applying (5.12) gives $\Delta s = (0.755, 0.894, 1.032, 1.174)$ for $T = (15, 20, 25, 30)$. These numbers are not quantitatively useful for estimating the width of the features in Figure 5.28. However, they do tell us that the broadening of the features we observe as T is increased is in line with expectations based on the fully linear case; the decreasing total effective resistance, which on its own should cause the features to become more peaked, is more than offset by the decrease in the denominator of (5.12). Due to the nonlinearity of the system, though, we cannot generalise this result over the full range of periods; for $T < 15$, rapidly growing dissipative losses may mean that features cease to narrow for decreasing T , and begin to broaden. Other variations could also emerge, such as a shift in the position of the peak.

Figure 5.28 does not show how the *magnitude* of the power capture varies with respect to wave period. The maximum values for the four plots shown are, in order of increasing period, $|P_C|_{max} = (0.0426, 0.0198, 0.0100, 0.0056)$. It is insightful to draw a comparison with the maximum power capture of a lone device at these same wave periods and for the same PTO resistance: the percentage enhancements over the lone device maxima are 30%, 44%, 47%, 56% respectively. The smaller gains at shorter wave periods point to a growing proportional influence of the nonlinear drag as the magnitude of the devices' motions increases relative to the wavelength (and hence to the size of the water particle orbits)²⁰.

5.3.1 Test cases

We chose three particular chains for the analysis in the following subsections, which we label and define here for convenience:

- Chain N3A – A three-device chain with $S = 0.15, L = 3/16 \times \lambda_{T=20}$.
- Chain N5A – A five-device chain with $S = 0.19, L = 3/16 \times \lambda_{T=20}$.
- Chain N5B – A five-device chain with $S = 0.09, L = 1/2 \times \lambda_{T=20}$.

²⁰This effect could be mitigated somewhat by increasing the PTO resistance, whereas in the present investigation it is fixed.

All three chains use the standard reference values $R = 0.15$, $C_D = 0.5$. The first two were chosen from small test series for $n = 3$ and 5 respectively, of which they returned the best results when the power capture values for the end device of the chain for wave periods $T = 15, 16, \dots, 30$ were summed with equal weighting (i.e. a flat spectrum). They are surely not the optimum configurations for this criterion, but ought to be reasonably close to it. Chain N5B was chosen because it gives the highest per-device mean power capture at the reference period value of 20.

5.3.2 Period-generalised power capture ratio

The results and discussion in the preceding section suggest that if the power capture of a particular device in a chain is known over the L - S domain for a particular wave period T_{ref} , we have a reasonably accurate representation for other values of wave period, too. Specifically, if we express the power capture as a proportion of its maximum for the given wave period and cast it in terms of the spacing and spring stiffness ratios as in Figure 5.28, the result, which we call the *period-generalised power capture ratio*, is approximately applicable for a range of wave period values either side of T_{ref} . This could prove a useful tool when it comes to finding parameters to optimise performance for a particular spectrum that describes a real sea state. Here we shed light on how such an approach might work, turning our attention to the response of particular chains (with fixed L and S) over a range of wave period values.

Figure 5.30 shows the period-generalised power capture ratio versus l and s for the end devices of three- and five-device chains, evaluated from a series with $T_{ref} = 20$. Superimposed onto these plots are example trajectories of $(l(T), s(T))$ as T is varied. Note that if we simplify matters by assuming M_a to be constant, (5.8) and (5.9) can be combined to eliminate T and give

$$s(l) = \frac{SL}{2\pi(1 + M_a)} l^{-1}. \quad (5.14)$$

Thus, for a given choice of S and L , the s and l values for different T lie approximately on a hyperbola, with slight perturbation due to the dependence of the added mass on the wave period. (5.14) shows that different parameter combinations giving equal products SL share the same trajectory; however, the location of points corresponding to specific T values is determined by the S and L values individually. In Figure 5.30, four approximate trajectories are drawn using (5.14) for $L = (3/16)\lambda_{T=20}$, and $S = 0.1, 0.15, 0.2$ and 0.25 . Also superimposed are the exact points $(l(T), s(T))$ corresponding to period values $T = 10, 12, \dots, 30$ for the particular chains N3A and N5A defined above in Section 5.3.1. Comparison of the Chain N3A data points to the $S = 0.15$ trajectory shows that the assumption of constant added mass used in the latter has a small, but noticeable, effect.

A very important observation here is that the form of the period-generalised power capture ratio for the devices at the end of the chains is a “good fit” for the hyperbolic trajectories. The plots here show that a device achieving near-maximum power capture at a certain wave period will perform well over a range of wave periods either side. This observation allows us to express more formally a point raised earlier – it is only the end

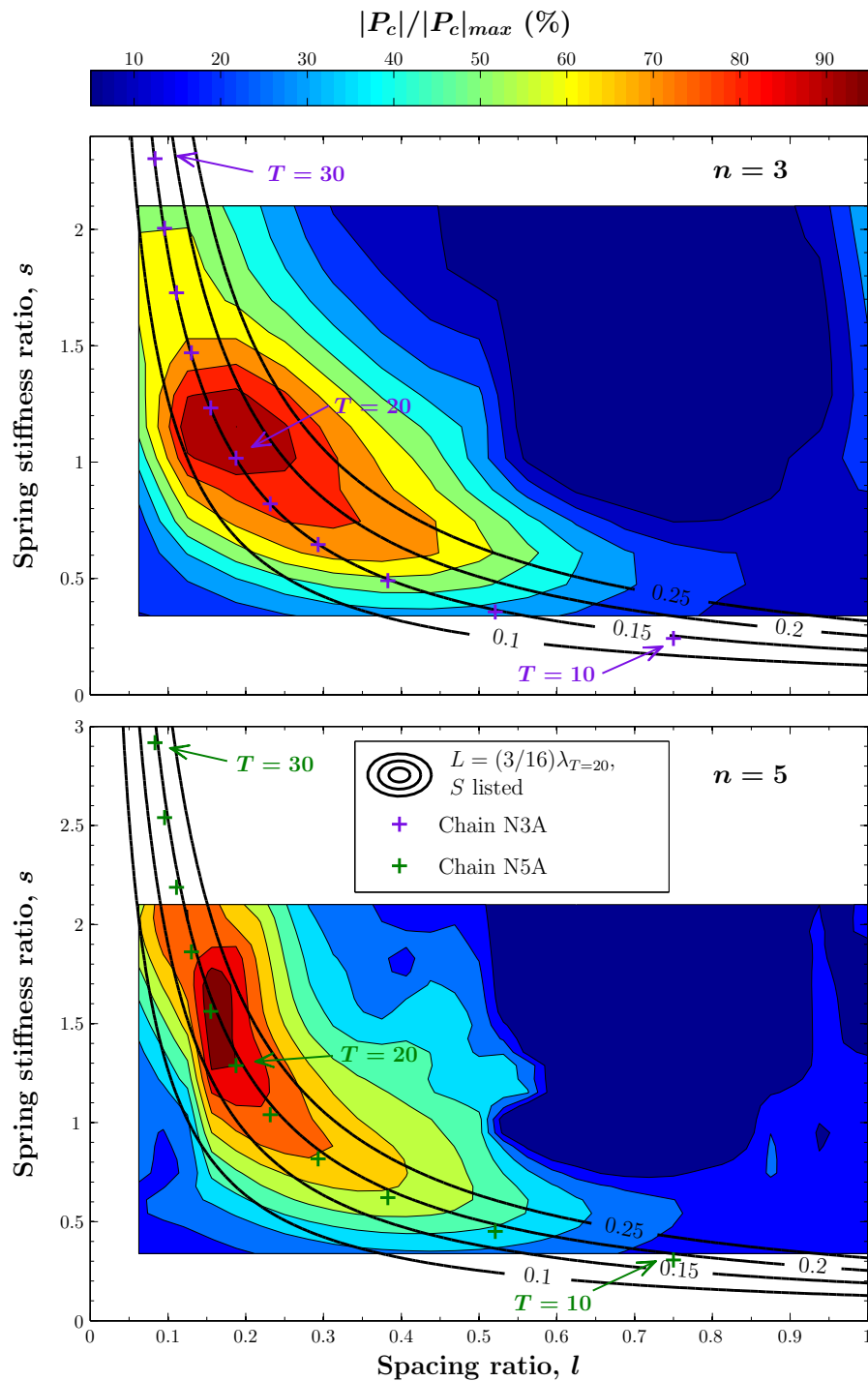


Figure 5.30: Period-generalised power capture ratio for the end device of three- and five-device chains, evaluated at $T_{ref} = 20$. The black lines show approximate trajectories $s(l)$ evaluated from (5.14), for the spacing given in the legend and the spring stiffness values labelling each line. The purple and green pluses show the exact trajectories $(l(T), s(T))$ evaluated from (5.8)–(5.9) for chains N3A and N5A (defined in section 5.3.1), for wave periods $T = 10, 12, \dots, 30$. Figure 4.1 allows conversion to period in seconds.

device, rather than the first device, that can deliver high power capture over a range of wave period values. This is obvious when we recall that the plots for the first device are approximately a mirror image of that of the end device about $l = 0.5$.

5.3.3 Estimated and actual power capture for particular chains

We have illustrated that the period-generalised power capture ratio can be used to assess qualitatively how well a certain device is likely to perform over a range of wave period values. We now address the question of whether an accurate quantitative assessment is in fact possible based on data from a single wave period value²¹.

Recall from earlier that for the case we examined ($n = 3, H = 1.25, R = 0.15$), the peak power capture for the end device increases relative to the corresponding maximum for a lone device for higher wave periods, from $\approx 30\%$ above at $T = 15$ to $\approx 55\%$ above at $T = 30$. If we were to assume a fixed proportionality of $|P_C|_{max}/|P_C|_{n=1,max} = 1.43$, based on the value at $T_{ref} = 20$, the peak value would be overestimated by about 8% at $T = 15$ and underestimated by about 11% at $T = 30$. These are not huge errors, and such an assumption might form the basis of a useful estimate. We apply this idea in the following method for estimating the power capture for a certain device at general L, S and T based on its period-generalised power capture evaluated at a particular T_{ref} :

1. Evaluate $l(L, T)$ and $s(S, T)$.
2. Find the period-generalised power capture ratio at (l, s) by interpolation (if necessary).
3. Determine the peak power capture for the device in question as a proportion of the corresponding maximum for the lone device (for the same H and R) at T_{ref} .
4. Determine the corresponding maximum power capture of the lone device at T .
5. Multiply the results from steps 2–4 together to obtain the power capture estimate.

The method could be expressed by the following equation:

$$|P_C|_{approx}(L, S, T) = \left[\frac{|P_C|}{|P_C|_{max}} \right]_{(l(L,T), s(L,T))} \left[\frac{|P_C|_{max}}{|P_C|_{n=1,max}} \right]_{T_{ref}} |P_C|_{n=1,max}(T) \quad (5.15)$$

In Figure 5.31, we present the power capture versus wave period for chains N3A and N5A, alongside estimates made using the method just described with the period-generalised power capture ratios shown in Figure 5.31. Note that the estimates are not returned for values of T where the (l, s) values fall outside the region of the domain for which we have data.

Overall, the estimates give reasonably good agreement with the actual values. For Chain N3A there is an rms difference of 0.0018 between the actual and estimated values,

²¹The method we describe in fact requires data for the *lone device* over the period range, but only at T_{ref} for the chain in question.

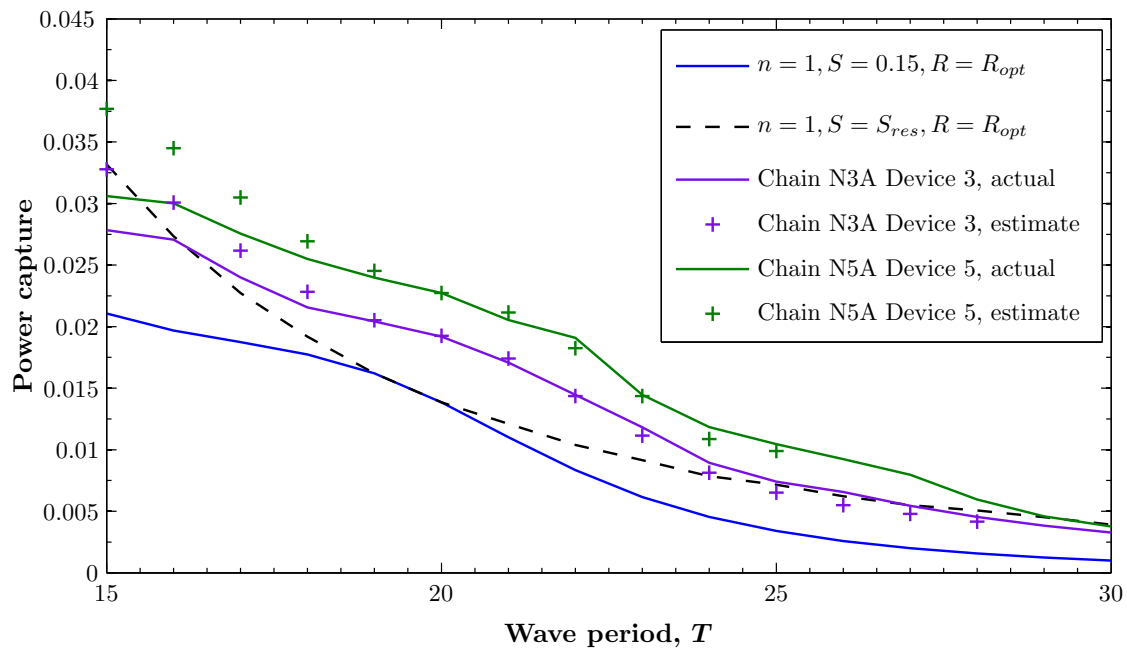


Figure 5.31: Power capture vs wave period for chains N3A and N5A, in comparison to two lone device scenarios. The black dotted line shows the lone device maximum for each period value, and the blue line is for a lone device with fixed spring stiffness $S = 0.15$ and only R optimised as a function of T (reproduced from Figure 4.10(a)). The chains have fixed L, R and S as defined in section 5.3.1. H and C_D have the standard reference values. Figure 4.1 allows conversion to period in seconds.

corresponding to 12% of the mean power capture over the included period range. Notice that the values are overestimated for $T < 20$ and underestimated for $T > 30$ (although $T = 21$ is an anomaly) as we predicted would occur above due to the assumption that the peak power capture is a fixed proportion of the corresponding lone device maximum. This effect is also compounded by the fact that the true power capture function is flatter at longer periods and more sharply peaked at shorter periods, relative to its shape at $T_{ref} = 20$. With a more detailed analysis, these effects could possibly be parameterised and a more accurate estimation method produced; that is beyond the scope of this investigation, and we will pay it no more attention other than to note that the method as it stands appears to give moderately useful estimates for the cases examined, with potential for improvement.

Focusing now on the power capture results from actual simulations of chains N3A and N5A over the period range, there are a number of observations to be made about Figure 5.31. Most importantly, for both chains, the end device achieves a power capture exceeding the maximum value possible for a lone device (i.e. resonant and with optimised PTO resistance) over most of the wave period range; specifically, over $16 \leq T \leq 29$ for Chain N5A and over $17 \leq T \leq 26$ for Chain N3A. The comparison to particular lone devices with fixed parameters is even more impressive – for the example with $S = 0.15$ shown in blue, even with a variable PTO resistance tuned to the optimum value at each wave period, the end device of Chain N5A achieves a power capture between $\approx 50\%$ and 400% higher over the entire period range. A further point to note is that the higher power capture of Chain N5A’s end device over that of Chain N3A is sustained at a roughly constant amount over the whole period range.

We have thus illustrated that the result previously shown to be true at a single wave period value – that particular devices in a chain can achieve vastly enhanced power capture relative to any lone device – is also true when considering the response over a wide range of period values. Another major finding detailed earlier in this chapter was that the per-device mean power capture for an entire chain cannot exceed that of a resonant, optimised lone device for a given wave period; does this result still apply in the context of a range of wave period values?

In Figure 5.32, the lone device with fixed parameters $R = S = 0.15$, which is resonant and optimised at $T = 20$, is compared with Chain N5B, which at $T = 20$ has half-wavelength spacing and achieves almost as high a per-device mean power capture as the aforementioned lone device. We extended the range of wave periods for investigation in this case down to $T = 10$, in order to show the appearance of a second local maximum in the power capture of Chain N5B at a period somewhere between 11 and 12. This corresponds to where the device spacing is 1.5 times the wavelength; the exact period at which this condition occurs is $T = \sqrt{3} \times 20 = 11.55$. We would expect to see a continued series of such local maxima as T is decreased further, appearing closer and closer together.

We note that at both of the local maxima seen in Figure 5.32, the per-device mean power capture of the chain is less than that of the lone device shown. In between the peaks, the chain performs significantly worse than the lone device. However, the power

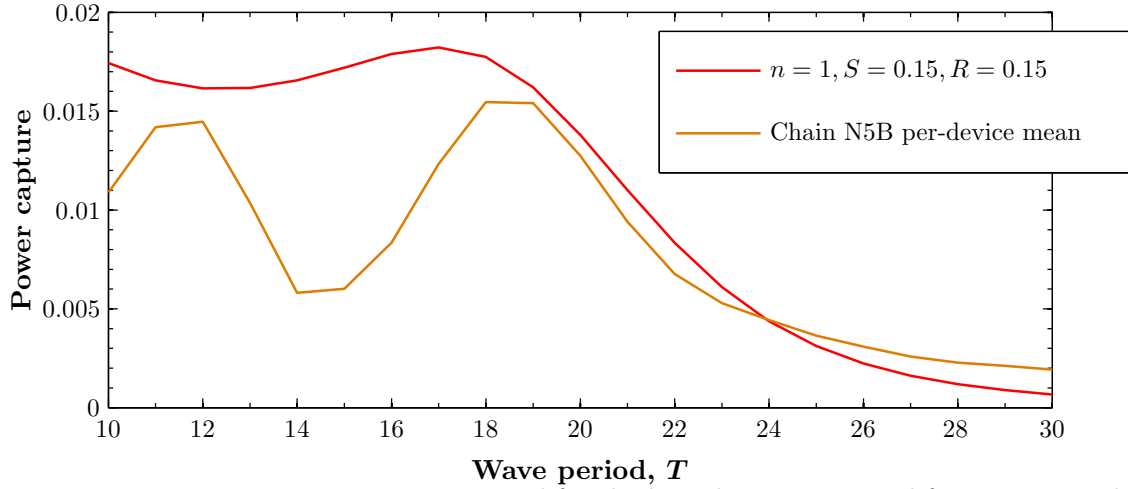


Figure 5.32: Power capture vs wave period for the lone device optimised for $T = 20$, and Chain N5B, which gives close to the optimum per-device mean power capture at $T = 20$ with its half-wavelength spacing. All other parameters have the standard reference values. Figure 4.1 allows conversion to period in seconds.

capture of the lone device falls away faster than that of the chain above $T = 20$, and the chain performs better for wave periods above where the curves cross at $T \approx 24$. This result can be visualised by considering the trajectory on the period-generalised power capture ratio plot, which could be adapted from Figure 5.21(c) for the per-device mean of a five-device chain. For Chain N5B, the $T = 20$ data point is located at the central maximum of the power capture. As T is increased from this, the trajectory matches the “horse-shoe” shape of the power capture curve well. As T is decreased, however, the trajectory moves into a region of low power capture, until coming near to another peak at $L \approx 1.5\lambda$.

Overall, these results do not show much promise for the prospects of achieving a greater total power capture with a linked chain than with the same number of lone devices. However, the scope of exploration is far too limited to be able to generalise and draw any conclusions on this matter. We explore the question further in the following chapter by venturing into the regime of polychromatic wave fields with some specific spectra.

5.4 Results at different wave heights

Up to this point in the chapter, results have all been from simulations using a fixed wave height of $H = 1.25$. In Chapter 4, we saw that due to nonlinearity, the capture width (a measure of efficiency) declined over the whole period range 10 – 30 as H was increased. Some qualitative change in the capture width curve as a function of period was also evident, explained by the nonlinear drag causing an increased effective resistance for higher wave heights.

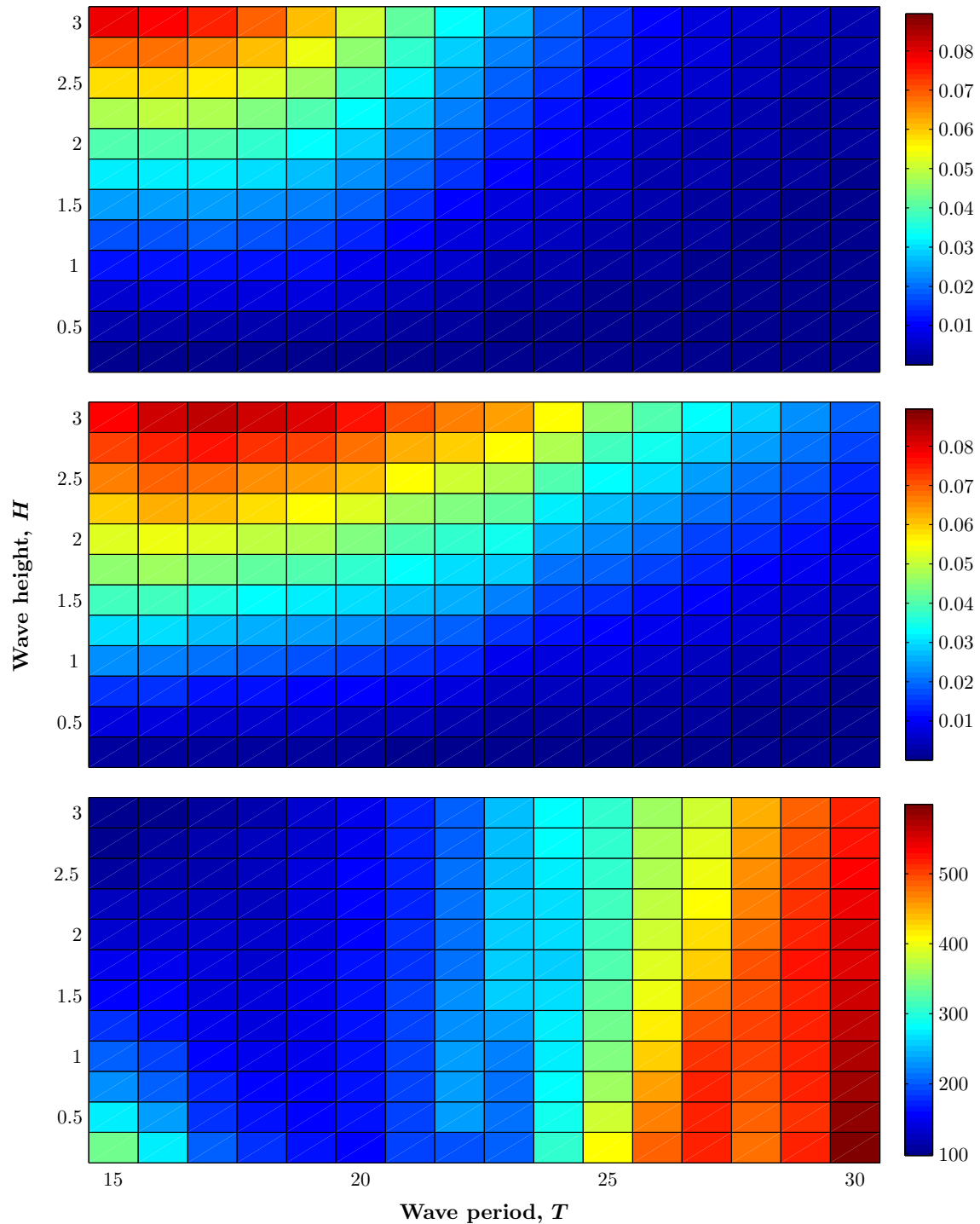


Figure 5.33: Top: Power capture matrix for the lone device with $R = S = 0.15$ (reproduced from Figure 4.12). Middle: power capture matrix for Device 5 of Chain N5A (defined in section 5.3.1). Bottom: Ratio of the power capture of Device 5 of Chain N5A to the lone device described above, expressed as a percentage. The drag coefficient is at its reference value $C_D = 0.5$. Note that the H -axis is inverted relative to the power capture matrices presented in Chapters 1 and 4. Figure 4.1 allows conversion to period in seconds.

Here we investigate the effect of varying wave height with just one example chain: Chain N5A, defined in Section 5.3.1. Figure 5.33 shows a comparison of the power capture matrices of the lone device with $R = S = 0.15$ and the end device of Chain N5A. The bottom plot in this figure shows the ratio of the latter to the former, as a percentage. We observe that while the period at which the maximum occurs for the lone device decreases as H increases, the opposite is true for the end device of Chain N5A. This causes the ratio of the power captures at $T = 15$ to decrease from over 3:1 to around 1:1 as the wave height increases. The ratio does not uniformly decrease with increasing H over the whole period range – in fact, at some wave periods (e.g. $T = 23$), there are instances where the ratio increases with increasing wave height.

Clearly, the power capture generally depends on both the wave period and the wave height in a non-trivial manner, and attention must be paid to both these variables in a serious attempt to optimise for a particular scenario. While the results for the particular wave height $H = 1.25$ appear reasonably indicative of the results over a wider height range, care must be taken in interpreting these too generally, especially when it comes to numerical results.

One final comment to be made is that the example presented here indicates that the potential power capture gains for certain devices in a chain over lone devices could be even greater at low wave heights, due to the reduced nonlinear drag effects.

5.5 Results for different PTO resistances

In Chapter 4, we saw that the lone device’s resonance condition was practically independent of R . Here we present evidence that a similar result applies for linked chains. Figure 5.34 shows how the power capture varies as a function of device spacing L and spring stiffness S for different R , for a particular three-device chain. Of course, the value of R moderates the height and breadth of the power capture curves, but the peak is found to occur at the same L and S values in all cases. The resolution in these plots is quite low, but is sufficient to be able to say that the sensitivity of our results and conclusions in this chapter to variations in R is certainly low.

5.6 Further explorations

A very limited set of model runs were undertaken in which different devices in the chain were assigned different values of certain parameters.

5.6.1 Non-uniform spacing and mixed stiffness of mooring and linkage lines

The configuration giving optimum power capture – for a particular device in the chain, or for the per-device mean – may be one in which the spacing between devices is non-uniform. However, in the small number of exploratory runs undertaken, we do not observe any instances in which the optimum power captures exceeded the maxima found

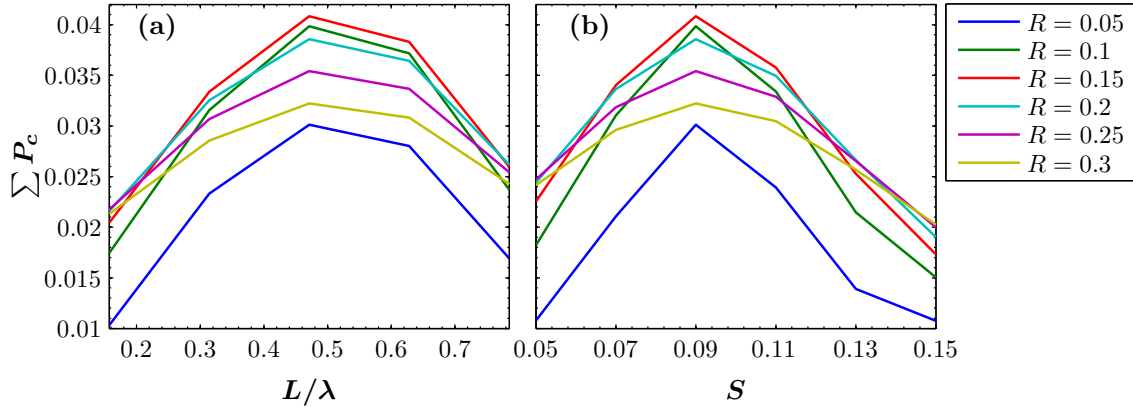


Figure 5.34: Total power capture for a three-device chain with R as shown in the legend and (a) $S = 0.09$ with L varied, (b) $L = 30 = 0.47\lambda$ with S varied. All other parameters are given by the reference parameter set (5.1).

for a chain of the same number of devices with uniform spacing. In particular, we attempted here to tap into “the best of both worlds” – strong oscillations at the incident wave frequency, with higher frequency oscillations superimposed – using chains with pairs of closely-spaced devices, linked by lines with high stiffness, separated by approximately half a wavelength from the adjacent pairs. For example, in one test case the devices’ starting positions were $\mathbf{x}_0 = \lambda \times (0, 0.1, 0.55, 0.65, 1.1, 1.2)$.

5.6.2 Zero resistance on select devices: *dummy devices*

If the aim is to maximise the power capture by a particular device in a chain, it is obvious that this will be best achieved by reducing the resistance acting on the other devices as much as possible. The maximum power capture achieved by the end device in chains where all devices have equal PTO resistance, shown in Figures 5.24-5.25, is therefore a pessimistic indication of what is possible in this regard.

To investigate what further gains might be achieved, we ran one test series with a three-device chain where Device 3 had the usual PTO resistance of 0.15, but the first two devices had zero PTO resistance – that is, the PTO resistance is the matrix $\mathbf{R} = \text{diag}\{0, 0, 0.15\}$. L and S were varied, with all other parameters fixed at their reference values. The highest power capture by Device 3 observed in the series was 0.0262; this is compared to the maximum of 0.0199 when all three devices have equal PTO resistance (and to the lone device maximum of 0.0138). The maxima in both cases occur at the same spacing and spring stiffness $(L/\lambda, S) = (3/16, 0.17)$, although in the present case there is also a second local maximum that is almost as large centred on $\sim (3/8, 0.1)$. The power contributions at the maximum power capture are shown in Figure 5.35, which can be compared to Figure 5.24(b) for $R = 0.15$. The amount of power being transferred from Devices 1 and 2 to Device 3 via the linkages is far higher than in any case examined earlier, and even larger power transfers are found at other (L, S) combinations in the

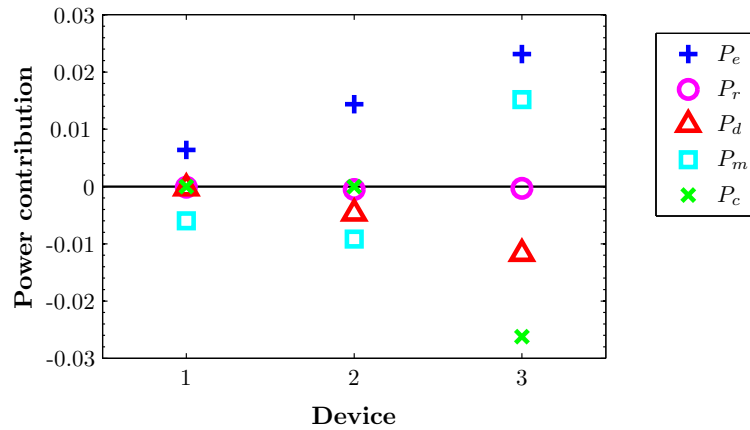


Figure 5.35: Power contributions for a three-device chain with $L = 3\lambda/16$, $S = 0.17$, PTO resistances $\mathbf{R} = \text{diag}\{0, 0, 0.15\}$ (i.e. zero resistance on the first two devices), and all other parameters given by the reference set.

series.

The concept explored here demonstrates potential for what we call “dummy devices”. These could be simple, cheaply-constructed bodies without mechanical components, linked to the true devices such that they passively transfer power to boost the devices’ power captures. Dummy devices could be of any shape or size, rather than replicas of the true devices as they are here.

As a final comment on these results, it should be noted that the optimum PTO resistance on Device 3 will surely be higher than the default value of 0.15 used in this test series. Thus, even greater power capture gains than those shown here should be possible with dummy devices.

Chapter 6

Towards a continuous wave spectrum

For a nonlinear system such as the one we are modelling, there are no guarantees that the behaviour for discrete single frequency inputs gives an accurate picture of how the system will behave in the more general, and more realistic, case. Here we present results of our investigation into the realm of polychromatic wave fields, or “semi-continuous” spectra. A small number of example scenarios were chosen to be investigated. Once again all quantities in the chapter are in nondimensional form unless it is stated otherwise. Conversions to S.I. units can be made using Table 3.2 and the period scale in Figure 4.1.

6.1 Methods and technical details

We used the Bretschneider spectrum (2.49) to give a representation of a sea state that is somewhat realistic while remaining simple and convenient. The spectrum is identical when expressed in dimensionless units – we repeat it here for convenience:

$$\Psi_B(f) = \frac{5H_s^2 f_p^4}{16 f^5} \exp \left[-\frac{5}{4} \left(\frac{f_p}{f} \right)^4 \right], \quad (6.1)$$

where f_p is the frequency at the peak of the spectrum, and H_s is the significant wave height. Note that (6.1) is easily integrated analytically to give

$$\int \Psi_B(f) df = \frac{-H_s^2}{16} \exp \left[-\frac{5}{4} \left(\frac{f_p}{f} \right)^4 \right]. \quad (6.2)$$

We generate a wave field for this spectrum by first choosing a set of wave periods T_j with uniform spacing $T_{j+1} - T_j = \Delta T$. The corresponding height of the j th wave field component is therefore (using (2.48) with (6.2)):

$$H_j = \frac{H_s}{\sqrt{2}} \sqrt{\exp \left[-\frac{5}{4} \left(\frac{T_j - \Delta T/2}{T_p} \right)^4 \right] - \exp \left[-\frac{5}{4} \left(\frac{T_j + \Delta T/2}{T_p} \right)^4 \right]}, \quad (6.3)$$

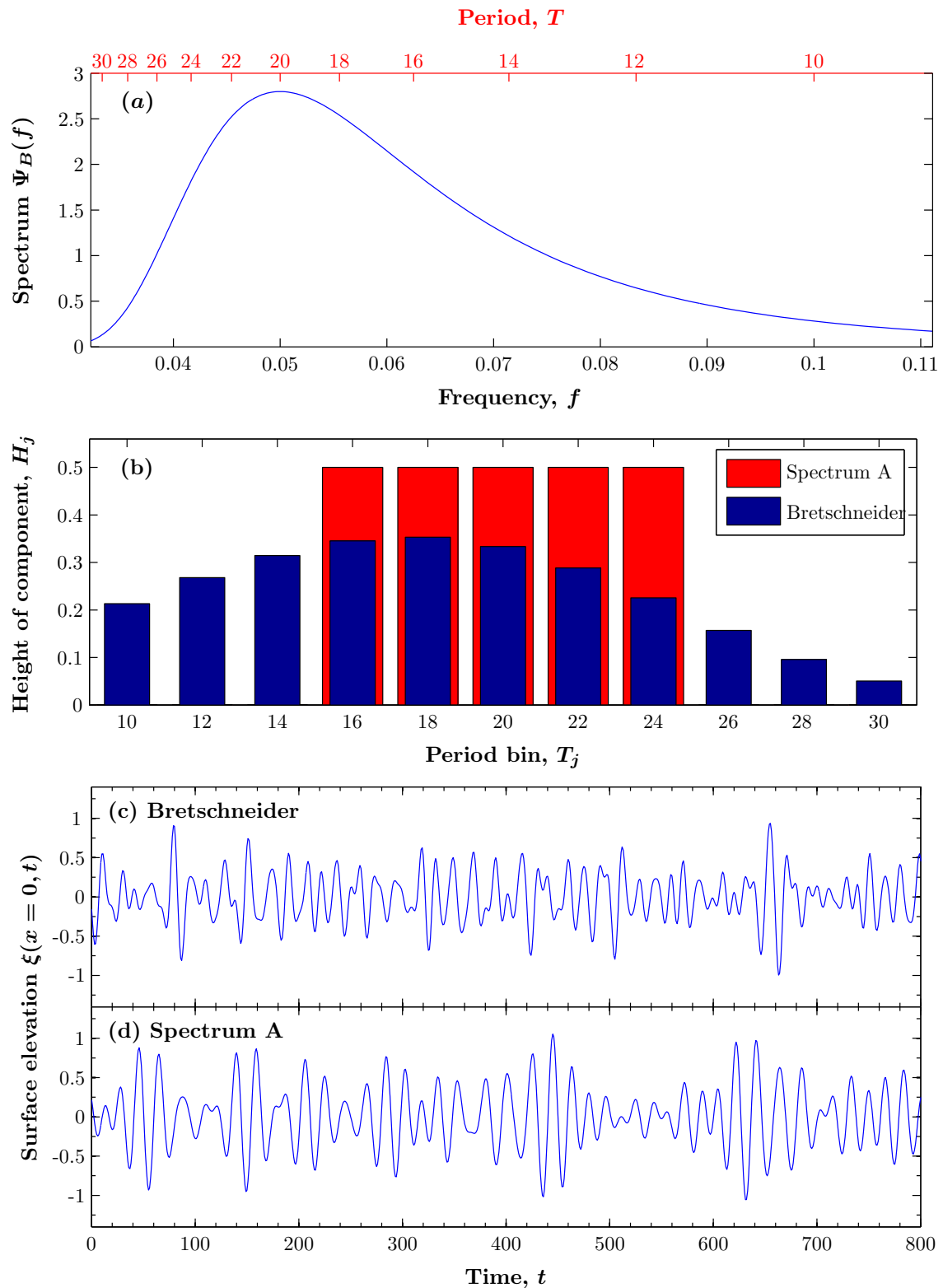


Figure 6.1: (a) Bretschneider spectrum with $T_p = 20$, $H_s = 1.25$. (b) Component heights for the Bretschneider spectrum and the idealised Spectrum A. (c)-(d) Example surface elevation records for the two discretised spectra, with the phases of the components chosen randomly from a uniform distribution on the interval $[0, 2\pi]$. Note that this figure, and all others in this chapter, are in nondimensionalised units. Figure 4.1 allows conversion to period in seconds.

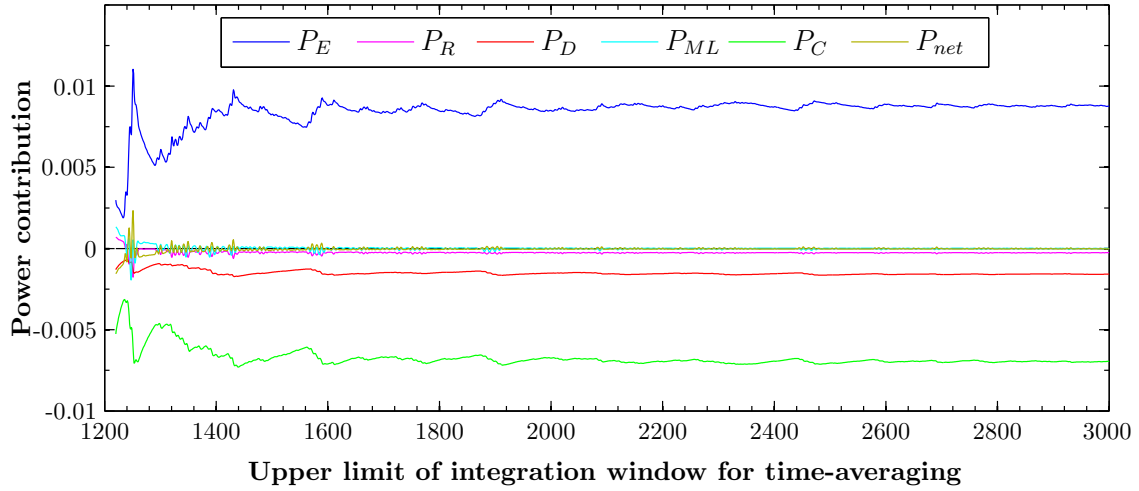


Figure 6.2: Convergence of the power contributions for a simulation of Device N1A, defined in section 6.1.1, forced by the Spectrum A wave field. The plot shows running averages of the terms from a starting point of $t = 1200$. Note that P_{net} is the sum of all other power terms, which we would expect to converge to zero.

where $T_p = 1/f_p$ is the period at the peak of the energy spectrum. Note that this exact approach accurately preserves the energy content of the spectrum.

For our exploration we chose the parameters $T_p = 20$ and $H_s = 1.25$ in nondimensionalised units¹, graphed in Figure 6.1(a). Using wave period bins centred on $T_j = 10, 12, \dots, 30$ (so $\Delta T = 2$) gives the component heights shown in blue in Figure 6.1(b). Note that the truncation of the spectrum loses 5% of the total energy, virtually all of it below $T = 9$. From here on, when we write “the Bretschneider spectrum” we refer specifically to this spectrum plotted in Figure 6.1.

We also employed an idealised spectrum, which gives the component heights shown in red in Figure 6.1(b); we call this “Spectrum A”. This simplified case allows for more straight-forward comparison to results from simulations with a monochromatic wave field. In Figures 6.1(c) and (d), example surface elevation records are shown for the Bretschneider and Spectrum A wave fields, respectively.

All simulations were run with a ramp-time $t_r = 1000$, and a total duration of 3000. To ensure the ramp had no effect on results, time-averaged power contributions were evaluated over the window $t \in [1200, 3000]$, giving 60 cycles of the spectral component with the longest period ($T = 30$). Figure 6.2 shows a running average of the device’s power contributions, from the starting point of $t = 1200$, for one simulation. The values are well-converged by the end, with a variation of $\approx 2\%$ in P_C over the range $[2800, 3000]$. We consider this an acceptable level of accuracy.

As well as finding the aggregate power values, we are interested in how the power

¹These correspond to 9.0 seconds and 2.5 metres for a 2 metre radius device. Such conditions are quite typical for sites along NZ’s west and southern coasts in depths $h \lesssim 100\text{m}$ [35].

is distributed amongst the Fourier components of the devices' motions – this may be assessed here by taking the power spectral density (PSD) of the devices' velocities. We use the common approach of estimating the PSD by evaluating the *periodogram* of the velocity, using the function `periodogram` in the MATLAB Signal Processing Toolbox. We take the velocity time series for $t = 1200, 1201, \dots, 3000$, giving a Nyquist frequency of 0.5, and apply a standard Hanning window to the data [8]. This delivers the one-sided spectral density, ϵ_{PSD} . The power capture in a frequency band $[f_1, f_2]$ is found from

$$P_C = 2R \int_{f_1}^{f_2} \epsilon_{PSD}(f) df, \quad (6.4)$$

which we evaluate in MATLAB using trapezoidal integration.

We opted to use the periodogram rather than the related methods of Welch or Bartlett [8], since noise reduction is not of high priority for this data and it is preferable to maintain a higher frequency resolution. Other spectral window functions such as the “boxcar” and the Tukey window were also tried, yielding subtle variations in the PSD but giving total power capture values consistent to within less than 1%. Note that these values are also in close agreement with those calculated by direct integration of the time series, giving confidence in our methods.

6.1.1 Test cases

We used a small number of test cases in the explorations presented below. The two test chains N5A and N5B are the same as those defined in the previous chapter in Section 5.3.1. We also label two different lone device cases for convenience. The full list is:

- Device N1A – A lone device with spring stiffness $S = 0.15$.
- Device N1B – A lone device with $S = 0.31$.
- Chain N5A – A five-device chain with $S = 0.19$ and spacing $L = 3/16 \times \lambda_{T=20}$.
- Chain N5B – A five-device chain with $S = 0.09, L = 1/2 \times \lambda_{T=20}$.

For all cases, we use PTO resistance $R = 0.15$ and drag coefficient $C_D = 0.5$.

6.2 Comparisons with monochromatic wave fields

One major point of interest is how closely the behaviour of the model here relates to the behaviour in monochromatic fields. Here we study the responses for a wave field generated from Spectrum A, which was chosen such that results for each spectral component² acting individually were already available (and presented in the previous chapters).

² $T_j = 16, 18, 20, 22, 24; H_j = 0.5 \forall j$

6.2.1 Lone device

We begin by examining the lone device N1A. Insofar as the time-average power terms for the device, one might predict that simply adding the monochromatic results for all the spectral components would give a reasonable estimate in polychromatic cases. Figure 6.3(a) shows the actual results for the Spectrum A wave field (left) alongside an estimate using the method just described (right). The method significantly overestimates the power capture, in this case at least. The lower power capture is due to a combination of lower power absorption and higher dissipation due to drag.

Figure 6.3(b) shows the power capture associated with the different forcing frequencies – estimated by integrating the PSD into bins as per (6.4) – compared with the monochromatic result for each individual spectral component. The monochromatic result is 46% higher for $T_j = 20$, falling away to 27% and 34% higher for $T_j = 16$ and 24, respectively.

In Chapter 4, we saw that the proportion of the incident power absorbed by the device (expressed by the capture width) diminishes with wave height, due predominantly to the increased importance of drag – see Figure 4.12(b). Does this play a role in reducing the power capture below what we would expect from a simple linear superposition? The answer is surely yes. We can form an alternative estimate, by assessing the power capture contributions we would expect from each motion period using the monochromatic capture width *evaluated not at H_j but at the same energy flux as the total field*. This was done by interpolating the data plotted in Figure 4.12(b) to the appropriate wave height for each period value. This method gives an estimate of $P_C = 0.0103$ for Spectrum A – closer to the observed value of 0.0093 than the previous estimate of 0.0127 shown in Figure 6.3(a), but still 11% too large. It is possible there are methods to give quantitatively accurate predictions of the power capture based on the monochromatic results; this is a topic for potential future work.

Figure 6.3(b) does not show how much of the power capture is associated with motion at frequencies outside of the range present in Spectrum A. In fact, there is only a tiny fraction of the total outside of this range: 0.2% at higher frequencies ($T < 16$), and 0.05% at lower frequencies ($T > 24$). Figure 6.3(c) shows the power spectral density of the device. Plotted on the same graph is the superposition of the PSDs for when the device is forced by each spectral component individually. There are several noteworthy features. First, the “background” of the PSD is vastly elevated compared with the monochromatic case. Second, we still see pronounced peaks coinciding with multiples of the incident frequencies (at the first harmonics, at least) but these are comparable in size to other peaks situated at the sums of the different incident frequencies. Third, in the low frequency oscillations there also appears to be a relation to the beat frequencies of the spectral components ($f_b = f_j - f_k$). While these features are of interest, though, from a practical perspective we reiterate that the vast bulk of the power capture here is still for motion at the fundamental frequencies of the spectrum.

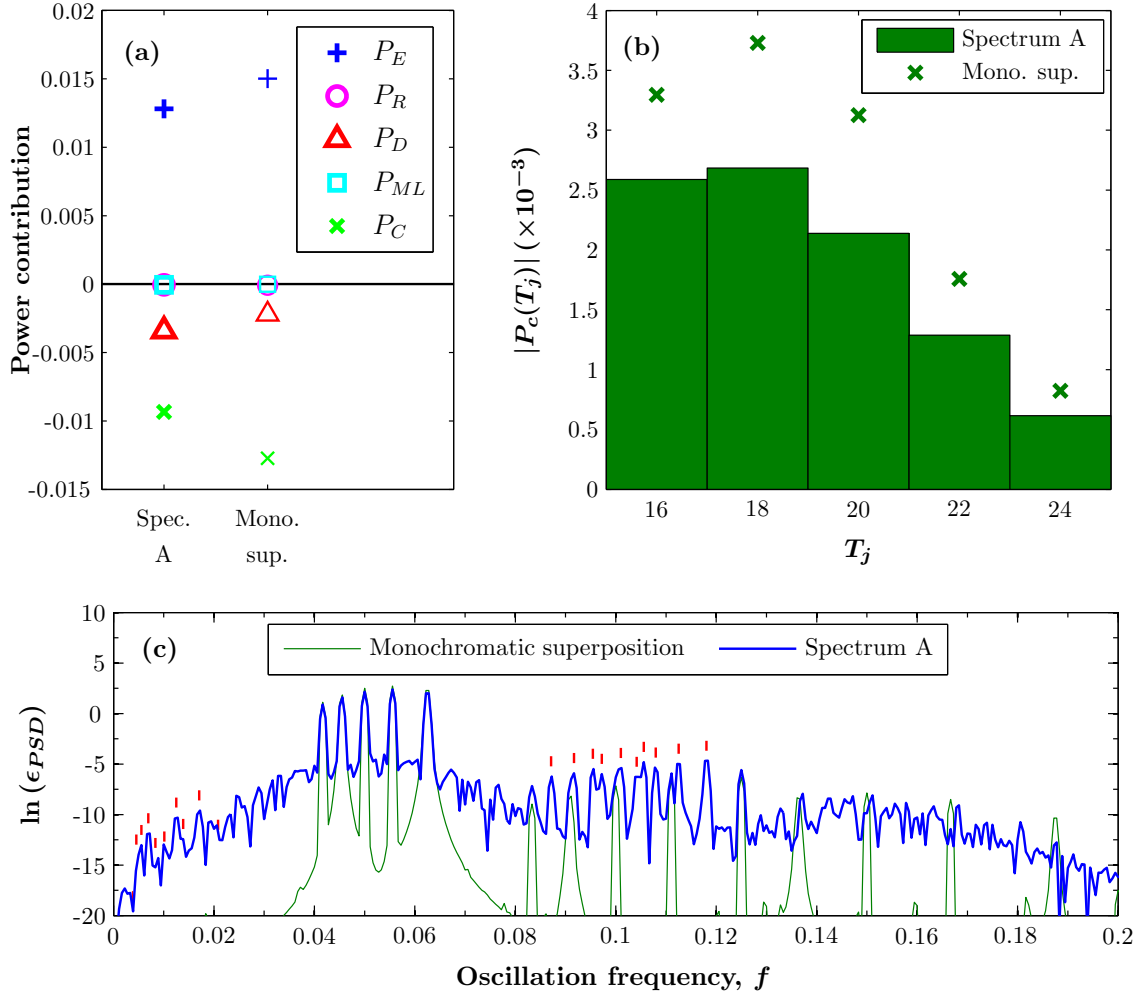


Figure 6.3: (a) Left: time-averaged power contributions for the lone device N1A when forced by Spectrum A. Right: Sum of the power contributions for the monochromatic forcing of each spectral component individually. (b) Bars: power capture associated with each of the forcing frequencies in Spectrum A, obtained by integrating the PSD into bins of width 2 centred on each value of T_j . Crosses: power capture for monochromatic forcing by each spectral component individually. (c) Blue: Power spectral density for the device when forced by Spectrum A. Green: Superposition of the PSDs for when the device is forced by each spectral component individually. The red dashes are plotted at the differences between, and the sums of, the spectral frequencies. Note that the vertical axis is logarithmic.

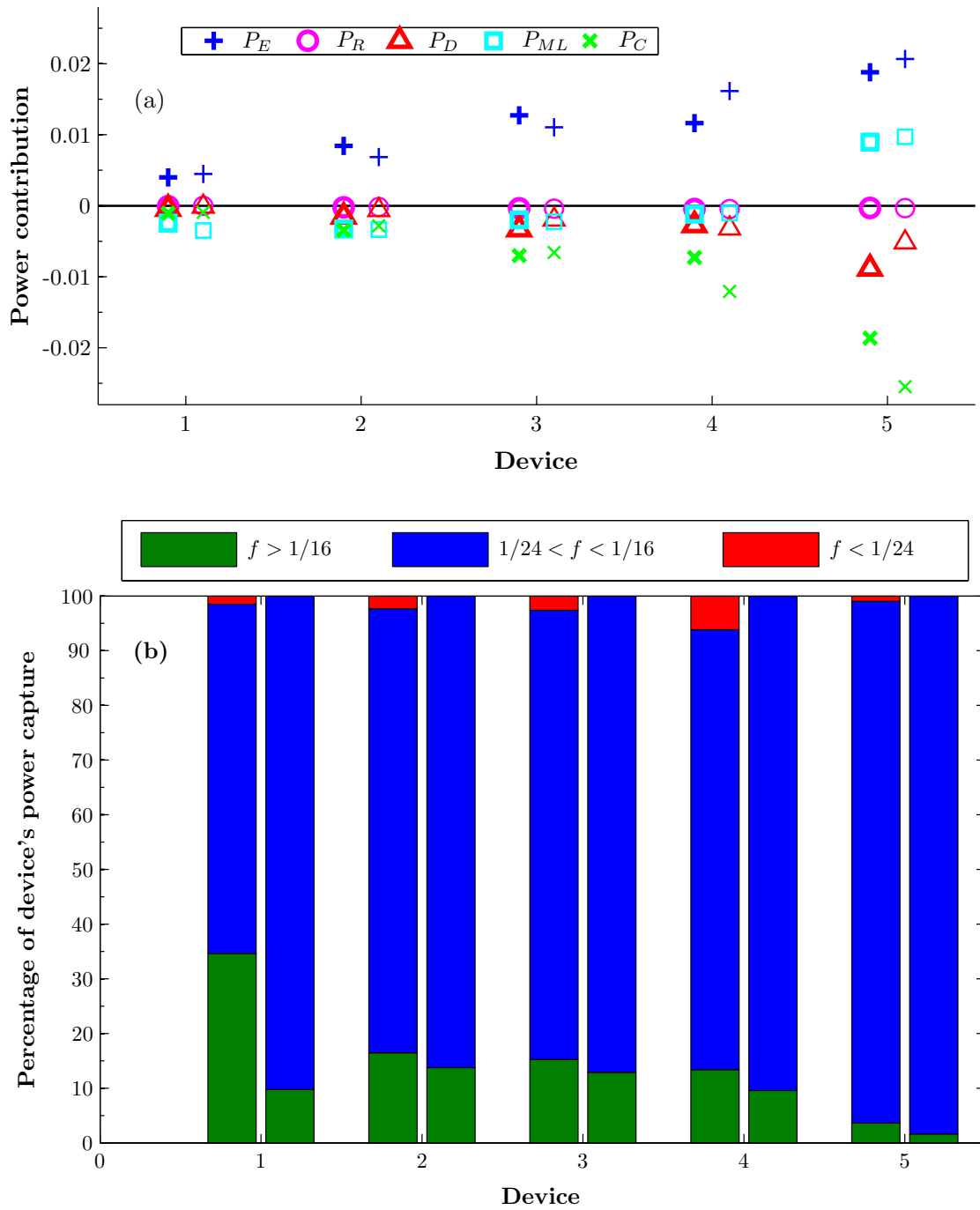


Figure 6.4: (a) The bold symbols on the left-hand side of each pair are the power contributions for each device of the N5A chain when forced by Spectrum A. The lighter symbols on the right-hand side of each pair give the sum of the values obtained when the N5A chain is forced by each spectral component of Spectrum A individually. (b) Percentage of the total power capture of each device associated with motion in three frequency bands: above, within, and below the range of Spectrum A. The left-hand and right-hand bar of each pair are as described in (a). The data were obtained by integrating the PSD.

6.2.2 Five device chain

Here we present a similar analysis to the previous section, this time for the N5A chain as defined in Section 6.1.1. Figure 6.4(a) shows the power contributions for the chain forced by Spectrum A, again compared with the sum of the values obtained when the chain is forced by each spectral component individually. Here the linear superposition significantly overestimates the power capture by the last two devices, but actually very slightly underestimates it for the first three. The power transfer by the moorings is estimated quite accurately. Overall, the results are qualitatively in line with what we would predict from the linear superposition.

In Figure 6.4(b), we show how the total power capture of each device is distributed with motion frequency. Unlike the lone device, there is a significant departure here from the monochromatic case. All devices show a higher proportion of power capture at high frequencies; especially Device 1, for which this constitutes over 30% of its (albeit small) total. All devices also show a small but significant percentage of power capture at frequencies below the spectral range. Device 4 exhibits a particularly strong response in this frequency band, constituting about 6% of its total power capture.

Figure 6.5(a) gives the PSD for all five devices in the N5A chain, along with the linear superposition of the PSDs obtained for forcing by the individual spectral components. The background level of the PSD is elevated many orders of magnitude higher than for the lone device, reflecting the greater nonlinearity of the linked chain. Peaks at harmonic frequencies of the spectral components are indistinguishable from this background level. Peaks at the beat frequencies can be clearly seen though, especially for Device 4, as shown in the close up of the low frequency range in subfigure (b).

Why does the chain respond to the low frequency beating so much more strongly than the lone device does? We performed additional test runs with a monochromatic wave field with $T = 50 \Rightarrow f = 0.02$. For device N1A this gives a power capture of 9.9×10^{-6} . For chain N5A, the mean power capture is 24 times as high at 2.4×10^{-4} , with the values for the individual devices ranging from twice as high (Device 1) to 50 times as high (Device 4). An explanation for why the chain performs so much better here is that, as we saw in Chapter 5, a chain can behave somewhat like a single body with the combined mass when the spacing is small relative to the wavelength (or close to a full wavelength). At $T = 50$, the spacing of the N5A chain is just 3% of the wavelength. Using linear theory (4.1) we predict the resonant spring stiffness at this period to be ≈ 0.023 for a single device; Device N1A is far off resonance with a spring stiffness ≈ 6.5 times this. S_{res} is proportional to mass, so for a five device chain behaving perfectly as a single body, resonance would be achieved with $S \approx 0.12$; Chain N5A's spring stiffness of 0.19 is reasonably close to this.

6.3 Performance of chains compared with lone devices

The question we are really interested in is, how do devices linked in a chain perform compared with a lone device? We showed in Chapter 5 that for a monochromatic wave

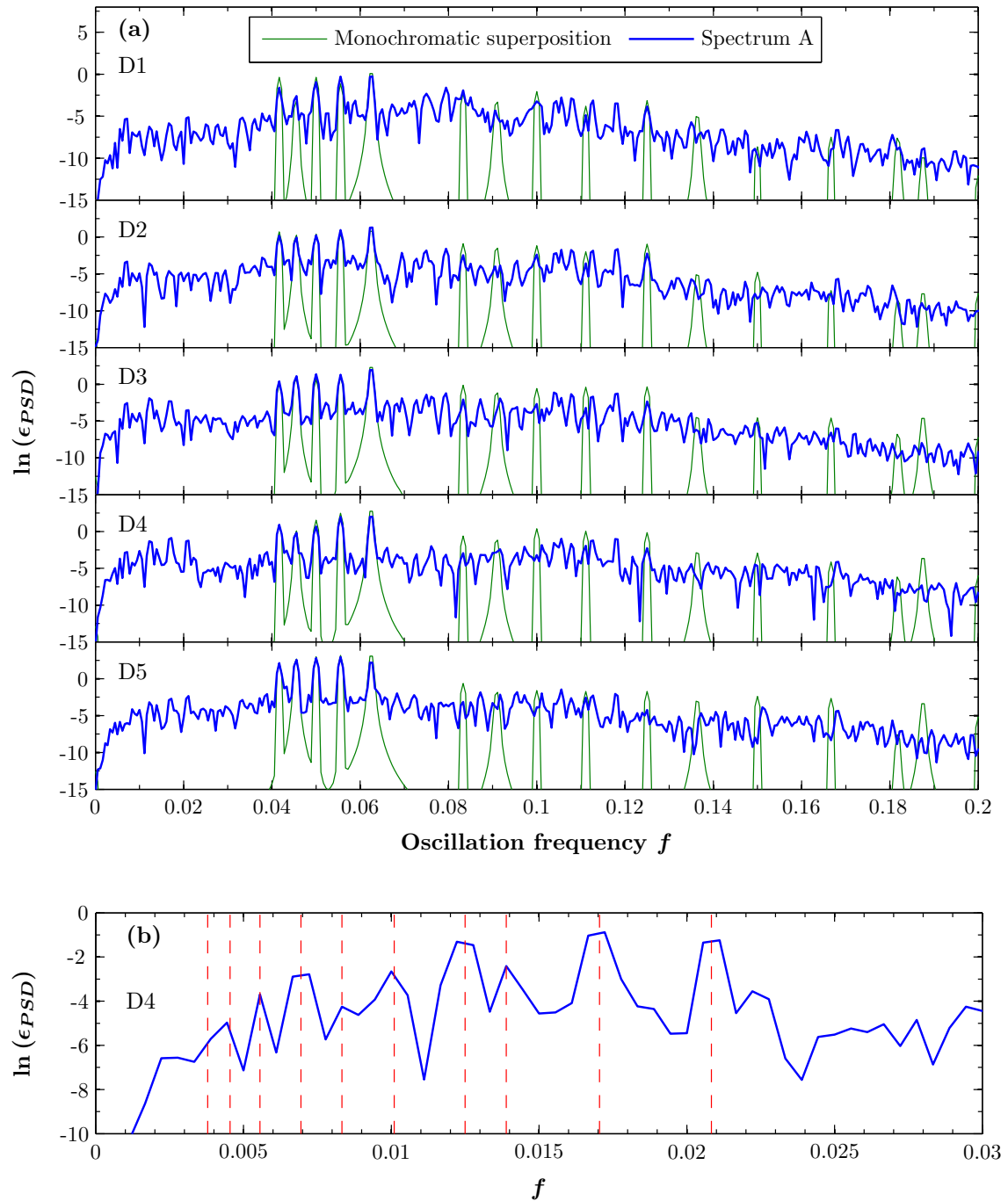


Figure 6.5: (a) Blue: Power spectral density for each device in the N5A chain, when forced by Spectrum A. Green: Superposition of the PSDs when the chain is forced by each spectral component individually. Note that this is a log plot. (b) Close-up of the low-frequency range for Device 4 in (a). The red dotted lines are drawn at beat frequencies $f_b = f_1 - f_2$ for the components of Spectrum A. Note that the vertical axis is logarithmic.

field of a given period, the per-device mean power capture for a chain cannot exceed that of a resonant lone device. We saw, however, that individual devices in a given chain can capture many times this much power and, furthermore, can exceed the optimum lone device power capture over a wide range of incident wave periods. Here we put these observations to the test with a more realistic wave field: the Bretschneider spectrum shown in Figure 6.1(b).

6.3.1 First test case

For our first test, we compare Chain N5B with Device N1A. Devices in Chain N5B are spaced half a wavelength apart for waves with $T = 20$, the peak period of the spectrum; for a monochromatic field of this period, the per-device mean power capture is virtually the same as that of Device N1A.

Figure 6.6(a) shows the time-averaged power contributions for these test cases in the Bretschneider wave field. Similarly to the monochromatic case with $T = 20$, the power is very evenly distributed across all five devices in the chain. However, the mean power capture for the chain is 25% lower than Device N1A here: 0.0052 compared to 0.0069.

Figure 6.6(b) illustrates how the devices' power captures are made up in terms of the Fourier components of the motion. The data shown are again obtained by integrating the PSD into the given period bins; for example, the bin labelled "10" covers $9 < T \leq 11$. Note that, in contrast to Spectrum A, the breadth of the Bretschneider spectrum means that there is overlap between the ranges of the fundamental frequencies (f_j), harmonic frequencies (nf_j), beat frequencies ($f_j - f_k$) and summed frequencies ($f_j + f_k$), making analysis of the PSD and the present figure more complicated. For both Chain N5B and Device N1A, the maximum responses come at an oscillation period near 20, with the chain displaying lower power capture at oscillation periods below, and slightly higher at oscillation periods above that. There is an anomaly: the chain exhibits a local maximum at the $T = 12$ bin, where it achieves almost the same mean power capture as the lone device. A very likely explanation for this is that the wavelength at $T = 11.55$ is $2/3$ of the device spacing – in other words, $L = 1.5\lambda_{T=11.55}$. Although the spring stiffness is well below the value to have the chain "resonate" at this wavelength³, the half-integer wavelength spacing appears to give rise to a strong peak. The fact that the power capture is quite evenly distributed amongst all five devices for this period bin is further evidence that adjacent devices are locking into anti-phase oscillations here. The peak may be further enhanced due to the overlap with the range of harmonic and summed frequencies (e.g. $1/12 = 2/24 = 1/20 + 1/30$).

6.3.2 Second test case

For the second test we use Chain N5A, for which it was shown in Figure 5.31 that Device 5 performs very favourably compared to any lone device for monochromatic

³For a lone device $S_{res}(T = 11.55) \approx 0.46$, so assuming that the modification to the resonant value (as explained in section 5.2.1) is of the same factor as at $T = 20$, a chain would achieve its maximum power capture with $S \approx 0.27$.

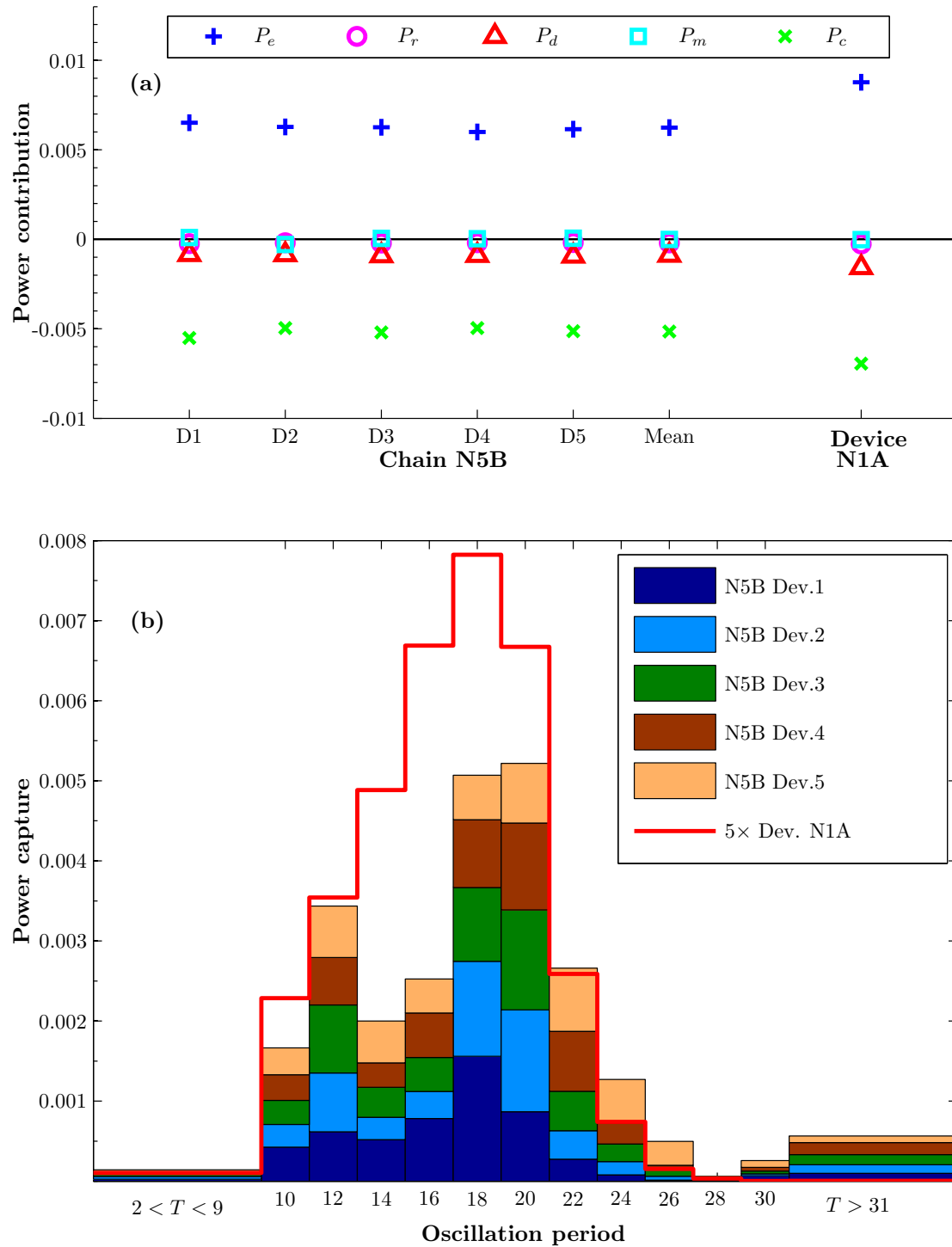


Figure 6.6: (a) Time-averaged power contributions for Chain N5B and Device N1A in the Bretschneider wave field. (b) Distribution of power capture with motion period, obtained by integrating the PSD into bins of width 2 centred on each value of T_j . The solid bars show the contribution for each device of Chain N5B, stacked to give the total for the chain. The red line is for Device N1A, multiplied by five for comparison to the chain. Figure 4.1 allows conversion to period in seconds.

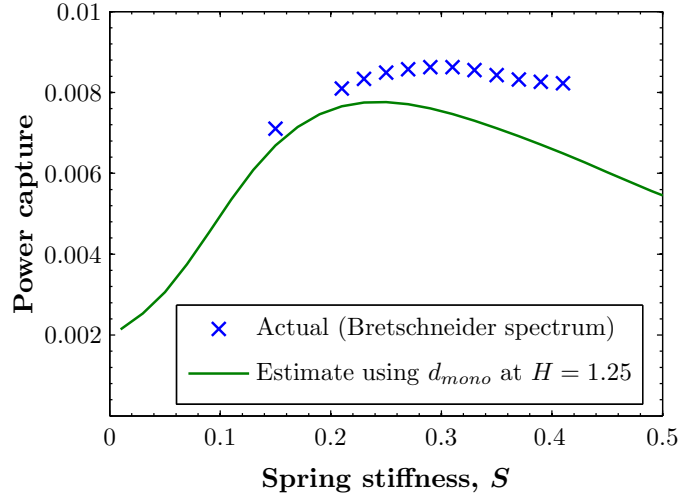


Figure 6.7: Blue crosses: power captured by a lone device with spring stiffness S in the Bretschneider wave field. Green line: estimate made using the monochromatic capture width data shown in Figure 4.6, as detailed in the main text.

fields with $15 < T < 30$. The device spacing is $L = 3/16 \times \lambda_{T=20} = 0.5\lambda_{T=12.25}$. For the lone device comparison, we wish to use the device giving the optimum power capture for this particular spectrum. Note that this will not necessarily be Device N1A simply because it is resonant at the peak period. In fact, since the device's capture width falls away with increasing wave period⁴, it is beneficial to have the device tuned to resonate at a period less than T_p ; the lower incident power is more than compensated for by the higher capture width.

As a brief aside, it should be possible to make a reasonable estimate of the spring stiffness required to give optimum power capture for a given spectrum, by taking monochromatic capture width curves for different S , multiplying them by the incident spectrum, and integrating to see which S value gives the highest result. As we have seen previously, however, a problem with this approach is that the capture width is not independent of incident power. Figure 6.7 shows actual power capture results for lone devices with different S when forced by the Bretschneider spectrum, along with one such attempt at an estimate using available monochromatic data. This attempt clearly underestimates the optimum S value, as well as the maximum power capture, but it does provide a ballpark figure from which to start investigation. Using data with H closer to the heights of the spectral components may give a more accurate result.

Looking at the actual power capture results in Figure 6.7, we see that the maximum is $P_C = 0.0086$, achieved with $S = 0.31 \approx S_{res}(T = 14)$. This is what we have called Device N1B. Figure 6.8(a) shows the time-averaged power contributions for Chain N5A and Device N1B in the Bretschneider wave field, and Figure 6.8(b) shows the breakdown of

⁴See Figure 4.12(b). Note that for low wave heights, the capture width is not simply monotonically decreasing with wave period, and has a small 'bump' around $T \approx 18$.

the power captures with Fourier components of the motion as explained for Figure 6.6(b).

First, we observe that the power captured by Device 5 is 0.015: 75% more than Device N1B. This is only slightly below the best percentage improvement over the resonant lone device observed in monochromatic cases. This confirms that, as predicted from Figure 5.31, it is possible for individual devices in a chain to achieve significantly enhanced power capture in wave fields with broad spectra.

Second, comparing with an example such as Figure 5.24(d), the performance of the other devices is not suppressed to the extent that we observe in the monochromatic case. Looking at Figure 6.8(b), we see that at certain oscillation periods (e.g. 18) Device 5 is capturing many times as much power as the other devices, but when averaged over the wider period range the power capture is more evenly distributed.

Finally, following on from this last point, we observe the surprising result that the *mean* power capture per device for Chain N5A actually exceeds that of Device N1B: 0.0092 compared with 0.0086. It appears that the wider bandwidth of the chain, which is weighted towards longer wave periods, more than compensates for the lower peak in power capture versus oscillation period. We note that this result should be viewed with slight caution, since truncation of the spectrum at $T = 9$ apparently has a greater effect on the power capture of Device N1B than Chain N5A. However, referring back to Figure 5.32 and its discussion, we expect that the power capture of the chain will not decline monotonically for smaller wave periods, but will exhibit more local maxima at periods for which the spacing is a half-integral multiple of the wavelength. Thus it appears most likely that the mean power capture of the chain would remain higher than that of the lone device.

In addition to the discussion in the last paragraph, it should also be emphasised that Chain N5A has not been optimised for this particular spectrum, while Device N1B has. It is therefore almost certain that Chain N5A's performance can be exceeded and the margin of improvement over Device N1B increased, but by how much it is impossible to say. Altogether, we believe it is very likely that this result is robust and, according to our model, a slightly higher total power capture can be achieved in a broad spectrum with a linked chain of devices than with the same number of lone devices.

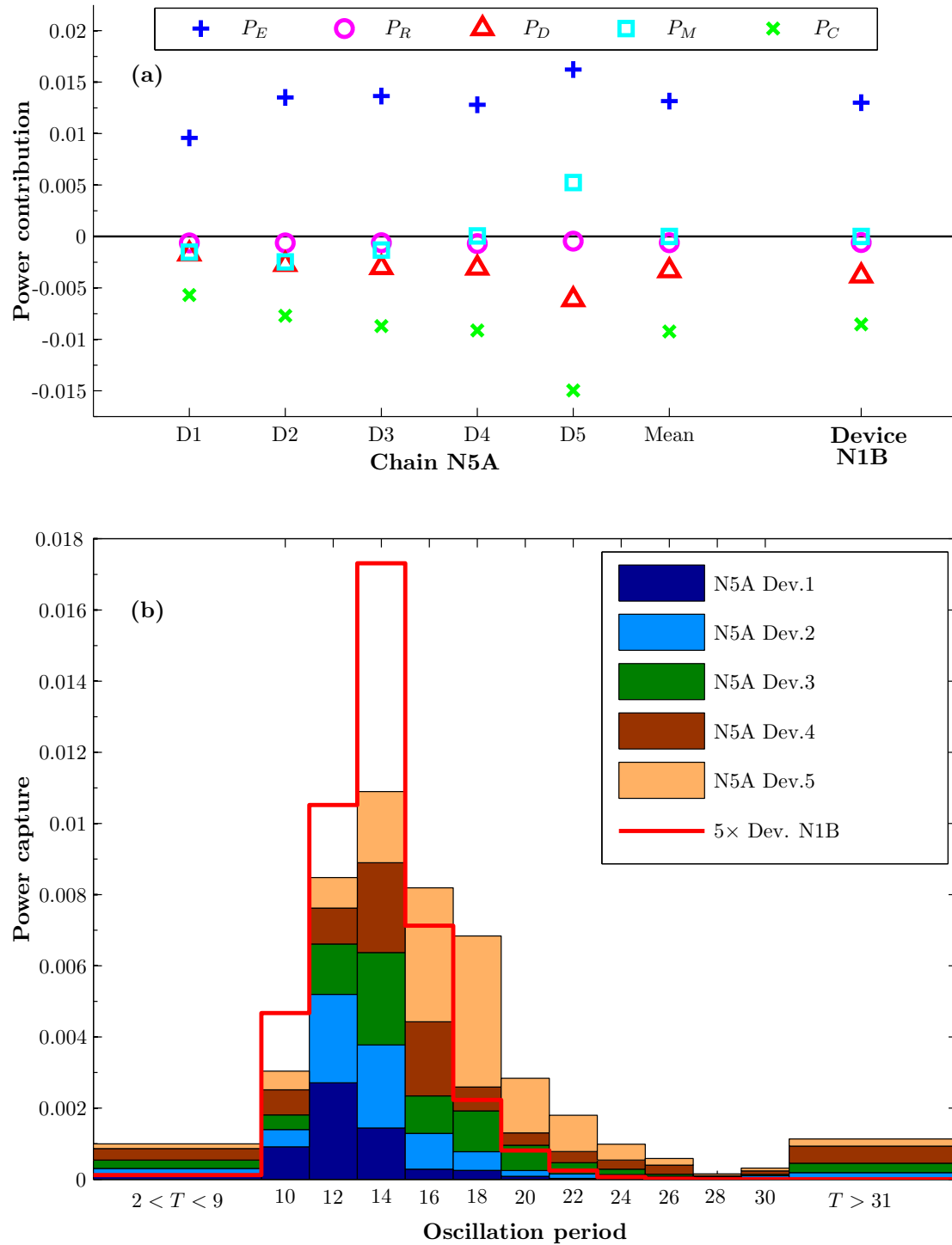


Figure 6.8: (a) Time-averaged power contributions for Chain N5A and Device N1B in the Bretschneider wave field. (b) Distribution of power capture with motion period, obtained by integrating the PSD into bins of width 2 centred on each value of T_j . The solid bars show the contribution for each device of Chain N5A, stacked to give the total for the chain. The red line is for Device N1B, multiplied by five for comparison to the chain. Figure 4.1 allows conversion to period in seconds.

Chapter 7

Conclusions

In this thesis we have described the development and use of an idealised 1-D computational model of a chain of surging point absorbers, linked together with lines that act as tension-only springs. We have used this model to explore the effects of the inter-device linkages throughout the parameter space, focusing predominantly on the metric of power capture. Our key findings, providing answers to the research questions laid out in Section 1.9, can be summarised as follows:

1. For linked devices, results can be substantially affected by whether the radiation force is calculated using a memory integral or using the Morison equation formulation with constant hydrodynamic coefficients. We conclude that the memory integral must be used to accurately capture the dynamics, even for a monochromatic incident wave field. (Chapter 3)
2. Our results suggest that for monochromatic incident waves, a linked chain cannot capture more power in total than the same number of devices could acting in isolation. The optimal lone device performance can be approximately equalled when the spacing between devices is a half-integral multiple of the wavelength, where the system dynamics are virtually identical to the lone device case. (Chapter 5)
3. However, simulations with a polychromatic incident wave field suggest that in a continuous wave spectrum, a linked chain could capture slightly more power overall than the same number of devices in isolation. This is apparently due to a broadened bandwidth (weighted towards better performance at longer wave periods) and a small but significant contribution to the power capture from motion at frequencies above and below the range of the incident spectrum. (Chapter 6)
4. For monochromatic incident wave fields, individual devices in a linked chain can attain significantly enhanced power captures relative to a lone device – perhaps more than twice as large – and this enhancement is maintained for polychromatic wave fields. The effect initially grows with chain length but is subject to diminishing returns. (Chapters 5 and 6)

These findings are contingent on a number of assumptions and conditions – such as unidirectional waves, no hydrodynamic interactions between devices, and idealised mooring/linkage, power take-off and drag forces – which were summarised in Section 3.16. The findings are also based on a limited exploration of the available parameter space; it is possible, for example, that the second conclusion could be overturned by tweaking the device spacing, line stiffness and PTO resistance individually for each component of the chain. A particular aspect that we have not explored is pretensioning of the mooring and linkage lines. The full range of parameters and options is immense, leaving much scope for further work.

Despite the simplicity and idealised nature of the model used in this study, we believe that the results offer useful guidance. The first conclusion listed above may be of interest to the wave energy modelling community, while the other findings offer several practical implications for wave energy schemes. If, as our third conclusion implies, it is indeed possible to attain similar levels of power capture by linking devices in an array rather than mooring each independently to the seabed, this idea could allow developers to reduce installation costs as well as disturbance to the marine ecology.

The most promising, and perhaps most important, discovery relates to the fourth conclusion. We have demonstrated the potential for passive power transfer along the linked chain through the action of the linkage lines. It may seem a pointless pursuit to maximise the performance of one device at the expense of the others here, but the observation inspires a novel concept that had not been conceived of at the beginning of this study: the use of “dummy devices” – cheaply produced bodies with no PTO system that exist solely to boost the power capture of the true devices. The most direct exploration of this idea was presented in Section 5.6.2, where the PTO resistance was set to zero on all but the end device in a three-device chain. This showed potential for dummy devices to yield even larger power capture gains than suggested by the main body of simulations, where all devices had the same PTO resistance. As evidenced by Figure 5.31, using as few as two dummy devices could give a better performance over an entire range of wave frequencies than having the device optimally tuned for each individual frequency. Of course, in reality there is no requirement that the dummy devices have the same form and characteristics as the true devices, and we have only scratched the surface of the idea here.

This last comment can be taken even further; while this study explored the concept of linked point absorbers through the frame of a particular geometry and set-up, we consider that the findings have much broader applications. In particular, the dummy device concept can be generalised to a class of ideas that use additional bodies and moorings to passively enhance the power capture. Engström et al provide a good example in [24], exploring the use of a supplementary submerged body connected below a heaving point absorber. As well as seeking to enhance the power capture in general, ideas such as these offer potential for customising a mass-produced device to suit specific local wave climates and environments, in a cost-effective way.

There are many open questions about the practical feasibility of the specific scheme we have proposed; do the kind of device spacings envisaged constitute an inefficient use

of space? Can mooring and linkage lines be designed for this kind of application, and will they give a similar response to that used in our model? What about the PTO system? How will the results change for wave fields incident at an angle to the chain axis? Or in the presence of ocean tides and currents? Could the chain have some sort of active or passive control to allow adaptive orientation and device spacing? Is the scheme only suitable for near-shore deployment? These (and other) questions necessitate further study. While some are in the realm of engineering and require physical experiments, some call for further development of the computational model. Logical next steps include: expanding the model to two or three dimensions; including hydrodynamic interactions between the devices; including the dynamics of the mooring and linkage lines; and incorporating a more realistic PTO model, such as a self-reacting point absorber design.

To conclude, it is apparent that the present work opens up a range of possibilities for a new approach to extracting energy from ocean waves.

Appendices

Appendix A

Power transfer by linkage line

Here we derive the result (5.7) for the (time-average) power transfer via the linkage line. This result is for two linked devices both oscillating sinusoidally about their starting positions with common frequency ω , displacement amplitudes A_1 and A_2 respectively, and Device 1 leading Device 2 with a phase difference of ϕ . That is,

$$x'_1 = A_1 \cos(\omega t), \quad (\text{A.1})$$

$$x'_2 = A_2 \cos(\omega t - \phi) \quad (\text{A.2})$$

$$= A_2 [\cos(\omega t) \cos \phi + \sin(\omega t) \sin \phi], \quad (\text{A.3})$$

where $\mathbf{x}' = \mathbf{x} - \mathbf{x}|_{t=0}$, and we have used the trigonometric identity

$$\cos(A \pm B) = \cos A \cos B \mp \sin A \sin B. \quad (\text{A.4})$$

Subtracting gives

$$x'_2 - x'_1 = [A_2 \cos \phi - A_1] \cos(\omega t) + A_2 \sin \phi \sin(\omega t) \quad (\text{A.5})$$

$$= A' \sin(\omega t + \sigma), \quad (\text{A.6})$$

where σ satisfies

$$\sin \sigma = \frac{A_2 \cos \phi - A_1}{A'}, \quad (\text{A.7})$$

$$\cos \sigma = \frac{A_2}{A'} \sin \phi, \quad (\text{A.8})$$

and we have used the identity

$$\sin(A \pm B) = \sin A \cos B \pm \cos A \sin B \quad (\text{A.9})$$

The force exerted by the linkage line (3.11) is non-zero when $x'_2 - x'_1 > 0$, which is satisfied here for $\sin(\omega t + \sigma) > 0$. Choosing σ in the range $[-\pi, \pi]$, the force is non-zero for

$$-\sigma/\omega < t < (\pi - \sigma)/\omega. \quad (\text{A.10})$$

The power transfer due to the linkage line for Device 1 is

$$(P_{ML})_1 = T^{-1} \int_{t_0}^{t_0+T} (F_{ML})_1 v_1 dt \quad (\text{A.11})$$

$$= - \frac{A_1 A' S \omega^2}{2\pi} \int_{-\sigma/\omega}^{(\pi-\sigma)/\omega} \sin(\omega t + \sigma) \sin(\omega t) dt \quad (\text{A.12})$$

$$= - \frac{A_1 A' S \omega^2}{2\pi} \int_{-\sigma/\omega}^{(\pi-\sigma)/\omega} \{\cos \sigma - \cos(4\omega t + \phi)\} dt, \quad (\text{A.13})$$

$$(\text{A.14})$$

where in the last line we used the identity

$$2 \sin A \sin B = \cos(A - B) - \cos(A + B). \quad (\text{A.15})$$

The second integral in (A.13) is zero, leaving simply

$$(P_{ML})_1 = - \frac{A_1 A' S \omega^2}{4\pi} \cos \sigma \frac{\pi}{\omega} \quad (\text{A.16})$$

$$= - \frac{A_1 S \omega}{4} A' \cos \sigma. \quad (\text{A.17})$$

Finally, using (A.8), we arrive at

$$(P_{ML})_{1,2} = \mp \frac{A_1 A_2 S \omega}{4} \sin \phi. \quad (\text{A.18})$$

Bibliography

- [1] Article 2, The United Nations Framework Convention on Climate Change.
- [2] Climate Action Tracker. <http://www.climateactiontracker.org/>. Accessed 3 May 2010.
- [3] WaveNet. Results from the work of the European Thematic Network on Wave Energy, 2003.
- [4] International Energy Agency. Key world energy statistics, 2010.
- [5] International Energy Agency. World energy outlook 2010, 2010.
- [6] G. Allan, M. Gilmartin, P. McGregor, and K. Swales. Levelised costs of wave and tidal energy in the UK: Cost competitiveness and the importance of 'banded' Renewables Obligation Certificates. *Energy Policy*, 39:23–39, 2011.
- [7] K. Anderson and A. Bows. Beyond 'dangerous' climate change: emission scenarios for a new world. *Philosophical Transactions of the Royal Society A*, 369:20–44, 2010. doi: 10.1098/rsta.2010.0290.
- [8] J. S. Bendat and A. G. Piersol. *Random Data: Analysis and Measurement Procedures*. Wiley-Interscience, 1971.
- [9] R. Berard. Power and Energy from the Ocean Energy Waves and Tides: A Primer. EPRI, 2007.
- [10] D. T. Brown and S. Mavrakos. Comparative study on mooring line dynamic loading. *Marine Structures*, 12:131–151, 1999.
- [11] K. Budal and J. Falnes. A resonant point absorber of ocean-wave power. *Nature*, 256:478–479, 1975.
- [12] R. Burrows, R. G. Tickell, D. Hames, and G. Najafian. Morison wave force coefficients for application to random seas. *Applied Ocean Research*, 19:183–199, 1997.
- [13] Carbon Trust. Future Marine Energy. Results of the Marine Energy Challenge: Cost Competitiveness and Growth of Wave and Tidal Stream Energy, 2006.

- [14] R. G. Carter and D. P. Hurdle. Wave power absorption by a small body moving in surge. *Applied Ocean Research*, 5(1):24–29, 1983.
- [15] A. J. Caska and T. D. Finnigan. Hydrodynamic characteristics of a cylindrical bottom-pivoted wave energy absorber. *Ocean Engineering*, 35:6–16, 2008.
- [16] A. S. Chitrapu and R. C. Ertekin. Time-domain simulation of large-amplitude response of floating platforms. *Ocean Engineering*, 22(4):367–385, 1995.
- [17] J. Cruz, editor. *Ocean Wave Energy: Current Status and Future Perspectives*. Springer, 2008.
- [18] M. A. Delucchi and M. Z. Jacobson. Providing all global energy with wind, water, and solar power, part ii: Reliability, system and transmission costs, and policies, and materials. *Energy Policy*, 39:1170–1190, 2011.
- [19] M. W. Denny, B. P. Gaylord, and E. A. Cowen. Flow and flexibility: II. The roles of size and shape in determining wave forces on the bull kelp. *Journal of Experimental Biology*, 200:3165–3183, 1997.
- [20] B. Drew, A. R. Plummer, and M. N. Sahinkaya. A review of wave energy converter technology. *Proceedings of the Institution of Mechanical Engineers*, 223:887–902, 2009. Part A: J. Power and Energy.
- [21] D. Dunnett and J. S. Wallace. Electricity generation from wave power in Canada. *Renewable Energy*, 34:179–195, 2009.
- [22] O. Edenhofer, R. Pichs-Madruga, Y. Sokona, K. Seyboth, D. Arvizu, T. Bruckner, J. Christensen, J.-M. Devernay, A. Faaij, M. Fishedick, B. Goldstein, G. Hansen, J. Huckerby, A. Jger-Waldau, S. Kadner, D. Kammen, V. Krey, A. Kumar, A. Lewis, O. Lucon, P. Matschoss, L. Maurice, C. Mitchell, W. Moomaw, J. Moreira, A. Nadai, L.J. Nilsson, J. Nyboer, A. Rahman, J. Sathaye, J. Sawin, R. Schaeffer, T. Schei, S. Schlmer, R. Sims, A. Verbruggen, C. von Stechow, K. Urama, R. Wiser, F. Yamba, and T. Zwickel. *IPCC Special Report on Renewable Energy Sources and Climate Change Mitigation, Summary for Policy Makers*. Cambridge University Press, Cambridge, United Kingdom and New York, NY, USA, 2011.
- [23] Electric Power Research Institute. E2I EPRI Assessment – Offshore Wave Energy Conversion Devices, 2004.
- [24] J. Engström, M. Eriksson, J. Isberg, and M. Leijon. Wave energy converter with enhanced amplitude response at frequencies coinciding with Swedish west coast sea states by use of a supplementary submerged body. *Journal of Applied Physics*, 106, 2009.
- [25] European Marine Energy Centre. <http://www.emec.org.uk/>.

- [26] D. V. Evans and P. McIver. Added mass and damping of a sphere section in heave. *Applied Ocean Research*, 6(1):45–53, 1984.
- [27] A. F. O. Falcão. Wave energy utilization: A review of the technologies. *Renewable and Sustainable Energy Reviews*, 14:899–918, 2010.
- [28] J. Falnes. Technical note: Comments on ‘Added mass and damping of a sphere section in heave’. *Applied Ocean Research*, 6(4):229–230, 1984.
- [29] J. Falnes. *Ocean Waves and Oscillating Systems*. Cambridge University Press, 2002.
- [30] J. Falnes. Optimum control of oscillation of wave-energy converters. *International Journal of Offshore and Polar Engineering*, 12(2):147–155, 2002.
- [31] J. Falnes. A review of wave-energy extraction. *Marine Structures*, 20:185–201, 2007.
- [32] F. Fitzgerald and L. Bergdahl. Including moorings in the assessment of a generic offshore wave energy converter: A frequency domain approach. *Marine Structures*, 21:23–46, 2008.
- [33] M. Folley and T. J. T. Whitaker. Analysis of the nearshore wave energy resource. *Renewable Energy*, 34:1709–1715, 2009.
- [34] M. Folley, T. J. T. Whitaker, and A. Henry. The effect of water depth on the performance of a small surging wave energy converter. *Ocean Engineering*, 34:1265–1274, 2007.
- [35] R. M. Gorman, K. R. Bryan, and A. K. Laing. Wave hindcast for the new zealand region: nearshore validation and coastal wave climate. *New Zealand Journal of Marine and Freshwater Research*, 37:567–588, 2003.
- [36] M. Greenhow and S. P. White. Optimal heave motion of some axisymmetric wave energy devices in sinusoidal waves’. *Applied Ocean Research*, 19:141–159, 1997.
- [37] H. T. Harvey & Associates. Developing wave energy in coastal California: Potential socio-economic and environmental effects, 2008. Report prepared for California Ocean Protection Council and California Energy Commission.
- [38] J. Hansen, M. Sato, P. Kharecha, D. Beerling, R. Berner, V. Masson-Delmotte, M. Pagani, M. Raymo, D. L. Royer, and J. C. Zachos. Target atmospheric CO₂: Where should humanity aim? *The Open Atmospheric Science Journal*, 2:217–231, 2008. doi:10.2174/1874282300802010217.
- [39] R. E. Harris, L. Johanning, and J. Wolfram. Mooring systems for wave energy converters: a review of design issues and choices. In *3rd International Conference on Marine Renewable Energy, MAREC*, London, 2004. The Institute of Marine Engineering, Science and Technology.

- [40] R. Heinberg and D. Fridley. The end of cheap coal. *Nature*, 468:367–369, 2010. Note this is a comment piece.
- [41] R. L. Hirsch, R. Bezdec, and R. Wendling. Peaking of world oil production: Impacts, mitigation, and risk management. Technical report, Department of Energy National Energy Technology Laboratory, February 2005.
- [42] M. K. Hubbert. Nuclear energy and the fossil fuels. Presented before the Spring Meeting of the Southern District, American Petroleum Institute, Plaza Hotel, San Antonio, Texas, March 1956.
- [43] A. Hulme. The wave forces acting on a floating hemisphere undergoing forced periodic oscillations. *Journal of Fluid Mechanics*, 121:443–463, 1981.
- [44] M. de St. Q. Isaacson. Nonlinear inertia forces on bodies. *Journal of the Waterway, Port, Coastal and Ocean Division*, (WW3):213–227, 1979.
- [45] L. C. Iversen. Experimental study of the deviation from linear behaviour for a submerged point absorber. *Applied Ocean Research*, 4(1):33–40, 1982.
- [46] M. Z. Jacobson and M. A. Delucchi. Providing all global energy with wind, water, and solar power, part i: Technologies, energy resources, quantities and areas of infrastructure, and materials. *Energy Policy*, 39:1154–1169, 2011.
- [47] E. R. Jefferys. Simulation of wave power devices. *Applied Ocean Research*, 6(1):31–39, 1984.
- [48] A. Kyllingstad. A low-scattering approximation for the hydrodynamic interactions of small wave-power devices. *Applied Ocean Research*, 6(3):132–139, 1984.
- [49] L. D. Landau and E. M. Lifshitz. *Fluid Mechanics*. Pergamon Press, 1963.
- [50] L. Le-Ngoc, A. I. Gardiner, R. J. Stuart, A. J. Caughley, and J. A. Huckerby. Progress in the development of a multi-mode self-reacting wave energy converter. In *Oceans 2010*, Oceans-IEEE, pages 1–7. IEEE, 2010.
- [51] J. Lighthill. Fundamentals concerning wave loading on offshore structures. *Journal of Fluid Mechanics*, 173:667–681, 1986.
- [52] Power Projects Limited. Development of Marine Energy in New Zealand, report prepared for Electricity Commission Energy Efficiency and Conservation Authority & Greater Wellington Regional Council, 2008.
- [53] B. Lloyd and A. S. Forest. The transition to renewables: Can PV provide an answer to the peak oil and climate change challenges? *Energy Policy*, 38:7378–7394, 2010.
- [54] P. McIver. Wave interaction with arrays of structures. *Applied Ocean Research*, 24:121–126, 2002.

- [55] P. McIver and D. V. Evans. The occurrence of negative added mass in free-surface problems involving submerged oscillating bodies. *Journal of Engineering Mathematics*, 18:7–22, 1984.
- [56] C. McLachlan. 'You don't do a chemistry experiment in your best china': Symbolic interpretations of place and technology in a wave energy case. *Energy Policy*, 12(37):5342–5350, 2009.
- [57] J. R. Morison, M. P. O'Brien, J. W. Johnson, and S. A. Schaaf. The force exerted by surface waves on piles. *Petroleum Transactions*, 189:149–156, 1950.
- [58] M. Mueller and R. Wallace. Enabling science and technology for marine renewable energy. *Energy Policy*, 36:4376–4382, 2008.
- [59] J. N. Newman. *Marine Hydrodynamics*. MIT Press, 1980.
- [60] J. N. Newman. Wave effects on multiple bodies. In M. Kashiwagi, editor, *Hydrodynamics in Ship and Ocean Engineering*, pages 3–26. RIAM, Kyushu University, 2001.
- [61] Intergovernmental Panel on Climate Change. Climate change 2007: Synthesis report, 2007.
- [62] D. J. Pizer. Maximum wave-power absorption of point absorbers under motion constraints. *Applied Ocean Research*, 15:227–234, 1993.
- [63] W. H. Press, S. A. Teukolsky, W. T. Vetterling, and B. P. Flannery. *Numerical Recipes in C: The Art of Scientific Computing*. Cambridge University Press, 2 edition, 1992.
- [64] A. A. E. Price. *New Perspectives on Wave Energy Converter Control*. PhD thesis, The University of Edinburgh, 2009.
- [65] W. Raman-Nair, B. Colbourne, M. Gagnon, and P. Bergeron. Numerical model of a mussel longline system: Coupled dynamics. *Ocean Engineering*, 35:1372–1380, 2008.
- [66] S. H. Salter. Wave power. *Nature*, 249:720–724, 1974.
- [67] T. Sarpkaya. On the force decompositions of lighthill and morison. *Journal of Fluids and Structures*, 15:227–233, 2001.
- [68] T. Sarpkaya and M. Isaacson. *Mechanics of Wave Forces on Offshore Structures*. Van Nostand Reinhold Company, 1981.
- [69] J. L. Sawin and E. Martinot. Renewables 2010 global status report. Technical report, REN21, 2010.

- [70] P. D. Schwartzman and D. W. Schwartzman. A solar transition is possible. Technical report, Institute for Policy Research and Development, March 2011.
- [71] R. E. H. Sims, R. N. Schock, A. Adegbululgbé, J. Fenhann, I. Konstantinavičiute, W. Moomaw, H. B. Nimir, B. Schlamadinger, J. Torres-Martnez, C. Turner, Y. Uchiyama, S. J. V. Vuori, N. Wamukonya, and X. Zhang. *Climate Change 2007: Mitigation. Contribution of Working Group III to the Fourth Assessment Report of the Intergovernmental Panel on Climate Change*, chapter Energy supply. Cambridge University Press, Cambridge, United Kingdom and New York, NY, USA, 2007.
- [72] M. J. Smith, R. Gorman, and C. L. Stevens. Marine (wave) resources. In *EnergyScape Basis Review*, pages 71–95. 2009.
- [73] S. Sorrell, R. Miller, R. Bentley, and J. Speirs. Oil futures: A comparison of global supply forecasts. *Energy Policy*, 2010.
- [74] C. L. Stevens, C. L. Hurd, and M. J. Smith. An idealized model of interaction between fronds of the large seaweed *Durvillea antarctica*. *Journal of Marine Systems*, 49:145–156, 2004.
- [75] C. L. Stevens, D. R. Plew, M. J. Smith, and D.W. Fredriksson. Hydrodynamic forcing of long-line mussel farms: observations. *Journal of Waterway, Port, Coastal, and Ocean Engineering*, 133:192–199, 2007.
- [76] E. D. Stoutenburg and M. Z. Jacobson. Optimizing offshore transmission links for marine renewable energy farms. In *Oceans 2010*, Oceans-IEEE. IEEE, 2010.
- [77] G. P. Thomas and D. V. Evans. A hydrodynamic model of a submerged lenticular wave energy device. *Applied Ocean Research*, 5(3):69–79, 1983.
- [78] T. W. Thorpe. A Brief Review of Wave Energy, May 1999. Report prepared for the UK Department of Trade and Industry.
- [79] UNFCCC. Outcome of the work of the ad hoc working group on long-term cooperative action under the convention, 2010.
- [80] P. C. Vicente, A. F. O. Falco, L. M. C. Gato, and P. A. P. Justino. Dynamics of arrays of floating point-absorber wave energy converters with inter-body and bottom slack-mooring connections. *Applied Ocean Research*, 31:267–281, 2009.
- [81] M. B. Widden, M. J. French, and Aggidis G. A. Analysis of a pitching-and-surfing wave-energy converter that reacts against an internal mass, when operating in regular sinusoidal waves. *Proceedings of the Institution of Mechanical Engineers*, 222:153–161, 2008. Part M: J. Engineering for the Maritime Environment.
- [82] J. Wolfram and M. Naghipour. On the estimation of morison force coefficients and their predictive accuracy for very rough circular cylinders. *Applied Ocean Research*, 21:311–328, 1999.

- [83] World Energy Council. *Survey of Energy Resources*. Elsevier, 2004.
- [84] WWF, ECOFYS and OMA. The energy report: 100% renewable by 2050, 2011.
- [85] Z. Yu and J. Falnes. State-space modelling of a vertical cylinder in heave. *Applied Ocean Research*, 17:265–275, 1995.